TOTAL IN-FLIGHT SIMULATOR (TIFS) – PRELIMINARY DESIGN REPORT

FLIGHT RESEARCH DEPARTMENT STAFF

CORNELL AERONAUTICAL LABORATORY, INC.

FOREWORD

This preliminary design report concerning the Total In-Flight Simulator (TIFS) was prepared by the Cornell Aeronautical Laboratory, Inc., Buffalo, New York, in partial fulfillment of the reporting requirements of USAF Contract No. F33615-67-C-1157, Project No. 684B. The work was administered under the direction of the Air Force Flight Dynamics Laboratory, Air Force Systems Command, Wright-Patterson Air Force Base, Ohio, with J. R. Pruner as Project Engineer.

The work reported in this document was conducted by the Flight Research Department of the Cornell Aeronautical Laboratory, Inc. Dr. P. A. Reynolds was the CAL Project Manager, and Mr. J. C. Seal was the Assistant Project Manager. This report covers the TIFS development through the period from 15 November 1966 to 15 June 1967. The authors of this report are many: R. H. Arendt, S. J. Asseo, W. Close, W. L. Deboy, J. N. Dittenhauser, S. L. Hazen, F. E. Pritchard, P. A. Reynolds, D. W. Rhoads, A. E. Schelhorn, R. J. Siracuse, and O. B. Tufts.

Although the TIFS development was carried out primarily by the Flight Research Department, significant supporting effort was supplied by other departments at CAL, in particular the Applied Mechanics and the Computer Services Departments. The entire TIFS project was under the supervision of Mr. W. O. Breuhaus, Head of the Flight Research Department.

This technical report has been reviewed and is approved.

C. B. WESTBROOK
Chief, Control Criteria Branch
Flight Control Division
Air Force Flight Dynamics Laboratory

ABSTRACT

The TIFS research airplane has been developed by the Cornell Aeronautical Laboratory under the sponsorship of the Air Force Flight Dynamics Laboratory. As the most advanced in-flight simulation vehicle yet developed, it has been designed to provide Total In-Flight Simulation. This capability depends on two basic features of the aircraft. First is the addition of an evaluation cockpit which is entirely separate from the normal airplane's safety pilots' cockpit. Second is the control by a variable stability system of not only the moments about all three axes, but also the forces acting along the three axes. This report describes the TIFS airplane development during the period from November 1966 to June 1967.

CONTENTS

CONTENTS (Cont.)

ILLUSTRATIONS

ILLUSTRATIONS (Cont.)

ILLUSTRATIONS (Cont.)

ILLUSTRATIONS (Cont.)

ILLUSTRATIONS (Cont.)

TABLES

NOMENCLATURE AND SYMBOLS

This list presents the standardized nomenclature and symbols used on the TIFS Program.

The following standard units are used:

Distance	-	feet
Time	-	seconds
Angle	-	radians or degrees
Force	-	pounds
Moments	-	foot-pounds
Mass	-	slugs

Axis Systems (See Figures A and 2.1)

The origin for these axis systems is located at the c.g. of the aircraft except when noted otherwise. These axis systems are orthogonal and positive according to the right hand rule.

x, y, z — body axes, x-z plane is in the plane of symmetry of the airplane with x directed forward parallel to the fuselage reference line, z directed downward, and y directed out the right wing. See Figure A.

x_s, y_s, z_s — stability axes, x_s-z_s plane is in the plane of symmetry of the airplane with $z_s = z_w$ and $y_s = y$. The stability axes become fixed in perturbation analysis, their positions given by the reference value of α.

x_w, y_w, z_w — wind axes, x_w is along the velocity vector (of airplane with respect to air) with $z_w = z_s$. The wind axes become fixed in perturbation analysis, their positions given by reference values of α and β.

x_E, y_E, z_E — earth surface axes, origin is fixed at the center of gravity of the airplane, z_E is located along the gravity vector of the airplane, x_E is pointed north, and y_E is pointed east. It is assumed to be an inertial coordinate system, and in perturbation analysis remain fixed relative to the earth.

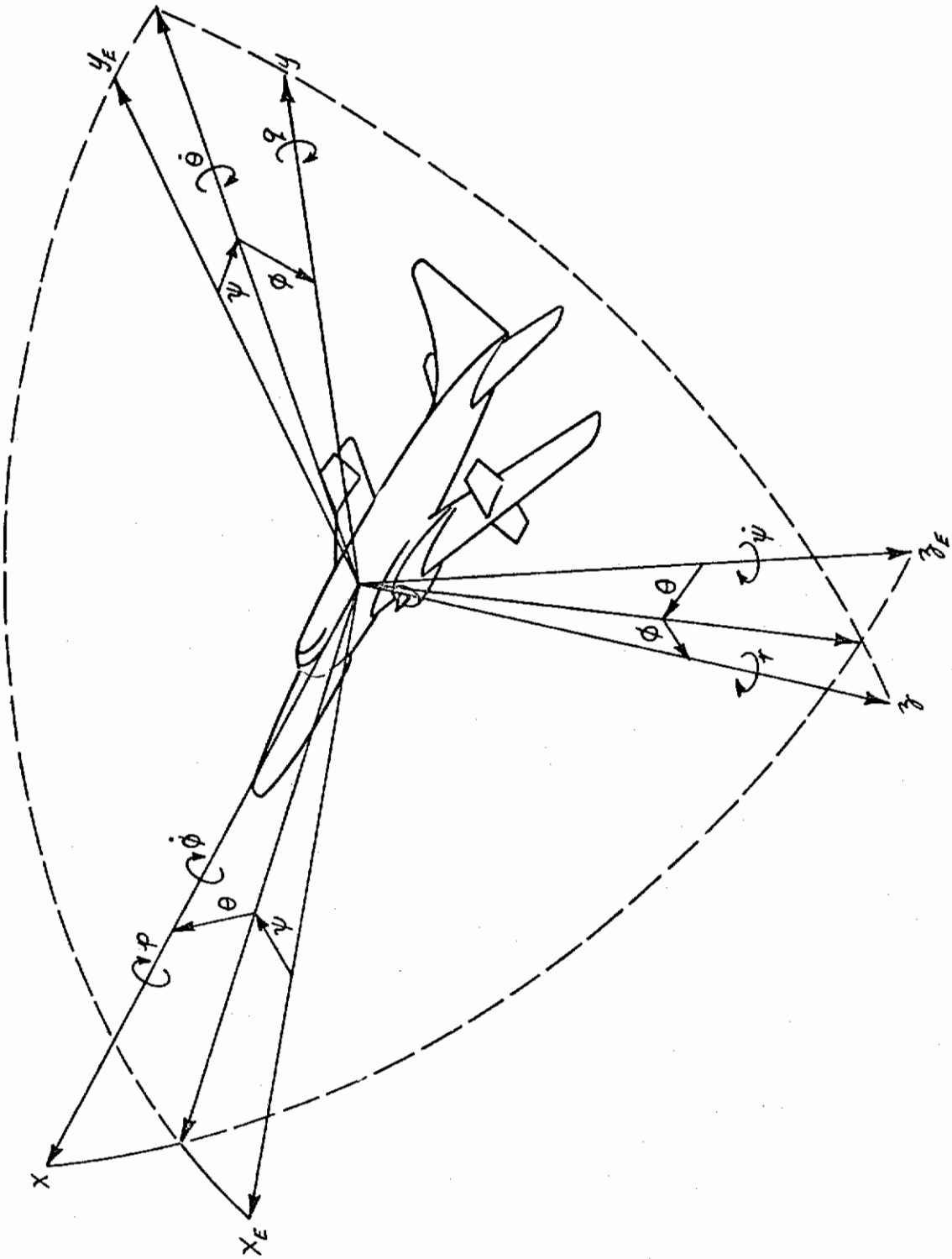

Figure A EULER ANGLES, EULER ANGLE RATES AND ANGULAR VELOCITY COMPONENTS

Vectors

$\vec{F}$	force vector, lb
$\vec{M}$	moment vector, ft-lb
$\vec{i}, \vec{j}, \vec{k}$	unit vectors in x, y, z direction respectively
$\vec{V}_I$	inertial velocity vector, ft/sec
$\vec{\omega}$	angular velocity vector, rad/sec or deg/sec

Aircraft Geometry

m	mass of aircraft, slugs
W	aircraft weight, lb
g	gravitational constant, 32.17 ft/sec^2
I_{xx}	moment of inertia about x -body axis, slug-ft^2
I_{yy}	moment of inertia about y -body axis, slug-ft^2
I_{zz}	moment of inertia about z -body axis, slug-ft^2
I_{xz}	product of inertia, body axes, slug-ft^2
c	reference chord, ft
b	reference span of wing, ft
S	reference area of wing, ft^2
z_T	thrust moment arm (positive along + z -body axis measured at x = 0), ft
i_T	thrust incidence angle defined relative to the x -body axis in the x-z plane (positive for thrust vector pointed upwards), rad or deg
i_H	horizontal tail incidence, positive for T.E. down, rad or deg
i_W	wing incidence, positive for T.E. down, rad or deg

Aircraft Motion Variables

V	true airspeed of c.g. of airplane, ft/sec
V_i	indicated airspeed, reading of a differential pressure airspeed indicator, knots or ft/sec

V_I	inertial speed of airplane in earth surface axes, ft/sec
u, v, w	true airspeed components along the body axes, ft/sec
u_I, v_I, w_I	inertial velocity components in the earth surface axes, ft/sec
u_g, v_g, w_g	gust velocities in the body axes, ft/sec
α	total angle of attack of airplane with respect to true airspeed, rad or deg
α_I	inertial angle of attack, referenced to inertial velocity vector, rad or deg
α_g	gust angle of attack, $\alpha_g \equiv \frac{w_g}{V}$ and $\alpha_g = \alpha - \alpha_I$ for small angles, rad or deg
ϵ	downwash angle, rad or deg
α_{VANE}	α vane displacement, rad or deg
β	total angle of sideslip with respect to true airspeed, rad or deg
β_I	inertial angle of sideslip, referenced to inertial velocity vector
β_g	gust sideslip, $\beta_g \equiv \frac{v_g}{V}$ and $\beta_g = \beta - \beta_I$ for small angles, rad or deg
β_{VANE}	β vane displacement, rad or deg
θ, ϕ, ψ	Euler angles for pitch, roll, and yaw respectively (see Figure A), rad or deg
γ	Flight path angle, positive for $\dot{h} > 0$, rad or deg
h	absolute altitude, ft
h_p	pressure altitude, ft
M	Mach number in terms of true airspeed
$\bar{q}$	dynamic pressure, $\bar{q} = \frac{1}{2}\rho V^2$, in. Hg or lb/ft^2
p	roll rate, component of angular velocity about x -body axis, rad/sec or deg/sec

q	pitch rate, component of angular velocity about y -body axis, rad/sec or deg/sec
r	yaw rate, component of angular velocity about z -body axis, rad/sec or deg/sec
a_x	longitudinal acceleration, positive along + x -body axis, ft/sec^2
a_y	lateral acceleration, positive along + y -body axis, ft/sec^2
a_z	normal acceleration, positive along + z -body axis, ft/sec^2
n_x	longitudinal accelerometer signal, positive along + x -body axis, $n_x = \frac{a_x}{g} + \sin\theta$, g units
n_y	lateral accelerometer signal, positive along + y -body axis, $n_y = \frac{a_y}{g} - \sin\phi\cos\theta$, g units
n_z	normal accelerometer signal, positive along + z -body axis, $n_z = \frac{a_z}{g} - \cos\phi\cos\theta$, g units
ρ	mass density of air, $slug/ft^3$
ℓ_x	distance from c.g. to a point on the x body axis, positive along positive x axis, ft

Forces and Moments

T	total thrust, lb
L	lift, lb, positive along negative z -wind axis
D	drag, lb, positive along negative x -wind axis
N	normal force, lb, positive along negative z -body axis
X	component of aerodynamic forces along the x -body axis, lb
Y	component of aerodynamic forces along the y -body axis, lb
Z	component of aerodynamic forces along the z -body axis, lb
$\mathcal{L}$	rolling moment about x -body axis, ft-lb
M	pitching moment about y -body axis, ft-lb
N	yawing moment about z -body axis, ft-lb

Control Deflections (See Figure 2.1)

δ_T	throttle displacement in cockpit, positive forward, deg
δ_e	elevator deflection, positive T.E. down, rad or deg
δ_a	total aileron deflection, positive right T.E. down, rad or deg $\delta_a = \delta_a^R - \delta_a^L$
δ_a^L	left aileron deflection, positive trailing edge down, rad or deg
δ_a^R	right aileron deflection, positive trailing edge down, rad or deg
δ_r	rudder deflection, positive T.E. left, rad or deg
δ_F	inboard Fowler flap deflection, positive T.E. down, rad or deg
δ_x	average engine thrust control displacement, positive for positive thrust, $\delta_x = \frac{\delta_x^R + \delta_x^L}{2}$
δ_y	average side force surface deflection, positive T.E. left, rad or deg, $\delta_y = \frac{\delta_y^R + \delta_y^L}{2}$
δ_z	average direct lift flap deflection positive right T.E. down, rad or deg, $\delta_z = \frac{\delta_z^R + \delta_z^L}{2}$

Nondimensional Coefficients

C_L	lift coefficient $C_L = \frac{L}{\bar{q}S}$
C_D	drag coefficient $C_D = \frac{D}{\bar{q}S}$
C_N	normal force coefficient $C_N = \frac{N}{\bar{q}S}$
C_y	lateral force coefficient $C_y = \frac{Y}{\bar{q}S}$
C_x	longitudinal force coefficient $C_x = \frac{X}{\bar{q}S}$
C_z	z -force coefficient $C_z = \frac{Z}{\bar{q}S}$
C_ℓ	rolling moment coefficient $C_\ell = \frac{L}{\bar{q}Sb}$
C_m	pitching moment coefficient $C_m = \frac{M}{\bar{q}Sc}$
C_n	yawing moment coefficient $C_n = \frac{N}{\bar{q}Sb}$
$C_{L_{(\alpha=0)}}$	lift coefficient at zero angle of attack, zero elevator deflection, etc.
C_{L_t}	lift coefficient at the trim condition

$C_{m_{(\alpha=0)}}$	moment coefficient at zero angle of attack, zero elevator deflection, etc.
$C_{D_{(\alpha=0)}}$	drag coefficient at zero angle of attack, zero elevator deflection, etc.
C_{D_t}	drag coefficient at the trim condition
C_h	hinge moment coefficient
T_c'	thrust coefficient based on thrust of one engine, $T_c' = \frac{\frac{1}{2}T}{\bar{q}S}$ for symmetric thrust

Stability Derivatives, Nondimensional

C_{L_α}	$\frac{\partial C_L}{\partial \alpha}$	rad^{-1}
$C_{L_{\delta_e}}$	$\frac{\partial C_L}{\partial \delta_e}$	rad^{-1}
$C_{L_{\delta_f}}$	$\frac{\partial C_L}{\partial \delta_f}$	rad^{-1}
C_{D_α}	$\frac{\partial C_D}{\partial \alpha}$	rad^{-1}
C_{m_α}	$\frac{\partial C_m}{\partial \alpha}$	rad^{-1}
$C_{m_{\dot{\alpha}}}$	$\frac{\partial C_m}{\partial \left(\frac{\dot{\alpha} c}{2V}\right)}$	rad^{-1}
C_{m_q}	$\frac{\partial C_m}{\partial \left(\frac{q c}{2V}\right)}$	rad^{-1}
$C_{m_{\delta_x}}$	$\frac{\partial C_m}{\partial \delta_x}$	rad^{-1}
$C_{m_{\delta_f}}$	$\frac{\partial C_m}{\partial \delta_f}$	rad^{-1}
C_{z_α}	$\frac{\partial C_z}{\partial \alpha}$	rad^{-1}
$C_{z_{\delta_e}}$	$\frac{\partial C_z}{\partial \delta_e}$	rad^{-1}
$C_{z_{\delta_f}}$	$\frac{\partial C_z}{\partial \delta_f}$	rad^{-1}
C_{y_β}	$\frac{\partial C_y}{\partial \beta}$	rad^{-1}

$C_{y_{\delta_r}}$	$\frac{\partial C_y}{\partial \delta_r}$	rad^{-1}
$C_{y_{\delta_y}}$	$\frac{\partial C_y}{\partial \delta_y}$	rad^{-1}
C_{l_p}	$\frac{\partial C_l}{\partial \left(\frac{pb}{2V}\right)}$	rad^{-1}
C_{l_r}	$\frac{\partial C_l}{\partial \left(\frac{rb}{2V}\right)}$	rad^{-1}
C_{l_β}	$\frac{\partial C_l}{\partial \beta}$	rad^{-1}
$C_{l_{\delta_r}}$	$\frac{\partial C_l}{\partial \delta_r}$	rad^{-1}
$C_{l_{\delta_a}}$	$\frac{\partial C_l}{\partial \delta_a}$	rad^{-1}
$C_{l_{\delta_y}}$	$\frac{\partial C_l}{\partial \delta_y}$	rad^{-1}
C_{n_p}	$\frac{\partial C_n}{\partial \left(\frac{pb}{2V}\right)}$	rad^{-1}
C_{n_r}	$\frac{\partial C_n}{\partial \left(\frac{rb}{2V}\right)}$	rad^{-1}
C_{n_β}	$\frac{\partial C_n}{\partial \beta}$	rad^{-1}
$C_{n_{\delta_r}}$	$\frac{\partial C_n}{\partial \delta_r}$	rad^{-1}
$C_{n_{\delta_a}}$	$\frac{\partial C_n}{\partial \delta_a}$	rad^{-1}
$C_{n_{\delta_y}}$	$\frac{\partial C_n}{\partial \delta_y}$	rad^{-1}

Subscripts

sub	c	command
sub	cg	center of gravity
sub	T	thrust
sub	y	along $+y$ axis
sub	z	along $+z$ axis

sub	t	trim
sub	m	model
sub	I	inertial
sub	g	gust
sub	x	along + x axis
sub	p	pilot's location
sub	m_T	model variable transformed to TIFS body axes

Superscripts

super	R	right
super	L	left

SECTION I

INTRODUCTION

The Total In-Flight Simulator (TIFS) is a highly advanced flight simulator that makes use of variable stability flight control concepts to achieve high-fidelity in-flight simulation. However, in addition to the simulation of the angular attitudes and motions, that is, simulation of airplane behavior, the TIFS is designed to provide a correct environment for the pilot. This report describes the status of the TIFS development to about 15 June 1967. Nearly all of the aeronautical, electronic and mechanical work done on the TIFS project to that date is described in detail herein.

1.1 PROJECT DESCRIPTION

The purpose of the TIFS program is the development of a Total In-Flight Simulator to be used in the investigation of handling qualities, cockpit displays and instrumentation, and control system research related to handling qualities criteria. TIFS will support design of large aircraft under current and future development. The simulator will have the capability, in flight, of duplicating the flight path, motions, attitudes, and the control system characteristics associated with the stability and control characteristics that are to be simulated, as well as the cockpit environment and outside visual references that are representative of those of large aircraft.

TIFS will utilize a C-131 aircraft as the basic airframe and will have a complete three axis, six-degree-of-freedom variable stability system with variable control feel and breakout force. That is, in addition to the usual three-axis control of pitch, roll and yaw, TIFS will have variable thrust (or drag), variable side force, and variable lift force capability. It will also have a cockpit with controllers, displays, and outside visual references representative of the aircraft being simulated and will have recording equipment that is compatible with existing data reduction facilities and which is capable of recording data for handling qualities, human transfer-function, and displays-research analysis.

After the ground checkout of the variable stability system, the aircraft will be modified to incorporate turbopropeller power plants, and other modifications will be made that are normally associated with the turbopropeller power plant installation. After modification of the C-131B to the TIFS supersonic transport (SST) configuration and immediately following the initial shakedown flights, data flights will be conducted. These flights will include an evaluation of the adequacy of SST visibility from the cockpit with the visor in its cruise position.

1.2 DESCRIPTION OF TIFS

The Total In-Flight Simulator airplane is a modified Convair C-131B with turbopropeller power. Two of the TIFS modifications are visually apparent, namely, the added nose section and the side-force surfaces. Figure 1.1 shows an SST nose, with visor up and down, and an alternate Advanced Manned Strategic Aircraft (AMSA) nose. Another major external change in the airplane which may not be apparent is the outboard plain (aileron-type) flap that replaces the original airplane Fowler flap.

CAL received from the USAF a C-131B airplane which will later be converted to the C-131H version. The conversion consists primarily of the installation of the Allison Propjet Engine, Model 501-D13D with an Aeroproducts A6441FN-606 propeller. The conversion will be done by the Allison Division of the General Motors Corporation. Fabrication of the TIFS nose sections, the side-force surfaces, and the plain flaps is being done for CAL under various subcontracts. More detailed descriptions of the various modifications to the C-131 are found elsewhere in this report.

Table 1-1 lists a few important data for the TIFS that are not included elsewhere in this report.

Figure 1.2 shows the TIFS airspeed placards the same as the C-131H (USAF designation of the Convair 580). TIFS modifications are being designed so that these placards need not be changed.

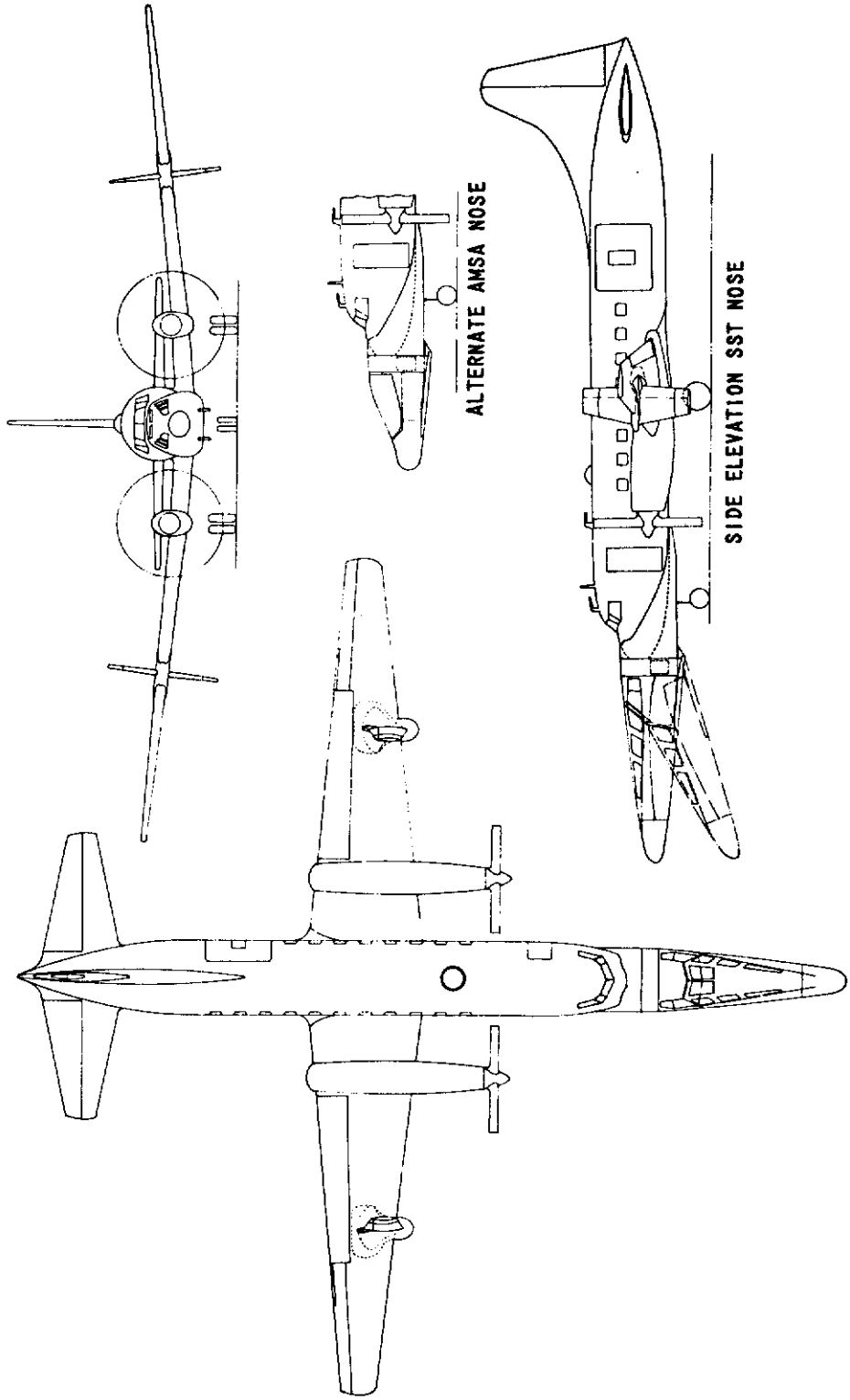

Figure 1.1 THE TOTAL IN-FLIGHT SIMULATOR

SOURCE: PAGE 11 OF ALLISON ENGINEERING DEPARTMENT REPORT 1208E
DETAIL TYPE SPECIFICATIOI
REVISED AND AMENDED
16 JULY 1966

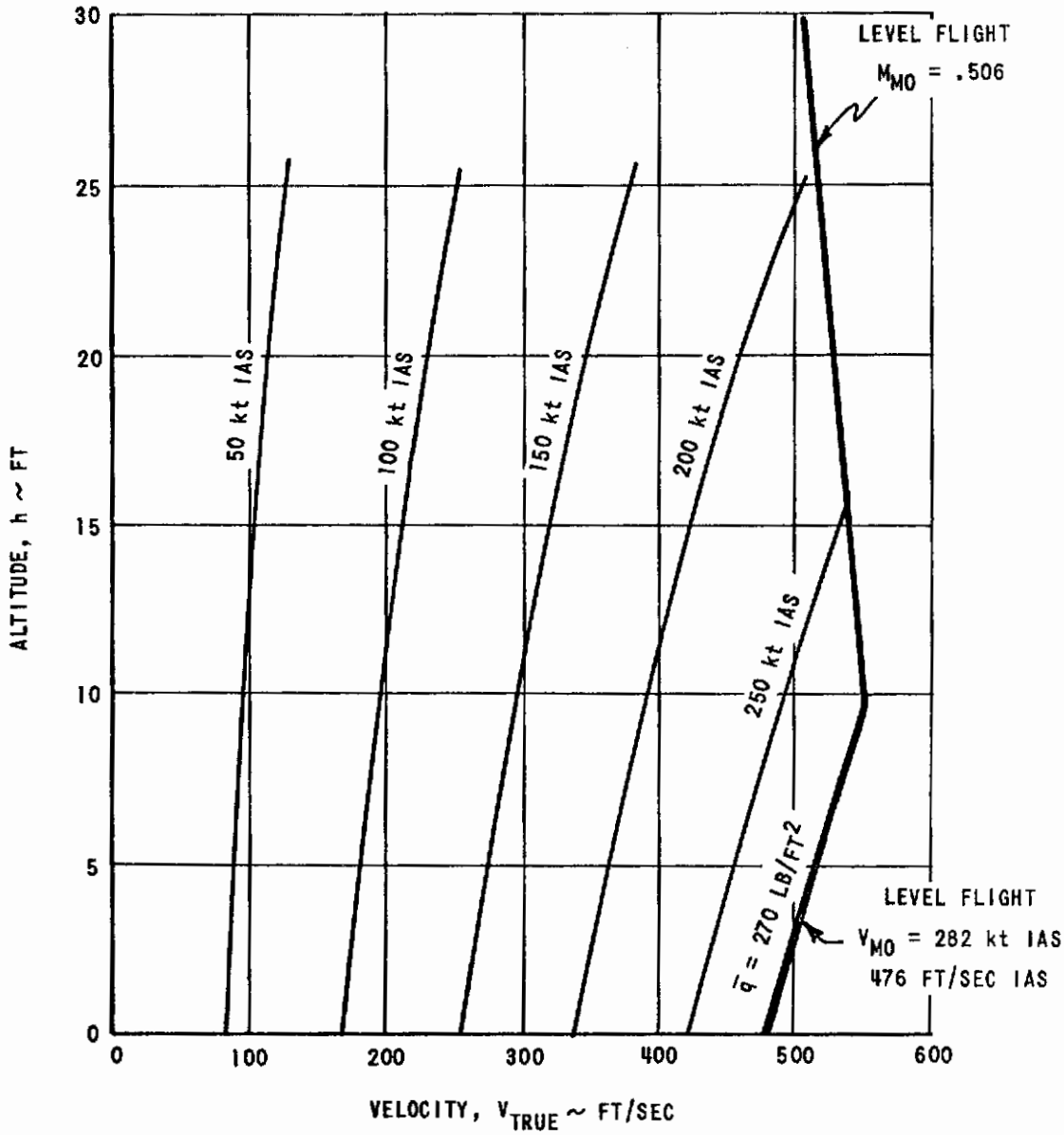

Figure 1.2 TIFS AIRSPEED PLACARDS

Table I-I
SOME TIFS GEOMETRIC DATA

WING SPAN b = 105.3 FT
WING REFERENCE CHORD c = 9.525 FT
WING AREA S = 920 FT^2
WING ASPECT RATIO $\mathcal{AR}$ = 12
WING ROOT CHORD INCIDENCE +4.0 DEG
HORIZONTAL TAIL INCIDENCE -0.5 DEG
MAXIMUM DESIGN GROSS WEIGHT 53,200 LB

1.3 ORGANIZATION OF THE REPORT

There are six major technical sections in this report which describe the TIFS development to date. Section II presents equations of motion, aerodynamic and physical data for TIFS, engine thrust, and propeller power effects. This section also describes the results of the first wind tunnel test of TIFS. The TIFS aerodynamic control surface requirements for simulation of a supersonic transport are described in Section III. The model-following variable stability loop design is described in Section IV. This section deals with designs accomplished using conventional techniques, while Section V deals with model-following design using linear optimal control techniques. The two methods are meant to be complementary. Section VI concerns mechanical and structural design of TIFS. It deals with such major aspects of TIFS development as the nose section, the side-force surfaces, the plain flaps, the hydraulic system, the fuselage structural modifications, and so on. Finally, Section VII deals with the design of the TIFS electronics, namely, sensors, feel systems, servos, patch panels, the model computer, pilots' instruments, control consoles, and the data recording system. Each section is as self-contained and independent of the others as is possible.

SECTION II

TIFS EQUATIONS OF MOTION AND DATA

This section presents equations of motion and data for the TIFS airplane as well as a discussion of the first wind tunnel test of TIFS. Section 2.1 gives the equations of motion in several forms. The equations of motion are derived first in an exact and general nonlinear form. Then, for use with the six-degree-of-freedom analog simulation, the equations are simplified through the use of several reasonable approximations. Axis transformations, necessary for variable stability simulations, are described, and finally, linearized longitudinal and lateral-directional equations are given.

TIFS data are given in several areas:

1. aerodynamics, static and dynamic derivatives, and also control derivatives,
2. mass and inertia, and other physical data,
3. engine static and dynamic thrust, and
4. propeller effects on aerodynamics.

Static aerodynamic data were both estimated theoretically and measured in the wind tunnel. Dynamic derivatives were estimated theoretically. The control derivatives for conventional control surfaces were determined from wind tunnel tests of the Convair Model T-29E. Side-force surface and direct lift flap control derivatives were estimated and later determined from wind tunnel tests of TIFS. Mass and inertia data have been determined on the basis of Convair 340 data and CAL estimates of the weights and locations of TIFS modifications. The mathematical model of the Allison propjet engines to be used for TIFS was derived from data supplied by Allison. Finally, propeller power effects, both direct and indirect, were estimated using theoretical methods together with T-29E wind tunnel powered model data.

2.1 EQUATIONS OF MOTION

This section consists of four subsections dealing in turn with exact nonlinear equations, approximate nonlinear equations, axis transformations, and linearized equations that are separated into uncoupled longitudinal and lateral-directional sets.

2.1.1 Exact Nonlinear Equations of Motion

This section presents the full, exact, nonlinear equations of motion for TIFS and also for the model airplane, written in both vector and matrix form for convenience. The particular form of the final matrix equations was originally developed for use during the General Purpose Airborne Simulator (GPAS) preliminary design study (Reference 2.1). Several auxiliary equations known to be necessary for TIFS are also given. Figure 2.1 shows the pertinent axis systems and the positive sense of the primary motion variables and aerodynamic coefficients.

In vector form, the force equations are independent of the choice of coordinate system:

$$\vec{F}_{gravity} + \vec{F}_{aero} + \vec{T} = m\dot{\vec{V}}_I + m\vec{\omega} \times \vec{V}_I \qquad (2\text{-}1)$$

where $\vec{V}_I$ is the velocity relative to an inertial coordinate frame. For our purposes, the earth's surface may be considered an inertial reference. In body axes, here defined directly from the water line - fuselage station - buttock line reference system, the vector equation may be written in the following matrix form:

$$mg\begin{bmatrix} -\sin\theta \\ \sin\phi\cos\theta \\ \cos\phi\cos\theta \end{bmatrix} + \frac{1}{2}\rho V^2 S\begin{bmatrix} C_x \\ C_y \\ C_z \end{bmatrix} + \begin{bmatrix} T_x \\ 0 \\ T_z \end{bmatrix} = m\begin{bmatrix} \dot{u}_I \\ \dot{v}_I \\ \dot{w}_I \end{bmatrix} + m\begin{bmatrix} 0 & -r & q \\ r & 0 & -p \\ -q & p & 0 \end{bmatrix}\begin{bmatrix} u_I \\ v_I \\ w_I \end{bmatrix} \qquad (2\text{-}2)^*$$

*The thrust components can also be written in terms of the magnitude (T) and incidence (i_T) of the thrust: $T_x = T\cos i_T$, $T_z = -T\sin i_T$

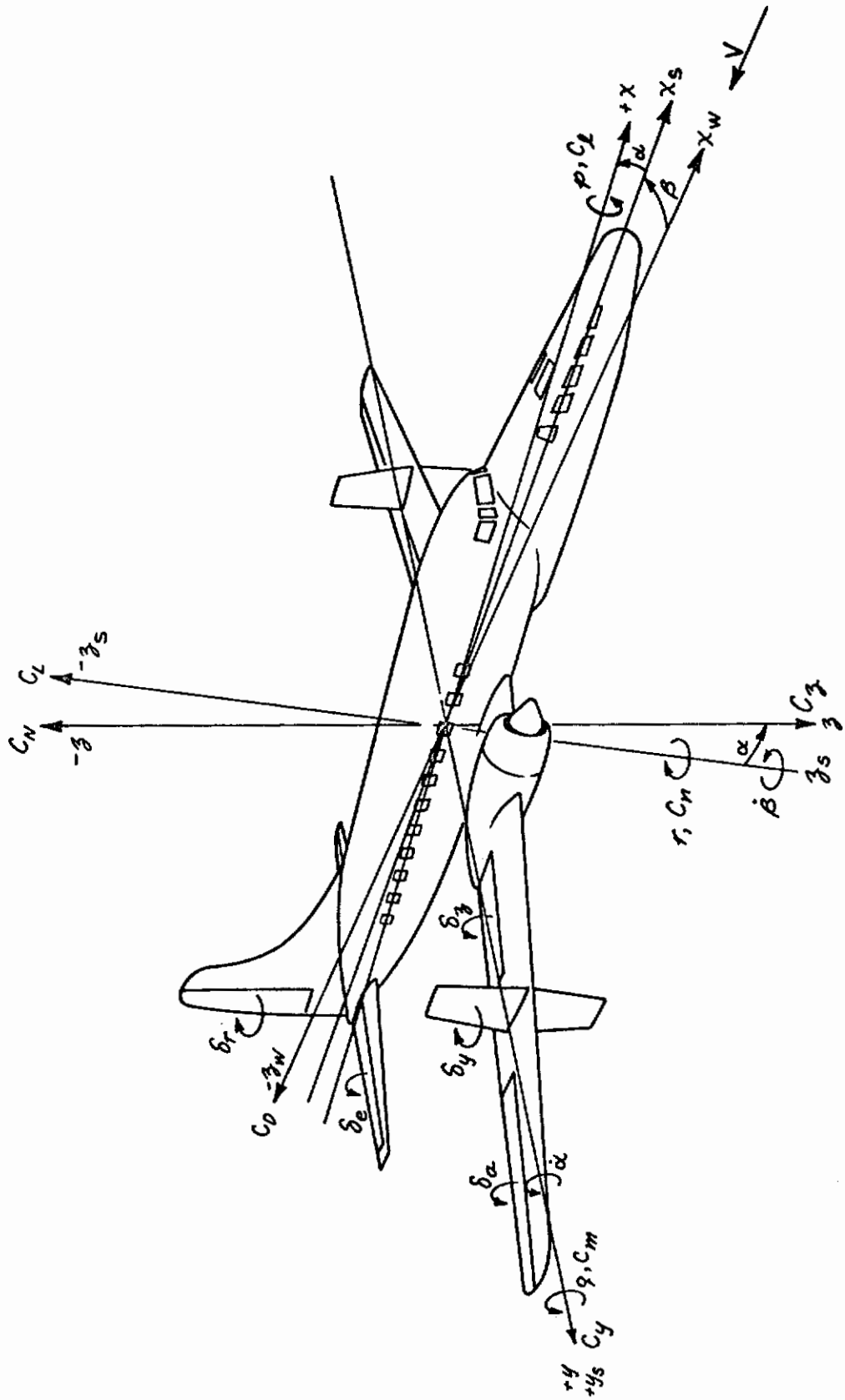

Figure 2.1 AXES AND SIGN CONVENTIONS FOR TIFS

where $V = V_I$ only in still air and $V_I^2 = u_I^2 + v_I^2 + w_I^2$. This matrix equation implies that the thrust vector $\vec{T}$ lies in the plane of symmetry of the airplane but is not otherwise constrained.

In some circumstances, it may be convenient to express the airplane aerodynamics in terms of lift, drag and the associated wind axis side-force coefficients; thus, we may write

$$\begin{bmatrix} C_x \\ C_y \\ C_z \end{bmatrix} = \left[L_{W \to B}\right] \begin{bmatrix} -C_D \\ C_Y \\ -C_L \end{bmatrix} = \begin{bmatrix} \cos\alpha_I \cos\beta_I & -\cos\alpha_I \sin\beta_I & -\sin\alpha_I \\ \sin\beta_I & \cos\beta_I & 0 \\ \sin\alpha_I \cos\beta_I & -\sin\alpha_I \sin\beta_I & \cos\alpha_I \end{bmatrix} \begin{bmatrix} -C_D \\ C_Y \\ -C_L \end{bmatrix} \qquad (2\text{-}3)$$

wind axes to body axes

The transformation matrix $\left[L_{W \to B}\right]$ in Equation 2-3 is the product of two separate orthogonal transformations which take the components of a vector from wind axes to body axes. These transformations are a sideslip (β_I) transformation first, then an angle of attack (α_I) transformation second.

In past studies, notably GPAS (Reference 2.1), it was concluded that there is a distinct advantage in using a special nonorthogonal set of force equations. Specifically, our nonorthogonal coordinate system is defined so that its x axis is directed into the relative wind and its y and z axes are coincident with the y and z body axes, respectively. In other words, the x axis is a wind axis and the y and z axes are body axes. The non-orthogonal (NO) axis system has the advantages for analog computation that:

1. The drag (x wind axis) equation appears in its simplest and most meaningful form.
2. The y and z force equations occur in their conventional body axis form.
3. The total velocity, V_I , is obtained directly by integration.

The one seeming disadvantage of the system, its nonorthogonality, is of no consequence in our applications.

The nonorthogonal force equations may be obtained by transforming the body axis equations (Equation 2-2) using the transformation matrix

$$\left[L_{B\to NO}\right] = \begin{bmatrix} \cos\alpha_I \cos\beta_I & \sin\beta_I & \sin\alpha_I \cos\beta_I \\ 0 & 1 & 0 \\ 0 & 0 & 1 \end{bmatrix} \tag{2-4}$$

body axes to nonorthogonal axes

Figure 2.2 shows both the body axes and nonorthogonal axes and the relation between them. Because of the nonorthogonality of the transformation, the inverse transformation must be accomplished by using the inverse matrix $\left[L_{B\to NO}\right]^{-1}$ rather than the transpose of $\left[L_{B\to NO}\right]$ as is usually done.

The nonorthogonal force equations are as follows:

$$mg \begin{bmatrix} -\sin\gamma \\ \sin\phi\cos\theta \\ \cos\phi\cos\theta \end{bmatrix} + \frac{1}{2}\rho V^2 S \begin{bmatrix} -C_D \\ C_y \\ C_z \end{bmatrix} + \begin{bmatrix} T_x \cos\alpha_I \cos\beta_I + T_y \sin\alpha_I \cos\beta_I \\ 0 \\ T_z \end{bmatrix}$$

$$= m \begin{bmatrix} \dot{V}_I \\ \dot{v}_I \\ \dot{w}_I \end{bmatrix} + m \begin{bmatrix} 0 \\ ru_I - pw_I \\ -qu_I + pv_I \end{bmatrix} \tag{2-5}$$

where

$$\sin\gamma = \cos\alpha_I \cos\beta_I \sin\theta - \sin\beta_I \sin\phi\cos\theta - \sin\alpha_I \cos\beta_I \cos\phi\cos\theta \tag{2-6}$$

$$u_I = V_I \cos\alpha_I \cos\beta_I \tag{2-7}$$

$$C_y = -C_D \sin\beta_I + C_Y \cos\beta_I \tag{2-8}$$

$$C_z = -C_D \sin\alpha_I \cos\beta_I - C_Y \sin\alpha_I \sin\beta_I - C_L \cos\alpha_I \tag{2-9}$$

Note that there are no angular velocity terms in the drag equation as in the other two. If there is no y component of thrust or if it is negligible, then a thrust term occurs only in the drag equation.

The moment equations are written in the conventional body axis matrix form:

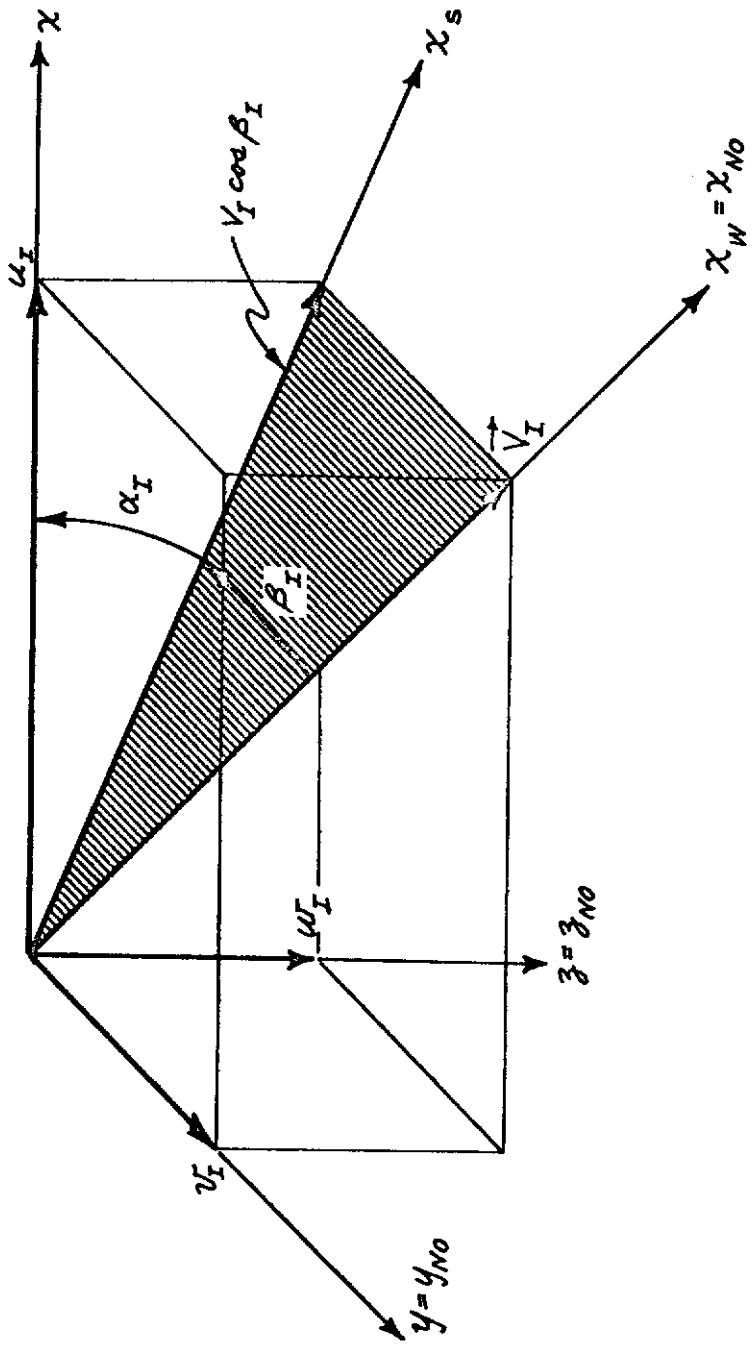

Figure 2.2 THE RELATION BETWEEN BODY AXES AND THE NONORTHOGONAL AXES

$$\frac{1}{2}\rho V^2 S \begin{bmatrix} b & 0 & 0 \\ 0 & c & 0 \\ 0 & 0 & b \end{bmatrix} \begin{bmatrix} C_\ell \\ C_m \\ C_n \end{bmatrix} + \begin{bmatrix} 0 \\ z_T T_x - x_T T_z \\ 0 \end{bmatrix} =$$

$$\begin{bmatrix} I_{xx} & 0 & -I_{xz} \\ 0 & I_{yy} & 0 \\ -I_{xz} & 0 & I_{zz} \end{bmatrix} \begin{bmatrix} \dot{p} \\ \dot{q} \\ \dot{r} \end{bmatrix} + \begin{bmatrix} 0 & -r & q \\ r & 0 & -p \\ -q & p & 0 \end{bmatrix} \begin{bmatrix} I_{xx} & 0 & -I_{xz} \\ 0 & I_{yy} & 0 \\ -I_{xz} & 0 & I_{zz} \end{bmatrix} \begin{bmatrix} p \\ q \\ r \end{bmatrix} \qquad (2\text{-}10)^*$$

By the form of the moment of inertia matrix, it may be seen that we are assuming that the airplane has a plane of symmetry. In vector form these equations would be written as

$$\vec{M}_{aero} + \vec{r}_T \times \vec{T} = \bar{\bar{I}} \cdot \dot{\vec{\omega}} + \vec{\omega} \times (\bar{\bar{I}} \cdot \vec{\omega}) \qquad (2\text{-}11)$$

where the tensor $\bar{\bar{I}}$, the moment of inertia tensor, changes the magnitude and direction of a vector on which it operates. In particular, the product $\bar{\bar{I}} \cdot \vec{\omega}$ is known as the angular momentum vector, often designated $\vec{H}$. The position vector $\vec{r}_T$ is normal to the thrust vector and has a magnitude equal to the distance between the airplane c.g. and the line of action of the total thrust vector.

The equations for the Euler angles are also written in the conventional form:

$$\dot{\psi} = \frac{q \sin\phi + r \cos\phi}{\cos\theta} \qquad (2\text{-}12)$$

$$\dot{\theta} = q \cos\phi - r \sin\phi \qquad (2\text{-}13)$$

$$\dot{\phi} = p + \left(\frac{\sin\phi \sin\theta}{\cos\theta}\right) q + \left(\frac{\cos\phi \sin\theta}{\cos\theta}\right) r \qquad (2\text{-}14)$$

*This equation, in its present form, will not accommodate an engine-out situation. A straightforward modification is required.

Several auxiliary equations, giving rate of climb and angles of attack and sideslip needed for TIFS design and analog computations are listed below:

$$\dot{h} = V_I \sin\gamma \tag{2-15}$$

$$\alpha_I = \tan^{-1}\frac{\omega_I}{u_I} = \sin^{-1}\frac{\omega_I}{V_I\cos\beta_I} \tag{2-16}$$

$$\beta_I = \sin^{-1}\frac{v_I}{V_I} \tag{2-17}$$

Accelerometer and vane signals depend on sensor location relative to the airplane center of gravity. In particular, at some location denoted by the vector $\ell_x\vec{i}$ * relative to the c.g., the accelerometer signals (in g's) are given by the following vector and matrix equations:

$$\begin{aligned}\vec{n}_x &= \frac{1}{mg}\left(\vec{F}_{aero}+\vec{T}\right)+\frac{1}{g}\dot{\vec{\omega}}\times\ell_x\vec{i}+\frac{1}{g}\vec{\omega}\times\left(\vec{\omega}\times\ell_x\vec{i}\right)\\ &= \frac{1}{g}\dot{\vec{V}}+\frac{1}{g}\vec{\omega}\times\vec{V}-\frac{1}{mg}\vec{F}_{gravity}+\frac{1}{g}\dot{\vec{\omega}}\times\ell_x\vec{i}+\frac{1}{g}\vec{\omega}\times\left(\vec{\omega}\times\ell_x\vec{i}\right)\end{aligned} \tag{2-18}$$

$$\begin{aligned}\begin{bmatrix}n_{x_x}\\ n_{y_x}\\ n_{z_x}\end{bmatrix} &= \frac{1}{mg}\left\{\frac{1}{2}\rho V^2 S\left[\begin{array}{c|c}C_x & T_x\\ C_y & 0\\ C_z & T_z\end{array}\right]\right\}+\frac{1}{g}\begin{bmatrix}0\\ \dot{r}\ell_x\\ -\dot{q}\ell_x\end{bmatrix}+\frac{1}{g}\begin{bmatrix}-(r^2+q^2)\ell_x\\ pq\ell_x\\ pr\ell_x\end{bmatrix}\\ &= \frac{1}{g}\begin{bmatrix}\dot{u}\\ \dot{v}\\ \dot{w}\end{bmatrix}+\frac{1}{g}\begin{bmatrix}0 & -r & q\\ r & 0 & -p\\ -q & p & 0\end{bmatrix}\begin{bmatrix}u\\ v\\ w\end{bmatrix}-\begin{bmatrix}-\sin\theta\\ \sin\phi\cos\theta\\ \cos\phi\cos\theta\end{bmatrix}\\ &\quad+\frac{1}{g}\begin{bmatrix}0\\ \dot{r}\ell_x\\ -\dot{q}\ell_x\end{bmatrix}+\frac{1}{g}\begin{bmatrix}-(r^2+q^2)\ell_x\\ pq\ell_x\\ pr\ell_x\end{bmatrix}\end{aligned} \tag{2-19}$$

These are all body axis components.

---

* For simplicity, we are ignoring displacements in the y and z direction.

The equation for the vertical acceleration in terms of n_x, n_y, and n_z is obtained by transforming the components of the vector $\vec{n}_{cg}$ into the earth surface reference frame. Therefore, we obtain

$$\ddot{h} = -g + g(n_x \sin\theta - n_y \sin\phi \cos\theta - n_z \cos\phi \cos\theta) \tag{2-20}$$

where g is the acceleration of gravity.

The matrix which transforms components of a vector in the earth surface system to components in the body axis system is

$$\left[L_{E\to B}\right] = \left[\phi\right]\left[\theta\right] = \begin{bmatrix} 1 & 0 & 0 \\ 0 & \cos\phi & \sin\phi \\ 0 & -\sin\phi & \cos\phi \end{bmatrix}\begin{bmatrix} \cos\theta & 0 & -\sin\theta \\ 0 & 1 & 0 \\ \sin\theta & 0 & \cos\theta \end{bmatrix}$$

$$\left[L_{E\to B}\right] = \begin{bmatrix} \cos\theta & 0 & -\sin\theta \\ \sin\phi\sin\theta & \cos\phi & \sin\phi\cos\theta \\ \cos\phi\sin\theta & -\sin\phi & \cos\phi\cos\theta \end{bmatrix} \tag{2-21}$$

The transformation $[\psi]$ which accounts for the heading angle (measured from true North) has been ignored since we are generally dealing with heading angles relative to some reference flight path. The inverse and transpose of $\left[L_{E\to B}\right]$ are identical, i.e.,

$$\left[L_{E\to B}\right]^{-1} \equiv \left[L_{E\to B}\right]^{T}$$

where the ^{T} means transpose.

2.1.2 The Axis Transformation Needed for Attitude Matching

The TIFS airplane is intended to simulate the environment and motions of the model airplane as experienced by the pilot of the model. Therefore, the cockpits of the respective airplanes must have the same trim attitude, and, for simulation purposes, the cockpit motions about this trim attitude, must, also be matched in the same axis system. When the attitude of the TIFS nose section matches that of the nose of the model, there will, in general, be some angle

between the two fuselage reference lines. We assume that this is simply a pitch attitude angle i_m. Figure 2.3 illustrates this angle which is measured positively from the TIFS x body axis to the model x body axis.

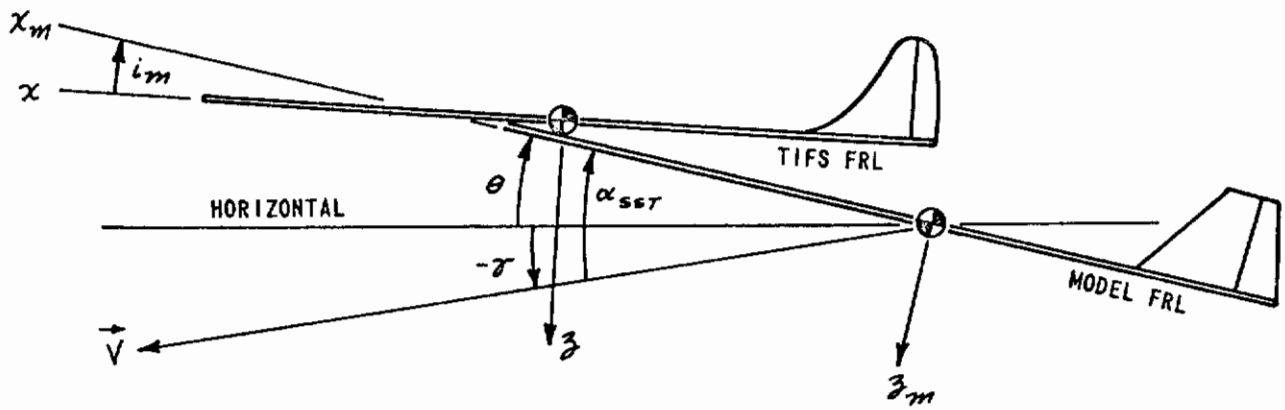

Figure 2.3 RELATION BETWEEN TIFS AND MODEL BODY AXES

This transformation could be accomplished implicitly because the model airplane equations could be written directly in the rotated body axes conforming to TIFS axes. However, it is useful to be able to observe the responses of the model in its conventional body axes rather than some rotated axes. For this reason, body axis motion variables of the model are transformed into the TIFS coordinate system as a separate operation during the design study simulations.

For all vector quantities, such as $\vec{V}$, $\vec{\omega}$, and $\vec{n}$, the vector components may be transformed from model body axes to TIFS body axes straightforwardly using the transpose of the transformation matrix

$$\left[L_{T \to m}\right] = \begin{bmatrix} \cos i_m & 0 & -\sin i_m \\ 0 & 1 & 0 \\ \sin i_m & 0 & \cos i_m \end{bmatrix} \qquad (2\text{-}22)$$

TIFS body axes to model body axes

For example, we have

$$\begin{bmatrix} p_{mT} \\ q_{mT} \\ r_{mT} \end{bmatrix} = \left[L_{T \to m}\right]^{T} \begin{bmatrix} p_m \\ q_m \\ r_m \end{bmatrix}$$

where the mT subscript denotes model airplane quantities expressed in the TIFS body axes.

Model variables that are related to vector components, such as α_m, may be transformed into TIFS coordinates by using the defining equations for those variables. For example, using Equation 2-16 for α_m, we obtain

$$\sin \alpha_{mT} = \frac{w_{mT}}{V_m \cos \beta_m} = \frac{-u_m \sin i_m + w_m \cos i_m}{V_m \cos \beta_m}$$

where $V_m \cos \beta_m$ is invariant under the $\left[L_{T-m}\right]^{-1}$ transformation. Now, for small α_{mT}, β_m and i_m and for $u_m \approx V_m$, we obtain

$$\alpha_{mT} = -i_m + \alpha_m$$

Obviously, certain quantities are invariant, such as V, h, and γ and their time derivatives, because they do not depend for their definition on the particular airplane coordinate system used. Other variables, such as β, are invariant only because $\left[L_{m \to T}\right]$ is a pitch attitude transformation which does not affect y axis components of vectors.

There is no simple, general way to transform the Euler angles ψ, θ, and ϕ since these are not components of a vector. However, as with the vector components, these angles are different in different coordinate systems and, for simulation, must be expressed in the proper coordinate system.

The model Euler angles are computed directly in transformed axes for the nonlinear, six-degree-of-freedom simulation. However, for the linear design simulations, the following small angle approximations, derived in Reference 2.2, are used to relate the angles of pitch and bank.

$$\left.\begin{aligned} \theta_{mT} &= \theta_m - i_m \\ \phi_{mT} &= \phi_m . \end{aligned}\right\} \qquad (2\text{-}23)$$

A complete discussion of the axis transformation is given in Reference 2.2.

2.1.3 Approximate Nonlinear Equations

For purposes of the nonlinear six-degree-of-freedom simulation of TIFS, approximate nonlinear equations are employed in order to conserve analog computing equipment. The particular approximations used have negligible effect on the computed results for the kinds of maneuvers considered in system design. Specifically, the approximations are as follows:

1. The inertia coupling terms (i.e., products of angular velocities p, q, and r) in the moment equations were neglected.
2. Whenever u_I appeared, it was replaced by V_I.
3. Cos $\alpha_I \approx 1$ and sin $\alpha_I \approx \alpha_I$; cos $\beta_I = 1$ and sin $\beta_I = \beta_I$.
4. In the z force equation, $-C_D \sin \alpha_I \cos \beta_I - C_L \cos \alpha_I - C_Y \sin \alpha_I \sin \beta_I$ was approximated by $-C_L$, and in the Y force equation, $-C_D \sin \beta_I + C_Y \cos \beta_I$ was replaced by its body axis equivalent, $+C_y$.
5. The approximations $\alpha_I = \frac{\omega_I}{V_I}$ and $\beta_I = \frac{v_I}{V_I}$ were introduced which when differentiated yielded

   $$\dot{\alpha}_I = \frac{\dot{\omega}_I}{V_I} - \alpha_I \frac{\dot{V}_I}{V_I}, \quad \dot{\beta}_I = \frac{\dot{v}_I}{V_I} - \beta_I \frac{\dot{V}_I}{V_I}$$

   However, the further approximation $\dot{\beta}_I = \frac{\dot{v}_I}{V_I}$ was used for the simulation.
6. The thrust vector, $\vec{T}$, acts along the x body axis.

The Euler angle computations made use of the exact equations, without approximation of any kind.

The nonlinear force and moment equations based on the above approximations together with several pertinent auxiliary equations are given in Section 4.4 of this report which discusses the six-degree-of-freedom simulation.

2.1.4 Linear Equations of Motion

The linear equations of motion were derived using conventional techniques and are based on the approximate nonlinear equations discussed in the preceding

subsection, 2.1.3. However, certain additional features are found in the linear equations that increase their versatility. The equations are linearized about the reference flight condition defined as follows:

1. all linear and angular accelerations are zero
2. all angular velocities are zero
3. $\phi_t = 0$ and $\beta_t = 0$
4. δ_{a_t}, δ_{r_t} and δ_{y_t} are zero.

Sines and cosines of angles are linearized according to the formulas

$$\sin(\alpha_t + \Delta\alpha) = \sin\alpha_t + \Delta\alpha\cos\alpha_t$$
$$\cos(\alpha_t + \Delta\alpha) = \cos\alpha_t - \Delta\alpha\sin\alpha_t$$

Similar formulas hold for other angles as well. Small angle approximations are further used so that $\cos\alpha_t = 1$ and $\sin\alpha_t = \alpha_t$, and similarly for θ_t and γ_t. Variables appearing in the denominators of terms are linearized using the binomial theorem, e.g.,

$$V^{-1} = (V_t + \Delta V)^{-1} \approx \frac{1}{V_t} - \frac{\Delta V}{V_t^2}$$

For convenience, the I subscript used in previous sections will be omitted here. Finally, incremental variables will be denoted with the symbol Δ except when the trim condition is assumed zero as indicated above.

2.1.4.1 Linear Longitudinal Equations

The equations are written in terms of α_x, θ and V where α_x is the local inertial angle of attack anywhere on the x body axis

$$\frac{\ell_x}{V_t} D_\alpha \dot\theta + g\Delta\theta + \dot V + D_V \Delta V + D_\alpha \Delta\alpha_x = -D_{\delta_x}\Delta\delta_x - D_{\delta_z}\Delta\delta_z \qquad (2\text{-}24)$$

$$\frac{\ell_x}{V_t}\ddot\theta - \left(1 + \frac{\ell_x}{V_t} Z_\alpha\right)\dot\theta - Z_\theta\Delta\theta + \frac{\alpha_t}{V_t}\dot V - Z_V\Delta V + \dot\alpha_x \qquad (2\text{-}25)$$
$$- Z_\alpha\Delta\alpha_x = Z_{\delta_e}\Delta\delta_e + Z_{\delta_z}\Delta\delta_z$$
$$\left(1 - \frac{\ell_x}{V_t} M_{\dot\alpha}\right)\ddot\theta - \left(M_q + \frac{\ell_x}{V_t} M_\alpha\right)\dot\theta - M_V\Delta V - M_{\dot\alpha}\dot\alpha_x$$

$$-M_\alpha \Delta\alpha_\chi = M_{\delta_e} \Delta\delta_e + M_{\delta_\chi} \Delta\delta_\chi + M_{\delta_\zeta} \Delta\delta_\zeta \tag{2-26}$$

where

$$\Delta\alpha_\chi = \Delta\alpha - \frac{\ell_\chi}{V_t}\dot{\theta} \tag{2-27}$$

$$\Delta n_\chi = \frac{V_t}{g}\left[\frac{\dot{V}}{V_t} - \alpha_t \dot{\alpha} + \alpha_t \dot{\theta}\right] + \Delta\theta \tag{2-28}$$

$$\Delta n_{\zeta_\chi} = \frac{V_t}{g}\left[\dot{\alpha}_\chi + \frac{\alpha_t}{V_t}\dot{V} - \dot{\theta}\right] + \theta_t \Delta\theta \tag{2-29}$$

$$\Delta\dot{h} = V_t(\Delta\theta - \Delta\alpha) + \gamma_t \Delta V \tag{2-30}$$

where

$$\gamma_t = \theta_t - \alpha_t \tag{2-31}$$

The dimensional derivatives are defined as follows:

$$D_V = \frac{1}{m}\left(\rho V_t S C_{D_t} - \frac{\partial T}{\partial V}\right)$$

$$D_\alpha = \frac{1}{m}\left(\bar{q} S C_{D_\alpha} + \alpha_t T_t - W\right)$$

$$D_{\delta_\chi} = -\frac{1}{m}\frac{\partial T}{\partial \delta_\chi}$$

$$D_{\delta_\zeta} = \frac{\bar{q}S}{m} C_{D_{\delta_\zeta}}$$

$$Z_V = \frac{1}{m V_t}\left(\rho V_t S C_{Z_t}\right)$$

$$Z_\alpha = \frac{\bar{q} S}{m V_t} C_{Z_\alpha}$$

$$Z_\theta = -\frac{g \theta_t}{V_t}$$

$$Z_{\delta_e} = \frac{\bar{q} S}{m V_t} C_{Z_{\delta_e}}$$

$$Z_{\delta_Z} = \frac{\bar{q} S}{m V_t} C_{Z_{\delta_Z}}$$

Note: $C_Z \approx -C_L$

$$M_V = \frac{\bar{q} S c}{I_{yy}}\left(\frac{2}{V_t} C_{m_t} + \frac{\partial C_m}{\partial V}\right) + \frac{Z_T}{I_{yy}} \frac{\partial T}{\partial V}$$

$$M_{\dot{\alpha}} = \frac{\bar{q} S c}{I_{yy}} \frac{c}{2V_t} C_{m_{\dot{\alpha}}}$$

$$M_\alpha = \frac{\bar{q} S c}{I_{yy}} C_{m_\alpha}$$

$$M_q = \frac{\bar{q} S c}{I_{yy}} \frac{c}{2V_t} C_{m_q}$$

$$M_{\delta_e} = \frac{\bar{q} S c}{I_{yy}} C_{m_{\delta_e}}$$

$$M_{\delta_Z} = \frac{\bar{q} S c}{I_{yy}} C_{m_{\delta_Z}}$$

$$M_{\delta_x} = \frac{Z_T}{I_{yy}} \frac{\partial T}{\partial \delta_x}$$

2.1.4.2 Linear Lateral-Directional Equations

The lateral-directional equations are written in two forms depending on whether $\ddot{\phi}$, $\dot{\phi}$, ϕ or $\dot{p}$, p, ϕ are used. Using the former set, we have the following equations written in terms of β_χ for a location off the airplane c.g.

$$-(\alpha_t + Y_p)\dot{\phi} - \frac{g}{V_t}\phi - \frac{\ell_\chi}{V_t}\dot{r} + \left(1 + \alpha_t \theta_t + \theta_t Y_p - Y_r + \frac{\ell_\chi}{V_t} Y_\beta\right) r + \dot{\beta}_\chi - Y_\beta \beta_\chi = Y_{\delta_a}\delta_a + Y_{\delta_r}\delta_r + Y_{\delta_y}\delta_y \tag{2-32}$$

$$\ddot{\phi} - L_p \dot{\phi} - \left(\frac{I_{xz}}{I_{xx}} + \theta_t\right)\dot{r} + \left(\theta_t L_p - L_r + \frac{\ell_\chi}{V_t} L_\beta\right) r - L_\beta \beta_\chi = L_{\delta_a}\delta_a + L_{\delta_r}\delta_r + L_{\delta_y}\delta_y \tag{2-33}$$

$$-\frac{I_{xz}}{I_{zz}}\ddot{\phi} - N_p \dot{\phi} + \left(1 + \theta_t \frac{I_{xz}}{I_{zz}}\right)\dot{r} + \left(\theta_t N_p - N_r + \frac{\ell_\chi}{V_t} N_\beta\right) r - N_\beta \beta_\chi = N_{\delta_a}\delta_a + N_{\delta_r}\delta_r + N_{\delta_y}\delta_y \tag{2-34}$$

where

$$\beta_\chi = \beta + \frac{\ell_\chi}{V_t} r \tag{2-35}$$

$$n_{y_\chi} = \frac{V_t}{g}\left[\dot{\beta}_\chi + (1 + \alpha_t \theta_t) r - \alpha_t \dot{\phi}\right] - \phi \tag{2-36}$$

Now since

$$\dot{\phi} = p + \theta_t r \tag{2-37}$$

the equations may be rewritten in terms of p and $\dot{p}$ instead of $\dot{\phi}$ and $\ddot{\phi}$ respectively.

$$-\alpha_t p - Y_p p - \frac{g}{V_t}\phi - \frac{\ell_x}{V_t}\dot{r} + \left(1 - Y_r + \frac{\ell_x}{V_t} Y_\beta\right) r$$

$$+\dot{\beta}_x - Y_\beta \beta_x = Y_{\delta_a}\delta_a + Y_{\delta_r}\delta_r + Y_{\delta_y}\delta_y \tag{2-38}$$

$$\dot{p} - L_p p - \frac{I_{xz}}{I_{xx}}\dot{r} + \left(-L_r + \frac{\ell_x}{V_t} L_\beta\right) r - L_\beta \beta_x$$

$$= L_{\delta_a}\delta_a + L_{\delta_r}\delta_r + L_{\delta_y}\delta_y \tag{2-39}$$

$$-\frac{I_{xz}}{I_{zz}}\dot{p} - N_p p + \dot{r} + \left(-N_r + \frac{\ell_x}{V_t} N_\beta\right) r - N_\beta \beta_x$$

$$= N_{\delta_a}\delta_a + N_{\delta_r}\delta_r + N_{\delta_y}\delta_y \tag{2-40}$$

and

$$n_{y_x} = \frac{V_t}{g}\left[\dot{\beta}_x + r - \alpha_t p\right] - \phi \tag{2-41}$$

The dimensional derivatives are defined as follows:

$$Y_\beta = \frac{\bar{q} S}{m V_t} C_{y_\beta}$$

$$Y_{\delta_a} = \frac{\bar{q} S}{m V_t} C_{y_{\delta_a}}$$

$$Y_{\delta_r} = \frac{\bar{q} S}{m V_t} C_{y_{\delta_r}}$$

$$Y_{\delta_y} = \frac{\bar{q} S}{m V_t} C_{y_{\delta_y}}$$

$$Y_p = \frac{\bar{q} S}{m V_t} \frac{b}{2V_t} C_{y_p}$$

$$Y_r = \frac{\bar{q} S}{m V_t} \frac{b}{2V_t} C_{y_r}$$

$$L_\beta = \frac{\bar{q} S b}{I_{xx}} C_{l_\beta}$$

$$L_{\delta_a} = \frac{\bar{q} S b}{I_{xx}} C_{l_{\delta_a}}$$

$$L_{\delta_r} = \frac{\bar{q} S b}{I_{xx}} C_{l_{\delta_r}}$$

$$L_{\delta_y} = \frac{\bar{q} S b}{I_{xx}} C_{l_{\delta_y}}$$

$$L_p = \frac{\bar{q} S b}{I_{xx}} \frac{b}{2V_t} C_{l_p}$$

$$L_r = \frac{\bar{q} S b}{I_{xx}} \frac{b}{2V_t} C_{l_r}$$

$$N_\beta = \frac{\bar{q} S b}{I_{zz}} C_{n_\beta}$$

$$N_{\delta_a} = \frac{\bar{q} S b}{I_{zz}} C_{n_{\delta_a}}$$

$$N_{\delta_r} = \frac{\bar{q} S b}{I_{zz}} C_{n_{\delta_r}}$$

$$N_{\delta_y} = \frac{\bar{q} S b}{I_{zz}} C_{n_{\delta_y}}$$

$$N_p = \frac{\bar{q} S b}{I_{zz}} \frac{b}{2V_t} C_{n_p}$$

$$N_r = \frac{\bar{q} S b}{I_{zz}} \frac{b}{2V_t} C_{n_r}$$

2.2 TIFS AERODYNAMIC AND PHYSICAL DATA

This section first presents a discussion of the results of the wind tunnel test of TIFS. The particular TIFS studied was the SST simulation configuration since it is longer than the AMSA configuration. Subsection 2.2.1 discusses the test results and compares them with estimates made before the tests. The static aerodynamics of TIFS can be obtained from the data given in the subsection. Additional aerodynamic data, primarily control and dynamic derivatives, are given in Subsection 2.2.2. Finally, physical data on weights and inertias, seat reference point, control surface deflection limits, and Fowler flap limits are in the last subsection.

2.2.1 TIFS Wind Tunnel Test

The TIFS wind tunnel tests, designated CVAL 471, were run with an unpowered (propellers off) 0.092 scale model of the C-131H* airplane with TIFS modifications incorporated. One hundred hours of testing were done at the Low Speed Wind Tunnel of General Dynamics, Convair Division, at San Diego between April 7 and 14, 1967.

The TIFS modifications included the addition of a forward SST cockpit and visor and side-force surfaces as well as substitutions of several flap configurations for the original Fowler flaps of the C-131H. The influence of the fuselage extension on the airplane stability and performance was determined. Also, these tests included measurements of the side-force surface and flap effectivenesses and their mutual interference effects.

Based on data in CVAL 104 (Reference 2.3), the equivalent full-scale reference center for all wind tunnel moment data is located at WL 36.00 in. and FS 381.30 in. This corresponds horizontally with 0.266c since the full-scale mean aerodynamic chord (MAC) is 114.3 in. and the leading edge of the mean aerodynamic chord is at FS 350.90 in. full-scale.

---

*The C-131H is understood to have the same airframe as the Allison Propjet conversion of the Convair 340. The wind tunnel model is referred to as a C-131H although it is not exactly so:

1. Table 2-1, which compares the empennages, shows a small difference in horizontal tail area.
2. The tail incidence used in CVAL 471 was $i_H = 0°$ rather than the $i_H = -0.5°$ of the C-131H airplane.
3. The turboprop engine nacelles used in CVAL 471 were approximations to the nacelles of the full-scale C-131H airplane.

The Reynolds number for the TIFS wind tunnel tests is approximately 1.2×10^6 based on the model MAC which is 10.516 in. Correspondingly, the dynamic pressure was 61.5 lb/ft^2 and the velocity was about 230 ft/sec. No attempt was made to apply Reynolds number corrections to the wind tunnel data.

Table 2-I
COMPARISON OF T-29E AND C-131H EMPENNAGES

MEASUREMENT	EQUIVALENT FULL-SCALE T-29E (REF. 2.3)	CONVAIR C-131H
OVERALL FUSELAGE LENGTH	79.1 ft	79.2 ft
HORIZONTAL TAIL AREA	250 ft^2	253 ft^2
HORIZONTAL TAIL LENGTH (FROM L.E. OF WING-FUSELAGE INTERSECTION TO HORIZONTAL TAIL HINGE)	46.0 ft	46.0 ft
VERTICAL TAIL AREA (ABOVE W.L. 94.8)	126.3 ft^2	126.3 ft^2
VERTICAL TAIL LENGTH (FROM L.E. OF WING-FUSELAGE INTERSECTION TO RUDDER HINGE)	46.7 ft	46.7 ft

2.2.1.1 Summary of Results

The wind tunnel tests show that TIFS essentially meets all aerodynamic predictions except those regarding the side-force surfaces. In particular, the side-force surface effectiveness is considerably smaller than required, and a substantial and unexpected flow separation on the wing due to the surfaces causes a large decrease in airplane lift coefficient and a large increase in induced drag. These results have necessitated a redesign of the side-force surfaces which will be evaluated in a forthcoming second wind tunnel test of TIFS.

The side-force surface (SFS) effectiveness was shown to depend on angle of attack, the effectiveness being greatest, and slightly exceeding the estimated value, at $\alpha = -4°$. At reasonable positive values of angle of attack, the SFS effectiveness is about 70% of the estimate. Analytical studies suggest that this is not adequate. Interference measurements designed to show the changes in side-force surface effectiveness due to direct lift flap (DLF) deflection showed that SFS effectiveness increases with DLF deflection either trailing edge up or down.

Tests showed that the direct lift, plain, outboard flaps are about as effective as estimated. For what are considered to be typical operating conditions, the effectiveness exceeds the estimate. The lift increment due to DLF deflection is highly nonlinear in character; the best linear range is centered about 5° trailing-edge up. Side-force surface deflections have negligible effect on flap effectiveness for representative angles of attack.

The TIFS (Nose) fuselage extension and the visor, the movable part of the fuselage extension, have a destabilizing effect in comparison with the basic C-131H as expected, but the amount of destabilization is slightly greater than estimated.

Although corrections for Reynolds number were not made, the drag increment due to TIFS modifications agrees approximately with estimates. The nose extension does not increase drag as much as expected while the increase due to side-force surfaces is higher than expected. The drag at zero lift with propellers off is increased about 30%.

Lift coefficient data with propellers off shows that with full down flap, Fowler flap inboard and plain flap outboard, the value of $C_{L_{max}}$ is decreased by no more than 20% compared with T-29E data previously measured for full Fowler flaps at zero thrust, propellers running.

Tests were made to show the effects of removing the nose gear door from the TIFS modification of the underside of the fuselage. The changes in lift coefficient and pitching moment coefficient are very small and certainly negligible. There was no measurable drag increase.

2.2.1.2 Stability with SST Forward Fuselage

Slopes measured at $\alpha = 0$ from Figure 2.4 show that the TIFS C_{m_α}, visor up, is -1.38 rad^{-1}*, whereas for the C-131H, it is 1.66 rad^{-1}. Therefore, the increment in C_{m_α} due to the addition of the SST nose, visor up, is +0.28 rad^{-1}. This is somewhat worse than the estimated incremental value of +0.23 rad^{-1}. The T-29E C_{m_α} values from CVAL 104 are

*Comparison of data from runs 87 (SFS on) and 17 (SFS off), CVAL 471, shows that the presence of the side-force surfaces affects both C_{m_α} and $C_{m_{C_L}}$. The data in this subsection is for side-force surfaces off.

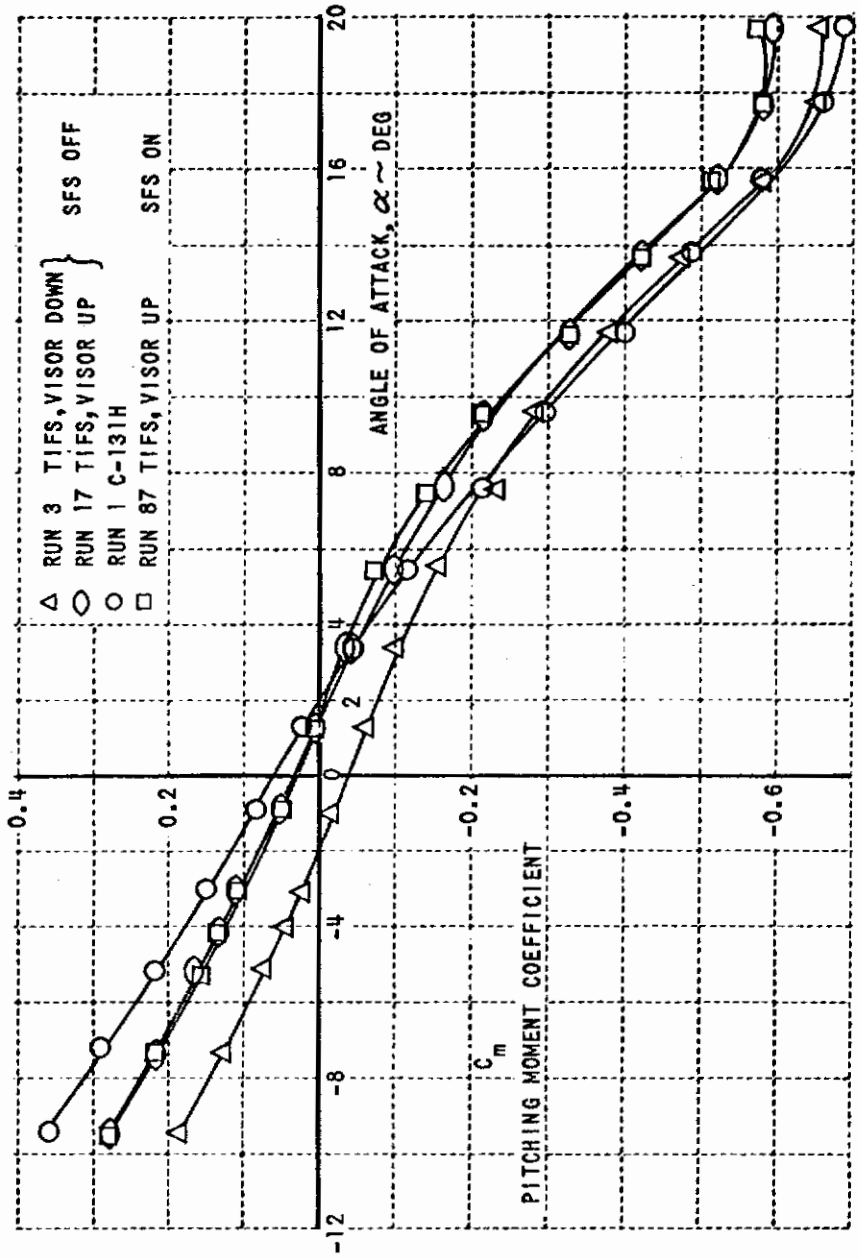

Figure 2.4 EFFECT OF TIFS MODIFICATIONS ON PITCHING MOMENT COEFFICIENT, $\beta = 0$

-1.26 and rad^{-1} for zero thrust (Reference 2.3, Fig. 10, Run 13), and -1.46 rad^{-1} for propellers off (Reference 2.3, Fig. 11, Run 163). The reason for the large discrepancy between the C-131H value, C_{m_α} = -1.66 rad^{-1}, and the T-29E propellers-off value, C_{m_α} = -1.46 rad^{-1}, has not been ascertained; these values should have been very nearly identical. The equivalent values of $C_{m_{C_L}}$ are -0.271 for the C-131H, -0.224 for TIFS with visor up, -0.205 for the T-29E at zero thrust, and -0.238 for the T-29E with propellers off.

When the visor is deflected downward 20°, the measured C_{m_α} is -1.15 rad^{-1} which is equivalent to $C_{m_{C_L}}$ = -0.187. From this, the increment in C_{m_α} due to the 20° visor deflection is +0.23 rad^{-1}.

With the value of C_{m_α} for the T-29E at zero thrust taken as a basis, the C_{m_α} for TIFS with visor up is -0.98; with the additional increment due to visor droop added, C_{m_α} is -0.75 rad^{-1}. These values, although considerably smaller than the C_{m_α} of the basic airplane, indicate that TIFS will have acceptable static stability. Moreover, the static stability loss due to the SST nose extension is offset by the c.g. positions to be used for TIFS, which are estimated to vary from about 10 to 20% of the MAC.

Figure 2.5, a plot of C_n vs β, was used to obtain incremental slopes between TIFS configurations with side-force surfaces off and the C-131H for static directional stability. C_{n_β} is +0.117 rad^{-1} with the SST nose installed and +0.153 rad^{-1} without it. Therefore, the increment in C_{n_β} due to the addition of the SST nose is -0.036 rad^{-1}. As for the longitudinal results, this value is larger than the estimated increment which was -0.019 rad^{-1}. When the visor is deflected downward 20°, the measured C_{n_β} is +0.093 rad^{-1}. From this, the increment due to the 20° visor deflection is -0.024 rad^{-1}. Figure 2.6 confirms this visor deflection increment for α = +4°. With the increment due to the SST nose added to the value of C_{n_β} for the T-29E at zero thrust (Reference 2.3), C_{n_β} for TIFS is +0.096 rad^{-1}; with both increments added, C_{n_β} is +0.072 rad^{-1}. Again, as for the longitudinal case, the directional static stability of TIFS, although much smaller than that of the T-29E, is acceptable.

Some of the difference in the no-propeller data of this test and the no-thrust but propellers running data of Reference 2.3 may be explained as propeller-fin effect. Qualitatively, such fin effects are

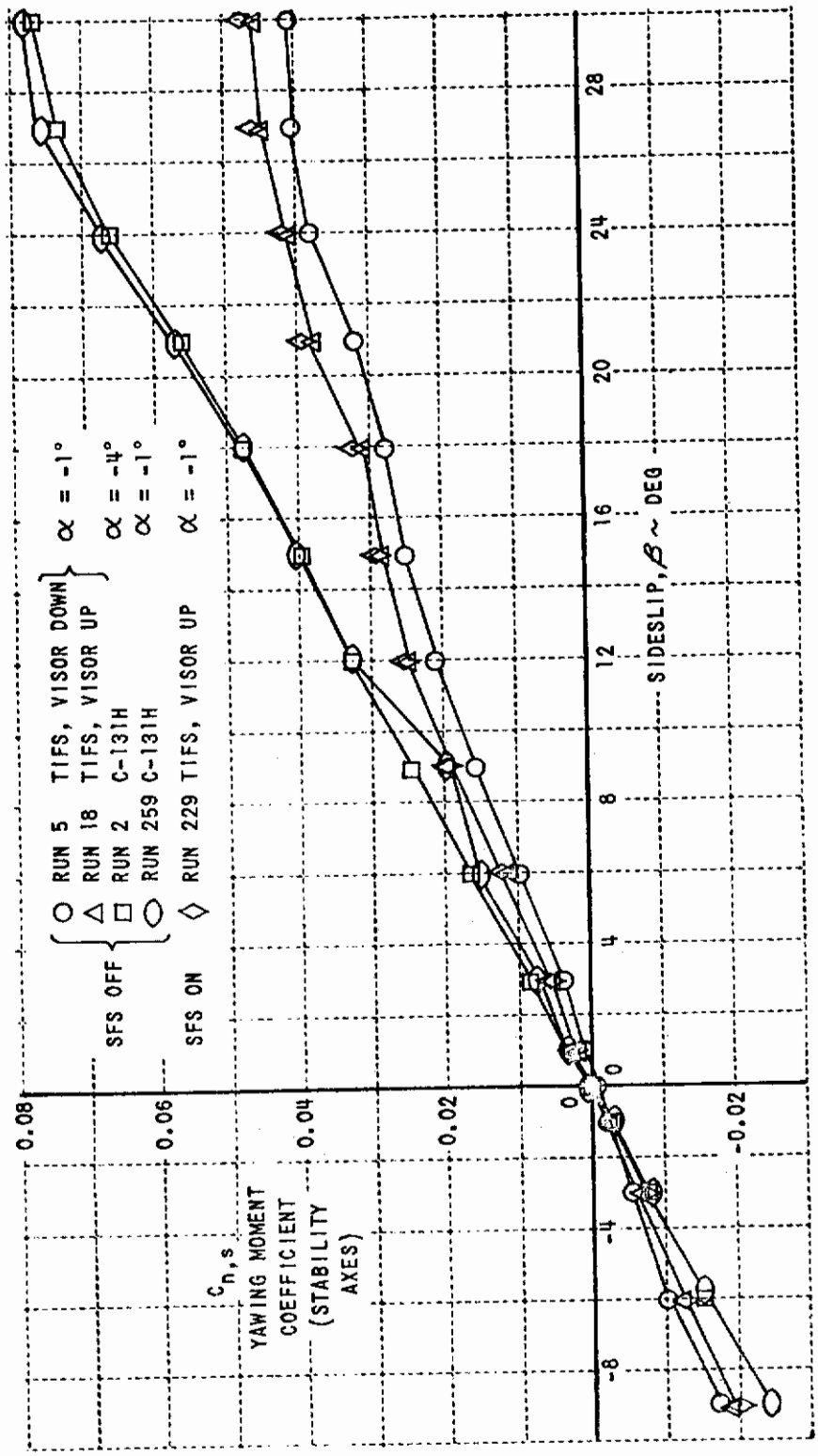

Figure 2.5 EFFECT OF TIFS MODIFICATIONS ON YAWING MOMENT COEFFICIENT, $\alpha = -1°$ AND $-4°$

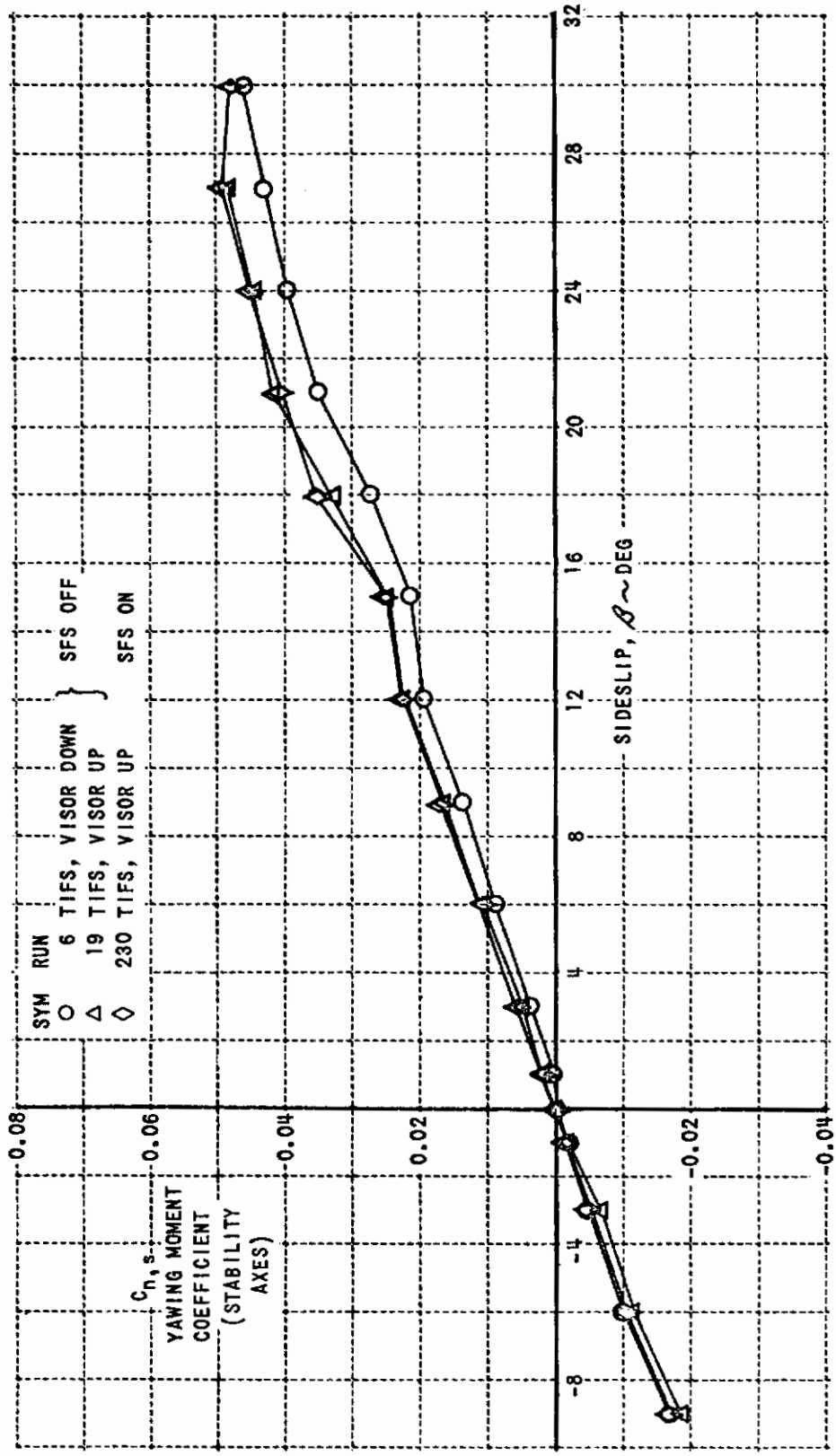

Figure 2.6 EFFECT OF TIFS MODIFICATIONS ON YAWING MOMENT COEFFICIENT, α = +4°

destabilizing for both the longitudinal and lateral results, as were the measurements in both cases.

2.2.1.3 Loads on the TIFS SST Nose with Visor Down

The incremental lift coefficient between TIFS with visor down 20° and the C-131H at $\alpha = 0°$ is about -0.017, which compares with -0.028 estimated. However, the lift increment is too small to be accurate from the test data. In fact, the incremental lift coefficient between visor up and the C-131H appears larger than that between visor down and visor up (see Figure 2.7) - a result which would lead one to question the accuracy of the data.

Two other measurements that pertain to visor loads are ΔC_m at constant α and ΔC_{m_α} between visor down 20° and the C-131H. The change in ΔC_m at $\alpha = 0°$ is -0.095 (see Figure 2.4) compared with an estimate of -0.137. The change in ΔC_{m_α} is from -1.66 to -1.15 or +0.51 rad^{-1} as noted previously. The increment of ΔC_{m_α} consistent with the estimated lift on the visor is +0.41 rad^{-1}.

The drag increment due to the TIFS SST nose with visor down 20° was estimated theoretically for $\alpha = 0°$ using slender body theory with cross flow. The value $\Delta C_D = 0.011$ was obtained. The measured increment between TIFS, visor down, and the C-131H is $\Delta C_D = 0.012$ at $\alpha = 0°$. This apparently good agreement between estimated and measured increments is quite likely fortuitous since the estimate ignored any aerodynamic influence of the SST nose with drooped visor on the remainder of the fuselage.

In view of the fact that the measured increments are small differences of large numbers and that there is reason to question the accuracy of the lift data, it is recommended that the estimated increments to used for design purposes. (See Reference 2.4 for further consideration of loads due to the TIFS SST nose with visor down.)

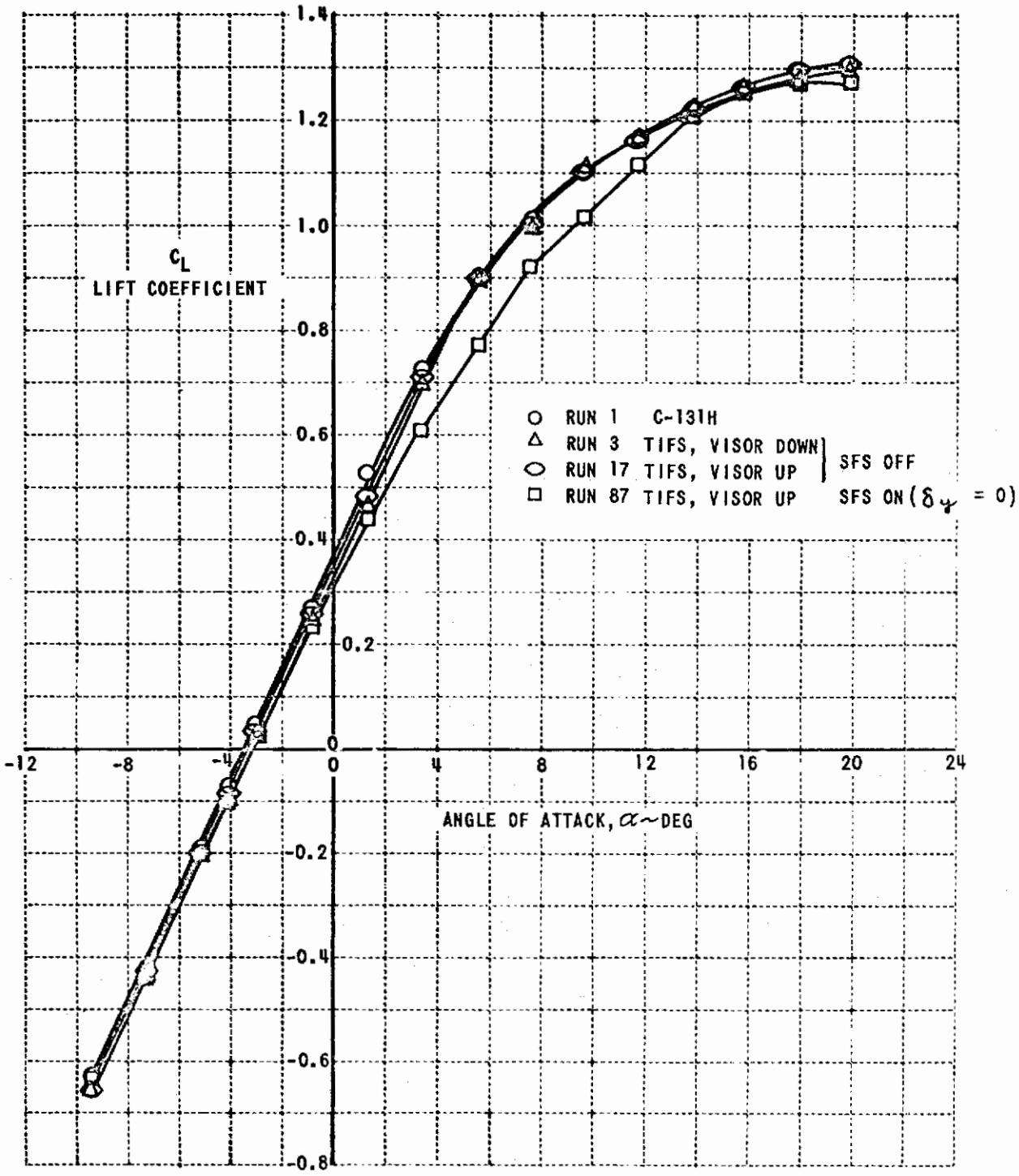

Figure 2.7 EFFECT OF TIFS MODIFICATIONS ON LIFT COEFFICIENT: $\delta_F = 0, \delta_j = 0$

2.2.1.4 Modification Effects on Lift and Drag - Flaps Up

Lift coefficients and drag coefficients versus angle of attack show expected results for the fuselage extension but entirely unexpected results for the side-force surfaces (see Figures 2.7 and 2.8). The fuselage extension has little effect on the slope of the lift curve: C_{L_α} = 6.2 rad^{-1} for C-131H, 6.1 rad^{-1} for TIFS less side-force surfaces. These values compare with 5.8 rad^{-1} estimated. The maximum lift coefficient is about 1.3, flaps up, and is not affected by the fuselage extension nor even significantly by the side-force surfaces. However, for the range of angle of attack with respect to the fuselage reference line between zero and fourteen degrees, there is a deficiency in lift and an accretion of drag which, along with observations from the tuft pictures, make clear the existence of appreciable unexpected interference and local separation of flow at the side-force surface and wing junctures. Forthcoming wind tunnel tests of the redesigned side-force surfaces should show considerable improvement.

2.2.1.5 Side-Force Surface Effectiveness Without Flaps

Peak effectiveness of the side-force surfaces occurs at α = -4°, as shown in Figure 2.9. The peak value is about what was estimated when allowances were made for reduced aspect ratio based on the gap between the surfaces and the wing. For angles of attack smaller or larger than -4°, the effectiveness drops off until at α = 4° it is about what has been estimated for infinite gap at the roots of the surfaces. "Infinite gap" assumes that the upper and lower side-force surfaces act independently in generating side-force; whereas "finite gap" designates the case estimated in which the opening between the side-force surface and the wing averaged about 5.5% of the side-force surface root chord.

Assuming that δ_y and β are equally effective in producing side-force surface force, the useful range of the side-force surface deflection is about $\pm$22° as may be construed from the δ_y = 0 yaw run (Run 26) in Figure 2.10. (Figure 2-11 confirms this conclusion for α = -1°.)

The side-force coefficient in wind axes for TIFS with δ_y = 0 has been plotted vs. sideslip in Figure 2.12 for comparison with the same data for the C-131H and for TIFS without side-force surfaces. The measured slopes, C_{Y_β}, are compared in Table 2-? with those estimated.

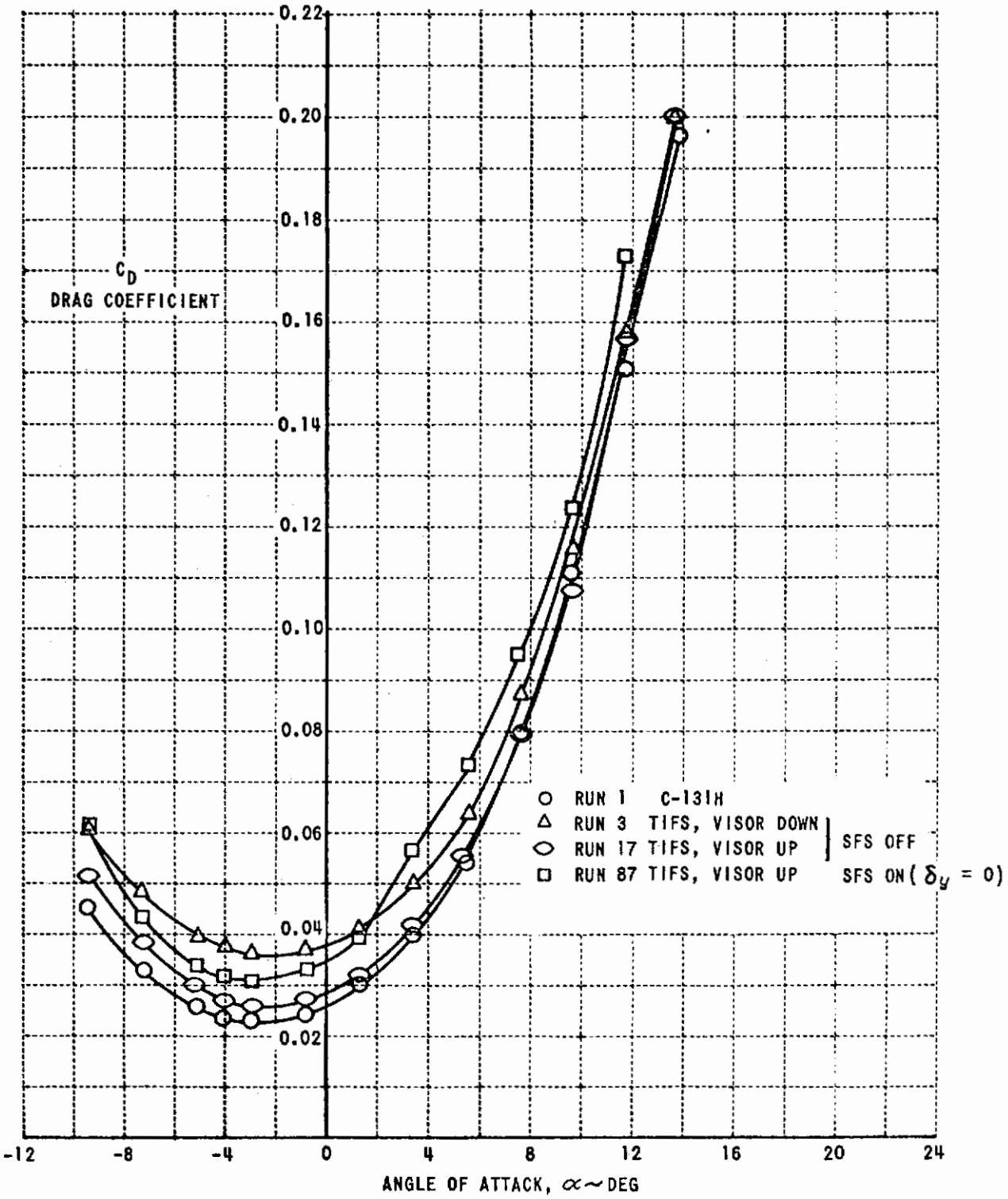

Figure 2.8 EFFECT OF TIFS MODIFICATIONS ON DRAG COEFFICIENT;
$\delta_F = 0, \delta_y = 0, \beta = 0$

EXTERNAL BALANCE

○ $\beta = 0$ $\quad C_{y_{\delta_y}} \approx \frac{\Delta C}{\Delta \delta_y}, \Delta\delta_y = +10° - (-5°)$

□ $\delta_y = 0$
× $\delta_y = 10$

SIDE-FORCE SURFACE BALANCE

$$C_{y_{\delta_y}} \approx \frac{\Delta(\text{SFS NORMAL FORCE})/\bar{q}\,S}{-\Delta\beta}$$

$\Delta\beta = +1° - (-1°)$

THIS ASSUMES THAT $\Delta\delta_y = -\Delta\beta$ AS REGARDS SIDE-FORCE SURFACE FORCE GENERATING CAPABILITY.

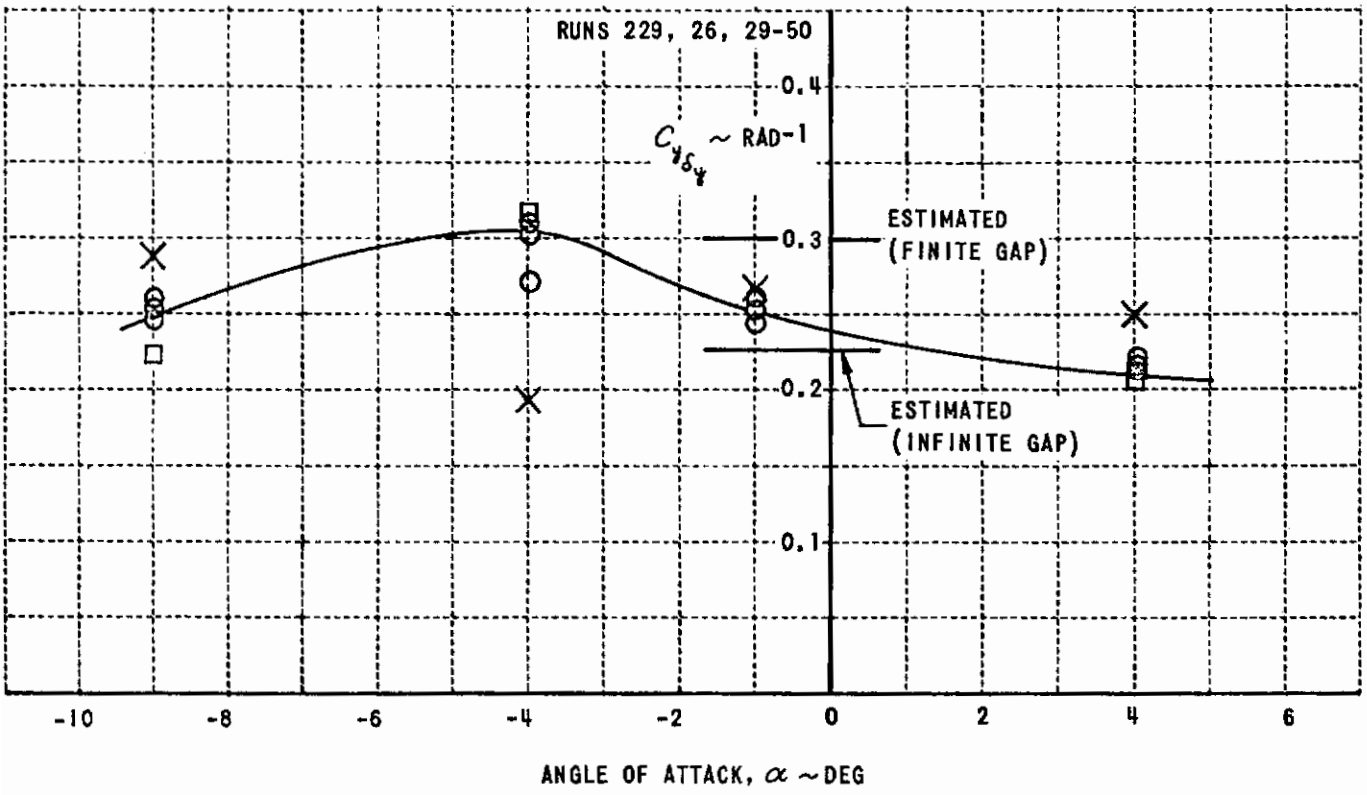

Figure 2.9 SIDE-FORCE EFFECTIVENESS, $\delta_y = 0$

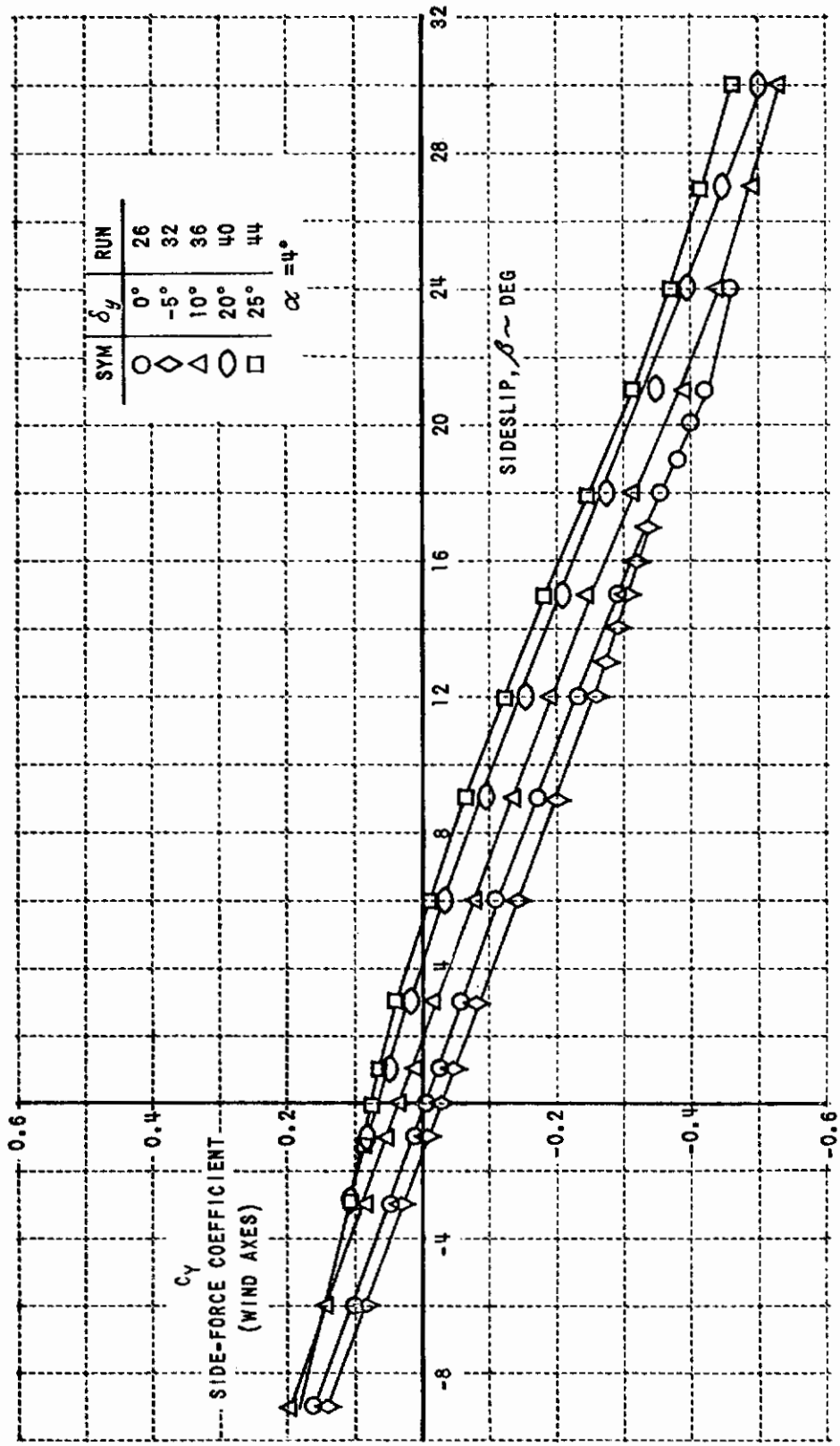

Figure 2.10 SIDE FORCE VS SIDESLIP AT VARIOUS SIDE-FORCE SURFACE ANGLES, α = +4°

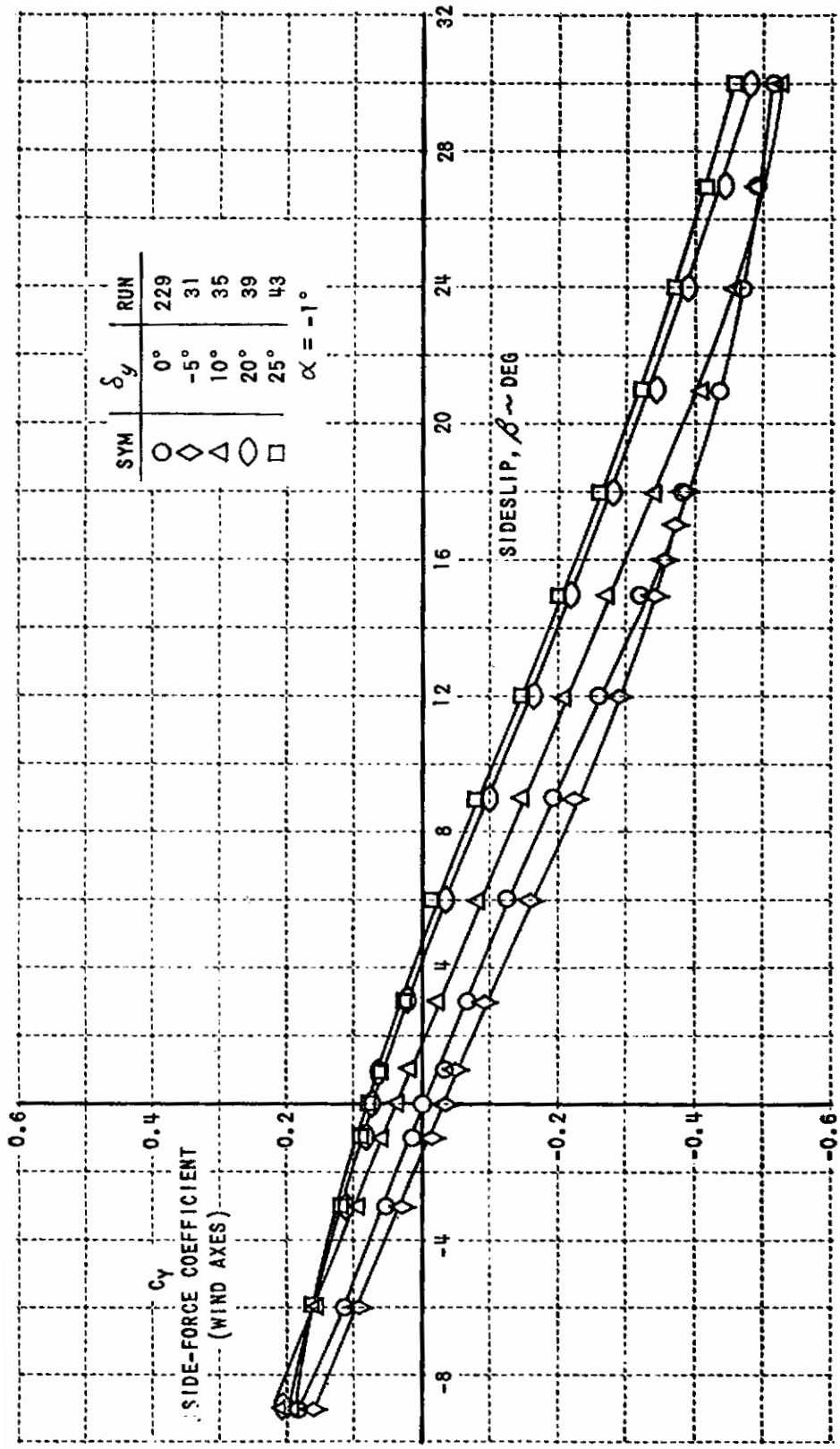

Figure 2.11 SIDE FORCE VS SIDESLIP AT VARIOUS SIDE-FORCE SURFACE ANGLES, α = -1°

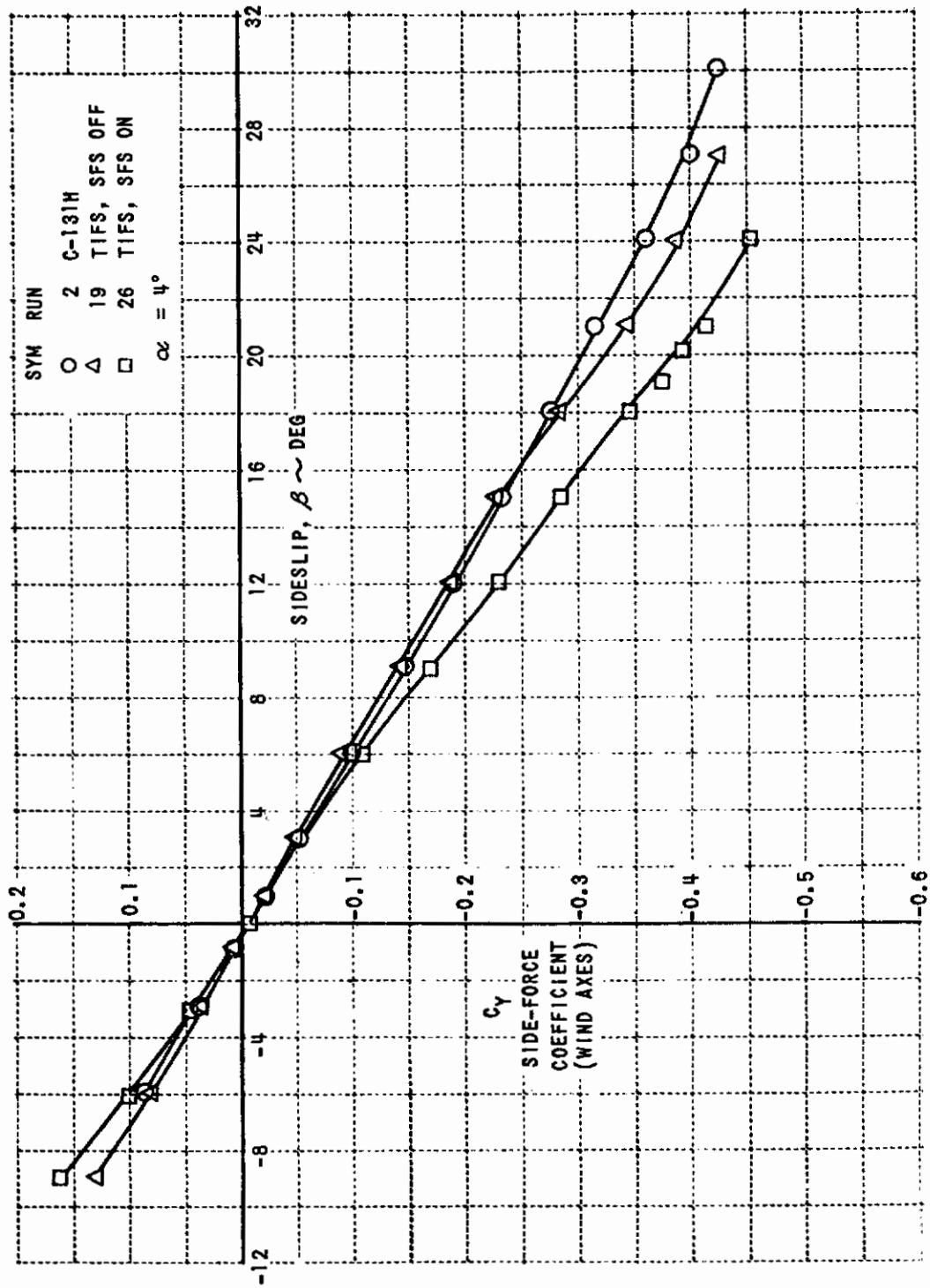

Figure 2.12 EFFECT OF TIFS MODIFICATIONS ON SIDE FORCE VS SIDESLIP, α =+4°

Table 2-2
COMPARISON OF MEASURED AND ESTIMATED C_{Y_β} (WIND AXES)

$\alpha = +4°, \beta = 0, \delta_y = 0$

CONFIGURATION	MEASURED (rad^{-1})	ESTIMATED (rad^{-1})
TIFS	-1.02	-1.22
TIFS LESS SFS	-0.80	-0.92
C-131H	-0.84	-0.92*

*FROM FIGURE 33, CVAL 104 (REF. 2.3), $T_c' = 0$.

Again, the smaller absolute magnitudes of the measured data can be charged to the lack of rotating propellers. There is no explanation for the reduction in C_{Y_β} at α = +4° for the TIFS less side-force surfaces when compared to the basic C-131H. In fact, from Figure 2.12 it is noted that such a trend reverses above β = 18°. As noted from the effectiveness tests and confirmed from the ΔC_{Y_β}, the side-force surfaces at this angle of attack are about equal in effectiveness to estimates based on infinite gaps at the roots. For α = -1° (Figure 2.13), the magnitude of the slope is -1.19 rad^{-1}, which is much closer to the value estimated for finite gap, and is a further reflection of the better effectiveness of the side-force surfaces for small negative angles of attack. Also, at α = -1°, it is noted that the SST nose consistently increases the side-force slope even for visor down as compared with the basic C-131H.

The side-force surfaces have little influence on rolling or yawing moments.

Hinge moments and normal force measurements from the strain gage balance showed the aerodynamic center to be between 17% and 20% of the side-force surface mean aerodynamic chord. This is substantially farther forward than was expected. Since the side-force surface hinge line is at 23% of the side-force surface mean aerodynamic chord, this data indicates an unstable hinge moment condition which is unacceptable from a fail-safe standpoint. This forward shift of the SFS aerodynamic center, which can probably be attributed to flow interference due to the wing, will be accounted for in the redesign of the side-force surfaces for the forthcoming second wind tunnel test of TIFS.

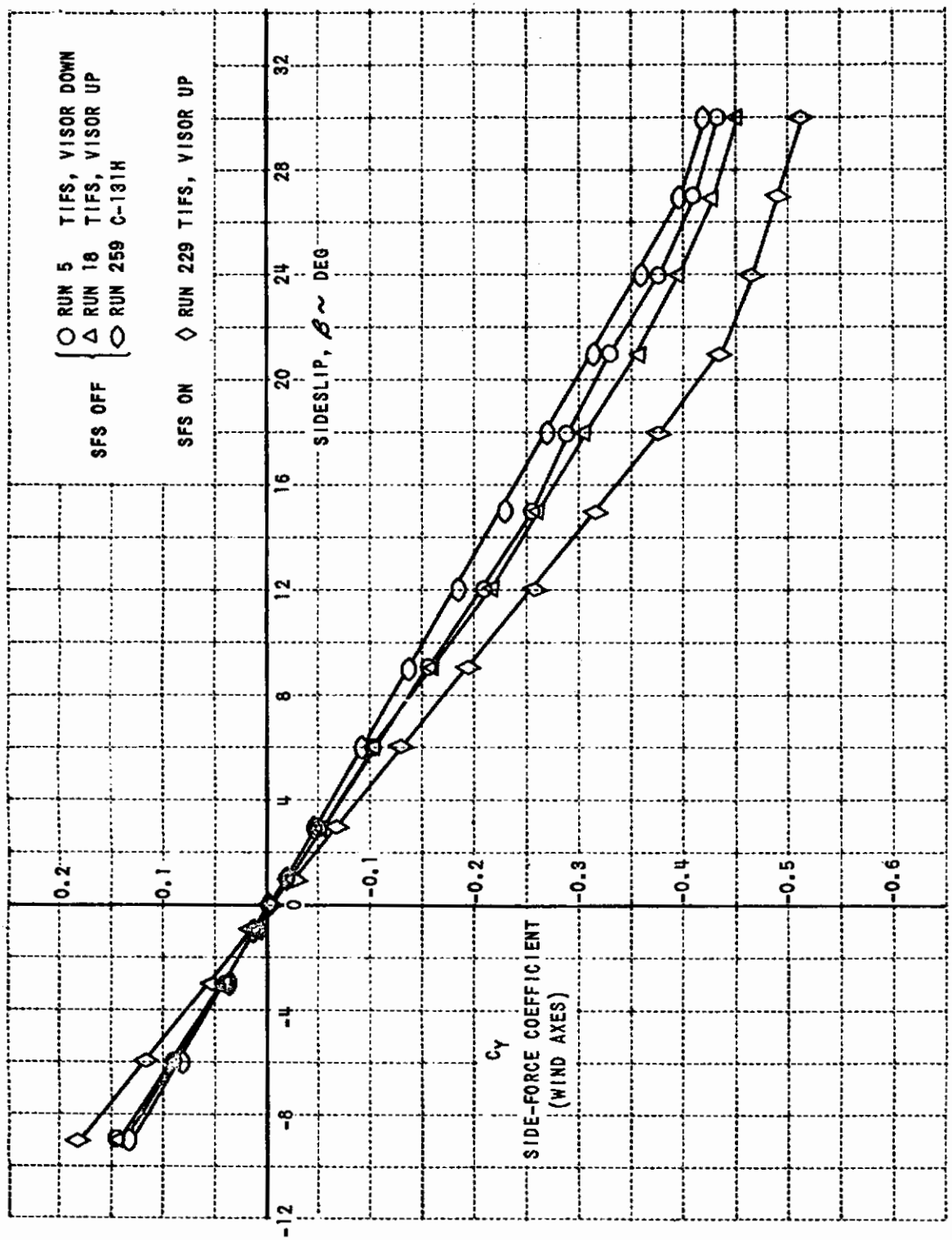

Figure 2.13 EFFECT OF TIFS MODIFICATIONS ON SIDE FORCE VS SIDESLIP, $\alpha = -1°$

2.2.1.6 Landing Flaps

The C_L vs α test with landing flaps was run and repeated during the CVAL 471 wind tunnel tests. These repeat runs were in good agreement and showed $C_{L_{max}} = 1.58$ at $\alpha = 10°$ (Figure 2.14). The inboard Fowler flaps were set at 45° and the outboard plain flaps were set at 40° for landing. The decrease in $C_{L_{max}}$ due to changing the outboard flaps from Fowler to plain was disappointingly large. As shown in Figure 2.14, $C_{L_{max}}$ for the T-29E wind tunnel tests is 1.95. However, the T-29E test was made with propellers operating and enough thrust to overcome propeller and slipstream drag ($T_C' = 0$). Some benefit in $C_{L_{max}}$ would be expected because of slipstream effects although it fails to materialize for flaps up. In fact, the flaps zero, $T_C' = 0$, data of CVAL 104 (Reference 2.3) (Figure 2.14) agree very well with the TIFS, propeller off side-force surface off data (Figure 2.7, visor up or down). See Section 2.3 for complete data for $T_C' \neq 0$.

2.2.1.7 Outboard Flaps

The C_L vs α runs, which are plotted in Figure 2.14, include separate tests of the inboard Fowler and the outboard plain flaps. The increment of lift coefficient at various angles of attack for full downward deflection of the outboard plain flaps is listed in Table 2-3.

Table 2-3
OUTBOARD PLAIN FLAP INCREMENT
$\delta_f = +40°$

α	ΔC_L
-5	0.45
0	0.40
5	0.33
10	0.27

The increment of lift coefficient based on a constant slope for $C_{L_{\delta_f}}$ of 1.1 rad^{-1} would amount to $\Delta C_L = 0.75$, too large by almost a factor of three (at $\alpha = 10°$) when compared with the measurement. Some change in slope at extreme flap angles should be expected, but it is believed that the side-force

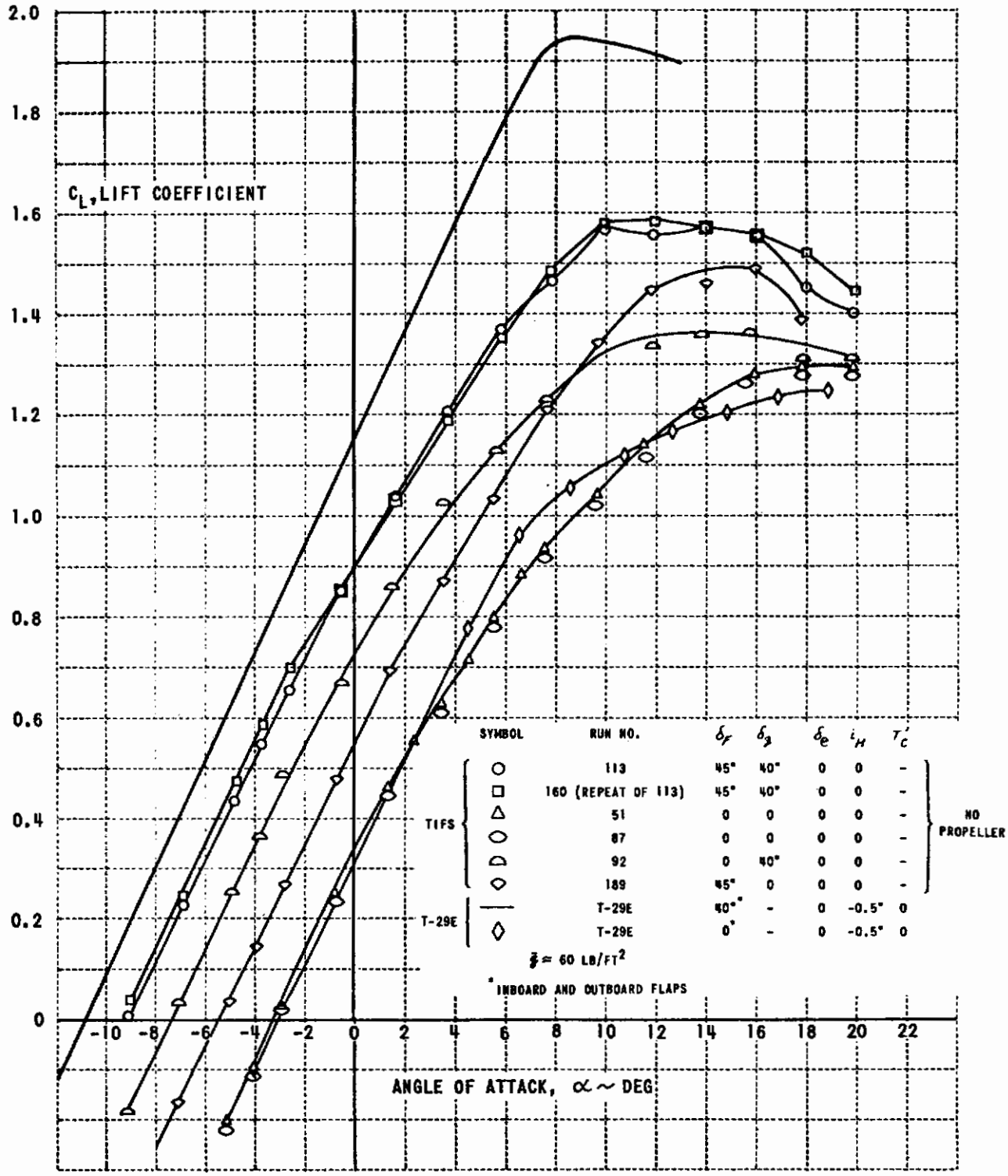

Figure 2.14 EFFECT OF TIFS FLAP CONFIGURATION ON LIFT COEFFICIENT

surfaces are appreciably influencing the loss of lift increment because of interference and flow separation. The fact that the estimated slope can be realized under conditions which give relatively little interference (i.e. smaller flap deflections) is shown in Figure 2.15. For $\alpha = -4°$ and $-15 < \delta_3 < +15°$ the estimated value of $C_{L_{\delta_3}}$ is actually exceeded.

Incremental pitching moment coefficient and drag coefficient data are given for the outboard plain flap in Figures 2.16 and 2.17 respectively. From data not included here, it is noted that the incremental moment tends to be of opposite sign to that shown in Figure 2.16 when the flap configuration includes like deflection of both inboard and outboard flaps. Evidently, whenever the inboard Fowler flaps are deflected, the changed downwash on the tail contributes so strongly to pitching moment (but in the opposite sense of that from the flap loads themselves) as to govern the net value of overall pitching moment. The negative increment of drag for some negative flap settings and positive angle of attack (Figure 2.17) apparently is the result of increasing the angle of attack for zero lift of the flapped portion of the wing. Recall that for a given ΔC_L, ΔC_m or ΔC_D the angle of the fuselage reference line is held constant in the wind tunnel.

2.2.1.8 Downwash

Wind tunnel tests were made for tail-off and tail-on configurations with horizontal stabilizer settings of -5°, 0°, +5°. The inboard Fowler flaps were set at 45° throughout these downwash tests, but the outboard direct lift flaps varied for each stabilizer setting through the following values: δ_3 = -40, -30, -15, 0, 15, 30 and 40°. The same flap settings were repeated for the tail-off tests.

When tail-off pitching moment is plotted vs angle of attack, it has in general a positive slope, i.e., the airplane less tail is unstable. The slope of the tail-on data is normally negative, and hence an intersection of the curves will occur. At such an intersection where both α and C_m are the same with and without the tail, the contribution of the tail to the moment is zero. Naturally, only data for a given flap setting are compared. At the point of intersection, the tail lift is assumed to be zero since it contributes

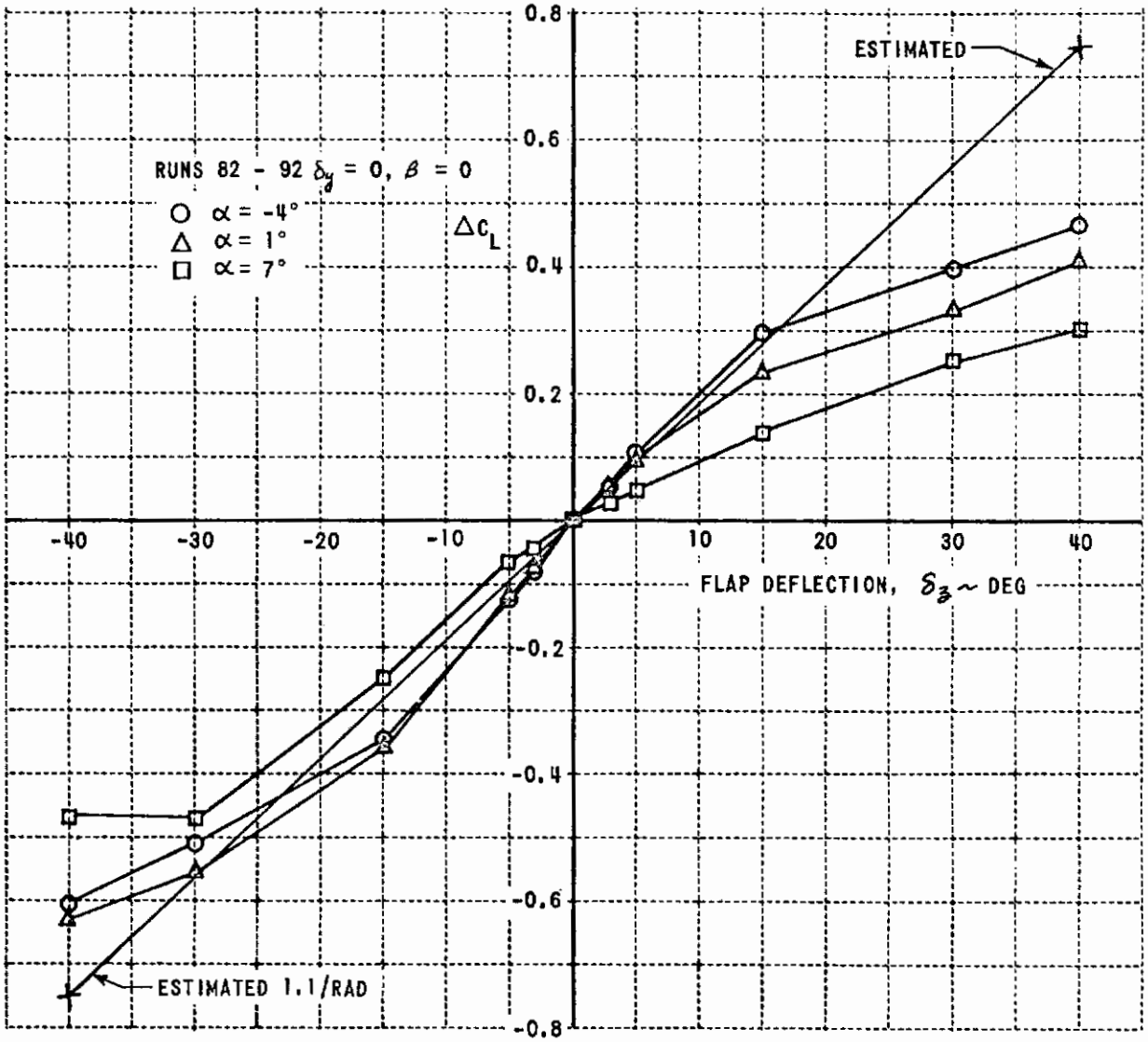

Figure 2.15 PLAIN FLAP LIFT COEFFICIENT INCREMENT VS FLAP ANGLE

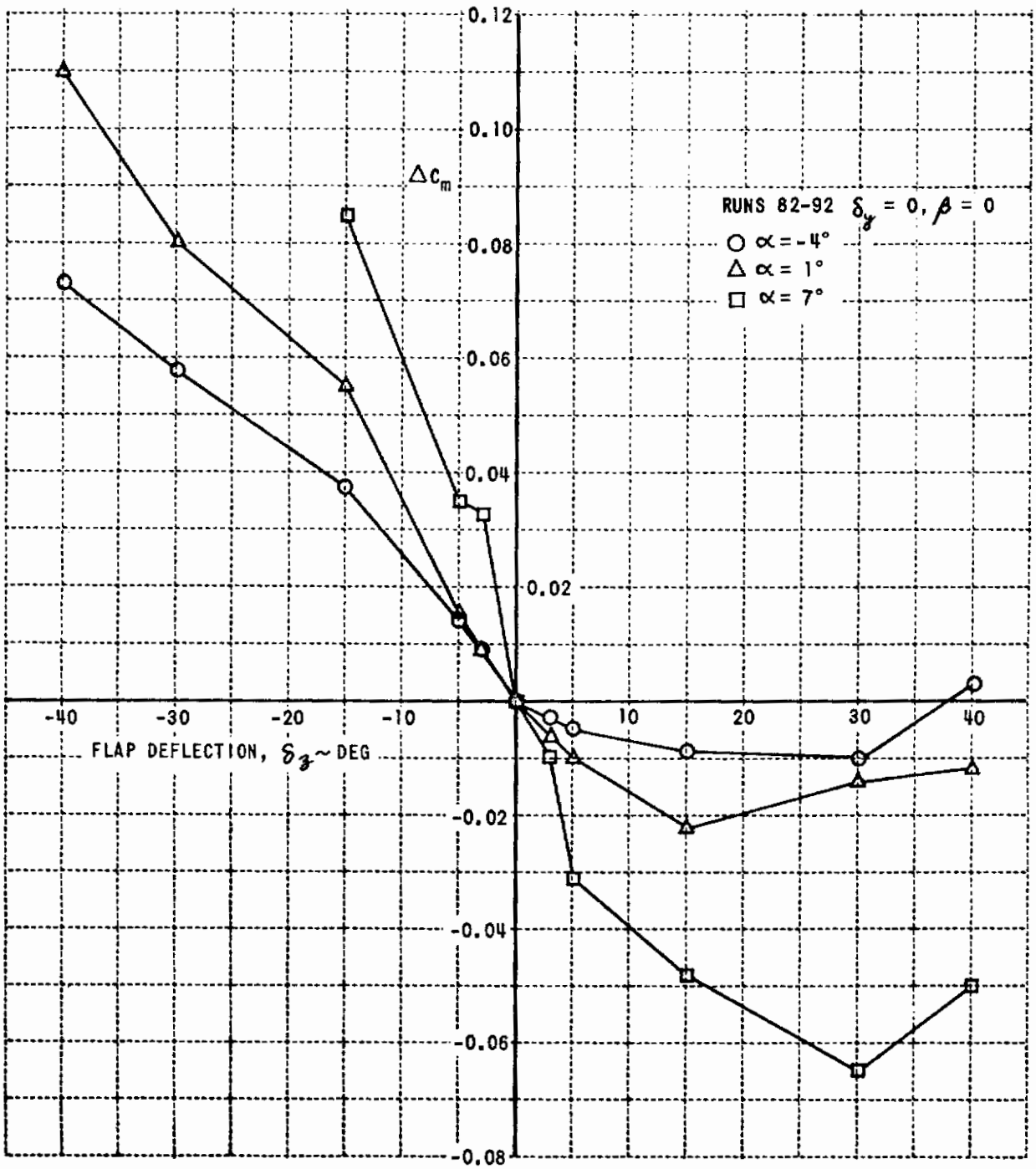

Figure 2.16 PLAIN FLAP MOMENT COEFFICIENT INCREMENT VS FLAP ANGLE

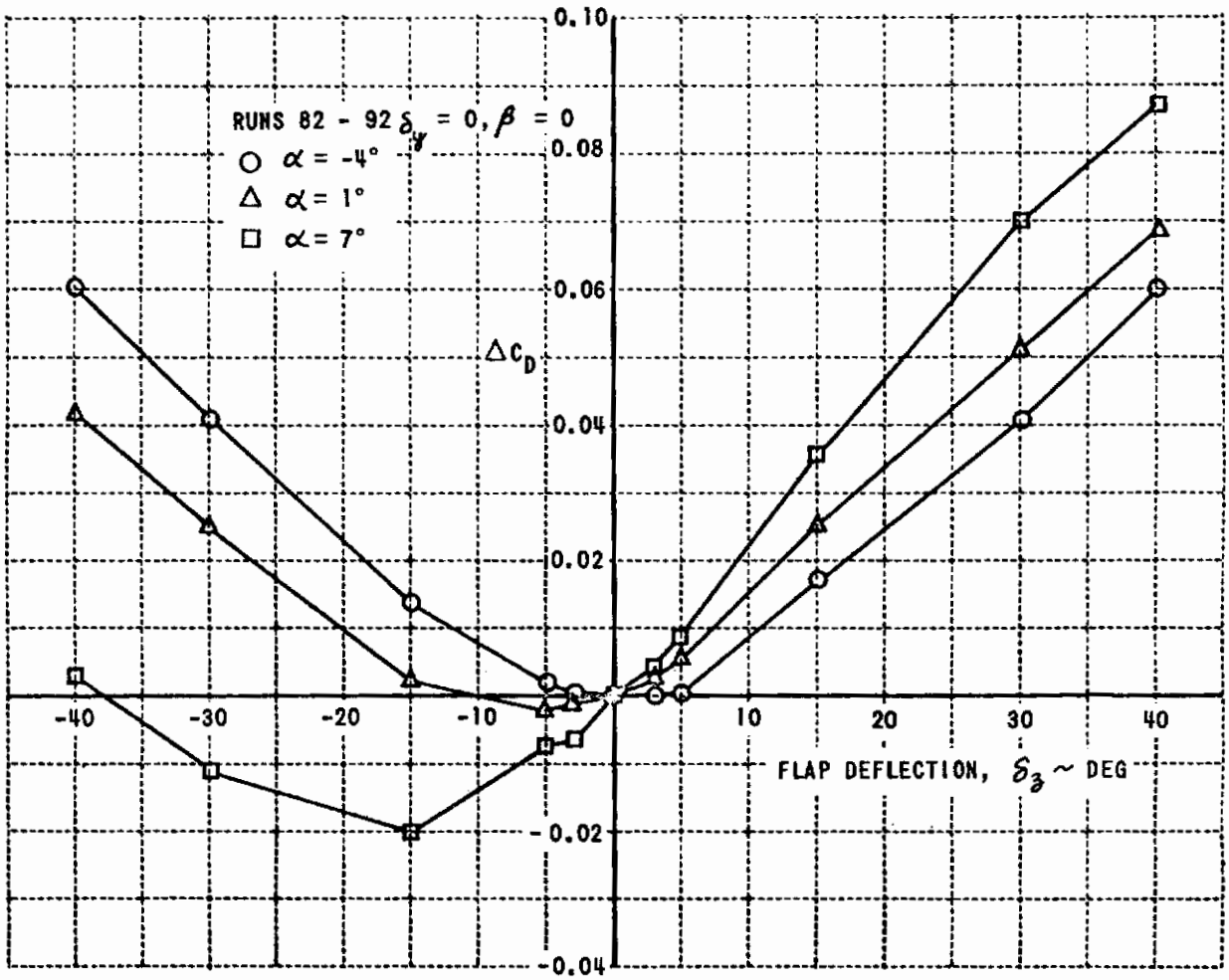

Figure 2.17 PLAIN FLAP DRAG COEFFICIENT INCREMENT VS FLAP ANGLE

no moment. The stabilizer setting must therefore correspond to the zero-lift angle of attack of the tail, which is zero for an untwisted tail of symmetrical section.

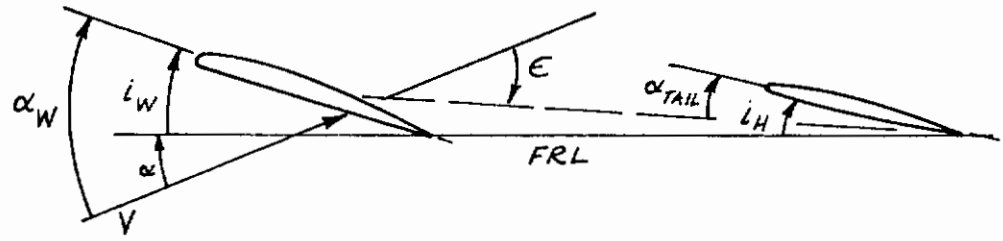

The relationship of the tail angle of attack to the downwash from the wing is shown in the accompanying sketch. It can be seen that

$$\alpha_{tail} = \alpha + i_H - \epsilon;$$

therefore, for α_{tail} = 0, which applies to the downwash tests described here,

$$\epsilon_{\alpha\, tail=0} = \alpha + i_H$$

The downwash angles are plotted in Figure 2.18 with δ_f, the outboard direct lift flap setting, as a parameter. It is noted that the greatest value for the slope $\frac{\Delta\epsilon}{\Delta\alpha}$ is 0.58 and occurs at δ_f = -40°; the least value is 0.41 at δ_f = +30°. There is no apparent explanation for the increase in the value of $\frac{\Delta\epsilon}{\Delta\alpha}$ between δ_f = 30° and 40°. With the relationship of downwash slope and outboard flap angle in mind, one may be puzzled to note that at the highest angles of attack, where separation might be expected to be extreme, the ϵ appears to recover for flap angles greater than, as well as less than, δ_f = 0°. Again it is noted that these downwash measurements were made with inboard Fowler flaps at 45°. The important result of these tests is that they show the downwash at the tail to be practically independent of the outboard direct lift flap positions.

2.2.1.9 Influence of Outboard Flaps on Side-Force Surfaces

Flap deflection increases side-force effectiveness as is shown in Figures 2.19 and 2.20. Perhaps the statement should be reversed to read lack of flap deflection reduces side-force effectiveness. The reverse statement is prompted by the fact that except at large absolute flap deflections the effectiveness is less than that estimated.*

*Estimation based on finite gap with δ_f = 0.

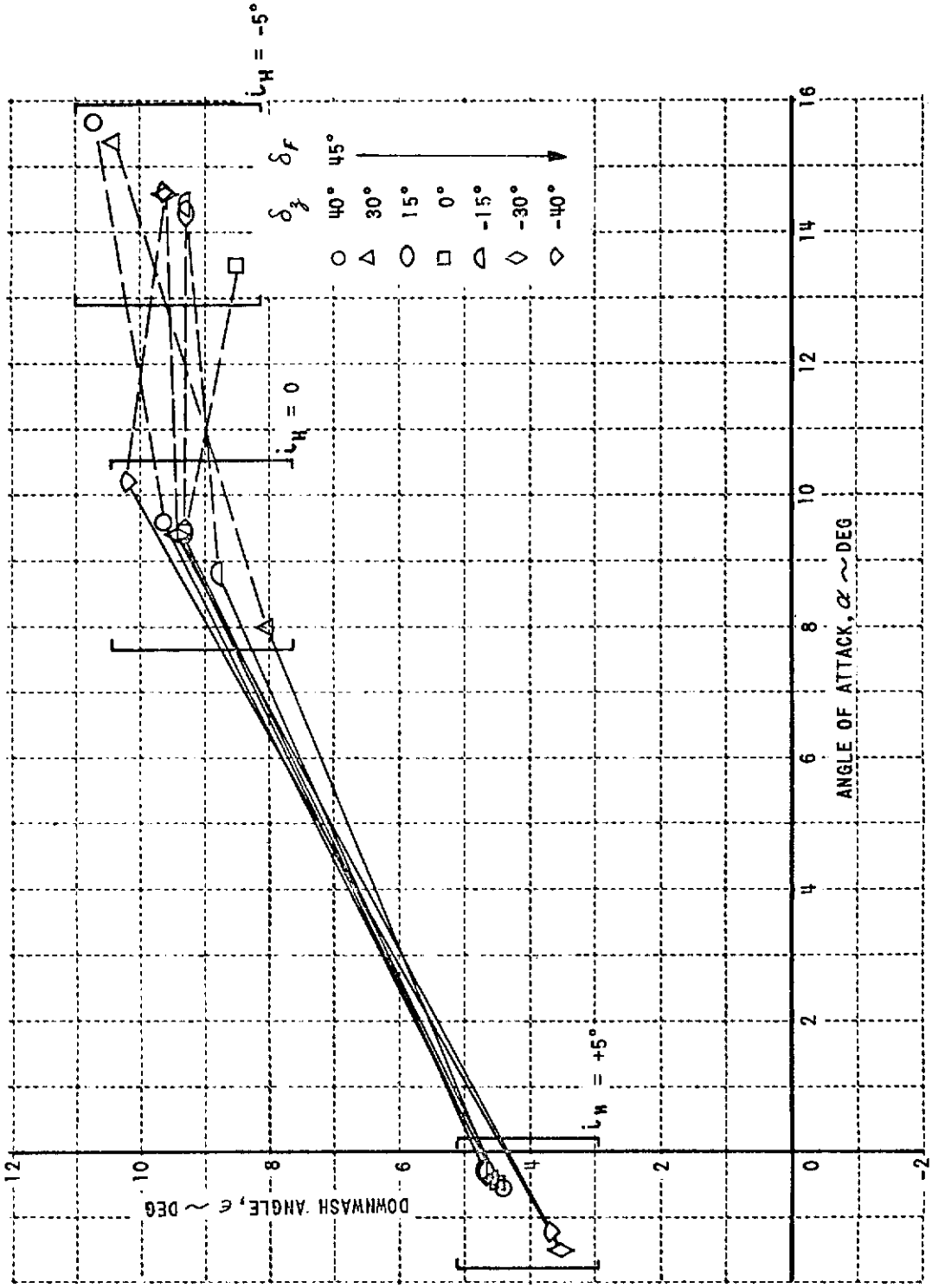

Figure 2.18 DOWNWASH ANGLE VS ANGLE OF ATTACK WITH VARIOUS PLAIN FLAP ANGLES AND FOWLER FLAPS AT 45°

Arguments for increased side-force effectiveness due to absolute flap angle might include one stating that boundary layer growth would tend to restrict flow through the gap at the root of the surfaces which increases the effectiveness of either the top or bottom side-force surfaces. Absolute flap angle would give higher adverse gradients and boundary layer growth. The opposite surface would not be expected to change, but a net increase in effectiveness would be noted. Another argument is based on second-order increases of average dynamic pressure due to changes in circulation which apply to both upper and lower surfaces. Neither argument appeals as being adequate to explain changes in effectiveness such as the nearly double effectiveness for -30° flap relative to near-zero flap (i.e. δ_y = +5°) shown in Figure 2.20.

Reports like Reference 2.5 show certain effects, such as backwash, which influence chordwise "$\bar{q}$" even for C_L = 0. Backwash effects, which are ordinarily neglected, should perhaps be included in estimates of wing interference on side-force surfaces.

2.2.1.10 Influence of Side-Force Surfaces on Drag in Yaw

The minimum increment of drag due to side-force surfaces, as noted earlier (Figure 2.8), is several times greater than estimated, measuring $\Delta C_D \approx 0.0060$ compared with 0.0018 estimated. Figure 2.8 also shows about the same increments of drag resulting from addition of side-force surfaces for α = -1° and -2°, which permits the comparison of Runs 23 and 24 with Run 18 of Figure 2.21. Figure 2.21 shows that the drag increases much more rapidly than an estimate of induced drag due to side-force surfaces would give. Incremental side-force surface drag coefficients were calculated and added to Run 18 to obtain the dashed curve of Figure 2.21. The much larger difference in measured drag coefficient is further evidence of flow separation due to the side-force surfaces that should be considerably alleviated with the redesigned side-force surfaces.

Data on effects of nose-gear door removed are seen to be insignificant as is also shown on Figure 2.21. Compare Runs 23 and 24. Analogous results showing insignificant drag increase for nose-gear door open were obtained in pitch (Runs 25 and 51); because of the negligible drag difference, these data are not presented.

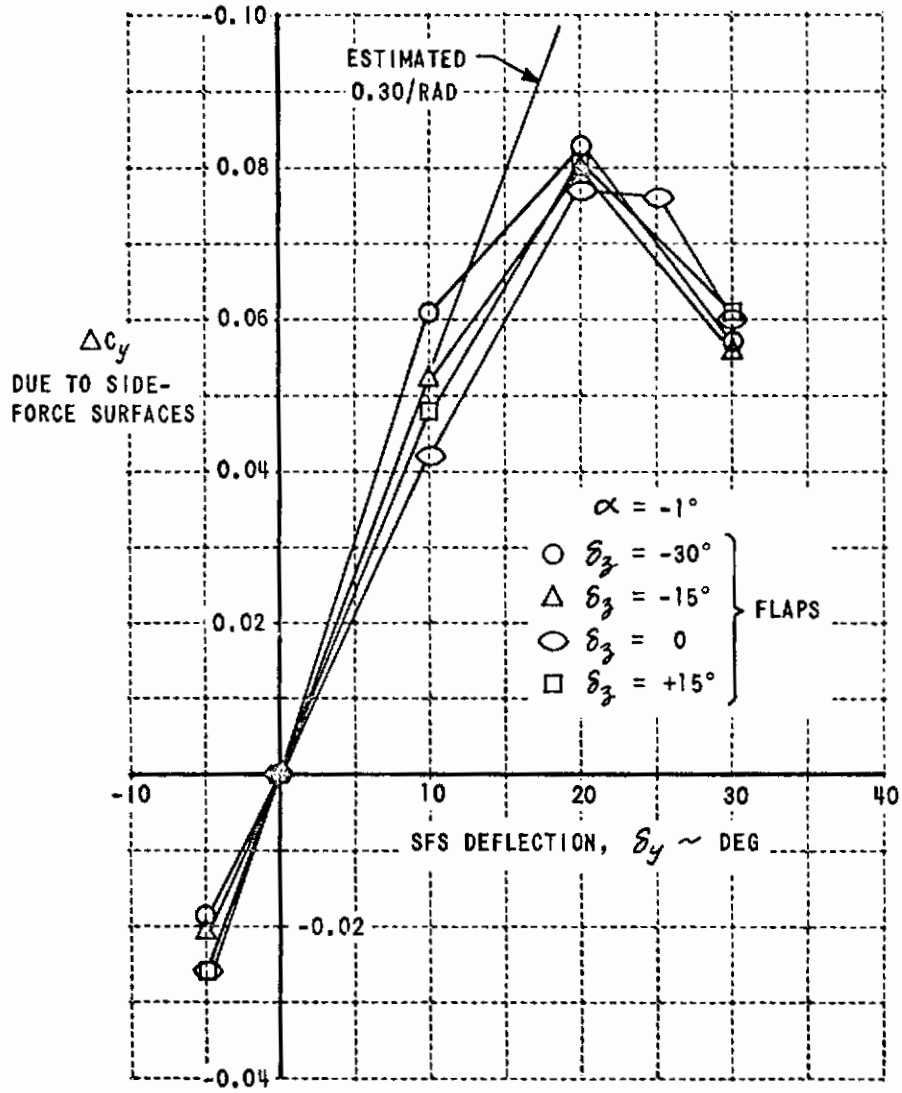

Figure 2.19 SIDE FORCE VS SIDE-FORCE SURFACE ANGLE FOR VARIOUS FLAP SETTINGS, α = -1°, β = 0

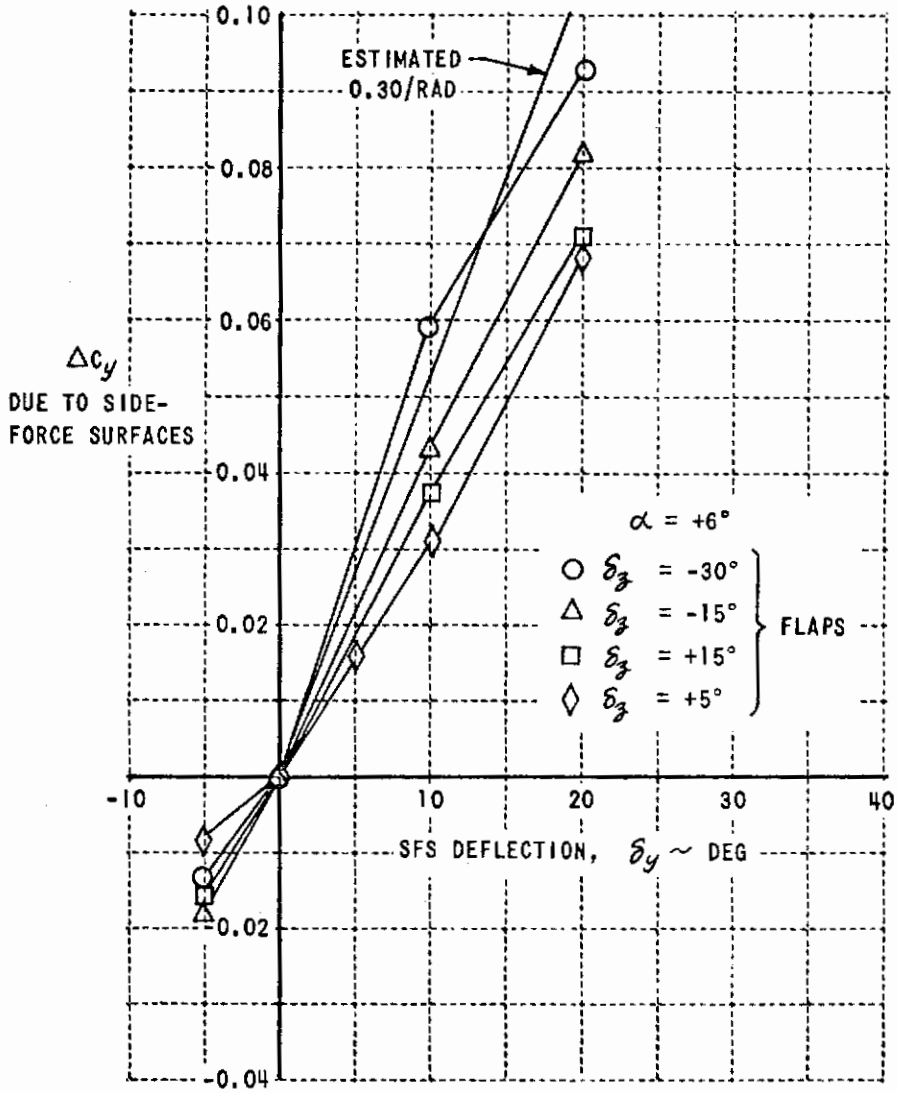

Figure 2.20 SIDE FORCE VS SIDE-FORCE SURFACE ANGLE FOR VARIOUS FLAP SETTINGS, α = +6°, β=0

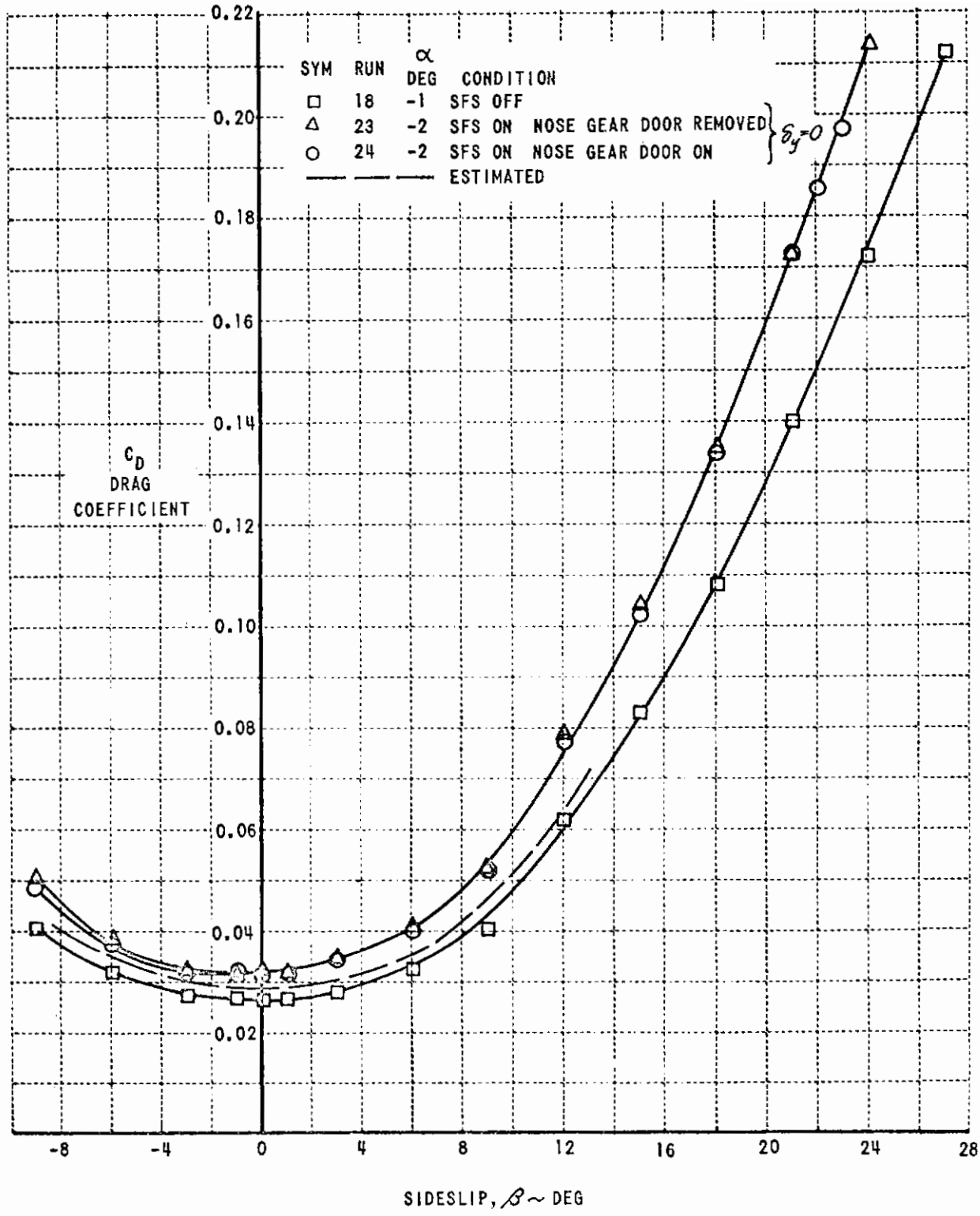

Figure 2.21 EFFECT OF TIFS SIDE-FORCE SURFACES ON DRAG COEFFICIENT VS SIDESLIP

2.2.1.11 Influence of Side-Force Surfaces on Flap Effectiveness

Side-force surface deflection is seen to have small influence on ability of outboard flaps to provide lift (Figure 2.22). At $\alpha = -1°$, the slope of $C_{L_{\delta_f}}$ decreases for positive flap angles as side-force surface angles increase from -5° to 20°. At $\alpha = 5°$, the value of δ_y has even less influence on the flap effectiveness than at $\alpha = -1°$.

Combined drag coefficient due to flaps and side-force surfaces is shown in Figure 2.23.

2.2.2 Additional Aerodynamic Data for TIFS

The wind tunnel tests of TIFS were designed to augment or supplement the test data given for the T-29E airplane in Reference 2.3. As a consequence, the data presented in Section 2.2.1 relate mostly to the TIFS modifications of the basic airplane. The present section tabulates additional aerodynamic data needed to describe the TIFS for purposes of variable stability loop design. Some of the data, mainly on control surface derivatives, come from Reference 2.3; the remaining data (mostly rotary and dynamic derivatives) have been estimated using the USAF Stability and Control DATCOM (Reference 2.6) and other sources. Table 2-4 presents the data.

Table 2-4

TIFS CONTROL, ROTARY AND DYNAMIC DERIVATIVES

(ALL MOMENT COEFFICIENTS ARE REFERRED TO .266c)

$C_{L_{\delta_e}} = +0.70\ \text{rad}^{-1}$

$C_{m_{\delta_e}} = -2.0\ \text{rad}^{-1}$

$C_{m_{\dot{\alpha}}} = -17\ \text{rad}^{-1}$

$C_{m_q} = -45\ \text{rad}^{-1}$

$C_{l_p} = -0.52\ \text{rad}^{-1}$

$C_{l_r} = +0.098 + 0.024\alpha, \text{rad}^{-1}$

α is in radians

δ_a is in radians

$C_{l_{\delta_a}} = -0.095 + 0.068|\delta_a|, \text{rad}^{-1}$

$C_{n_{\delta_a}} = 0$

$C_{l_{\delta_r}} = +0.037\ \text{rad}^{-1}$

$C_{n_{\delta_r}} = -0.13\ \text{rad}^{-1}$

$C_{y_{\delta_a}} = 0$

$C_{y_{\delta_r}} = +0.35\ \text{rad}^{-1}$

$C_{y_p} = 0$

$C_{y_r} = 0$

$C_{n_p} = -0.016 - 0.28\alpha, \text{rad}^{-1}$

$C_{n_r} = -0.12\ \text{rad}^{-1}$

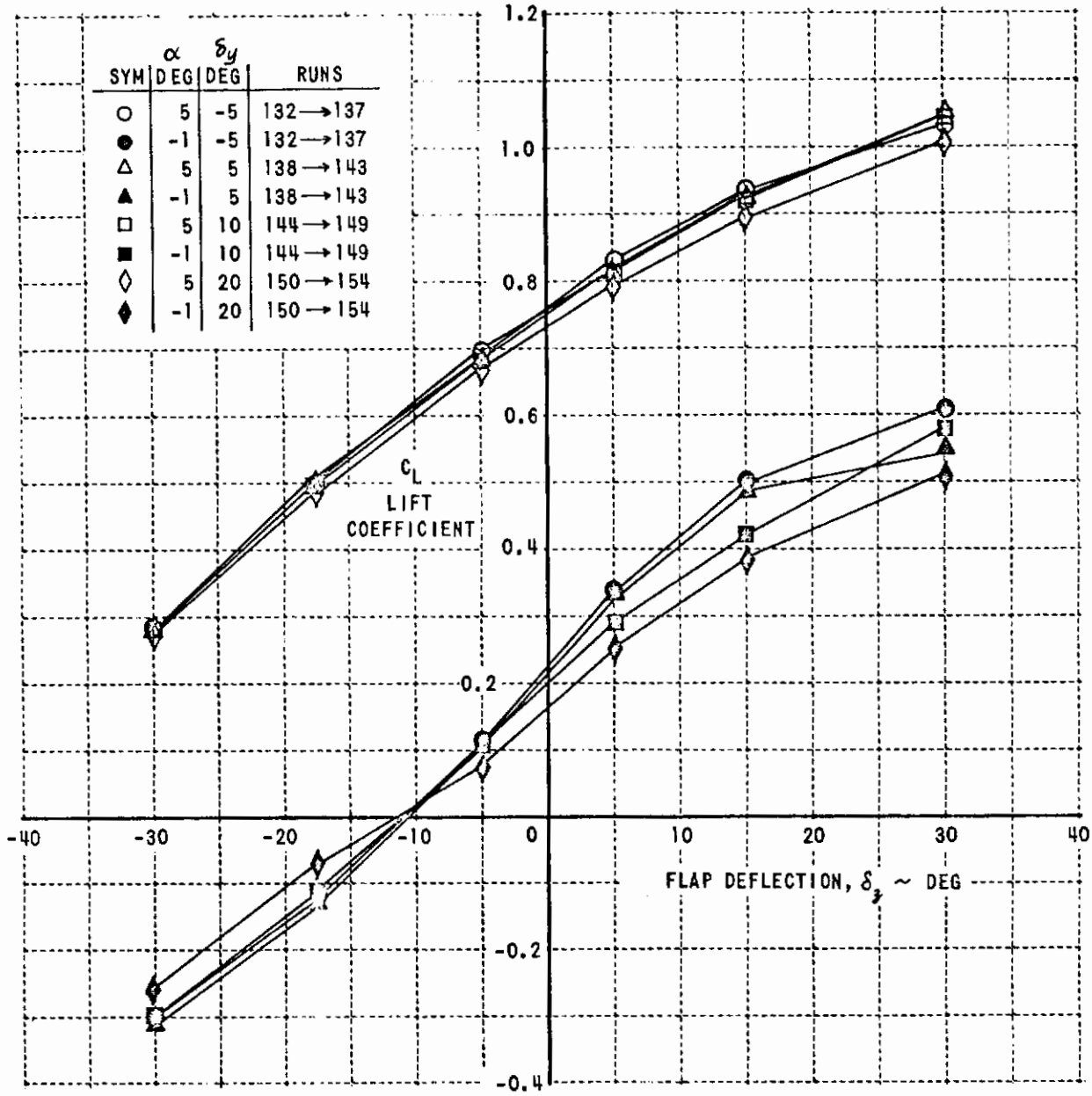

Figure 2.22 EFFECT OF SIDE-FORCE SURFACES ON LIFT DUE TO DIRECT LIFT FLAPS

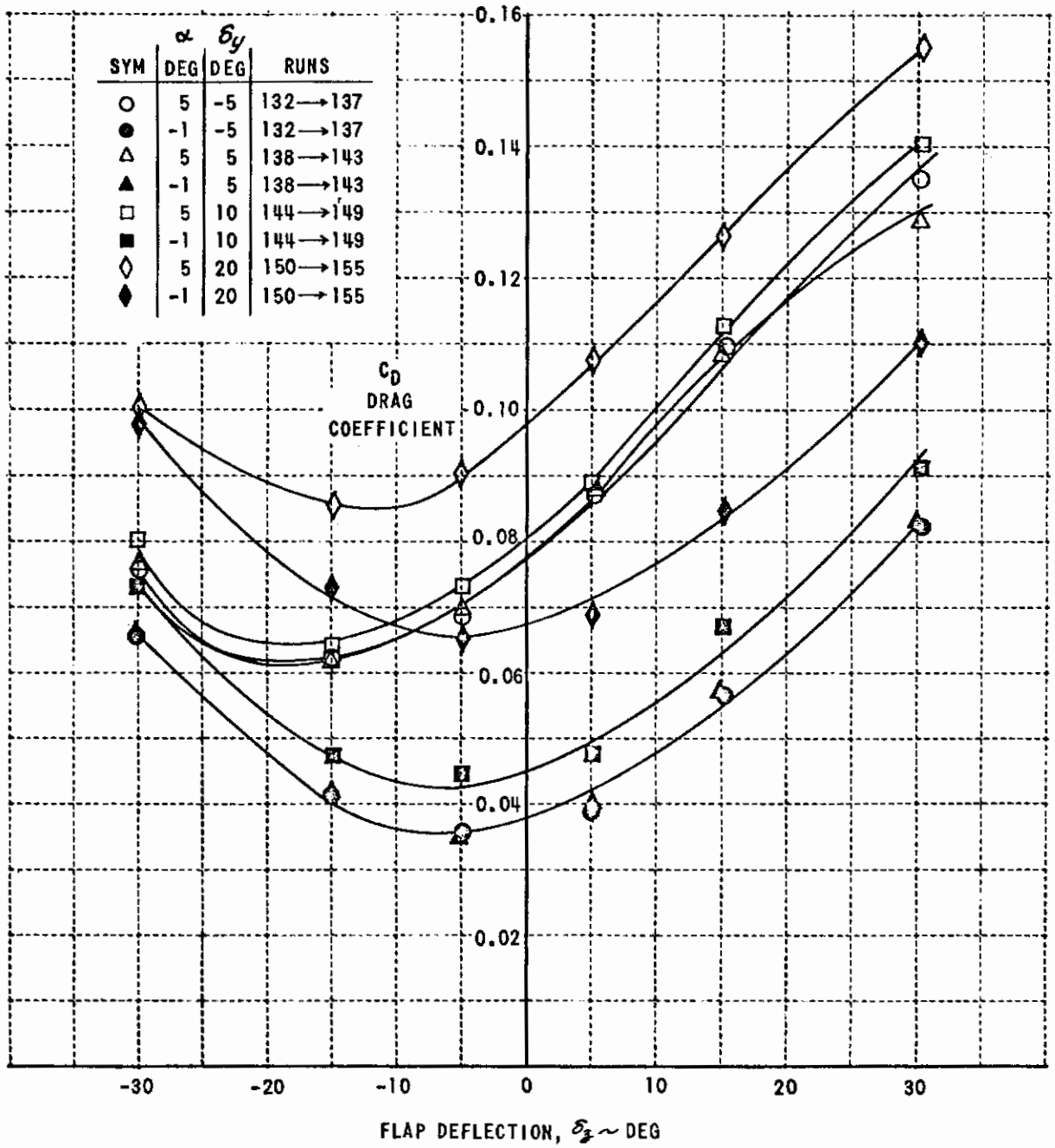

Figure 2.23 EFFECT OF SIDE-FORCE SURFACES ON DRAG DUE TO DIRECT LIFT FLAPS

These data are in good agreement with the data presented for the CV-340 in Reference 2.7.

The aerodynamic effects of the TIFS landing gear have been estimated using wind tunnel data from Figures 27 and 8 of Reference 2.3. The increments for gear down that are valid for all lift coefficients from 0.2 to stall and for $\delta_F = 40°$ are as follows:

Increments due to extending landing gear:

$$\Delta C_L = 0$$

$$\Delta C_D = +0.027$$

$$\Delta C_{m_{.266c}} = -0.015$$

Though these increments should not be precisely constant, they are nearly so and for purposes of the TIFS analyses, may be considered constant.

2.2.3 TIFS Physical Data

A three-view drawing of the TIFS is shown in Section I along with certain important dimensions of the airplane. This section contains a listing of weights and moments of inertia, control surface deflection limits, and other data of use in variable stability system design.

2.2.3.1 Weights and Inertias

The data in Table 2-5 taken from Reference 2.8 are early estimates of the inertias of TIFS for three weights used in variable stability loop analyses. The data were computed using a digital computer program developed for the TIFS program. The horizontal location of the c.g. is referred to the leading edge of the mean aerodynamic chord (MAC) which is at FS 350.90 in. The MAC measures 114.3 in.

Table 2-5
TIFS WEIGHTS, INERTIAS AND CG LOCATIONS
(DATA FROM REFERENCE 2.8)

	WEIGHT LB	x_{cg} FS, INCH	% MAC	z_{cg} WL, INCH	I_{xx} SLUG-FT^2	I_{yy} SLUG-FT^2	I_{zz} SLUG-FT^2	I_{xz} * SLUG-FT^2
GEAR UP	42,000	366.6	13.7	35.8	207,000	468,000	659,000	3000
	45,000	368.1	15.0	35.6	251,000	469,000	704,000	3000
	50,000	370.8	17.4	36.4	383,000	469,000	837,000	3000
GEAR DOWN	42,000	368.8	15.6	34.1	209,000	469,000	658,000	2000
	45,000	370.2	16.9	34.0	253,000	469,000	702,000	2000
	50,000	372.7	19.0	34.9	385,000	470,000	834,000	2000

*THESE ARE VERY ROUGH ESTIMATES.

2.2.3.2 Seat Reference Point

The TIFS seat reference point is located at fuselage station -34.0 inches and water line 24.5 inches for the SST nose. This location is the common point where TIFS motions and SST motions are matched.

2.2.3.3 Control Surface Deflection Limits

The following control surface limits are either those of the basic C-131H airplane for the conventional controls or the design values for the outboard plain (direct lift) flap and the side-force surfaces.

Aileron: $-48° \leq \delta_a \leq +48°$

Elevator: $-25° \leq \delta_e \leq +12°$

Rudder: $-18° \leq \delta_r \leq +18°$

Side-Force Surface: $-30° \leq \delta_y \leq +30°$

Direct Lift Flap: $-40° \leq \delta_z \leq +40°$

2.2.3.4 Inboard Flap Limits

The limit deflections of the inboard Fowler flap are $0 \leq \delta_F \leq +40°$. The aerodynamically determined limit on inboard Fowler flap deflection is given as a function of airspeed in Figure 2.24.

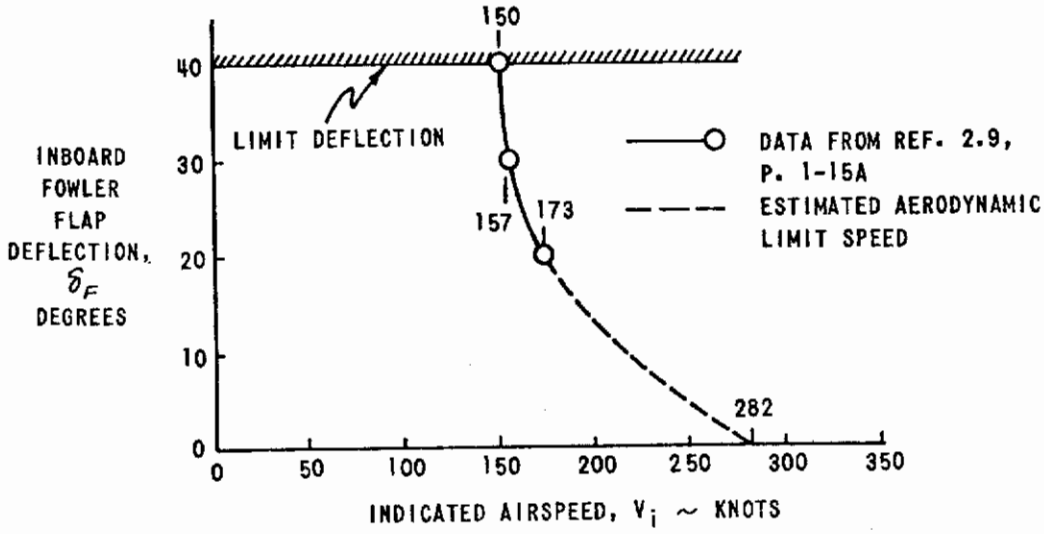

Figure 2.24 MAXIMUM AIRSPEED WITH INBOARD FOWLER FLAPS EXTENDED

2.3 PROPELLER POWER EFFECTS

The turboprop engines of TIFS make an important contribution to the simulation capability. The static and dynamic thrust response to throttle movement must be estimated so that a proper closed-loop thrust control system can be designed as part of the total simulation system. The direct and indirect effects of engine thrust on the motion of the TIFS must be estimated to properly assess the performance of a closed-loop simulation system whether it be of the model-following type or the response-feedback type. A preliminary model of the engines and their effect on the aircraft motion is defined in the paragraphs below.

2.3.1 TIFS Engine Thrust Model

A mathematical model of the thrust characteristics of the Allison Propjet Engine (Model 501-D13D) has been developed which includes both static and dynamic effects. The details of this development are given in Reference 2.10.

The model expresses total thrust (two engines) as a function of airspeed, altitude and thrust control position and is applicable to a range of airspeed from 169 to 507 ft/sec (true) and an altitude range from sea level to 25,000 ft. Its dynamic response is that of a second-order system (for outputs up to 0.1 maximum thrust) with an undamped natural frequency of 14 rad/sec and a damping ratio of 0.5. For larger outputs, the thrust is rate-limited at 9,000 lb/sec.

The model is based on static and dynamic data obtained from the Allison Division of General Motors Corporation and uses curve-fitting techniques to approximate the various static coefficients. Shaft horsepower for various speeds, altitudes and thrust control positions is converted to thrust using propeller data provided (Aeroproducts A6441 FN-606 propeller). The model was then synthesized in the following way.

For each of six altitudes, thrust was plotted versus thrust control position with velocity as parameter. This resulted in the following relationship for the static thrust

$$T_s = (\delta_x - 34^\circ)\frac{dT}{d\delta_x} \tag{2-42}$$

where 34° is the δ_x (thrust control position) for zero thrust and $\frac{dT}{d\delta_x} = f(V, h)$. Then $\frac{dT}{d\delta_x}$ was plotted versus velocity, with altitude as parameter. For a given altitude, this plot was fitted linearly:

$$\frac{dT}{d\delta_x} = \left.\frac{dT}{d\delta_x}\right)_{V=0} + \frac{d\left[\frac{dT}{d\delta_x}\right]}{dV} V$$

The final step was to plot $\left.\frac{dT}{d\delta_x}\right)_{V=0}$ and $\frac{d\left[\frac{dT}{d\delta_x}\right]}{dV}$ versus altitude, leading to the linear approximations:

$$\left.\frac{dT}{d\delta_x}\right)_{V=0} = \left.\frac{dT}{d\delta_x}\right)_{\substack{V=0\\h=0}} + \frac{d\left[\frac{dT}{d\delta_x}\right]_{V=0}}{dh} h$$

and

$$\frac{d\left[\frac{dT}{d\delta_x}\right]}{dV} = \left.\frac{d\left[\frac{dT}{d\delta_x}\right]}{dV}\right)_{h=0} + \frac{d\left\{\frac{d\left[\frac{dT}{d\delta_x}\right]}{dV}\right\}}{dh} h$$

After making the proper sequential substitutions, the static thrust takes the form

$$T_s = (\delta_x - 34^\circ)\left[K_1 + K_2 h + V(K_3 + K_4 h)\right] \qquad (2\text{-}43)$$

where

$$K_1 = \left.\frac{dT}{d\delta_x}\right)_{\substack{V=0\\h=0}} \qquad K_3 = \left.\frac{d\left[\frac{dT}{d\delta_x}\right]}{dV}\right)_{h=0}$$

$$K_2 = \frac{d\left[\frac{dT}{d\delta_x}\right]_{V=0}}{dh} \qquad K_4 = \frac{d\left\{\frac{d\left[\frac{dT}{d\delta_x}\right]}{dV}\right\}}{dh}$$

The following numerical values have been obtained for the K's

$$K_1 = 320 \text{ lb/deg}$$

$$K_2 = -0.00632 \frac{\text{lb/deg}}{\text{ft}}$$

$$K_3 = -0.364 \frac{\text{lb/deg}}{\text{ft/sec}}$$

$$K_4 = 8.88 \times 10^{-6} \left(\frac{\text{lb/deg}}{\text{ft/sec}}\right)/\text{ft}$$

An accuracy index was obtained for the static thrust model by calculating (using the model) all the data points which had been used to develop it. A comparison of computed points with the original data points led to a relationship of "percentage data points" versus "percent error." Results showed, for example, that 70% of the data points were less than 5% in error and 90% of the data points were less than 10% in error. This degree of accuracy was felt to be sufficient considering the particular problem to which the model is to be applied.

The combined static and dynamic model for the total thrust of two engines takes the form

$$\ddot{T} + 2\zeta\omega_n\dot{T} + \omega_n^2 T = \omega_n^2 (\delta_x - 34^\circ)\left[K_1 + K_2 h + V(K_3 + K_4 h)\right] \qquad (2\text{-}44)$$

where

$$\omega_n = 14 \text{ rad/sec}$$

$$\zeta = 0.5$$

$$|\dot{T}| \leq 9000 \text{ lb/sec}$$

and the values of the K'_Δ are as listed above.

A Fortran IV digital computer program written for IBM 7090 Mod. 2 for calculation of engine transients using an elaborate dynamic engine model has been made available to CAL by Allison. It is being studied to determine the feasibility of adaptation to the IBM 360 to be used in checking out the design of the TIFS throttle servo.

2.3.2 Thrust Vector Location and Direct Power Effects

The propeller thrust and normal force act approximately parallel and normal to the fuselage waterlines of the C-131H with the point of action at WL 29.6 and FS 226.3. The reference point for the wind tunnel moment measurements was WL 36.0 and FS 381.3 or .266c. The direct power effects are as follows for α in degrees and $T'_c = \frac{\frac{1}{2}T}{\bar{q}S}$:

For $\delta_f = 0°$, $\Delta C_{L_{direct}} = (.00103 + .00157\ T'_c) + (.00182 + .0377\ T'_c)\ \alpha$

$$\Delta C_{m_{direct}} = (.001 + .108\ T'_c) + (.00246 + .00373\ T'_c)\ \alpha \qquad (2\text{-}45)$$

For $\delta_f = 40°$ $\Delta C_{L_{direct}} = (.00164 + .00249\ T'_c) + (.00182 + .0377\ T'_c)\ \alpha$

$$\Delta C_{m_{direct}} = (.002 + .109\ T'_c) + (.00246 + .00373\ T'_c)\ \alpha \qquad (2\text{-}46)$$

This data can be approximated for system design purposes by the following for α in degrees:

$$\left.\begin{aligned} \Delta C_{L_{direct}} &= .038\ T'_c\ \alpha \qquad (2\text{-}47) \\ \Delta C_{m_{direct}} &= .11\ T'_c \qquad (2\text{-}48) \end{aligned}\right\} \quad 0° \leq \delta_f \leq 40°$$

The details of this development can be found in Reference 2-11.

2.3.3 Indirect Power Effects on the Longitudinal Aerodynamics

The propeller slipstream produces changes in dynamic pressure and flow direction over portions of the wing and the empennage. These incremental forces and moments have been computed using the methods in DATCOM Section 4.6 (Reference 2.6), supplemented by Convair wind tunnel data taken with a powered model (Reference 2.3, Figures 12, 27 and 28). The details of this development can be found in Reference 2.11.

The methods of estimating the pitching moment increment did not check with the wind tunnel data very well. A particularly large effect, which is not easily estimated, is the increment due to downwash angle at the horizontal tail. This increment can be estimated using the DATCOM methods, but it was decided that more confidence should be placed in the powered model tests. Therefore, the DATCOM methods were used to complete the other parts of the total ΔC_m and these effects were subtracted from the measured ΔC_m to derive the tail downwash increment.

For the flaps-down condition, both the tail downwash increment and the dynamic pressure increment were adjusted to match the wind tunnel measurement of the tail contribution to ΔC_m.

The increments to C_L and C_m are not zero at $T_c' = 0$ because the addition of propellers, even though running at $T_c' = 0$, does cause flow changes.

The results are as follows for α in degrees and, again, $T_c' = \frac{\frac{1}{2}T}{\bar{q}S}$ and the moment coefficients are referred to .266c.

For $\delta_F = 0$

$$\left.\begin{aligned} \Delta C_{L_{INDIRECT}} &= \left(.00194 + .1314T_c' - .834T_c'^2\right) + \left(-.00240 + .0855T_c' - .297T_c'^2\right)\alpha \\ \Delta C_{m_{INDIRECT}} &= \left(-.0129 + 1.085T_c' + 2.81T_c'^2\right) + \left(-.000214 - .0154T_c' + .246T_c'^2\right)\alpha \end{aligned}\right\} \quad (2\text{-}49)$$

$$\Delta C_{D_{INDIRECT}} = 0$$

For $\delta_F = 40°$

$$\left.\begin{aligned} \Delta C_{L_{INDIRECT}} &= \left(-.0322 + .546T_c' + .208T_c'^2\right) + \left(-.00240 + .0680T_c' - .256T_c'^2\right)\alpha \\ \Delta C_{m_{INDIRECT}} &= \left(.120 + .165T_c' - .0185T_c'^2\right) + \left(-.000213 + .0549T_c' + .0804T_c'^2\right)\alpha \end{aligned}\right\} \quad (2\text{-}50)$$

$$\Delta C_{D_{INDIRECT}} = 0$$

This data can be approximated for system design purposes by the following for α in degrees:

For $\delta_F = 0$

$$\left.\begin{aligned} \Delta C_{L_{INDIRECT}} &= .005 + (-.001 + .035\, T_C')\alpha^* \\ \Delta C_{m_{INDIRECT}} &= 1.25\, T_C' \\ \Delta C_{D_{INDIRECT}} &= 0 \end{aligned}\right\} \quad (2\text{-}51)$$

For $\delta_F = 40°$

$$\left.\begin{aligned} \Delta C_{L_{INDIRECT}} &= -.03 + .56\, T_C' + (-.0024 + .053\, T_C')\alpha \\ \Delta C_{m_{INDIRECT}} &= .12 + .056\, T_C'\alpha \\ \Delta C_{D_{INDIRECT}} &= 0 \end{aligned}\right\} \quad (2\text{-}52)$$

2.3.4 Indirect Power Effects on the Lateral Aerodynamics

The action of the rotating slipstream on the wing and the vertical tail produces changes in C_n, C_ℓ, and C_y. Reference 2.3 (Figures 39 and 53) contains data suitable for design purposes. The effects of power are not simple functions of thrust coefficient, but a useful qualitative picture can be obtained by a rough fitting of analytical results to the experimental data.

Figure 39 of Reference 2.3 indicates that for flaps up ($\delta_F = 0°$ and β in degrees):

$$\Delta C_n = -.05\, T_c'\beta \quad \text{at all } \alpha\text{'s and } \beta\text{'s} \quad (2\text{-}53)$$

$$\text{and } \Delta C_y = -.04\, T_c'\beta \quad \text{at all } \alpha\text{'s} \quad (2\text{-}54)$$

$$\text{Also at } \alpha = -1°,\ \Delta C_\ell = .006, \text{ for } \beta > 0$$
$$= 0, \text{ for } \beta \leq 0 \quad (2\text{-}55)$$
$$\text{and at } \alpha = 4°,\ \Delta C_\ell = 0, \text{ for } \beta > 0$$
$$= -.004\, T_c'\beta \quad \text{for } \beta \leq 0.$$

The wind tunnel data are for both inboard and outboard Fowler flaps deflected, but because no other data exist, the data will be used also for deflected inboard Fowler flaps alone. Figure 53 of Reference 2.3 gives the following results ($\delta_F = 40°$ and β in degrees):

*This expression is not nearly so good as the other approximations in Equations 2-51 and 2-52.

$$\Delta C_n = -.05\, r_c' \quad \text{at all } \alpha\text{'s and } \beta\text{'s} \tag{2-56}$$

$$\Delta C_y = -.02\, r_c' (\beta + 5) \text{ at all } \alpha\text{'s} \tag{2-57}$$

$$\text{At } \alpha = -1°,\ \Delta C_l = .05\, r_c' \quad \text{for } |\beta| \leq 4° \qquad \text{At } \alpha = 4°,\ \Delta C_l = .008\, r_c' (\beta + 4) \tag{2-58}$$

For system design purposes, the low β values of these increments as listed in Table 2-6 will probably be satisfactory.

Table 2-6

POWER EFFECTS ON LATERAL-DIRECTIONAL COEFFICIENTS

	ΔC_n	ΔC_y	ΔC_l
$\delta_r = 0$	$-.05\, r_c'$	0	0
$\delta_r = 40°$	$-.05\, r_c'$	$-.1\, r_c'$	$.04\, r_c'$

2.4 REFERENCES

2.1 Clark, D.C. and Kroll, J.: General Purpose Airborne Simulator-Conceptual Design Report. CAL Report No. BM-1950-F-1, July 1965.

2.2 Hazen, S.L.: Model Incidence Angle. CAL TIFS Memo No. 71 (revised), 26 June 1967.

2.3 Deering, G.F.: Wind Tunnel Tests of a Powered .092 Scale Model of the T-29E Airplane. General Dynamics, Convair, San Diego. Report No. CVAL 104, 4 March 1952.

2.4 Reynolds, P.A. and Tufts, O.B.: Visor Loads and Effects of the TIFS SST Nose on Structural Load Calculations. CAL TIFS Memo No. 81, 16 June 1967.

2.5 Alford, William J. Jr.: Theoretical and Experimental Investigation of the Subsonic-Flow Fields Beneath Swept and Unswept Wings with Tables of Vortex-Induced Velocities. NACA Technical Report 1327, 1957.

2.6 USAF Stability and Control DATCOM. Wright-Patterson AFB, Ohio, October 1960. Revised November 1965.

2.7 Anonymous: Comparison of Stability Derivatives Between Model 240 and Model 340. General Dynamics, Convair, San Diego. Doc. No. DC-340-100, no date.

2.8 Mast, R.: Definition of the Moments of Inertia of the TIFS Airplane. CAL TIFS Memo No. 38, 8 March 1967.

2.9 Anonymous: Flight Manual, Prop-Jet Convair. General Motors, Allison Division, Publication No. 1CC1-1. 4 October 1960, with revisions.

2.10 Rhoads, D.W.: Mathematical Flight Model of Allison Propjet Engine, Model 501-D13D. CAL TIFS Memo No. 41, 15 February 1967.

2.11 Reynolds, P.A.: TIFS Propeller Power Effects. CAL TIFS Memo No. 88, July 13, 1967.

SECTION III

CONTROL REQUIREMENTS

The TIFS controls have been designed to provide as much aerodynamic effectiveness and as much authority as can be practically produced within reasonable cost and time limitations. Also, the positioning servos have been designed to produce surface deflection, rate and acceleration limits as large as practicable. The limits that do exist are basic to the question of simulator capability and are the subject of a short discussion in this section.

The first objective of this section is to point out the generally known fact that for a linear system with linearly independent controls, the control time history required to produce a given motion starting from a given initial condition is unique, and to point out the less generally known fact that this control time history can be easily calculated. The specification of a particular motion of the model to be duplicated determines the required TIFS control time history uniquely regardless of the particular control technique employed, whether it be model following, response feedback, a hybrid of the two, or any other technique.

The second objective is to calculate the control position requirements for TIFS to simulate the SST doing various extreme maneuvers.

3.1 UNIQUENESS OF THE CONTROL

Let a linear system with equations of motion

$$\dot{x} = Fx + Gu \tag{3-1}$$

where x is the $n \times 1$ state vector, u is an $m \times 1$ control vector, F is $n \times n$ and G is $n \times m$, be specified.

If G has rank m, that is, if the individual controls making up the u vector are linearly independent, then $G^T G$ is invertible and Equation 3-1 can be solved for u to give

$$u = (G^T G)^{-1} (G^T \dot{x} - G^T F x) \tag{3-2}$$

Suppose a particular time history, $x_1(t)$, is specified for $t \geq 0$. Then a time history for u,

$$u_1(t) = (G^T G)^{-1} (G^T \dot{x}_1(t) - G^T F x_1(t)) \tag{3-3}$$

can be calculated. Now suppose that there is another control time history $u_2(t)$ producing the same motion $x_1(t)$ for all $t \geq 0$. Then $\dot{x}_1(t) = F x_1(t) + G u_2(t)$, and this relation can be used in Equation 3-3 to give

$$\begin{aligned} u_1(t) &= (G^T G)^{-1} \left[G^T F x_1(t) + G^T G u_2(t) - G^T F x_1(t) \right] \\ &= u_2(t) \end{aligned}$$

Therefore, the condition that G be of rank m is sufficient for uniqueness of the control time history. The fact that it is also necessary is proven by noting that if G has rank less than m then a $\Delta u \neq 0$ can be found such that $G \Delta u = 0$. Then the control $u_1(t) + \Delta u$ also produces $x_1(t)$.

3.2 THE CONTROL TO PRODUCE PERFECT MODEL FOLLOWING

TIFS, like all other aircraft in normal flight conditions, has linearly independent controls. It makes no sense to design an aircraft otherwise. But TIFS, unlike other aircraft, has six linearly independent controls, a number equal to the degrees of freedom, and therefore, can match perfectly the linear and angular perturbations of any other aircraft about a steady flight condition.* When the speed, altitude and rate of climb or descent in the steady flight condition can also be matched, the entire flight path of the evaluation cockpit of the TIFS can match perfectly the flight path of the simulated aircraft's cockpit.

These facts can be expressed analytically by saying that it is possible to find a TIFS control time history $u(t)$ such that

$$G_p \, u(t) = F_m \, x_p(t) - F_p \, x_p(t) + G_m \, v(t) \tag{3-4}$$

*When the steady speeds of TIFS and the simulated aircraft are not equal, the amplitude of motion over which the perfect matching can be obtained is limited.

where TIFS satisfies

$$\dot{x}_p = F_p x_p + G_p u \tag{3-5}$$

and the simulated aircraft satisfies

$$\dot{x}_m = F_m x_m + G_m v \tag{3-6}$$

Substitution of Equation 3-4 into Equation 3-5 gives

$$\dot{x}_p = F_m x_p + G_m v \tag{3-7}$$

which implies that if $x_p(0) = x_m(0)$ then $x_p(t) = x_m(t)$ for all $t > 0$.*

Equation 3-4 can be solved for $u(t)$ by using the property of control independence. Since the rank of G_p is m, an $m \times n$ matrix M can be found such that MG has an inverse. There may be more than one such matrix M. By multiplying Equation 3-4 by M_1, we derive the control as

$$u_1 = (M_1 G_p)^{-1} \left[M_1 (F_m - F_p) x_p + M_1 G_m v \right]$$

and by multiplying by M_2 we obtain

$$u_2 = (M_2 G_p)^{-1} \left[M_2 (F_m - F_p) x_p + M_2 G_m v \right]$$

But $u_1 = u_2$ for <u>all</u> v and x_p. This implies that

$$(M_1 G_p)^{-1} M_1 (F_m - F_p) = (M_2 G_p)^{-1} M_2 (F_m - F_p)$$

and

$$(M_1 G_p)^{-1} M_1 G_m = (M_2 G_p)^{-1} M_2 G_m$$

Therefore, it makes no difference which matrix M we pick.

M can always be chosen as G_p^T if a more convenient choice for computation is not obvious. This gives

$$u(t) = (G_p^T G_p)^{-1} \left\{ G_p^T \left[F_m - F_p \right] x_p(t) + G_p^T G_m v(t) \right\} \tag{3-8}$$

*The general conditions giving the capability for perfect model following using one arbitrary dynamic system to match another are discussed in Addendum 2 to Reference 3.1.

Also since this control time history gives $x_p(t) = x_m(t)$, the control can be expressed entirely in terms of model variables as

$$u(t) = (G_p^T G_p)^{-1} \left\{ G_p^T \left[F_m - F_p \right] x_m(t) + G_p^T G_m v(t) \right\} \qquad (3\text{-}9)$$

3.3 RESULTS USING THE SST MODEL

The TIFS control time histories, neglecting servo actuator dynamics, required to simulate the Boeing SST in its nominal landing approach condition are investigated in this subsection. The transformations for state variables for use in calculating the control requirements in cruise are also given. Time did not permit inclusion of results for cruise simulation in this report.

The data for landing approach simulation are given in Table 3-1. The results for a vigorous turning pullup from the three-degree landing approach path are given in Figures 3.1a and 3.1b. It is assumed that the pilot overdrives the elevator control to achieve a faster response and then returns the control to the steady state position for an incremental 0.7 g pullup. The aileron input is such that a steady bank angle of 30 degrees is reached in roughly six seconds. No rudder input to the SST model is assumed. The maximum required TIFS control positions and rates for this maneuver are listed in Table 3-2. All of these are within the TIFS capabilities, although it is noted that the side-force surface and flap deflections are large enough to extend into the nonlinear range of surface effectiveness and should be corrected upward by a significant amount. The large deflection of the side-force surfaces is due primarily to the difference in SST and NC-131H values for Y_β in this flight condition and the peak of roughly five degrees of sideslip generated during this maneuver.

Since α and β will probably not be matched in favor of cockpit acceleration, the equations for cruise simulation must be written in terms of the state variables $\int n_{z_p}$ and $\int n_{y_p}$. The transformations T_{LAT} and T_{LONG} must be used on the state variables and the equations become

$$\dot{z} = TFT^{-1}z + TGu \qquad (3\text{-}10)$$

where $z = Tx$

Table 3-1

DATA FOR NOMINAL LANDING APPROACH SIMULATION OF THE SST

(MATRIX ENTRIES FOR ANGLES MEASURED IN DEGREES)

QUANTITY	TIFS		SST	
$W \sim lb$	50,000		408,262	
$V \sim ft/sec$	217		220	
$h \sim ft$	0		0	
$\gamma \sim deg$	-3		-3	
$Flaps \sim deg$	$\delta_f = 40$		30/50	
$\delta_{e_{TRIM}} \sim deg$	+2.84		--	
$\delta_{T_{TRIM}} \sim deg$	59.6		--	
$\delta_{g_{TRIM}} \sim deg$	3.2		--	
	LONG	LAT	LONG	LAT
f_{11}	-1.395	-1.772	-.02708	-1.660
f_{12}	-.00295	0	-.00051	~ 0
f_{13}	+.02585	+.3338	+.00109	+2.08
f_{14}	-.847	-1.143	+.028	-1.982
f_{21}	1	1	1	1
f_{22}	0	0	0	0
f_{23}	0	0	0	0
f_{24}	0	0	0	0

$$X_{LONG} = \begin{bmatrix} \dot{\theta} \\ \Delta\theta \\ \Delta V \\ \Delta\alpha \end{bmatrix} \qquad X_{LAT} = \begin{bmatrix} \dot{\phi} \\ \phi \\ \dot{\psi} \\ \beta \end{bmatrix}$$

QUANTITY	TIFS		SST	
	LONG	LAT	LONG	LAT
f_{31}	0	-.03164	+.229	-.03308
f_{32}	-.5614	0	-.5614	~ 0
f_{33}	-.03625	-.1887	-.05840	-.1175
f_{34}	+.3894	+.6295	+.3711	-.0904
f_{41}	+1.00	+.0680	+.783	+.125
f_{42}	+.00771	+.1482	+.00798	+.1457
f_{43}	-.07818	-1.001	-.07684	-1.039
f_{44}	-.8947	-.1859	-.6402	-.0149
g_{11}	-1.13	-1.34	-.176	+.815
g_{12}	+.0002755	+.660	+.000243	+.0318
g_{13}	-.1740	-.125	0	0
g_{21}	0	0	0	0
g_{22}	0	0	0	0
g_{23}	0	0	0	0
g_{31}	0	-.0048	0	-.00843
g_{32}	+.002706	-.796	+.00347	-.0763
g_{33}	+.0431	-.00045	0	0
g_{41}	-.1048	0	.0450	+.0052
g_{42}	-.000027	+.0529	-.000270	-.0253
g_{43}	-.162	+.0446	0	0

Table 3-2

TIFS CONTROL MAXIMUM POSITIONS AND RATES FOR TURNING PULLUP FROM A LANDING APPROACH SIMULATING AN SST

SURFACE	MAXIMUM POSITION		MAXIMUM RATE		
	REQUIRED DEG	DESIGN DEG	REQUIRED DEG/SEC	DESIGN (NO LOAD) DEG/SEC	DESIGN (UNDER LOAD) DEG/SEC
FLAPS	18	$\pm$40	37	55	40
SIDE-FORCE SURFACES	17	$\pm$30	12.0	72	60
THROTTLE	68	90	1.2	--	--
ELEVATOR	-15	-25 +12	30	72	60
RUDDER	3.5	$\pm$18	1	72	60
AILERON	7	$\pm$48	31	72	60

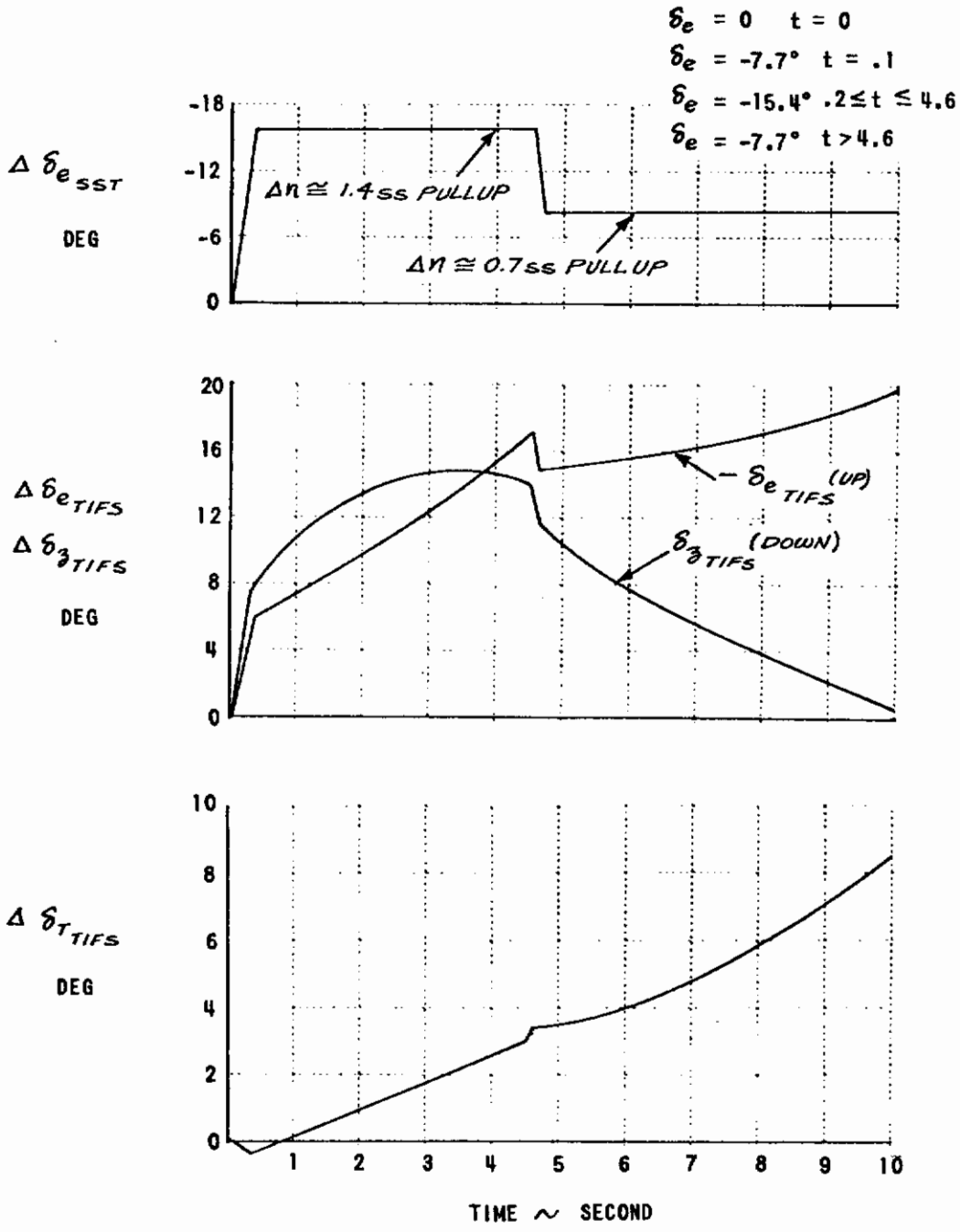

Figure 3.1a LONGITUDINAL SURFACES - NOMINAL LANDING APPROACH

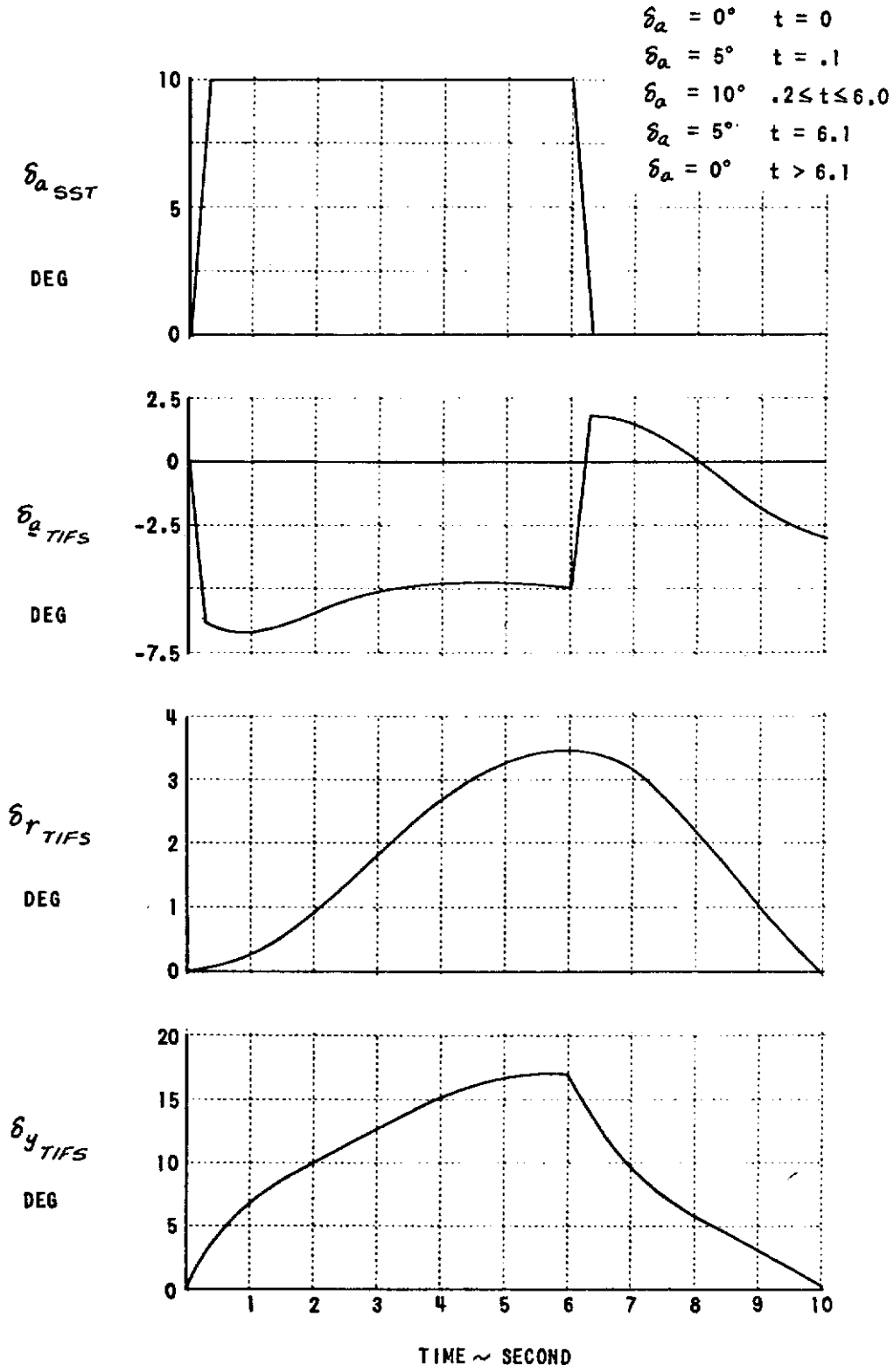

Figure 3.1b LATERAL SURFACES - NOMINAL LANDING APPROACH

The transformations are

$$\begin{bmatrix} \dot{\theta} \\ \Delta\theta \\ \Delta V \\ \int n_{z_p} \end{bmatrix} = \begin{bmatrix} 1 & 0 & 0 & 0 \\ 0 & 1 & 0 & 0 \\ 0 & 0 & 1 & 0 \\ \frac{\ell_p}{g} & -\frac{V}{g} & 0 & \frac{V}{g} \end{bmatrix} \begin{bmatrix} \dot{\theta} \\ \Delta\theta \\ \Delta V \\ \Delta\alpha \end{bmatrix}$$

for the longitudinal state, and

$$\begin{bmatrix} \dot{\phi} \\ \phi \\ \dot{\psi} \\ \Delta\psi \\ \int n_{y_p} \end{bmatrix} = \begin{bmatrix} 1 & 0 & 0 & 0 & 0 \\ 0 & 1 & 0 & 0 & 0 \\ 0 & 0 & 1 & 0 & 0 \\ 0 & 0 & 0 & 1 & 0 \\ 0 & 0 & \frac{\ell_p}{g} & \frac{V}{g} & \frac{V}{g} \end{bmatrix} \begin{bmatrix} \dot{\phi} \\ \phi \\ \dot{\psi} \\ \Delta\psi \\ \beta \end{bmatrix}$$

for the lateral state, where the lateral system has been augmented to include the equation $\dot{\psi} = \frac{d}{dt}\Delta\psi$.

3.4 REFERENCES

3.1 Asseo, Sabi, J.: Application of the Model Following Concept to a Servo Problem. CAL TIFS Memorandum No. 64, 28 June 1967.

SECTION IV

TIFS MODEL-FOLLOWING SYSTEM DESIGN

4.1 INTRODUCTION

This section presents a summary of design considerations and procedures required to develop a satisfactory variable stability system employing the model-following system technique. The model-following system (MFS) has been used successfully in the past to simulate various types of aircraft. When compared with the response-feedback technique (RFS) of variable stability systems, a considerable advantage is realized due to a substantial reduction in the amount of in-flight calibration required. MFS, however, has its problems, not the least of which is the requirement for careful system design to ensure an acceptable level of accuracy with respect to the motions being simulated. It is this requirement with which this section is concerned.

In concept, the MFS is straightforward. The motion outputs of the simulator are to match those of the airplane to be simulated as defined by its equations of motion, i.e., the model. This is accomplished by comparing the responses of the model due to pilot control inputs with those of the simulator. This difference or error then commands the appropriate aerodynamic surface or other controller in an attempt to reduce this error to zero. The degree of this reduction is a measure of the accuracy of the simulation.

Generally speaking, the appropriate controller is that which has a primary effect on the particular motion parameter to be matched, e.g., elevator to control pitch angle. However, a given controller has an effect on motions other than those with which it is primarily associated, and under some circumstances these "secondary" effects can be important factors in design.

The TIFS MFS capability is enhanced as compared with previous CAL systems due to the addition of direct lift and side-force controllers to the "inherent" airplane controllers; elevator, rudder, ailerons, and throttles. Thus, forces along, and moments about, all three axes of the simulator can be controlled. This additional capability does not, in itself, insure satisfactory

model following. By definition, accurate model following of any single variable represents a closed-loop (feedback) control system, the very essence of which is a high gain transfer function. In this case, the gain (which for analysis purposes is variable) is the ratio of simulator controller movement to the error between the reference variable and the controlled variable. In some cases, the magnitude of a given gain may be limited due to structural and measurement noise to a point where simulation of the model response is seriously degraded. Thus, the designer may find it necessary to alter his basic concept of parameter-controller relationship and indeed add more control loops and compensation to compel the accuracy of model response simulation to meet the criteria he has established.

The design effort implied above and described in this section is generally divided into three parts. (Despite this convenient breakdown, fundamental design philosophy noted above applies in all cases.) They are:

1. Longitudinal mode design, using small perturbation linear equations of motion.
2. Lateral-directional mode design, using small perturbation linear equations of motion.
3. Six-degree-of-freedom (6 DOF) design using longitudinal -- lateral-directional coupled equations, Euler angle representation and nonlinear aerodynamics where applicable.

Practical considerations dictated design on a linear basis first (where primary effects could be studied without the added complication of the large and complex nonlinear representation), followed by application of these concepts to the more complete 6 DOF loop design. At the time of this writing, work was just beginning on the 6 DOF loop design. Thus, 6 DOF results are unavailable and only the effort leading to analog representation of the model and TIFS is described.

The model used throughout the linear preliminary design phase is that of a typical supersonic transport (SST). Readily available data from a previous simulator design program made this choice a reasonable one. The 6 DOF representation is based on the latest available data for the Boeing SST. However, progressive design efforts will not be restricted to the SST type aircraft, but will include such configurations as the Advanced Manned Strategic Aircraft (AMSA).

4.2 LINEAR LONGITUDINAL MODE DESIGN

4.2.1 General Design Considerations and Criteria

Specifically, TIFS requires that accelerations, velocities and displacements be matched at the pilot's station so that the pilot's motion cues match those of the airplane to be simulated. The design accuracy is based on the pilot's sensitivity of each parameter and for this study, it is desired to match accelerations and rates to within 5 percent and displacements to within 3 percent. Final accuracy will, of course, depend upon the accuracy of measurements made from the TIFS airplane.

As noted in the introduction, the basic approach is to close a control loop to that control surface which is most effective in controlling a particular variable. However, several problems arise with this approach. Sometimes the control surface controls two or more variables much better than any other surface. For instance, the elevator is a very effective pitching moment controller and therefore is used to handle pitch angle. However, the elevator also controls angle of attack better than the flaps and velocity better than the throttles. Sometimes the control surface function changes with maneuvering flight. For example, as the aircraft is rolled, the elevator becomes less of a pitch controller and more of a heading controller. Problems of this nature will be investigated during the 6 DOF design phase.

This analysis is made on the basis of classical step inputs. The advantage of this is that such inputs are repeatable and the effect of design changes can be examined on a consistent basis. However, it must be noted that normal pilot inputs are generally slower than a step (such inputs can be approximated by a series of ramps) and therefore, less demanding on model following. The reason for this is the smaller high frequency content of the ramp as compared with the step. Acceleration matching is especially critical in this respect; a step input produces a step response. Thus, designing on the basis of step inputs is conservative in that the model following is likely to be better under normal flying conditions.

4.2.2 Single Loop Analysis

One of the major problems of designing a model-following system is determining a simple method of looking at the total system. Writing the transfer function from the model inputs to the TIFS output for three controllers and multiloops requires many terms. The significance of any one loop or term is lost. The following method of analyzing the system was developed to help determine methods of obtaining satisfactory model following. For illustration, a θ loop to the elevator will be used. (Transfer functions are generally functions of the Laplace operator "s" which, for convenience, is omitted.)

$$\Delta\theta = \frac{\theta}{\delta_c}\Delta\delta_e + \frac{\theta}{\delta_x}\Delta\delta_x + \frac{\theta}{\delta_z}\Delta\delta_z \qquad (4\text{-}1)$$

The error ϵ_θ is equal to $\Delta\theta_m - \Delta\theta$, hence

$$\Delta\delta_e = \frac{\delta_e}{\epsilon_\theta}\left[\Delta\theta_m - \Delta\theta\right] \qquad (4\text{-}2)$$

Substituting Equation 4-1 into Equation 4-2 yields

$$\Delta\delta_e = \frac{\delta_e}{\epsilon_\theta}\left[\Delta\theta_m - \frac{\theta}{\delta_c}\Delta\delta_e - \frac{\theta}{\delta_x}\Delta\delta_x - \frac{\theta}{\delta_z}\Delta\delta_z\right] \qquad (4\text{-}3)$$

Solving Equation 4-3 for δ_e :

$$\Delta\delta_e = \frac{\frac{\delta_e}{\epsilon_\theta}}{1+\frac{\theta}{\delta_e}\frac{\delta_e}{\epsilon_\theta}}\left[\Delta\theta_m - \frac{\theta}{\delta_x}\Delta\delta_x - \frac{\theta}{\delta_z}\Delta\delta_z\right] \qquad (4\text{-}4)$$

Substituting Equation 4-4 into Equation 4-1 and rearranging gives

$$\Delta\theta = \frac{\frac{\theta}{\delta_c}\frac{\delta_e}{\epsilon_\theta}}{1+\frac{\theta}{\delta_c}\frac{\delta_e}{\epsilon_\theta}}\Delta\theta_m + \left(1-\frac{\frac{\theta}{\delta_c}\frac{\delta_e}{\epsilon_\theta}}{1+\frac{\theta}{\delta_e}\frac{\delta_e}{\epsilon_\theta}}\right)\left[\frac{\theta}{\delta_x}\Delta\delta_x + \frac{\theta}{\delta_z}\Delta\delta_z\right] \qquad (4\text{-}5)$$

Equation 4-5 shows that one way to achieve excellent model following is to make $\frac{\frac{\theta}{\delta_c}\frac{\delta_e}{\epsilon_\theta}}{1+\frac{\theta}{\delta_e}\frac{\delta_e}{\epsilon_\theta}} = 1$ over the frequency range required. If unlimited gain $\left(\frac{\delta_e}{\epsilon_\theta}\right)$ is available, the foregoing can be accomplished by using a large constant value. In lieu of this capability, $\frac{\delta_e}{\epsilon_\theta}$ may be a compensation network designed to

achieve the desired result. In general, the effect of $\frac{\delta_e}{\epsilon_\theta}$ is to make the airplane follow only the $\Delta\theta_m$ output of the model, minimizing the effects of pitching due to the airplane's $\Delta\delta_x$ and $\Delta\delta_z$. It may be noted that $\frac{\theta}{\delta_x}$ and $\frac{\theta}{\delta_z}$ are frequency-dependent and contribute to the values of the closed-loop system roots as does the denominator $1 + \frac{\theta}{\delta_e}\frac{\delta_e}{\epsilon_\theta}$.

4.2.3 Feedforward Gains

Model following of accelerations requires TIFS responses to frequencies much higher than the model short period frequency. A step input to the model produces a step change in acceleration and to match this step change would require very high gains. Since these gains are not available, feedforward gains on the state variables and their derivatives are used. For example, assume a step input to the linearized drag equation, Equation 4-6.

$$\dot{V} = D_V \Delta V + D_\alpha \Delta\alpha + D_\theta \Delta\theta + D_{\delta_x}\Delta\delta_x \tag{4-6}$$

at time $\tau = 0$, $\Delta V = \Delta\alpha = \Delta\theta = 0$.

$$\dot{V}_m = D_{\delta_T}\Delta\delta_{T_m} \tag{4-7}$$

$$\dot{V} = D_{\delta_x}\Delta\delta_x \tag{4-8}$$

In order to match accelerations, $\dot{V}_m$ must equal $\dot{V}$; thus,

$$\dot{V}_m = D_{\delta_x}\Delta\delta_x$$

or

$$\Delta\delta_x = \frac{1}{D_{\delta_x}}\dot{V}_m \tag{4-9}$$

Therefore, by feeding forward $\frac{1}{D_{\delta_x}}\dot{V}_m$, the correct initial $\Delta\delta_x$ command will be obtained to produce $\dot{V} = \dot{V}_m$. Another use of feedforward is indicated below. It may be illustrated by assuming a simple $\frac{\theta}{\theta_m}$ closed-loop system to which $\frac{\delta_e}{\theta_m}$ feedforward is added (dotted line).

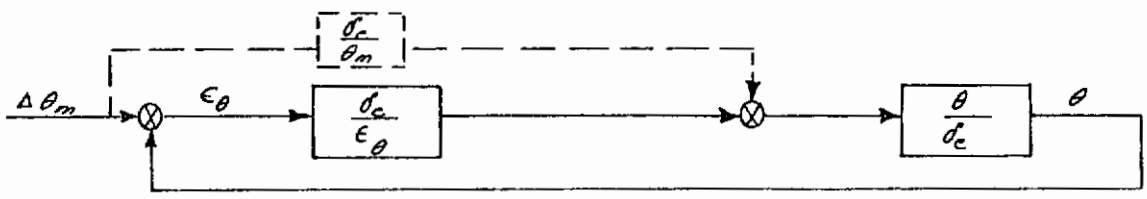

The system transfer function can be shown to be:

$$\frac{\theta}{\theta_m} = \frac{\frac{\theta}{\delta_e}\left[\frac{\delta_e}{\epsilon_\theta} + \frac{\delta_e}{\theta_m}\right]}{1 + \frac{\theta}{\delta_e}\frac{\delta_e}{\epsilon_\theta}}$$

Thus, in addition to the ability to adjust $\frac{\delta_e}{\epsilon_\theta}$, the gain $\frac{\delta_e}{\theta_m}$ can be made a function of frequency ($\frac{\delta_e}{\theta_m} = as^2 + bs$), affecting the transient portion of the response without changing the steady state value.

4.2.4 Axis and Position Transformations

As previously noted, the TIFS airplane is designed to match the model motions as experienced by the pilot. Therefore, the cockpits of the respective airplanes will be oriented similarly. However, the SST cockpit floor is designed to have a 4 degree angle relative to waterlines of the SST. The TIFS cockpit floor is presently designed to be parallel with the waterlines of the Convair. Therefore, there will be an incidence angle between the respective body axes. This incidence must be taken into account for model following of p and r and their derivatives.

Matching the motions at the cockpit requires matching the "local" lateral and normal velocities and accelerations. Therefore, the model parameters must be referred to some reference position before they can be compared to TIFS parameters. For the purposes of this report, model variables are transformed to either the TIFS center of gravity or to the pilot's station.

4.2.5 Control Loops Investigated

Previous experience (see References 4.1, 4.2, and 4.3) has shown that θ, q, and $\dot{q}$ loops should go to the elevator. Also, V, $\int_{t_0}^{t} V dt$, and $\dot{V}$ loops should go to the throttle system. However, TIFS is the first variable stability airplane to have direct lift control and, therefore, complete matching of the model. Thus, in addition to the θ to δ_e and V to δ_χ loops used, control loops to the flaps are chosen from n_z, $\int_{t_0}^{t} n_z$, $\dot{\alpha}$, α and $\int_{t_0}^{t} \alpha\, dt$. As these variables must be matched at the same point in space, their error signals are defined as below:

$$\epsilon_{n_z} = \Delta n_{z_{m_{TCG}}} - \Delta n_z = \Delta n_{z_m} + \frac{\ell_m - \ell_T}{g}\dot{q}_m - \Delta n_z$$

$$\epsilon_{\int n_z} = \int_{t_o}^{t} (\Delta n_{z_{m_{TCG}}} - \Delta n_z)\, dt$$

$$\epsilon_\alpha = \Delta\alpha_{m_{TCG}} - \Delta\alpha = \Delta\alpha_m - \frac{\ell_m - \ell_T}{V_t} q_m - \Delta\alpha$$

$$\epsilon_{\dot\alpha} = \dot\alpha_{m_{TCG}} - \dot\alpha = \dot\alpha_m - \frac{\ell_m - \ell_T}{V_t}\dot{q}_m - \dot\alpha$$

$$\epsilon_{\int\alpha} = \int_{t_o}^{t} (\Delta\alpha_{m_{TCG}} - \Delta\alpha)\, dt$$

where ℓ_m = distance of model c.g. to simulation pilot's station, and
ℓ_T = distance of TIFS c.g. to simulation pilot's station.

4.2.6 Discussion of Results

Using single loop analysis, the gains were calculated that would be required to achieve 1 percent accuracy up to model short period frequencies. (This is essentially an "unlimited gain" situation.) These gains were $\frac{\delta_e}{\epsilon_\theta}$ = -80, $\frac{\delta_e}{\epsilon_q}$ = -20, $\frac{\delta_\gamma}{\epsilon_\alpha}$ = -1000, and $\frac{\delta_x}{\epsilon_V}$ = 500. Figure 4.1 shows the results. With the error traces expanded ten times the model trace, the errors cannot be distinguished. As Δn_z is a much faster signal, there are some initial errors. Figure 4.2 shows the same loops closed, but with high gains that might be achievable. The α model following is unsatisfactory.

Figure 4.3 shows an α system with nine control loops instead of four. The gains are realizable, but there are still sizable errors in α and n_z model following. To eliminate initial errors, $\dot{q}_m$ and $\dot{V}_m$ are fed forward. The particular feedforward gains used, $\frac{\delta_\gamma}{\dot{q}_m}$, $\frac{\delta_e}{\dot{q}_m}$ and $\frac{\delta_x}{\dot{V}_m}$, are calculated as follows.

$$\frac{\delta_\gamma}{\dot{q}_m} = \frac{1}{Z_{\delta_z}}\left[\frac{\ell_m - \ell_T}{V_m}\right], \quad \frac{\delta_e}{\dot{q}_m} = \frac{1}{M_{\delta_e}}, \quad \frac{\delta_x}{\dot{V}_m} = \frac{1}{D_{\delta_x}}$$

To minimize errors in $\Delta\alpha$ and Δ , feedforward gains are used to the flaps and elevator, respectively. These gains, $\frac{\delta_\gamma}{\alpha_m}$ and $\frac{\delta_e}{q_m}$, were optimized on the computer to give minimum errors. The block diagram of the α system with the feedforward gains is shown in Figure 4.4, and the analog results are shown in Figures 4.5 and 4.6.

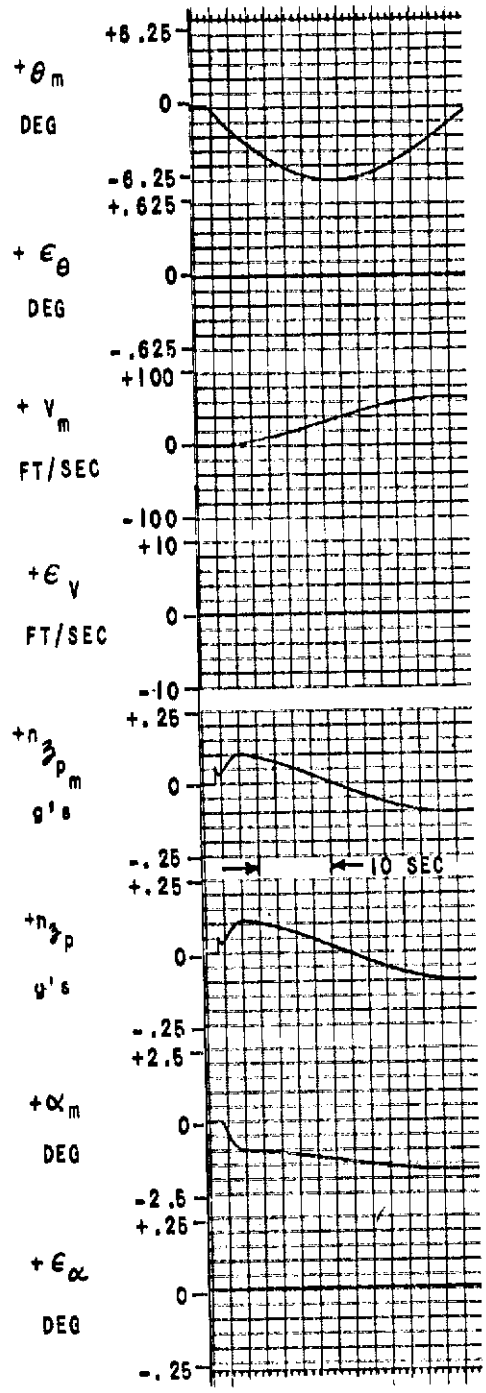

MODEL-FOLLOWING GAINS

$\delta_e/\epsilon_\theta = -80$, $\delta_e/\epsilon_q = -20$

$\delta_x/\epsilon_V = 500$, $\delta_z/\epsilon_\alpha = -1000$

Figure 4.1 HIGH GAIN, MINIMUM COMPARISON LOOP SYSTEM, δ_{e_m} COMMAND

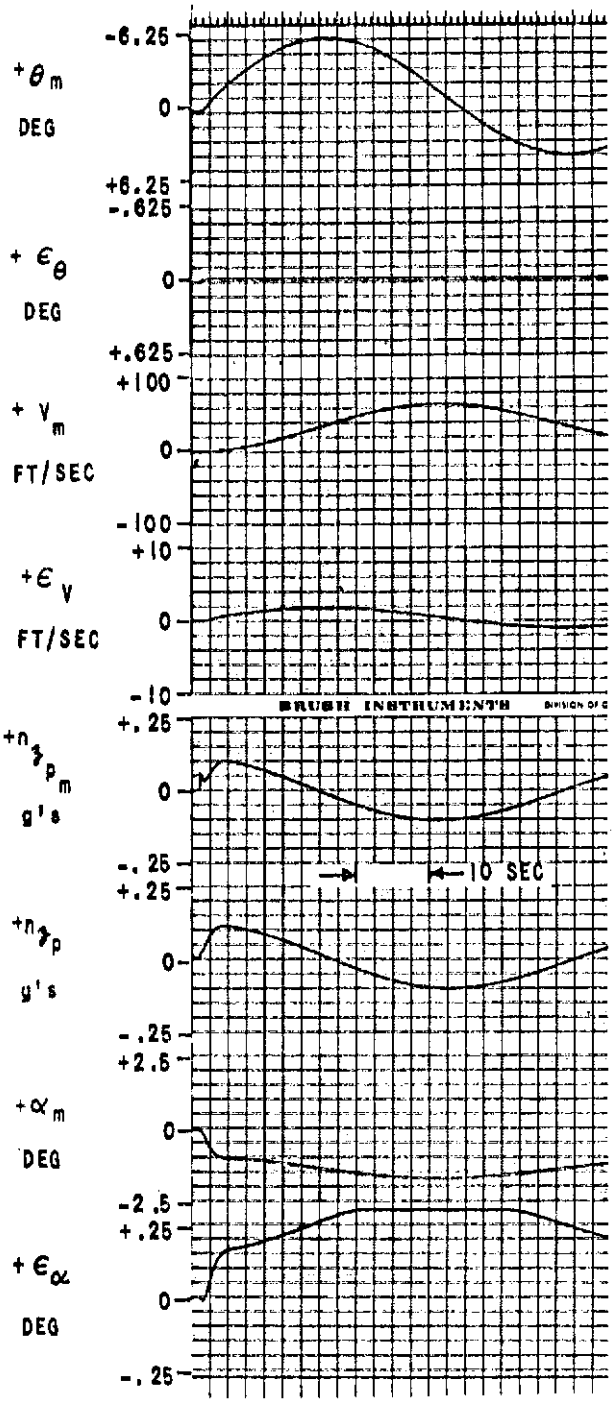

MODEL-FOLLOWING GAINS

$\delta_e/\epsilon_\theta = -20$, $\delta_e/\epsilon_q = -5$,

$\delta_x/\epsilon_V = 20$, $\delta_z/\epsilon_\alpha = -20$

Figure 4.2 REALIZABLE GAINS, MINIMUM COMPARISON LOOP SYSTEM, δ_{e_m} COMMAND

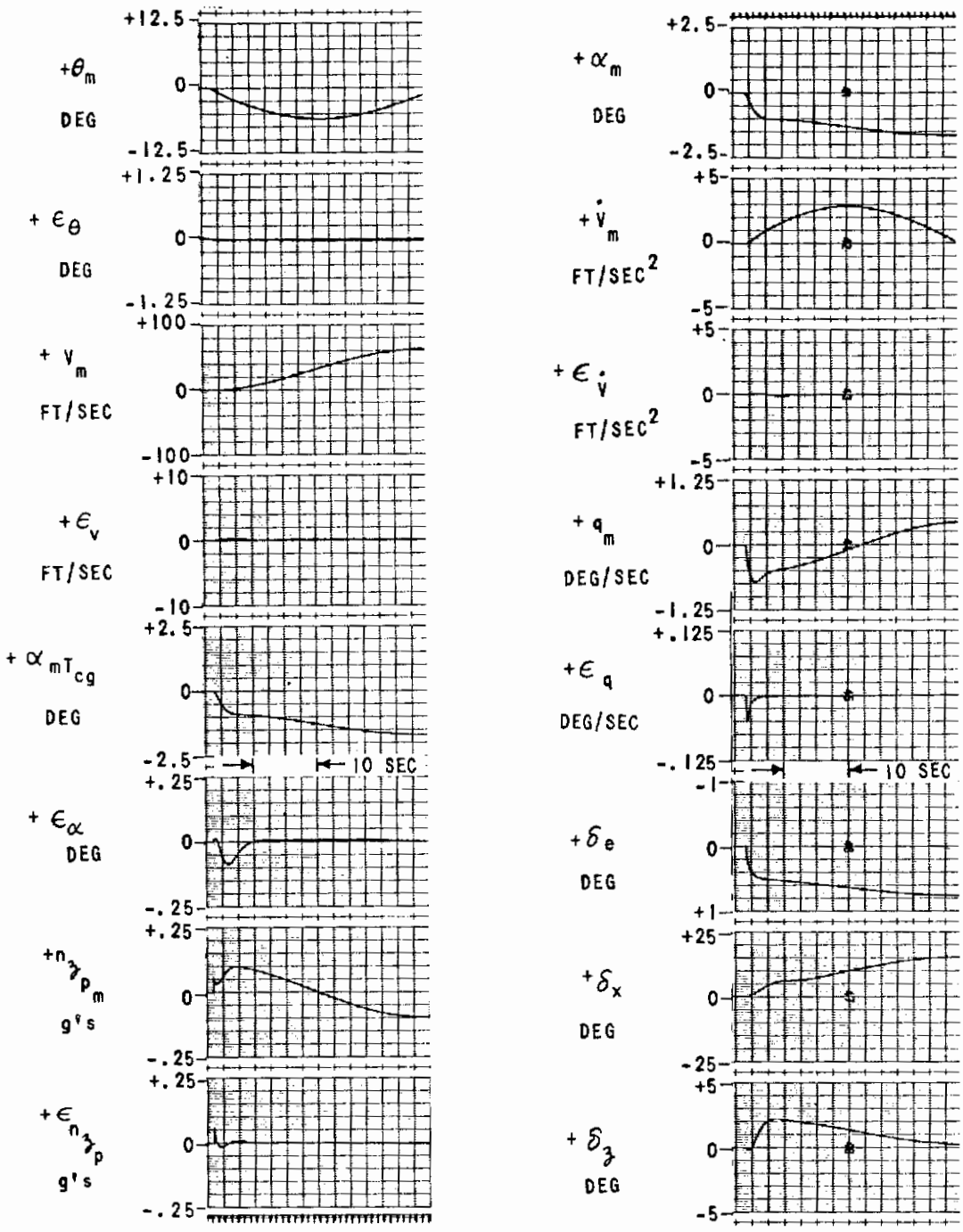

MODEL-FOLLOWING GAINS

$\delta_e/\epsilon_\theta = -15$, $\delta_e/\epsilon_q = -3$, $\delta_e/\epsilon_{\dot{q}} = -.2$, $\delta_x/\epsilon_V = 10$, $\delta_x/\epsilon_{\dot{V}} = 1$, $\delta_x/\epsilon_{\int V} = 0$

$\delta_z/\epsilon_\alpha = -10$, $\delta_z/\epsilon_{\dot{\alpha}} = -1$, $\delta_z/\epsilon_{\int\alpha} = -10$

Figure 4.3 α SYSTEM WITH REALIZABLE GAINS, NO FEEDFORWARD - δ_{e_m} COMMAND

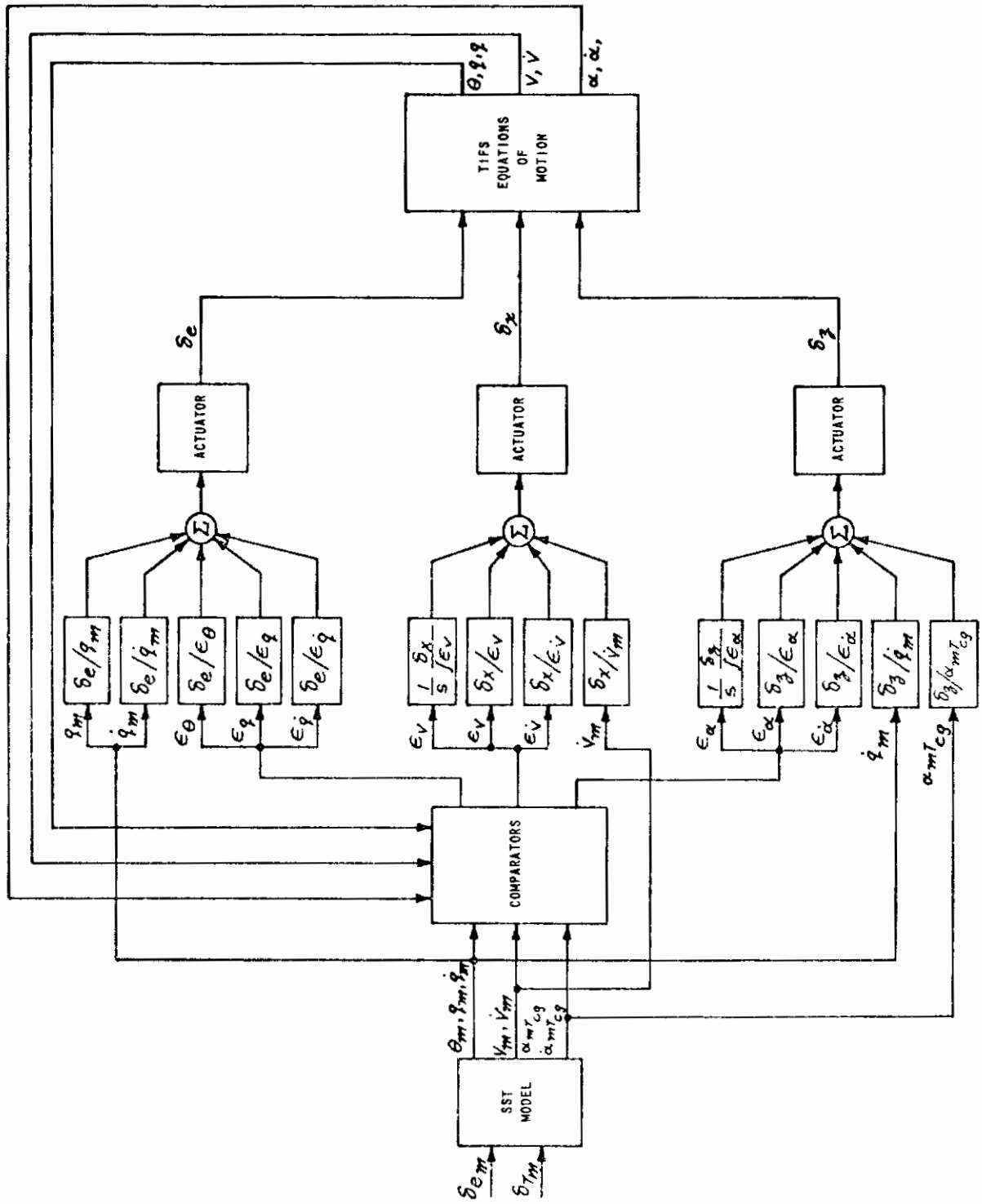

Figure 4.4 α SYSTEM BLOCK DIAGRAM

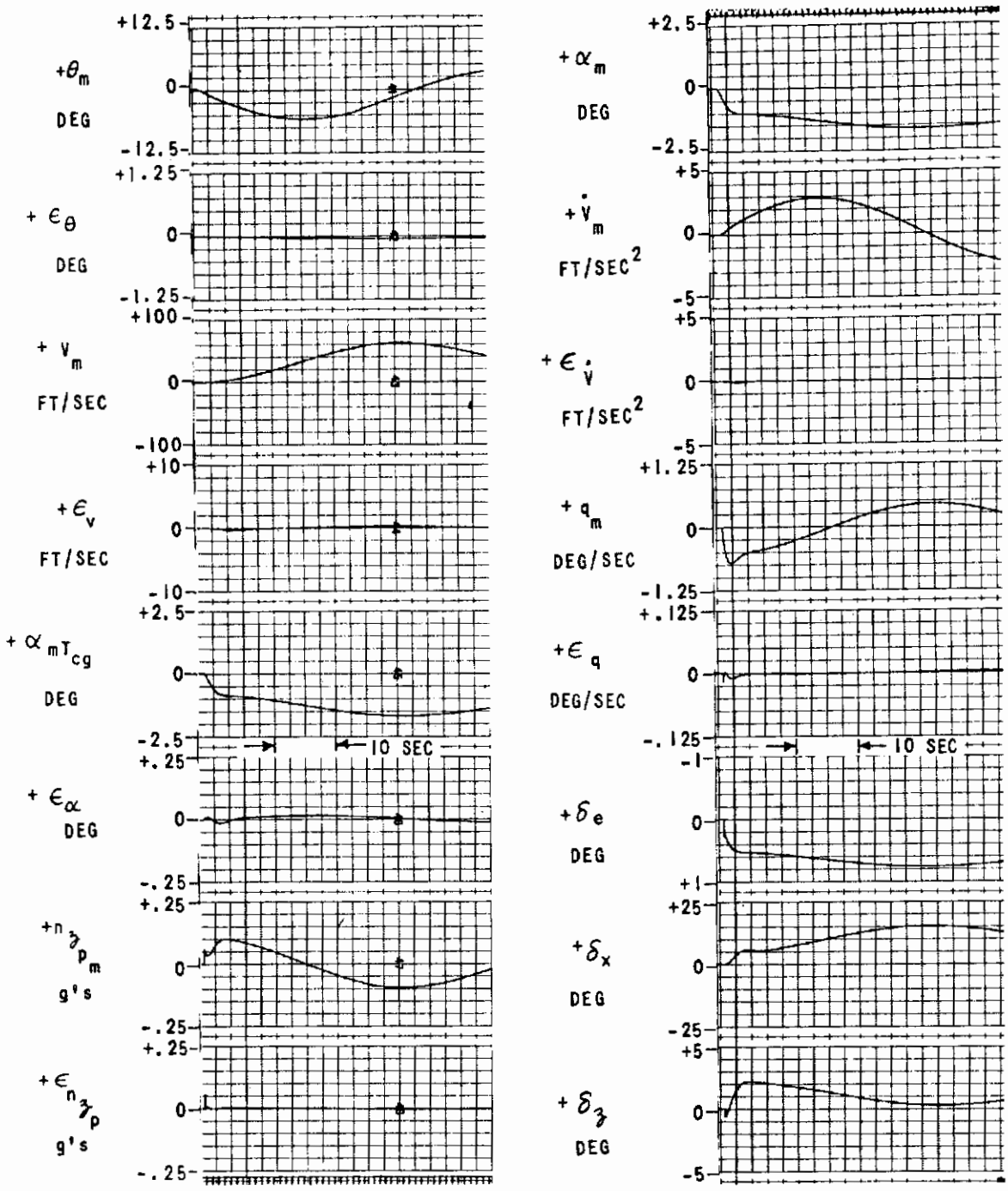

MODEL-FOLLOWING GAINS

$\delta_e/\epsilon_\theta = -15$, $\delta_e/\epsilon_q = -3$, $\delta_e/\epsilon_{\dot{q}} = -.2$, $\delta_e/\dot{q}_m = -.146$, $\delta_e/q_m = -.49$

$\delta_x/\epsilon_V = 10$, $\delta_x/\epsilon_{\dot{V}} = 1$, $\delta_x/\epsilon_{\int V} = 10$, $\delta_x/\dot{V}_m = 8.4$

$\delta_z/\epsilon_\alpha = -10$, $\delta_z/\epsilon_{\dot{\alpha}} = -1$, $\delta_z/\epsilon_{\int\alpha} = -10$, $\delta_z/\dot{q}_m = .74$, $\delta_z/\alpha_m = -2$

Figure 4.5 α SYSTEM WITH REALIZABLE GAINS AND FEEDFORWARD - δ_{e_m} COMMAND

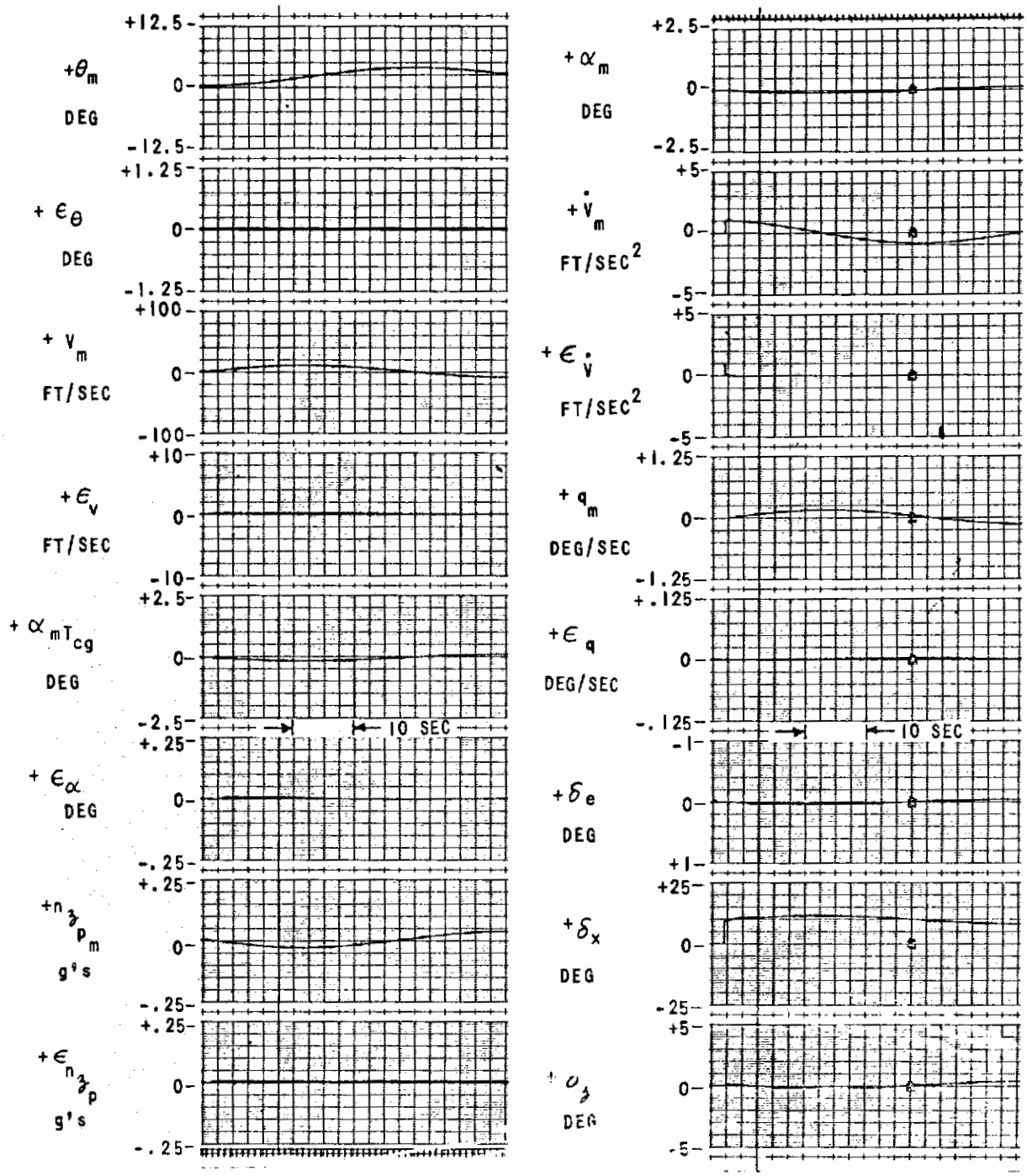

MODEL-FOLLOWING GAINS

$\delta_e/\epsilon_\theta = -15$, $\delta_e/\epsilon_q = -3$, $\delta_e/\epsilon_{\dot{q}} = -.2$, $\delta_e/\dot{q}_m = -.146$, $\delta_e/q_m = -.49$

$\delta_x/\epsilon_V = 10$, $\delta_x/\epsilon_{\dot{V}} = 1$, $\delta_x/\epsilon_{\int V} = 10$, $\delta_x/\dot{V}_m = 8.4$

$\delta_z/\epsilon_\alpha = 10$, $\delta_z/\epsilon_{\dot{\alpha}} = -1$, $\delta_z/\epsilon_{\int\alpha} = -10$, $\delta_z/q_m = .74$, $\delta_z/\alpha_m = -2$.

Figure 4.6 α SYSTEM WITH REALIZABLE GAINS AND FEEDFORWARD - δ_{T_m} COMMAND

Feedforward gains depend upon a specific flight condition and a knowledge of the control derivatives involved. Thus, the values used in this investigation to provide acceptable model following may be wrong for other flight conditions. The range of values required for these gains throughout the spectrum of flight conditions will be the subject of future investigation. It is possible that simple gain programs with dynamic pressure and fuel remaining will provide the proper adjustments.

The block diagram of Figure 4.7 shows an n_z system, wherein a Δn_z signal is fed to the flaps. A weak $\int \epsilon_\alpha dt$ loop was included to bound the errors in $\Delta\alpha$. Analog results are shown on Figure 4.8. Figure 4.9 shows the results of a combination n_z, α system. This may be used where, for practical reasons (structural and measurement noise), Δn_z is a better signal than $\Delta\alpha$. Note that as in the basic n_z system, feedforward gains are used.

Table 4-1 lists the estimated maximum allowable gains based, in part, on previous in-flight experience. Reasonable estimates for the elevator and throttle loop gains have been obtained from practical experience with CAL's B-26 in-flight simulator, the T-33 variable stability airplane, and from the General Purpose Airborne Simulator program using the Lockheed JetStar airplane. Loop gains to the direct lift flaps are based on engineering estimates and have yet to be verified from flight experience. Design to acceptable model-following accuracy as presented in this report is based on not exceeding the gain values given in Table 4-1.

Table 4-1

ESTIMATED MAXIMUM ALLOWABLE GAINS

$\delta_e/\epsilon_e = -15$	$\delta_x/\epsilon_{\int V} = +10$	$\delta_z/\epsilon_{\int\alpha} = -10$
$\delta_e/\epsilon_q = -3$	$\delta_x/\epsilon_V = +10$	$\delta_z/\epsilon_\alpha = -10$
$\delta_e/\epsilon_{\dot{q}} = -.2$	$\delta_x/\epsilon_{\dot{V}} = +1$	$\delta_z/\epsilon_{\dot{\alpha}} = -1$

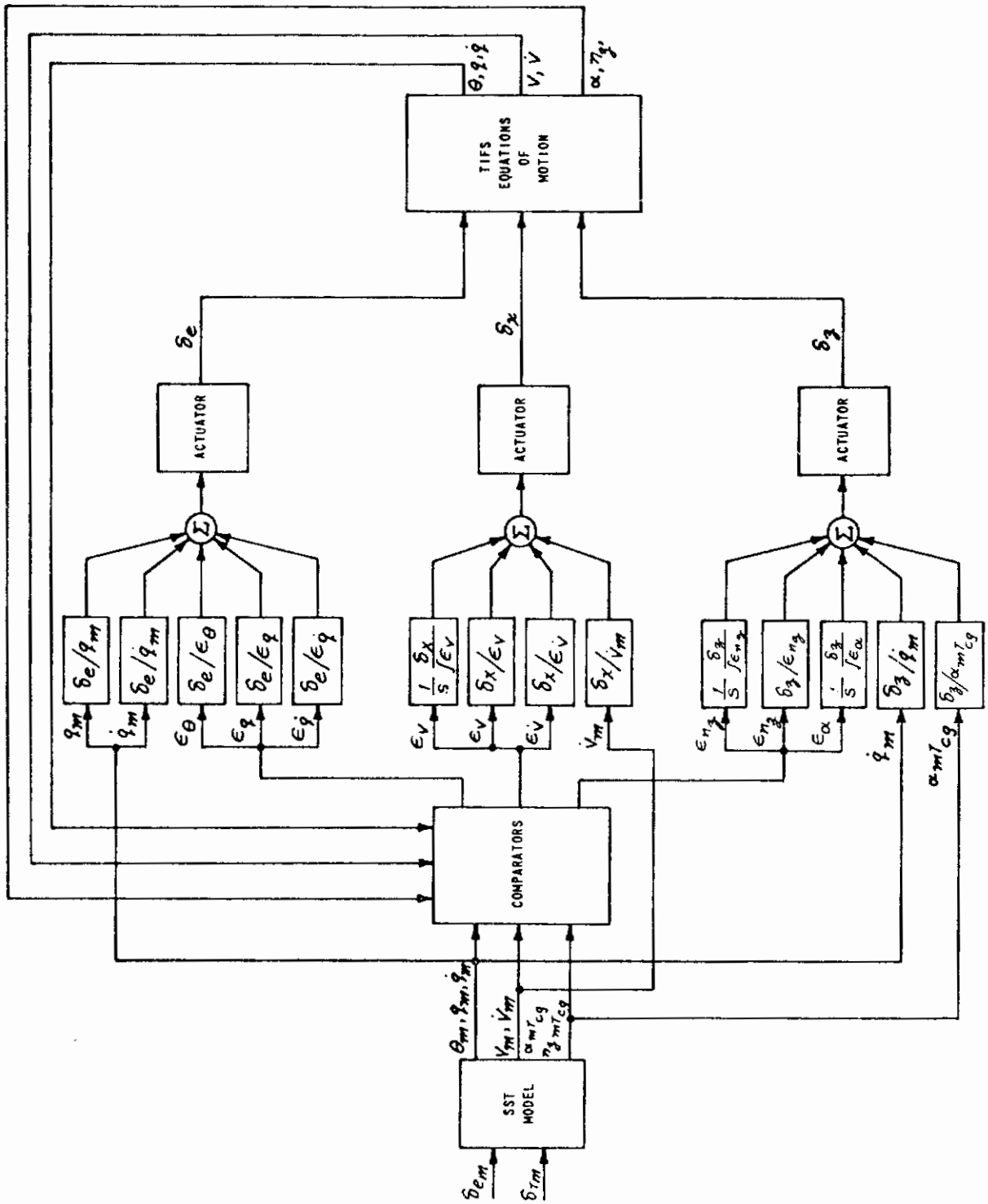

Figure 4.7 n_z SYSTEM BLOCK DIAGRAM

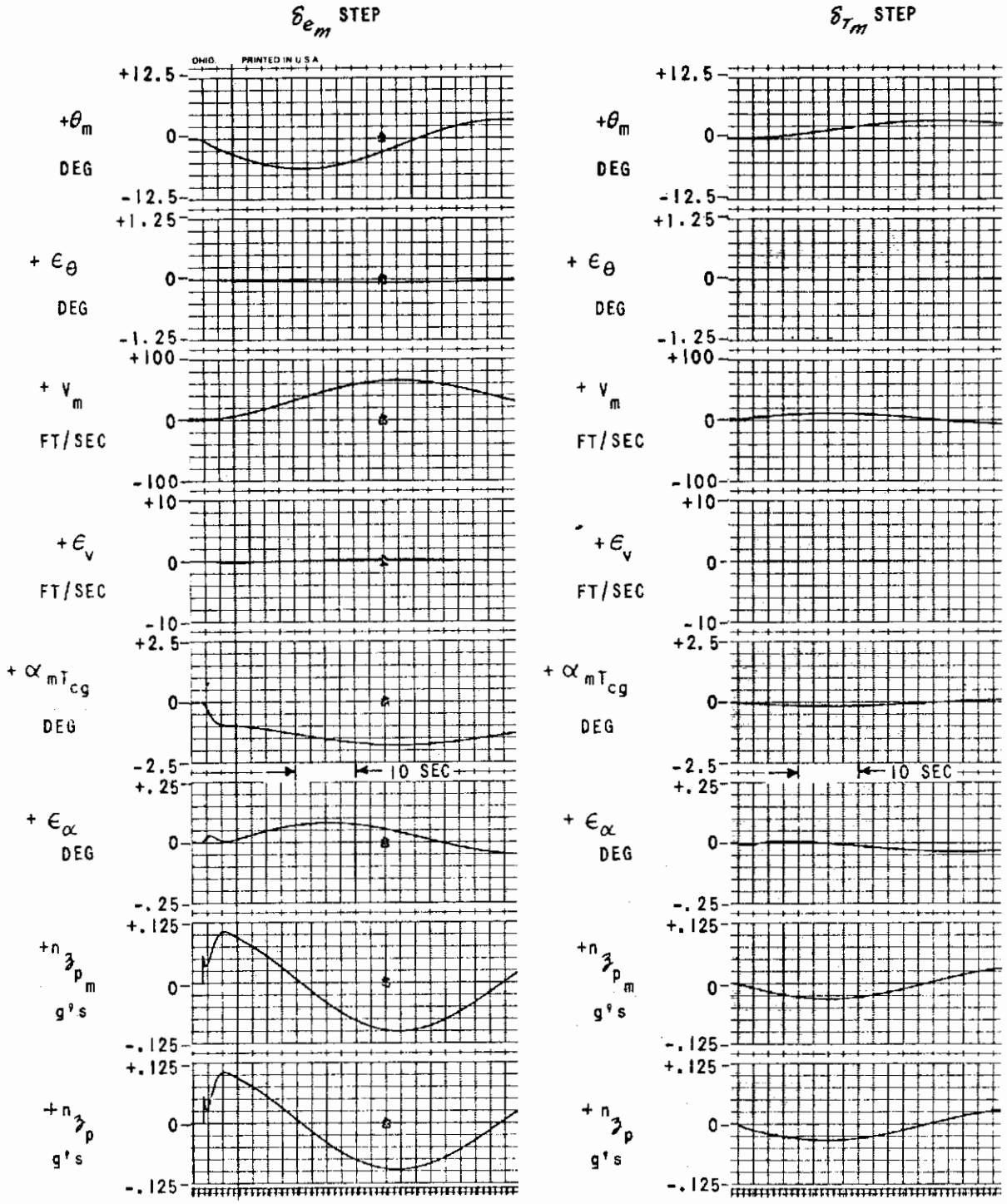

MODEL-FOLLOWING GAINS

$\delta_e/\epsilon_\theta = -15$, $\delta_e/\epsilon_q = -3$, $\delta_e/\epsilon_{\dot{q}} = -.2$, $\delta_e/\dot{q}_m = -.146$, $\delta_e/q_m = -.49$

$\delta_x/\epsilon_V = 10$, $\delta_x/\epsilon_{\dot{V}} = 1$, $\delta_x/\epsilon_{\int V} = 10$, $\delta_x/\dot{V}_m = 8.4$

$\delta_z/\epsilon_{n_z} = -10$, $\delta_z/\int\epsilon_{n_z} = -10$, $\delta_z/\int\epsilon_\alpha = -.2$, $\delta_z/\alpha_m = -2.$, $\delta_z/\dot{q}_m = .74$

Figure 4.8 n_z SYSTEM WITH REALIZABLE GAINS AND FEEDFORWARD - δ_{e_m} AND δ_{T_m} COMMAND

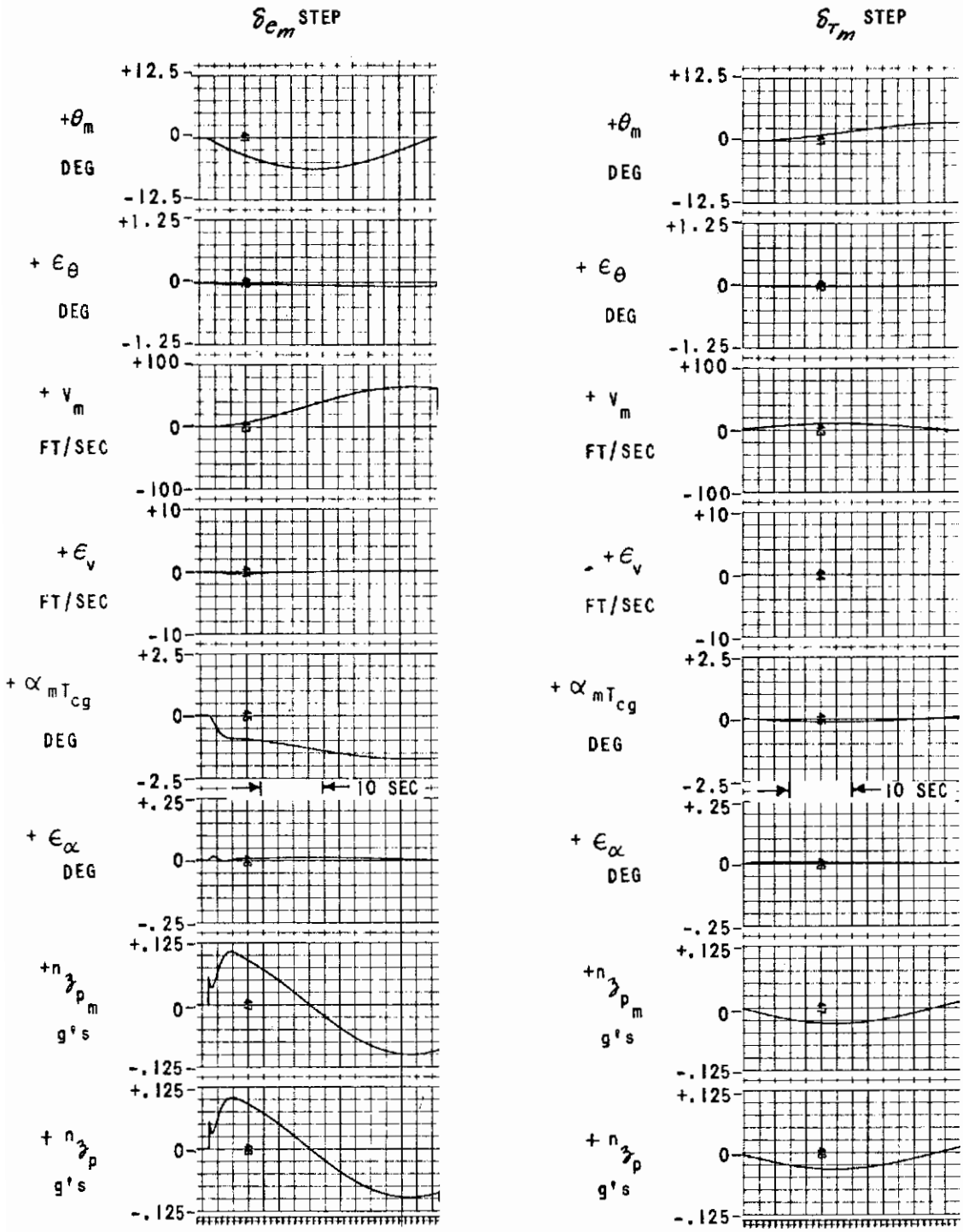

MODEL-FOLLOWING GAINS

$\delta_e/\epsilon_\theta = -15$, $\delta_e/\epsilon_q = -3$, $\delta_e/\epsilon_{\dot{q}} = -.2$, $\delta_e/\dot{q}_m = -.146$, $\delta_e/q_m = -.49$

$\delta_x/\epsilon_V = 10$, $\delta_x/\epsilon_{\dot{V}} = 1$, $\delta_x/\epsilon_{\int V} = 10$, $\delta_x/\dot{V}_m = 8.4$

$\delta_z/\epsilon_{n_z} = -10$, $\delta_z/\epsilon_\alpha = -10$, $\delta_z/\epsilon_{\int\alpha} = -1$, $\delta_z/\alpha_m = -2$, $\delta_z/\dot{q}_m = .74$

Figure 4.9 COMBINATION n_z AND α SYSTEM WITH REALIZABLE GAINS AND FEEDFORWARD - δ_{e_m} AND δ_{T_m} COMMAND

4.3 LINEAR LATERAL-DIRECTIONAL MODE DESIGN

In this subsection, the design of the TIFS lateral-directional model-following system is discussed. The discussion begins with a general description of the control loop design and leads into an explanation of the various systems developed as well as a presentation of the time histories for the respective systems. Also included are simplified block diagrams and root locus sketches.

4.3.1 Control Loop Design

Theoretically, lateral-directional model following can be achieved by utilizing any of the three control surfaces to match three linearly independent variables defining the lateral motions of the aircraft. In order to attain good model-following results with reasonable gains, however, a discriminating choice of control loops must be made.

An attempt is made in the preliminary design study to obtain at least two different loop configurations. One design would incorporate model following with ϕ, r, and β as the primary feedback parameters. This system is referred to as the "β system." A second design utilizes ϕ, r, and n_y as the primary control variables and is referred to as the "n_y system." A third system is also developed utilizing ϕ, β, and n_y as primary feedback signals with r as a secondary feedback parameter. This system is presented as an alternate to the n_y system.*

The easiest loops to design are the aileron control loops owing to the relatively high open-loop gain of the $\phi/\delta_a(s)$ transfer function. Because of this high gain, ϕ matching of better than 1 percent can be attained with reasonable δ_a/ϵ_ϕ gains.

Improving the ϕ response are model-following loops on p and $\dot{p}$ to insure good high frequency responses to aileron inputs. The model-following loops then will have the aileron controlled by errors in the rolling motions.

---

*It is to be understood throughout that β of the TIFS center of gravity is compared with the model β transferred to the TIFS center of gravity, and p of the model (from which ϕ is generated) is referred to the TIFS body axes for comparison with p of TIFS. The same is true for r. n_y is the lateral acceleration at the pilot station in both cases

Design of the rudder and side-force control loops was not quite as straightforward. From past experience, it is known that the rudder is a strong β controller, however, the rudder is also a direct yaw controller. As a result, investigations were made to determine the effects of:

1. Controlling yawing moments with the rudder, and sideslip with the side-force controller,
2. Controlling yawing moments with the rudder, and lateral acceleration with the side-force controller, and
3. Controlling sideslip with the rudder, and lateral acceleration with the side-force controller.

The resulting systems are the "β system," "n_y system," and "alternate n_y system," respectively.

The β system resulted in good model following in yaw, sideslip and lateral acceleration. The n_y system model followed well in yaw and acceleration but sideslip control was poor. The alternate n_y system is at least as good in model following as the β system. In all three systems, the roll responses are controlled by the ailerons and, as described, follow to within 1 percent.

The block diagrams for the β system and the alternate n_y system are presented in Figures 4.10 and 4.11 respectively. Table 4-2 is a listing of loop closures and gains utilized for the model-following systems described in this section. These gains are no higher than the maximum estimated capability based on (as in the longitudinal design phase) in-flight experience of previous simulation programs. It was assumed that gains to the side-force surfaces could be at least as high as those to the rudder.

The control loop design can be summarized as follows:

β System: The model following in the linearized three-degree-of-freedom simulation is good. However, the study was made only for the speeds-matched condition and should be investigated in great detail for other flight conditions.

n_y System: The β following is inadequate in the n_y system, and therefore, this design can be discounted for the model-following conditions investigated here (trim velocities the same for both model and simulator).

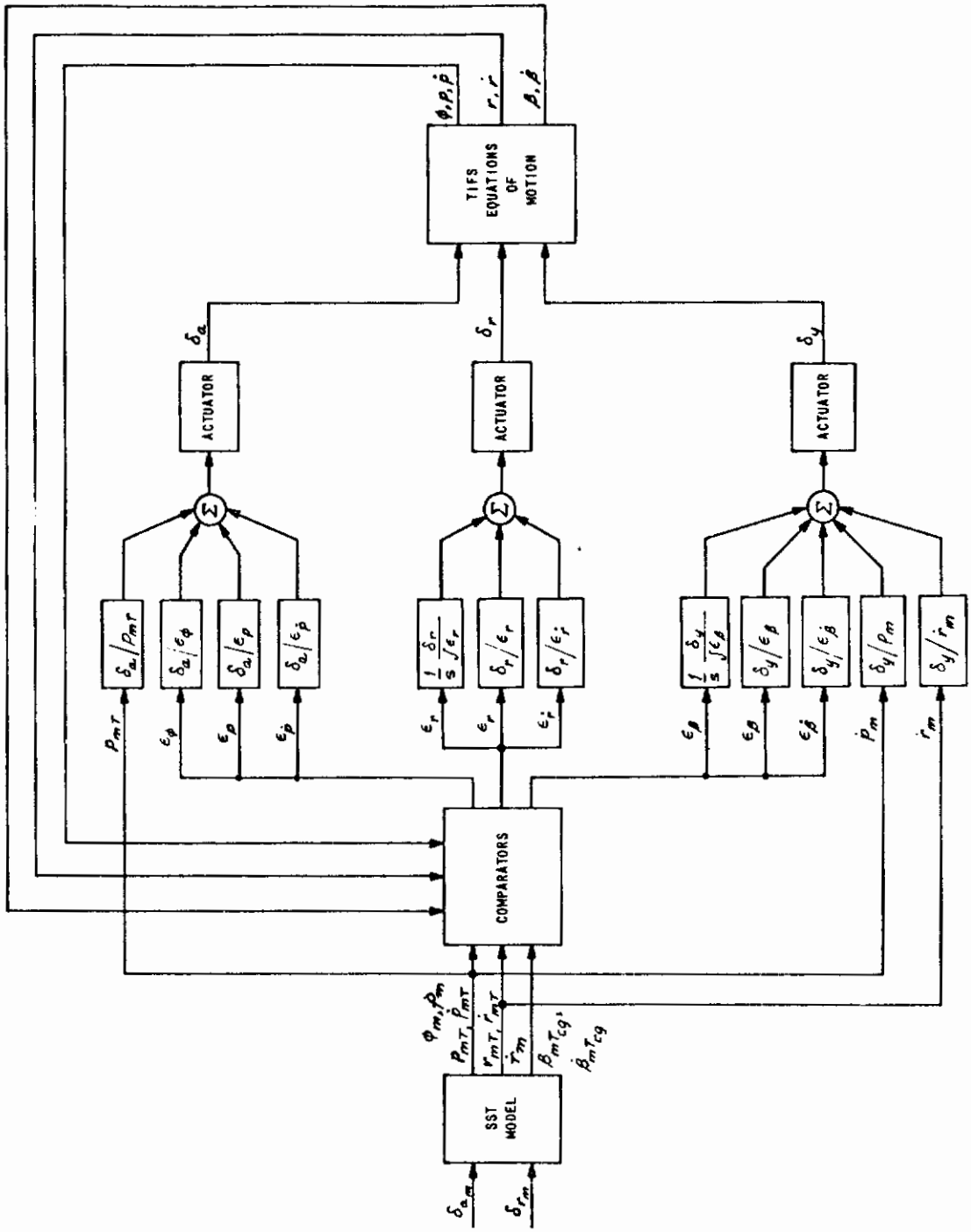

Figure 4.10 β SYSTEM BLOCK DIAGRAM

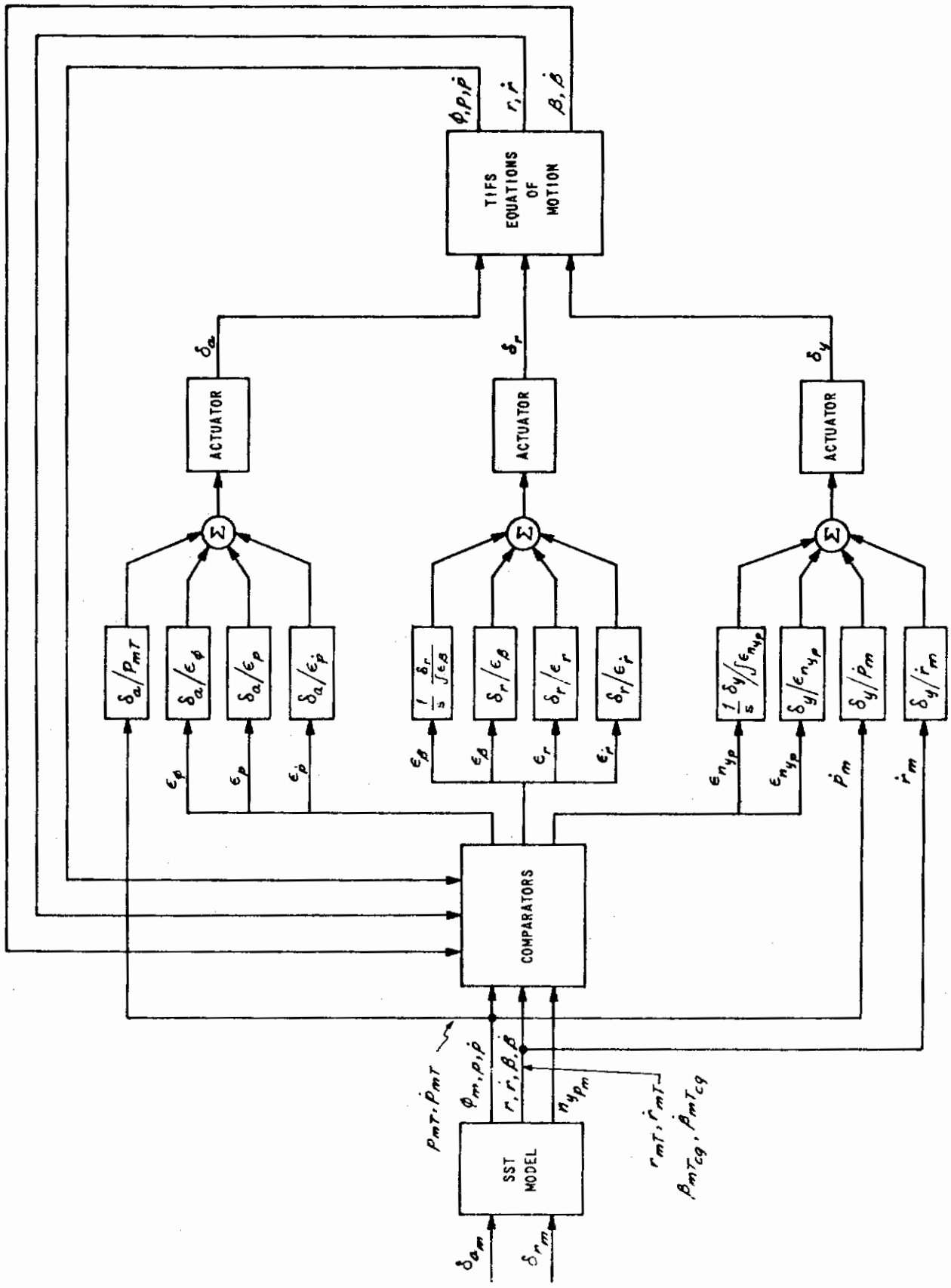

Figure 4.11 ALTERNATE n_y SYSTEM BLOCK DIAGRAM

Table 4-2
LOOP CLOSURES AND GAINS UTILIZED FOR THE MODEL-FOLLOWING SYSTEM

	β SYSTEM				ALTERNATE n_y SYSTEM		n_y SYSTEM
	UNLIMITED GAINS	LIMITED GAINS	LIMITED GAINS WITH INTEGRAL CONTROL	LIMITED GAINS WITH INTEGRAL CONTROL AND FEEDFORWARD	UNLIMITED GAINS	LIMITED GAINS WITH INTEGRAL CONTROL AND FEEDFORWARD	WITH INTEGRAL CONTROL AND FEEDFORWARD
δ_a/ϵ_ϕ	-20	-10	-10	-10	-10	-10	-10
δ_a/ϵ_p	-10^2	-2	-2	-2	-20	-2	-2
$\delta_a/\epsilon_{\dot{p}}$	-.8	-.5	-.5	-.5	- 5	-.5	-.5
δ_a/p_{mT}	0	0	-	-.25	0	-.25	-.25
$\delta_r/\int\epsilon_\beta$	0	0	0	0	+10	+10	0
δ_r/ϵ_β	0	0	0	0	+100	+10	0
$\delta_r/\int\epsilon_r$	0	0	-10	-10	0	0	-10
δ_r/ϵ_r	-10^2	-4	-4	-4	-4	-4	-4
$\delta_r/\epsilon_{\dot{r}}$	-5	-.2	-.2	-.2	-.2	-.2	-.2
$\delta_y/\int\epsilon_\beta$	0	0	+10	+10	0	0	0
δ_y/ϵ_β	$+10^3$	+10	+10	+10	0	0	0
$\delta_y/\epsilon_{\dot{\beta}}$	$+10^2$	+1	+1	+1	0	0	0
$\delta_y/\int\epsilon_r$	0	0	0	0	0	0	0
δ_y/ϵ_r	0	0	0	0	0	0	0
$\frac{\delta_y}{\int\epsilon_{n_{y_p}}}$	0	0	0	0	0	+25	25
$\frac{\delta_y}{\epsilon_{n_{y_p}}}$	0	0	0	0	+500	+10	10
δ_y/p_m	0	0	0	+.075	+.15	+.15	.15
δ_y/r_m	0	0	0	+3.6	+3.0	+3.0	3.0

The equations of motion can be used to show that when p, r, and n_y are perfectly matched, β will also be matched. But small errors in the p, r, and n_y model following rapidly generate significant errors in β. Also, any initial mismatch in β will not be erased in the n_y system and noise in the simulation may produce drift in β of TIFS even though p, r, and n_y are following well. The p, r, and n_y responses did model follow well in the n_y system. After some deliberation on this model-following configuration, two conclusions were drawn:

1. The β following was poor because there was no control for this variable, and
2. The n_y system might prove of significant value in other than the matched flight conditions investigated here.

For SST flight conditions outside the TIFS flight envelope, direct matching of all variables is impossible. In these cases, it is important to match parameters which are significant pilot cues. If attitudes and accelerations are not matched, the simulation will be unrealistic. If β is not matched, the pilot would not very readily observe this as long as ϕ, p, r, and n_y are matched. Therefore, the n_y system may yield the desired model-following results. Investigation of the n_y configuration should be carried out in some detail in flight conditions other than the speed-matched case.

Alternate n_y System: As previously noted, the model following resulting from this system gave results at least as good as those for the β system. β and r are controlled by the rudder with an integral control on the error in sideslip. This results in "tight" control on β and reasonable control on r. Control of ψ, however, may be less acceptable because of the absence of an $\int \epsilon_r$ feedback. (Integral control on the errors in r gives objectionable results when combined with the integral control on β.) Because pilots are more aware of errors in heading than of errors in sideslip, it should be determined what, if any, degradation exists in ψ matching for this tight control of β together with the lack of an $\int \epsilon_r$ feedback. This too should be determined in the later stages of the design program.

4.3.2 Unlimited Gain β System

As previously noted, the theory behind model following implies that the model-following errors can be reduced to any desired level by increasing the model-following gains. That this is indeed true is illustrated with the time histories presented in Figures 4.12 and 4.13. These analog records represent the results obtained when unusually high gains are utilized. It should be emphasized that we do not advocate using these gains in the system, but rather use these records as an example of "excellent" model following.

Insight into the effect of high loop gains can be obtained by root locus analysis of the aileron channel. As discussed in earlier sections of this report, the system becomes decoupled as gains are increased and the analysis is the same as that for the single-input, single-output servo system sketched below. From this diagram, the closed-loop transfer function is obtained:

$$\left.\frac{\phi}{\phi_m}\right|_{CL} = \frac{\left[\frac{\delta_a}{\epsilon_\phi} + s\frac{\delta_a}{\epsilon_p}\right]\left[\frac{\phi}{\delta_a}(s)\right]}{1+\left[\frac{\delta_a}{\epsilon_\phi} + s\frac{\delta_a}{\epsilon_p}\right]\left[\frac{\phi}{\delta_a}(s)\right]}$$

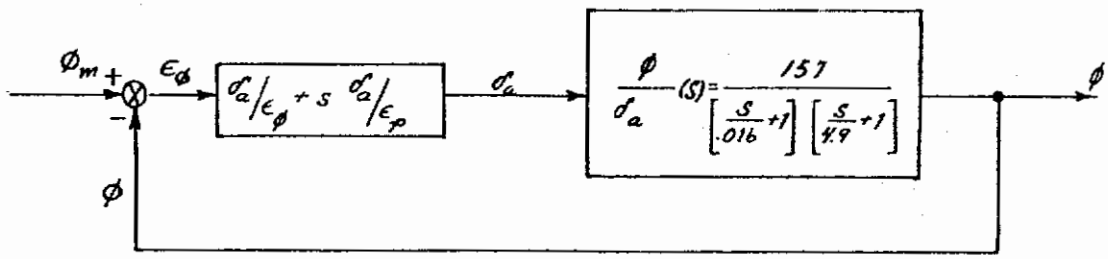

The root locus diagrams of Figure 4.14 indicate the effects on the roots due to:

1. Setting the δ_a/ϵ_p gain to zero and increasing the gain, and
2. Including the δ_a/ϵ_p compensation and increasing the δ_a/ϵ_ϕ gain.

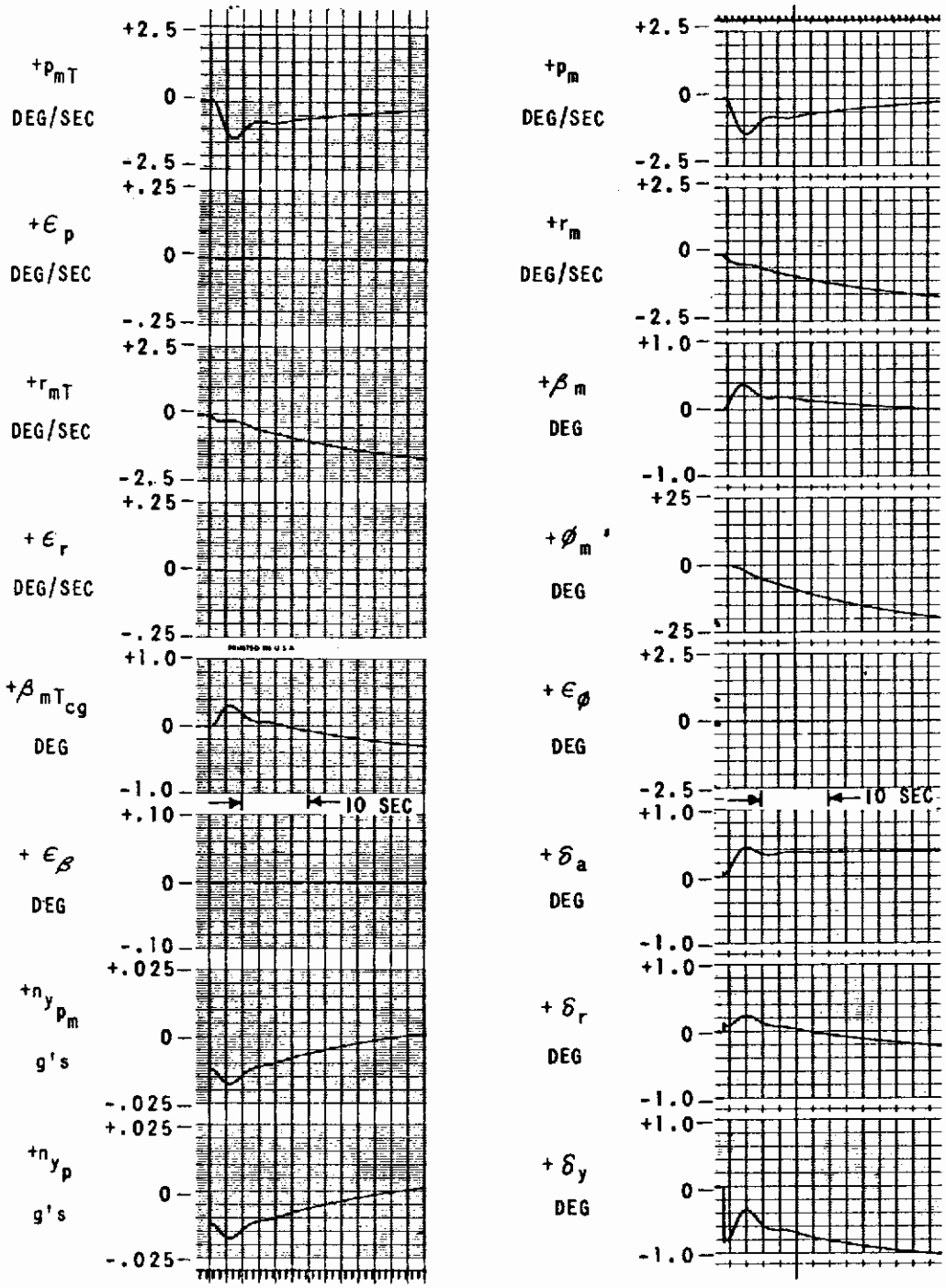

MODEL-FOLLOWING GAINS

$\delta_a/\epsilon_\phi = -20$, $\delta_a/\epsilon_p = -100$, $\delta_a/\epsilon_{\dot{p}} = -.8$, $\delta_r/\epsilon_r = -100$

$\delta_r/\epsilon_{\dot{r}} = -5$, $\delta_y/\epsilon_\beta = +1000$, $\delta_y/\epsilon_{\dot{\beta}} = +100$

Figure 4.12 β SYSTEM MODEL-FOLLOWING, UNLIMITED GAIN CONFIGURATION δ_{r_m} = +.5° STEP

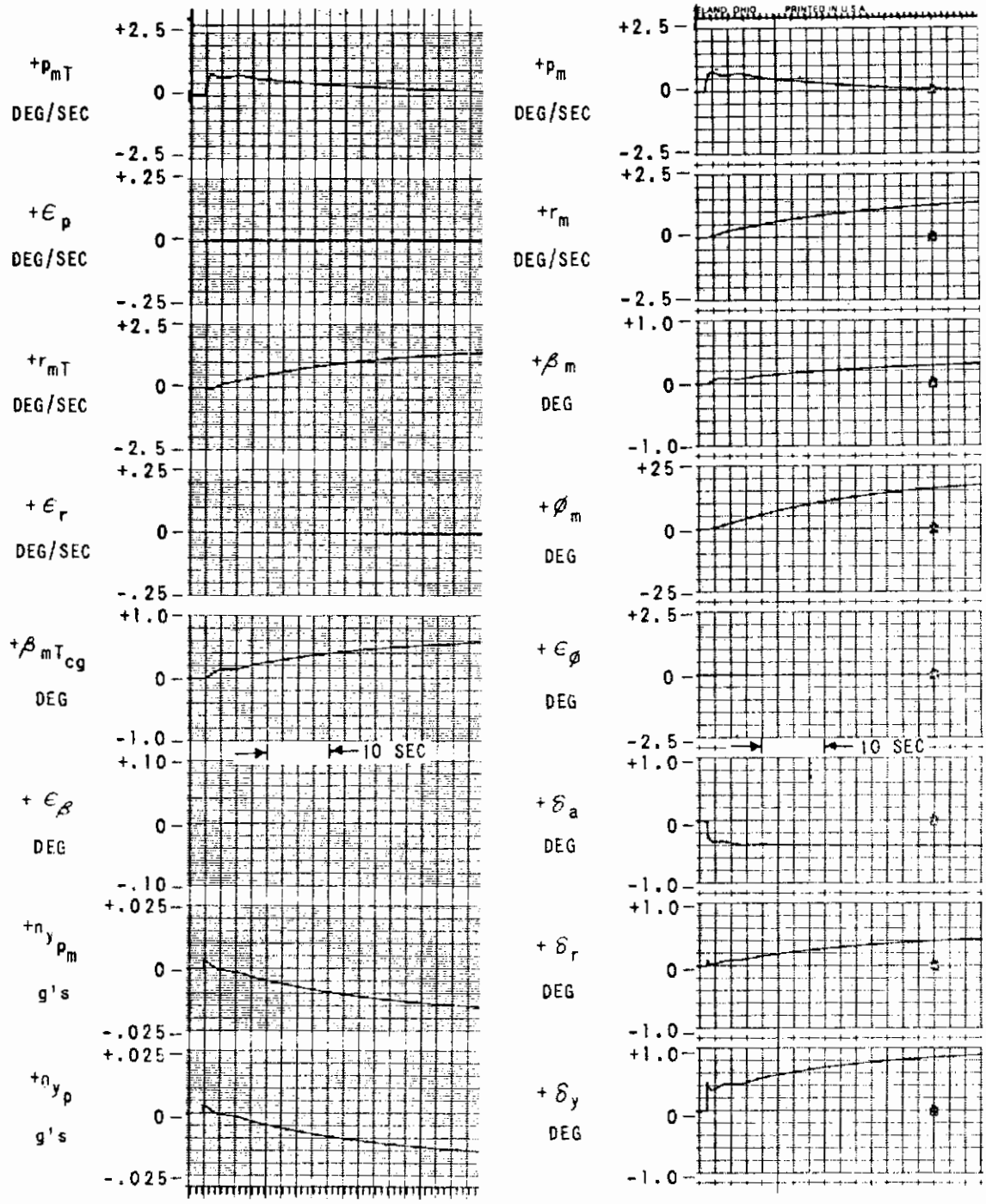

MODEL-FOLLOWING GAINS

$\delta_a/\epsilon_\phi = -20$, $\delta_a/\epsilon_p = -100$, $\delta_a/\epsilon_{\dot{p}} = -.8$, $\delta_r/\epsilon_r = -100$

$\delta_r/\epsilon_{\dot{r}} = -5$, $\delta_y/\epsilon_\beta = +1000$, $\delta_y/\epsilon_{\dot{\beta}} = +100$

Figure 4.13 β SYSTEM MODEL-FOLLOWING, UNLIMITED GAIN CONFIGURATION $\delta_{a_m} = -.5°$ STEP

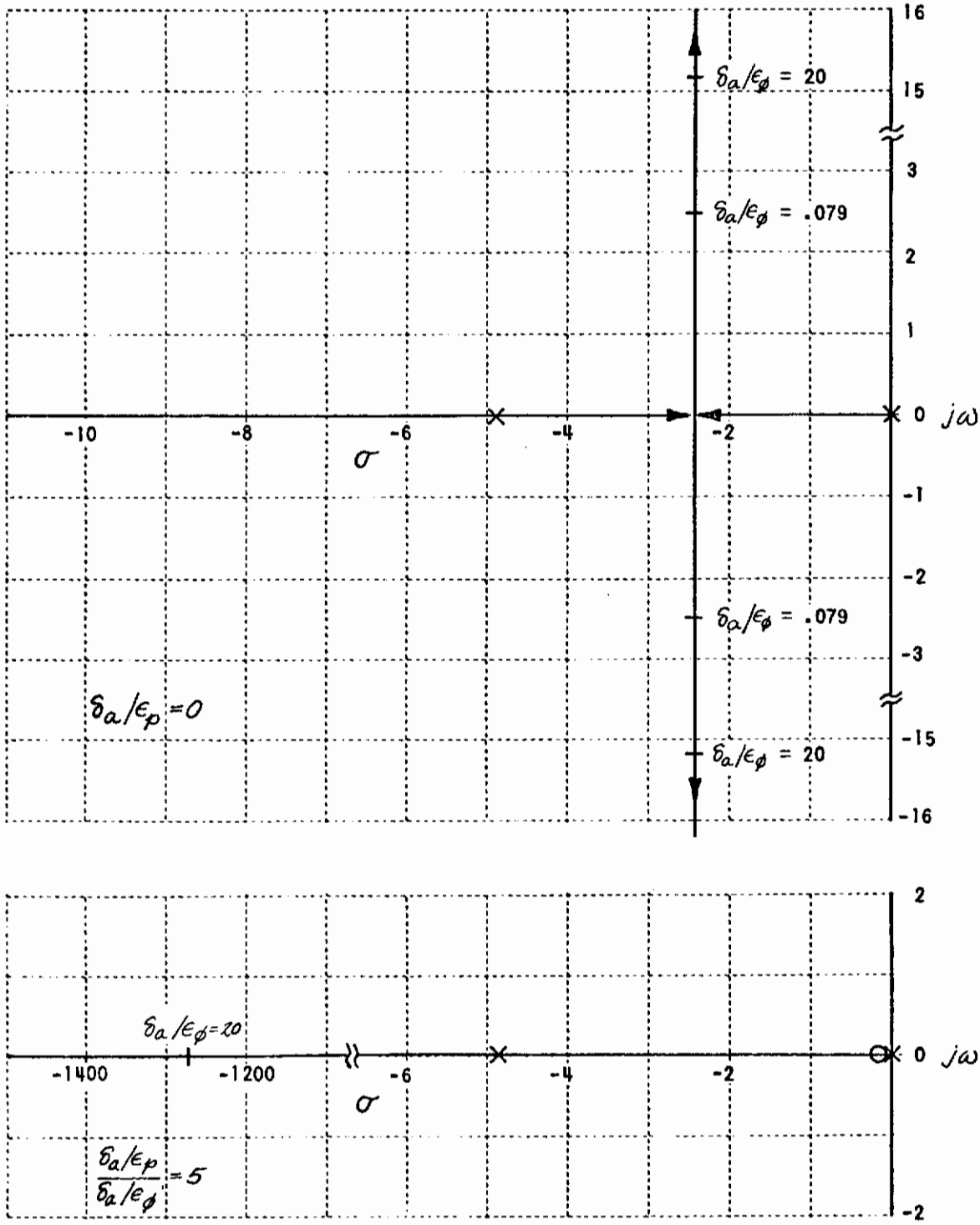

Figure 4.14 ϕ/ϕ_m ROOT LOCUS DIAGRAM

A comparison of these two figures demonstrates that the high gain loop alone will not yield satisfactory results since the system damping tends toward zero. The inclusion of the δ_a / ϵ_p loop effectively changes the aileron from a lightly damped second-order system to a first-order, wide bandwidth system.

Analysis of the $r/\sigma_r(s)$ and $\beta/\sigma_y(s)$ loops can be carried out in an analogous manner to obtain the closed-loop transfer functions for the respective yaw and sideslip loops. As discussed in Section 4.2, the high gain system tends to decouple the loops enabling this analysis to be effected.

4.3.3 β System Development

It is a foregone conclusion that there are practical limitations to the system gains that can be utilized in aircraft control systems. Reducing the gains from the level utilized in the high gain design to practical levels degenerated the model following substantially. With these reduced gains and without any additional compensation, the TIFS is not able to match high frequency model responses and in some variables is not even able to match steady state values. This is readily apparent in the time histories of Figures 4.15 and 4.16.

Since heading angle (ψ) is an important pilot cue, an integrator is used on the error in yaw rate ($r \approx \dot{\psi}$) to provide better matching on both yaw rate and heading. The ϵ_r integral, as anticipated, reduced the steady state error in r to zero and obviously aided in ψ matching. (In the actual mechanization, ψ will probably be used in place of the integral of r.) Similarly, an integral ϵ_β loop was added to provide zero steady state β errors. The time histories for this intermediate system are shown in Figures 4.17 and 4.18.

From the responses in Figures 4.17 and 4.18, it can be seen that although the low frequencies are matched well there are still substantial errors in the transients. This is most apparent in the lateral acceleration traces. To alleviate this situation, it was decided to feed $\dot{p}_m$ and $\dot{r}_m$ as direct inputs to the side-force controller and p_{mT} as a direct input to the ailerons. The effect of this feedforward was to greatly enhance the high frequency response as illustrated in Figures 4.19 and 4.20.

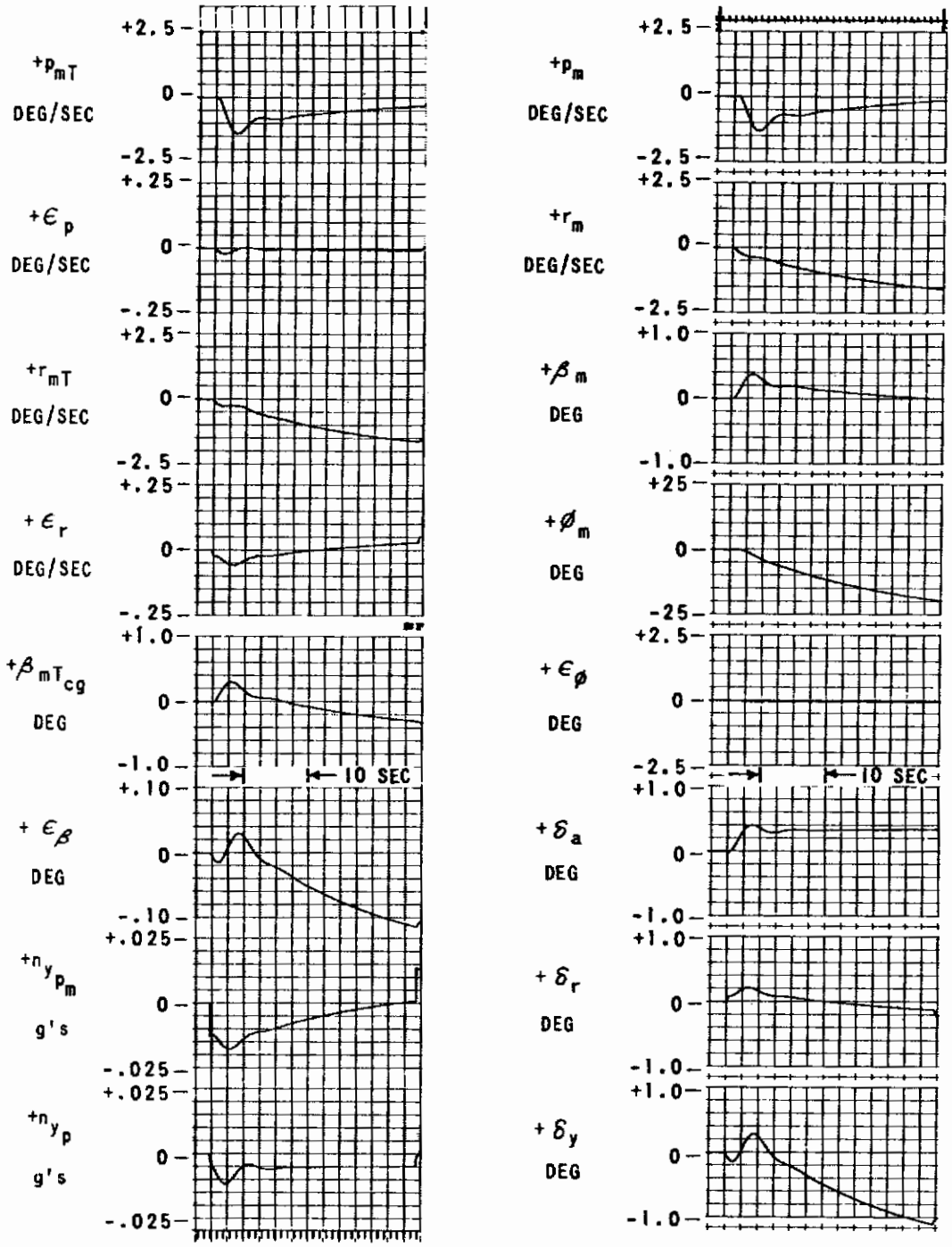

MODEL-FOLLOWING GAINS

$\delta_a/\epsilon_\phi = -10$, $\delta_a/\epsilon_p = -2.0$, $\delta_a/\epsilon_{\dot{p}} = -.5$, $\delta_r/\epsilon_r = -4.0$,

$\delta_r/\epsilon_{\dot{r}} = -.2$, $\delta_y/\epsilon_\beta = +10$, $\delta_y/\epsilon_{\dot{\beta}} = +1.0$

Figure 4.15 β SYSTEM MODEL-FOLLOWING, LIMITED GAINS WITH MINIMUM NUMBER OF MODEL-FOLLOWING LOOPS

δ_{r_m} = +0.5° STEP

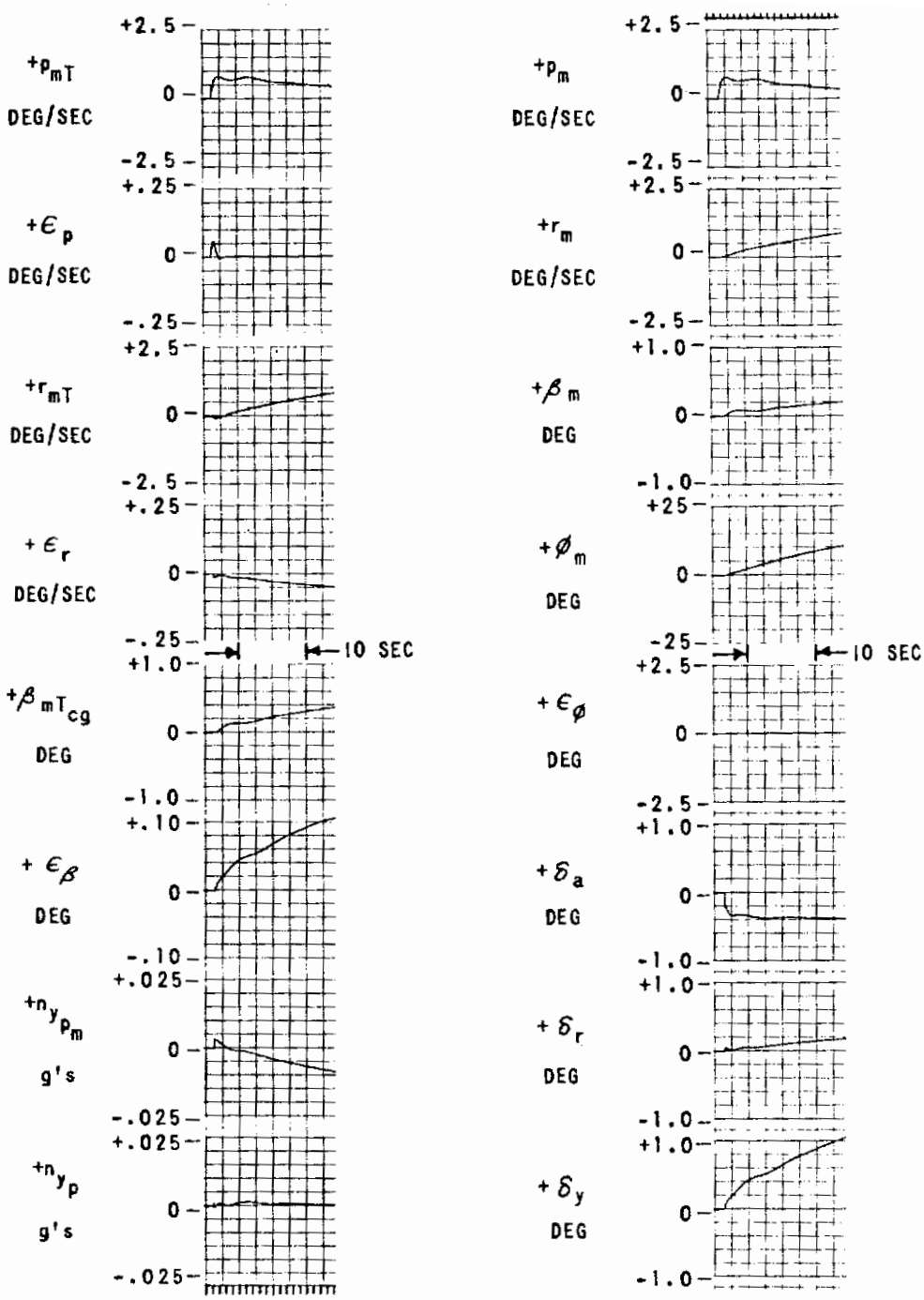

MODEL-FOLLOWING GAINS

$\delta_a/\epsilon_\phi = -.10$, $\delta_a/\epsilon_p = -2.0$, $\delta_a/\epsilon_{\dot{p}} = -.5$, $\delta_r/\epsilon_r = -4.0$,

$\delta_r/\epsilon_{\dot{r}} = -.2$, $\delta_y/\epsilon_\beta = +.10$, $\delta_y/\epsilon_{\dot{\beta}} = +1.0$

Figure 4.16 β SYSTEM MODEL-FOLLOWING, LIMITED GAINS WITH MINIMUM NUMBER OF MODEL-FOLLOWING LOOPS

δ_{a_m} = -0.5° STEP

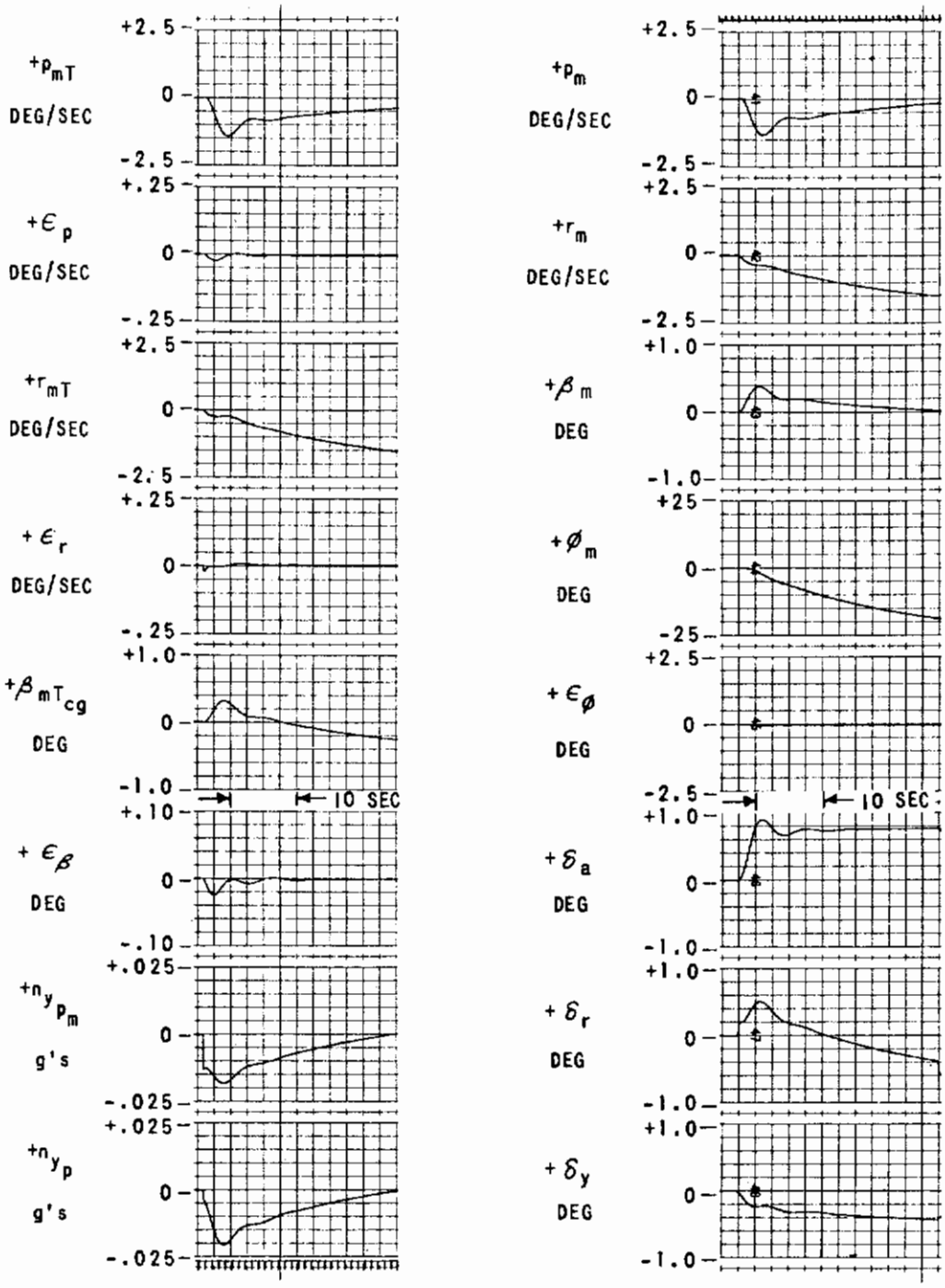

MODEL-FOLLOWING GAINS

$\delta_a/\epsilon_\phi = -10.0$, $\delta_a/\epsilon_p = -2.0$, $\delta_a/\epsilon_{\dot{p}} = -0.5$, $\delta_r/\epsilon_r = -10.0$, $\delta_r/\epsilon_r = -4.0$,
$\delta_r/\epsilon_{\dot{r}} = -.2$, $\delta_y/\epsilon_\beta = +10.0$, $\delta_y/\epsilon_\beta = +10.0$, $\delta_y/\epsilon_{\dot{\beta}} = +1.0$

Figure 4.17 β SYSTEM MODEL-FOLLOWING, LIMITED GAINS WITH INTEGRAL CONTROL δ_{r_m} = +0.5° STEP

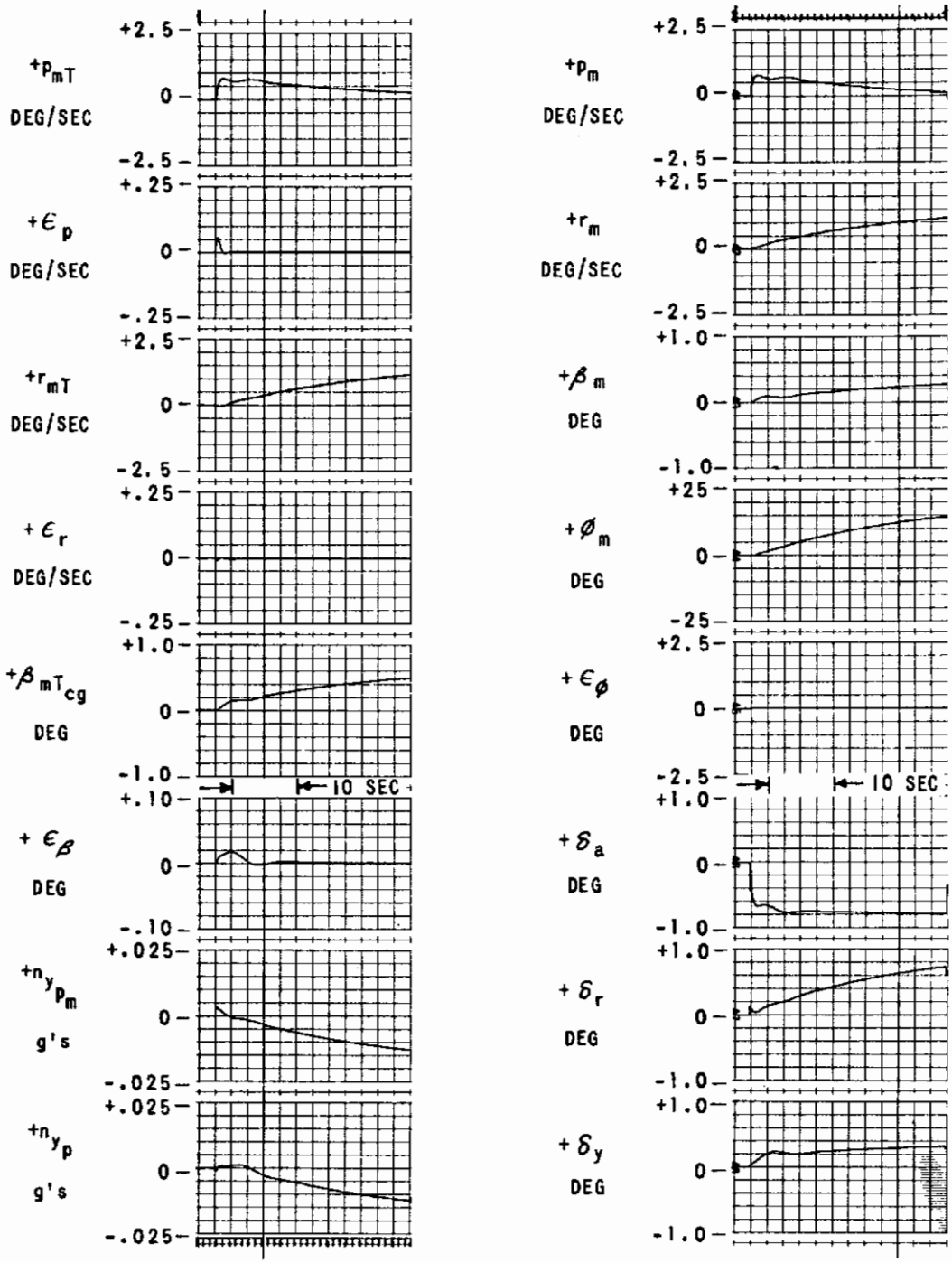

MODEL-FOLLOWING GAINS

$\delta_a/\epsilon_\phi = -10.0$, $\delta_a/\epsilon_p = -2.0$, $\delta_a/\epsilon_{\dot{p}} = -0.5$, $\delta_r/\int\epsilon_r = -10.0$, $\delta_r/\epsilon_r = -4.0$,
$\delta_r/\epsilon_{\dot{r}} = -.2$, $\delta_y/\int\epsilon_\beta = +10.0$, $\delta_y/\epsilon_\beta = +10.0$, $\delta_y/\epsilon_{\dot{\beta}} = +1.0$

Figure 4.18 β SYSTEM MODEL-FOLLOWING, LIMITED GAINS WITH INTEGRAL CONTROL
$\delta_{a_m} = -0.5°$ STEP

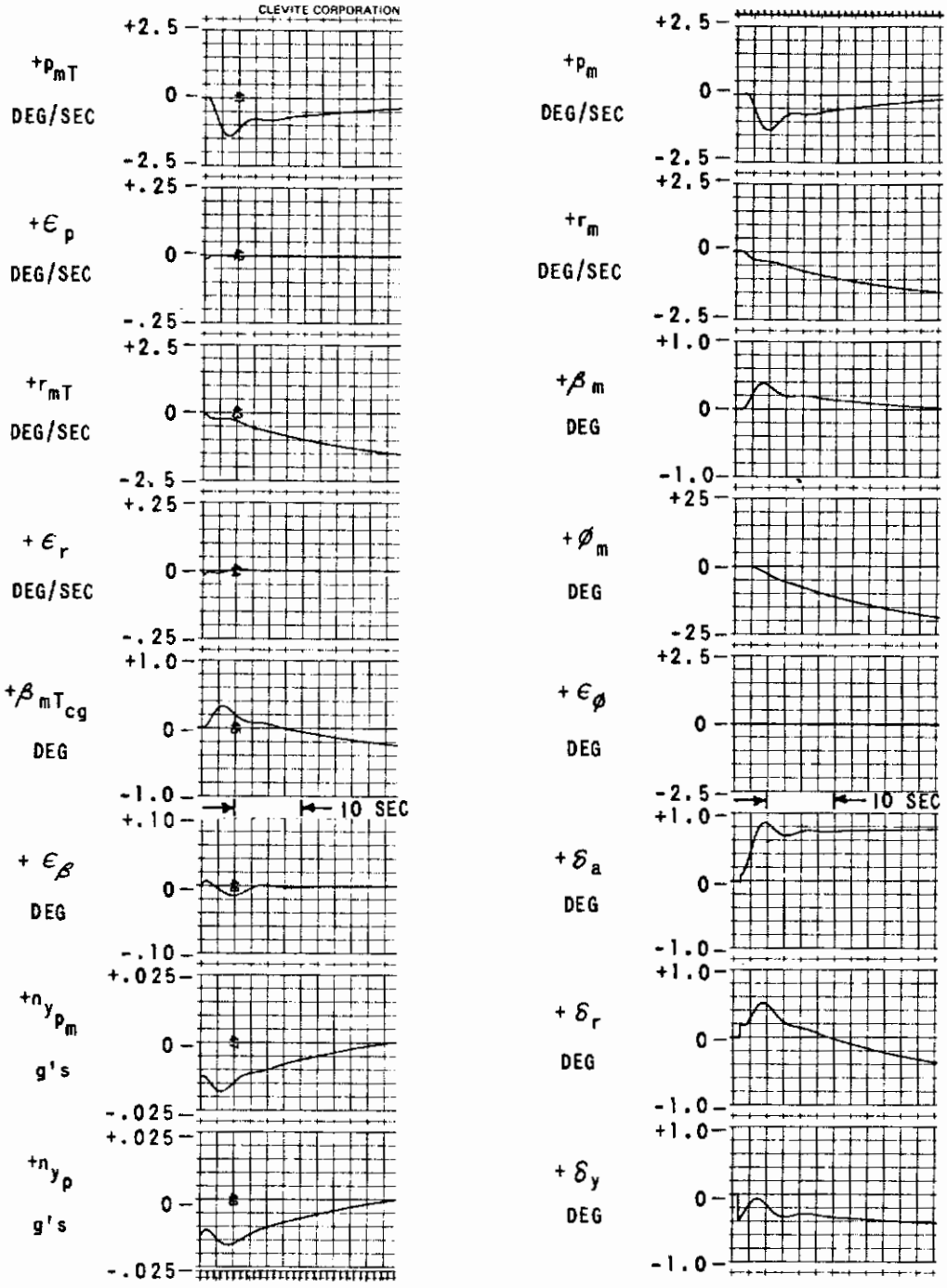

MODEL-FOLLOWING GAINS

$\delta_a/\epsilon_\phi = -10$, $\delta_a/\epsilon_p = -2.0$, $\delta_a/\epsilon_{\dot{p}} = -0.5$, $\delta_a/p_{mT} = -0.25$, $\delta_r/\epsilon_r = -10$, $\delta_r/\epsilon_r = -4.0$, $\delta_r/\epsilon_{\dot{r}} = -.2$, $\delta_y/\epsilon_\beta = +10$, $\delta_y/\epsilon_\beta = +10$, $\delta_y/\epsilon_{\dot{\beta}} = +1.0$, $\delta_y/\dot{p}_m = +.075$, $\delta_y/\dot{r}_m = 3.6$

Figure 4.19 β SYSTEM MODEL-FOLLOWING, LIMITED GAINS WITH BOTH INTEGRAL CONTROL AND FEEDFORWARD δ_{r_m} = +0.5° STEP

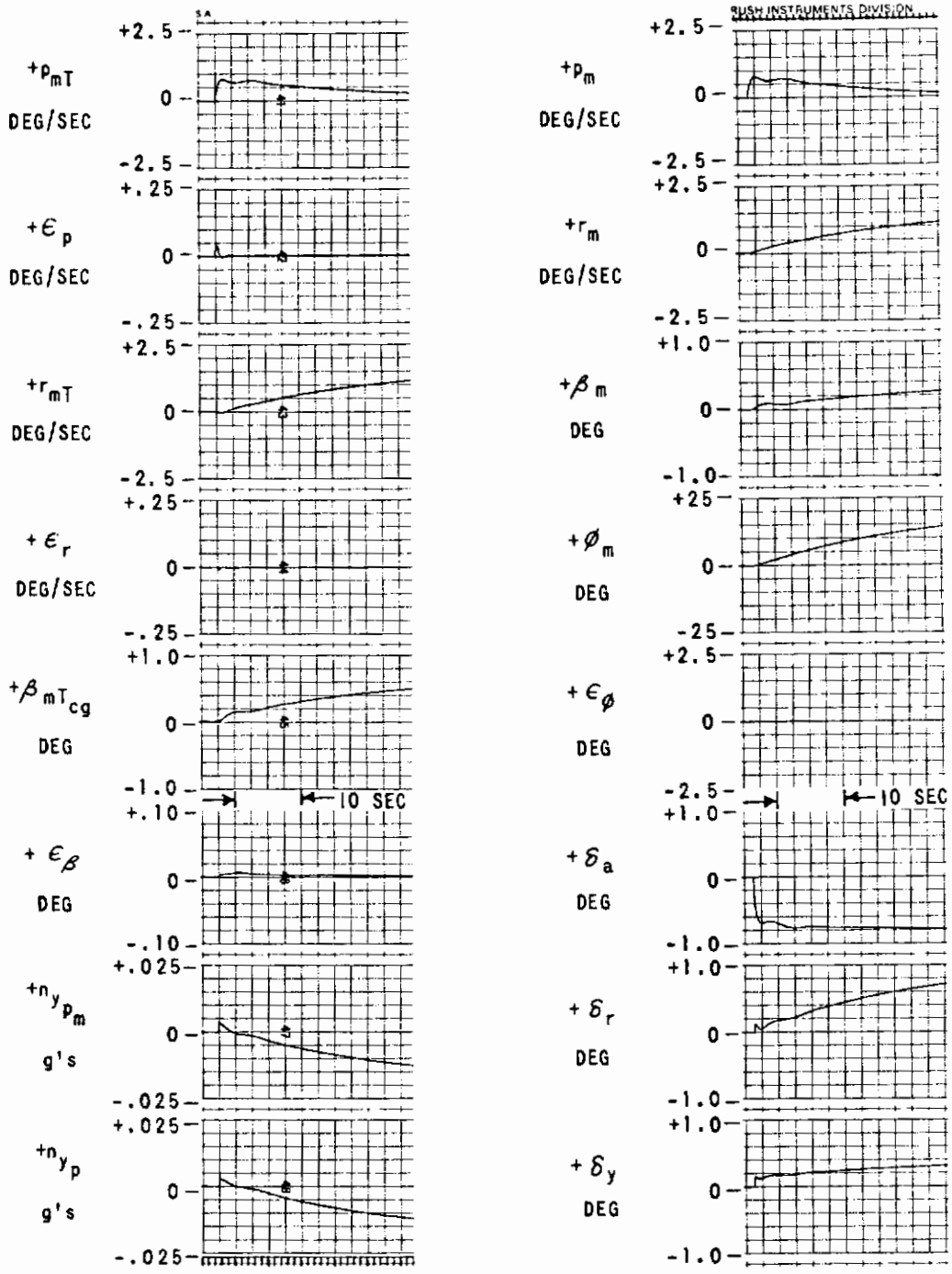

MODEL-FOLLOWING GAINS

$\delta_a/\epsilon_\phi = -10$, $\delta_a/\epsilon_p = -2.0$, $\delta_a/\epsilon_{\dot{p}} = -0.5$, $\delta_a/p_{mT} = -0.25$, $\delta_r/\int\epsilon_r = -10$, $\delta_r/\epsilon_r = -4.0$, $\delta_r/\epsilon_{\dot{r}} = -.2$, $\delta_y/\int\epsilon_\beta = +10$, $\delta_y/\epsilon_\beta = +10$, $\delta_y/\epsilon_{\dot{\beta}} = +10$, $\delta_y/\dot{p}_m = +.075$, $\delta_y/\dot{r}_m = 3.6$

Figure 4.20 β SYSTEM MODEL-FOLLOWING, LIMITED GAINS WITH BOTH INTEGRAL CONTROL AND FEEDFORWARD δ_{a_m} = -0.5° STEP

Theoretically, the effect of feedforward inputs is to change the location of the zeros of the system transfer functions. More design work should be done in the lateral-directional analysis to determine more exactly the analytical effects of feedforward input and to predict more accurately the feedforward gain. In the preliminary design study, the feedforward gains were adjusted to yield the "best" analog transient responses.

The time histories in Figures 4.19 and 4.20 represent the response of the β system. A comparison of these records with those of Figures 4.12 and 4.13, which represent the ideal system, indicates that the final β system with feedforward inputs is an acceptable model-following design.

As in the longitudinal analysis, the model inputs are more severe than those anticipated during a simulation flight. Therefore, the model-following results in both the six-degree-of-freedom simulation and the final three-degree-of-freedom system should, if anything, be better than those presented here.

4.3.4 Alternate n_y System Development

The design of the n_y system was performed in a manner analogous to that utilized for the β system. The model-following loops were closed and the system gains increased to extremely high levels. Runs were made and the time histories obtained to establish a standard to which the final system time histories could be compared. Finally, the loop gains were reduced to realizable levels and the necessary compensation added. As in the β system, the compensation included model following on derivative signals, integral control on ϵ_β and ϵ_{n_y} and model feedforward inputs. The gains used for the time histories are cataloged in Table 4-2, which is a summary of the various loops utilized in each system and the gains used in obtaining all of the time histories.

The time histories of a high gain n_y alternate system are compared with those of the limited gain case noted above in Figures 4.21 and 4.22. From these records, it is apparent that the limited gain configuration produces results which match the results of the unlimited gain case extremely well. The errors in the position signals and rate signals are no worse than 3 percent and the accelerations are matched to within 5 percent. It should be noted that

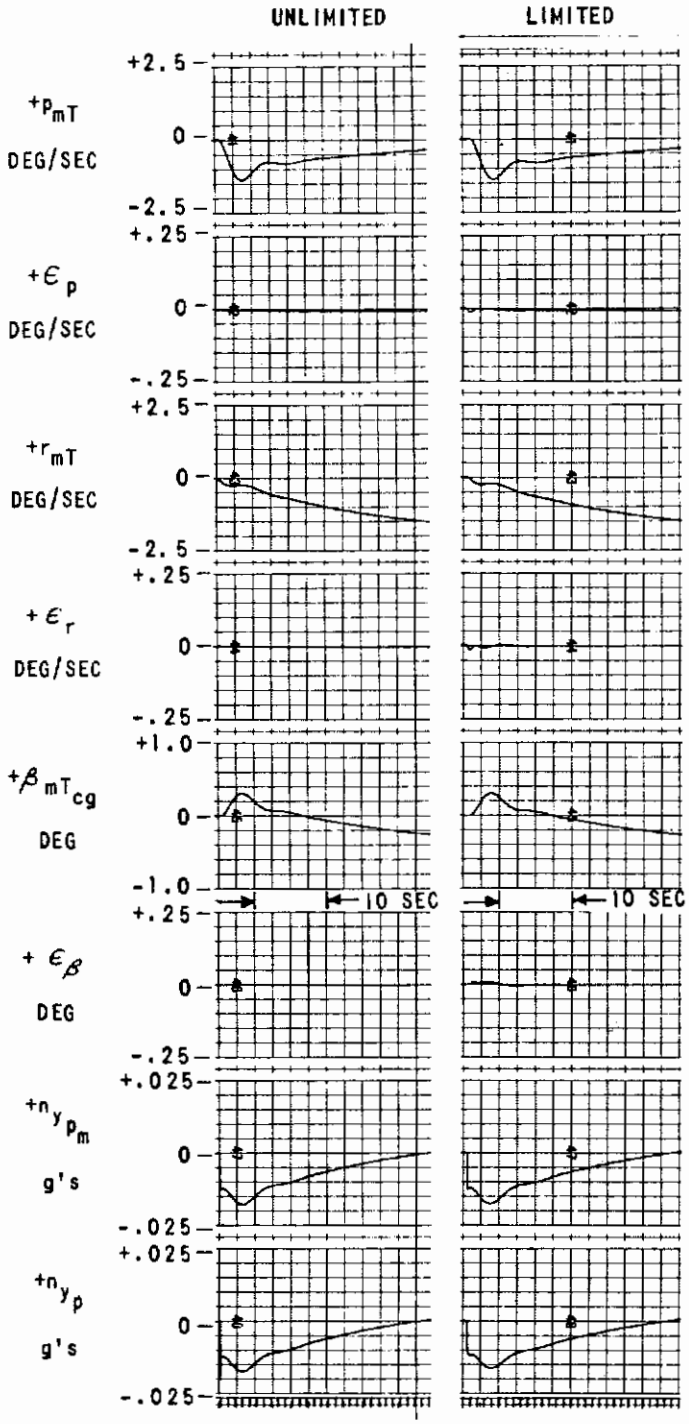

MODEL-FOLLOWING GAINS

		UNLIMITED	LIMITED
δ_a/ϵ_ϕ	=	-10	-10
δ_a/ϵ_p	=	-20	-2
$\delta_a/\epsilon_{\dot{p}}$	=	-5	-.5
δ_a/p_{mT}	=	0	-.2
$\delta_r/\int\epsilon_\beta$	=	+10	+10
δ_r/ϵ_β	=	+100	+10
δ_r/ϵ_r	=	-4	-4
$\delta_r/\epsilon_{\dot{r}}$	=	-.2	-.2
$\delta_y/\int\epsilon_{n_{y_p}}$	=	0	+25
$\delta_y/\epsilon_{n_{y_p}}$	=	+500	+10
$\delta_y/\dot{p}_m$	=	+.15	+.15
$\delta_y/\dot{r}_m$	=	+3.0	+3.0

Figure 4.21 n_y SYSTEM MODEL-FOLLOWING, COMPARISON OF UNLIMITED GAIN CONFIGURATION WITH ALTERNATE n_y SYSTEM
δ_{r_m} = +0.5° STEP

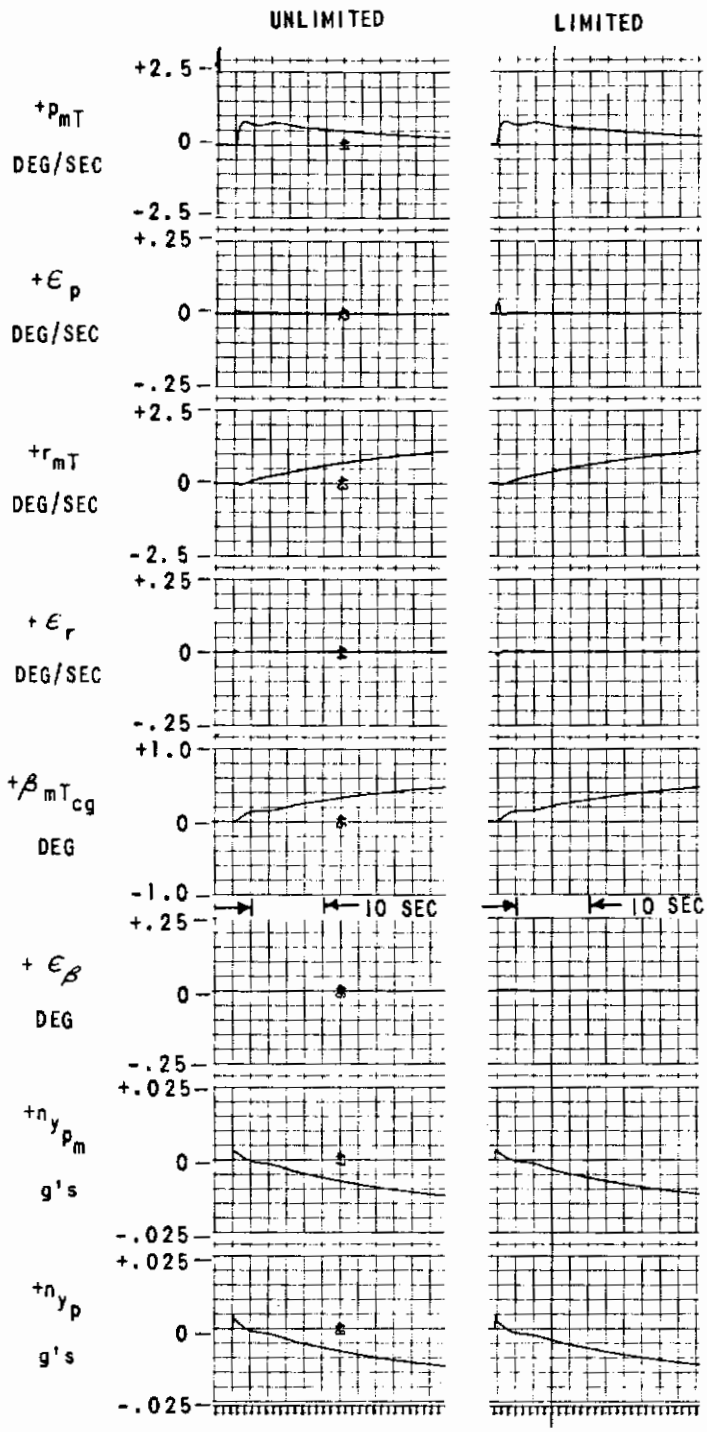

MODEL-FOLLOWING GAINS

		UNLIMITED	LIMITED
δ_a/ϵ_ϕ	=	-10	-10
δ_a/ϵ_p	=	-20	-2
$\delta_a/\epsilon_{\dot{p}}$	=	-5	-.5
δ_a/p_{mT}	=	0	-.2
δ_r/ϵ_β	=	+10	+10
δ_r/ϵ_β	=	+100	+10
δ_r/ϵ_r	=	-4	-4
$\delta_r/\epsilon_{\dot{r}}$	=	-.2	-2
$\delta_y/\epsilon_{n_{y_p}}$	=	0	+25
$\delta_y/\epsilon_{n_{y_p}}$	=	+500	+10
$\delta_y/\dot{p}_m$	=	+.15	+.15
$\delta_y/\dot{r}_m$	=	+3.0	+3.0

Figure 4.22 n_y SYSTEM MODEL-FOLLOWING, COMPARISON OF UNLIMITED GAIN CONFIGURATION WITH ALTERNATE n_y SYSTEM
δ_{a_m} = -0.5° STEP

these errors are the maximum errors that occur and generally appear during the transient response to step inputs and then reduce to zero in a matter of seconds. Theoretically, at least, the steady state errors are zero due to the integral control on β and n_y. The errors in ϕ are small because of the inherently high gain of the $\phi/\delta_a(s)$ transfer function.

4.3.5 Servo Response

During the preliminary design study, the dynamics of the control surfaces are of significant interest. In the analytical design work, the servo effects were not included because the control servo bandwidths are relatively higher than aircraft frequencies and the degree of complexity is greatly increased when servo dynamics are included. The servo dynamics are included in all of the analog computer work, however.

The surface servos for all three surfaces were programmed as second-order servos with damping ratios of 0.7. The time histories of Figures 4.23 through 4.24 represent TIFS responses to model inputs, rudder and aileron respectively, with both 10-Hz surface servos and 4-Hz surface servos. From these responses there appears to be no degradation due to the slower actuators. Figures 4.25 and 4.26, however, are time histories of the same system with an expanded time scale. From these records, the difference in the initial responses can be seen. The higher frequency responses take approximately 2-1/2 times as long to reach a steady state level for the 4-Hz servo as would be expected. There is not much difference in the responses after 0.2 second. It is not felt that this difference seriously degrades the model-following system. However, to improve the capabilities for gust alleviation and structural mode simulation and to enhance closed-loop stability, the higher bandwidth servos are needed. The conclusion to be drawn is that while it is desirable to have 7 to 10-Hz surface servos from the standpoint of simulation capability, 4-Hz surface servos would not prove disastrous. This conclusion is based on the linear three-degree-of-freedom simulation and should be verified in the later design work. Note that the above comments are relevant to longitudinal, as well as lateral-directional, mode design. Experience has shown that the servo characteristics do play such an important role in the model-following system that the results obtained here should be verified by further investigation.

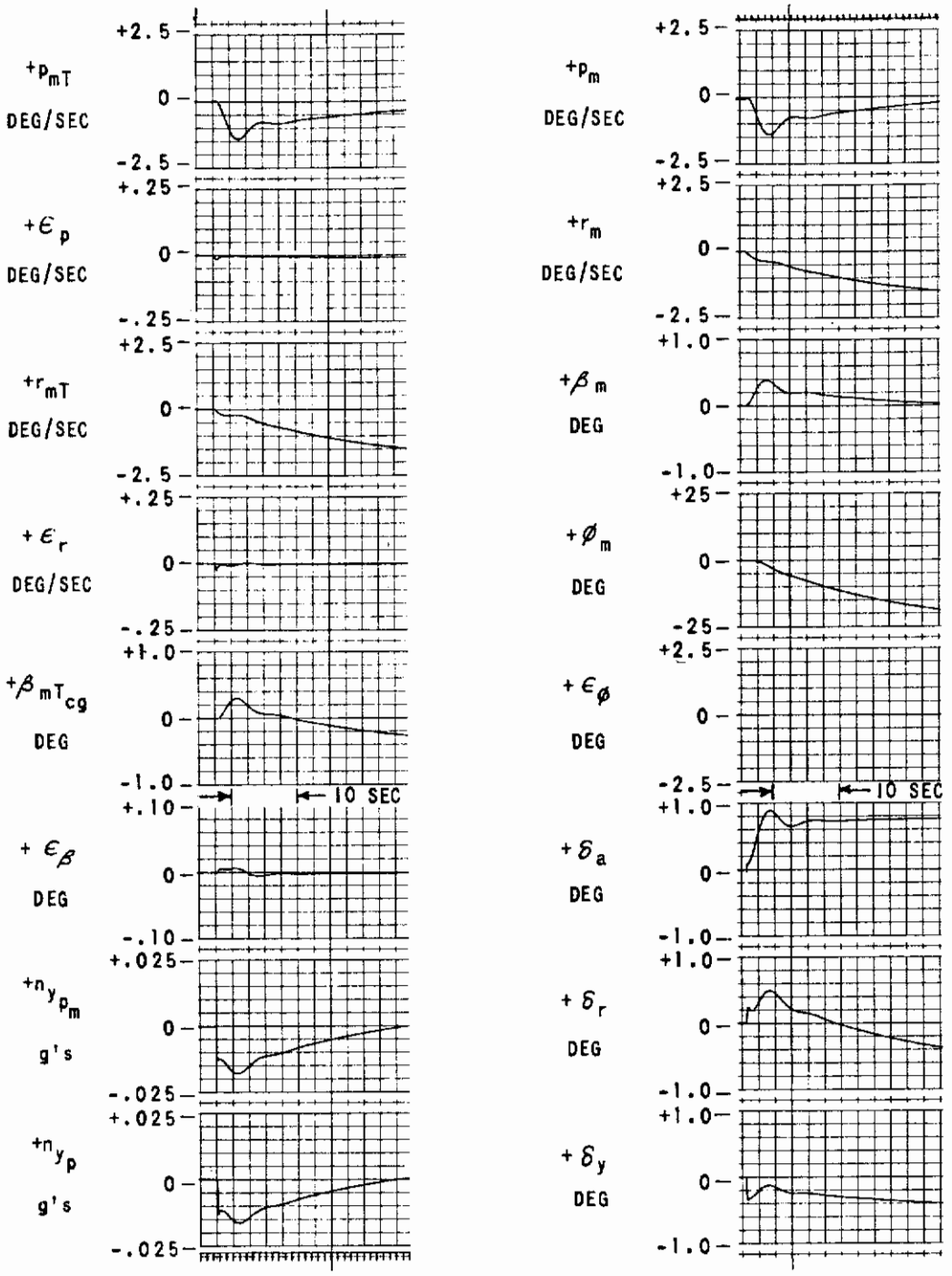

Figure 4.23a ALTERNATE n_y SYSTEM MODEL-FOLLOWING, COMPARISON OF SYSTEM RESPONSES - 10 Hz SURFACE SERVOS

δ_{r_m} = +0.5° STEP

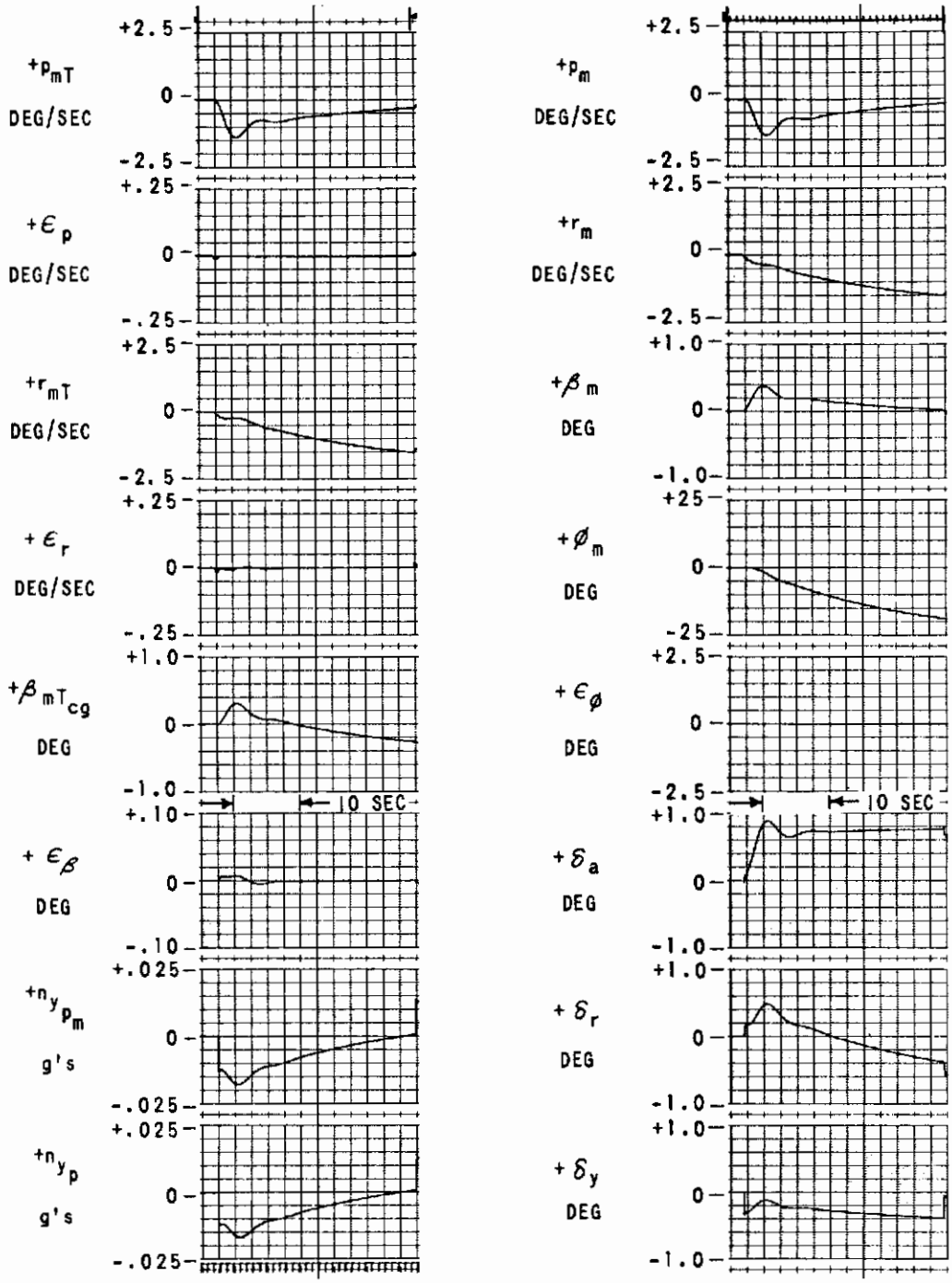

Figure 4.23b ALTERNATE n_y SYSTEM MODEL-FOLLOWING, COMPARISON OF SYSTEM RESPONSES - 4 Hz SURFACE SERVOS

δ_{r_m} = +0.5° STEP

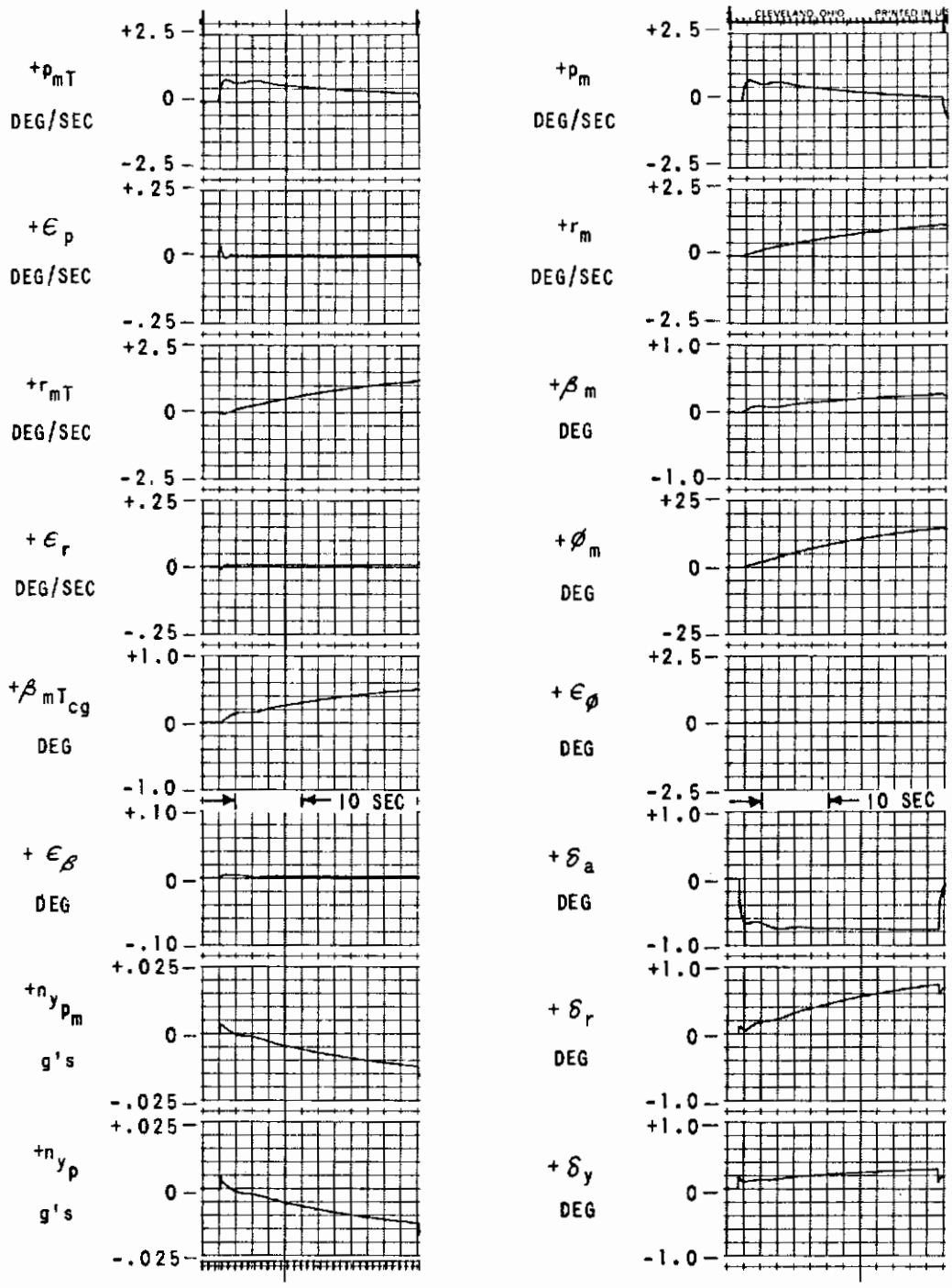

Figure 4.24a ALTERNATE n_y SYSTEM MODEL-FOLLOWING, COMPARISON OF SYSTEM RESPONSES - 10 Hz SURFACE SERVOS

δ_{a_m} = -0.5° STEP

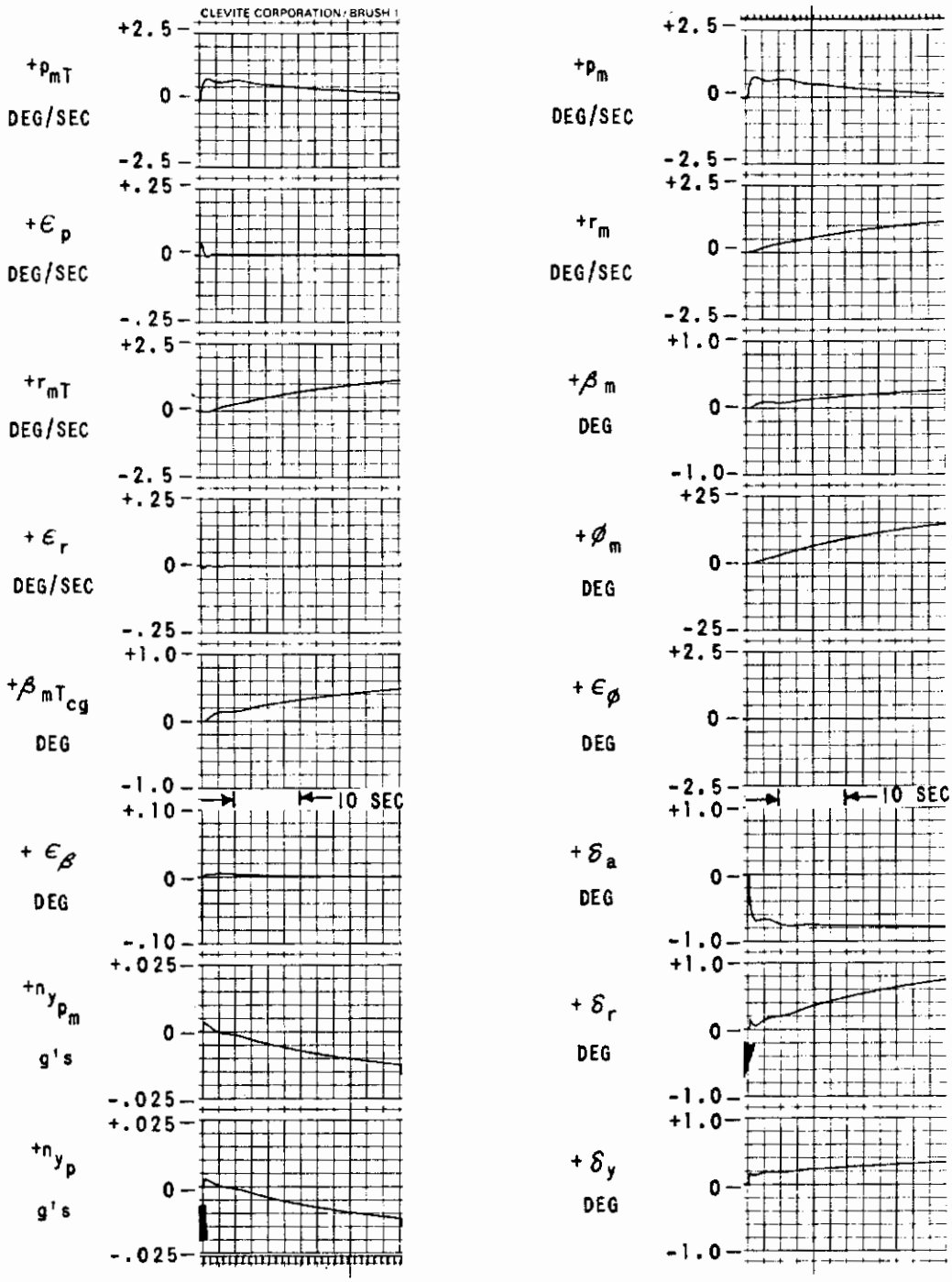

Figure 4.24b ALTERNATE n_y SYSTEM MODEL-FOLLOWING, COMPARISON OF SYSTEM RESPONSES - 4 Hz SURFACE SERVOS

δ_{a_m} = -0.5° STEP

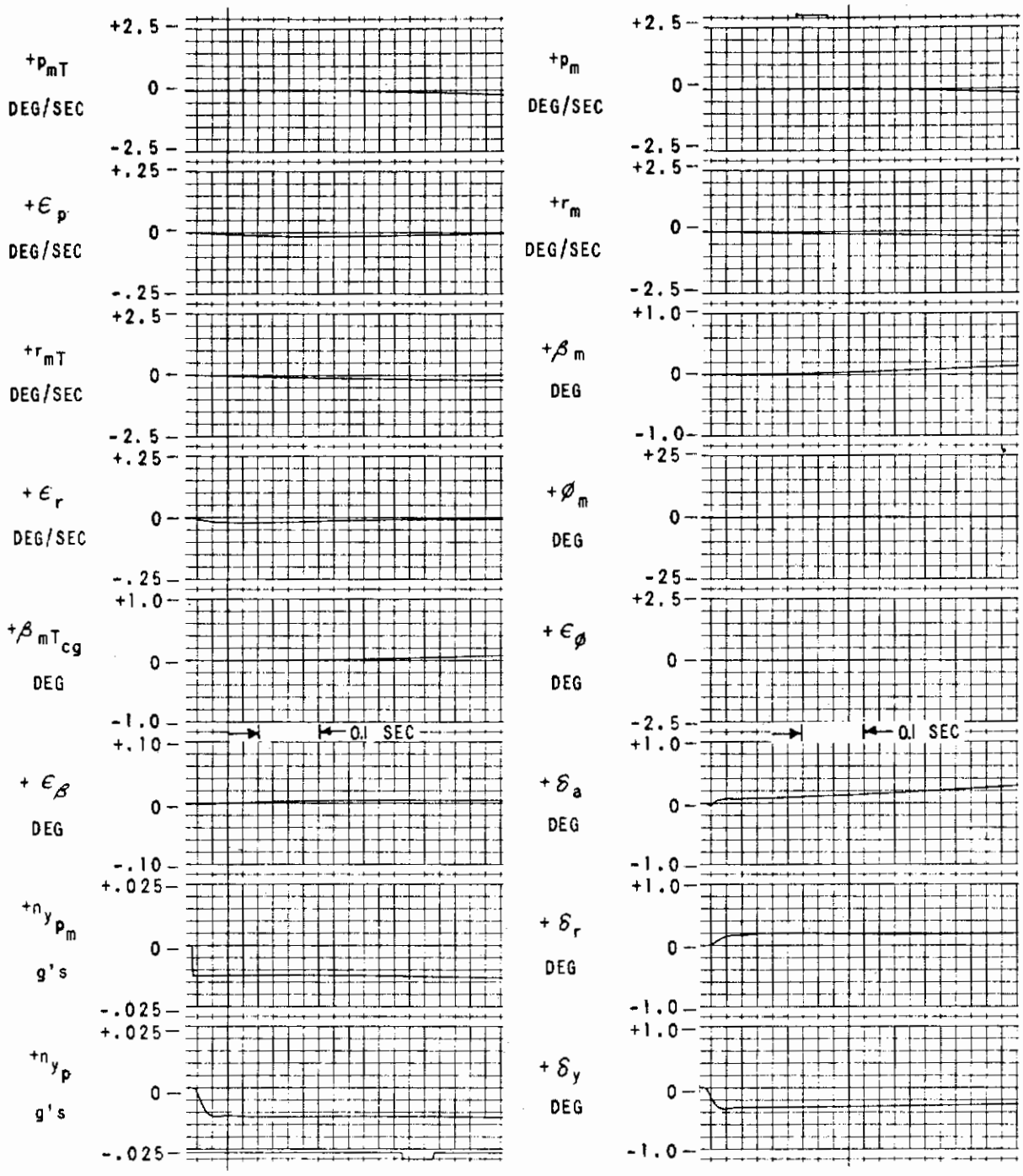

Figure 4.25a ALTERNATE n_y SYSTEM MODEL-FOLLOWING, COMPARISON OF SYSTEM TRANSIENT RESPONSES - 10 Hz SURFACE SERVOS δ_{r_m} = +0.5° STEP, EXPANDED TIME SCALE

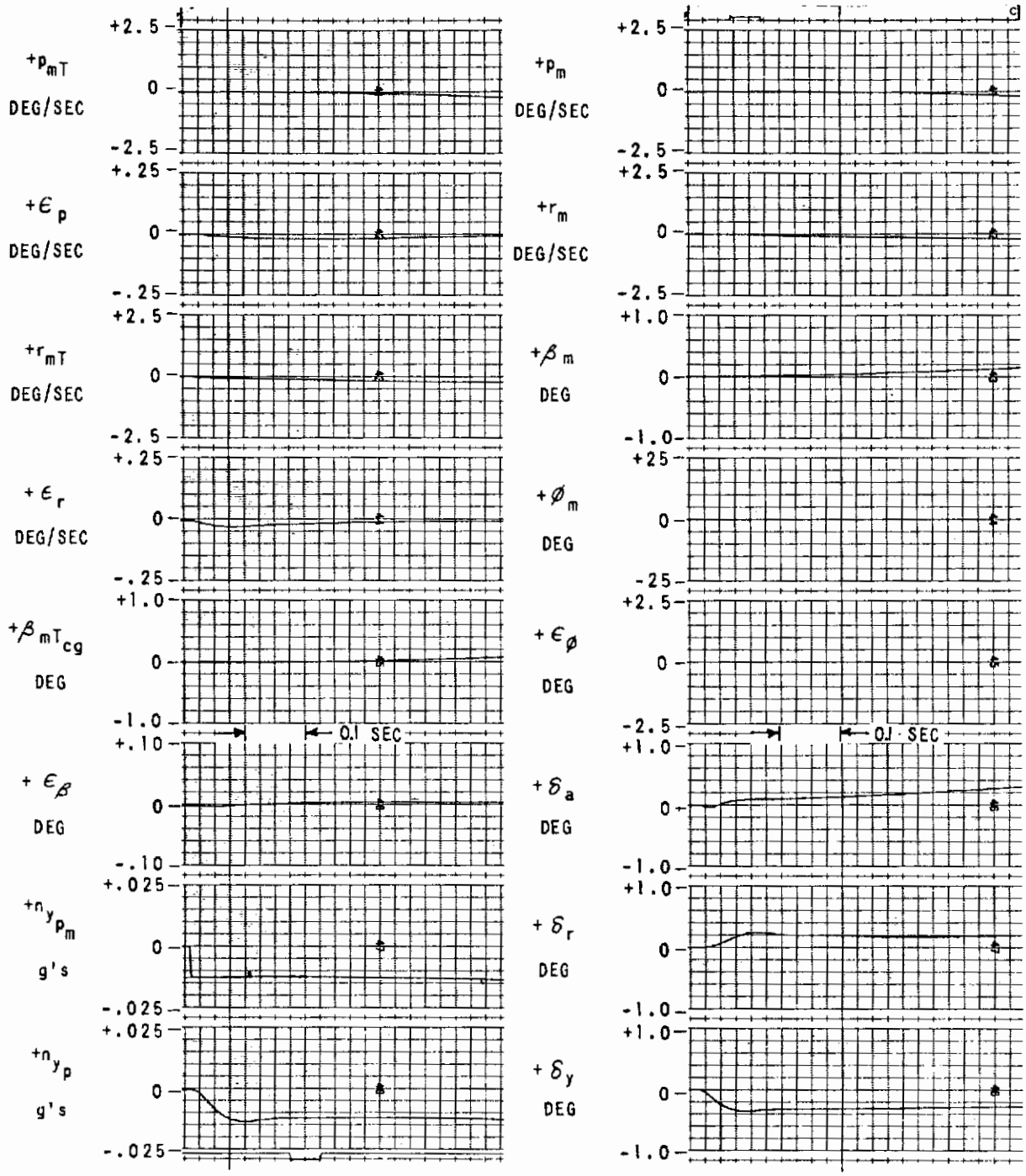

Figure 4.25b ALTERNATE n_y SYSTEM MODEL-FOLLOWING, COMPARISON OF SYSTEM TRANSIENT RESPONSES - 4 Hz SURFACE SERVOS δ_{r_m} = +0.5° STEP, EXPANDED TIME SCALE

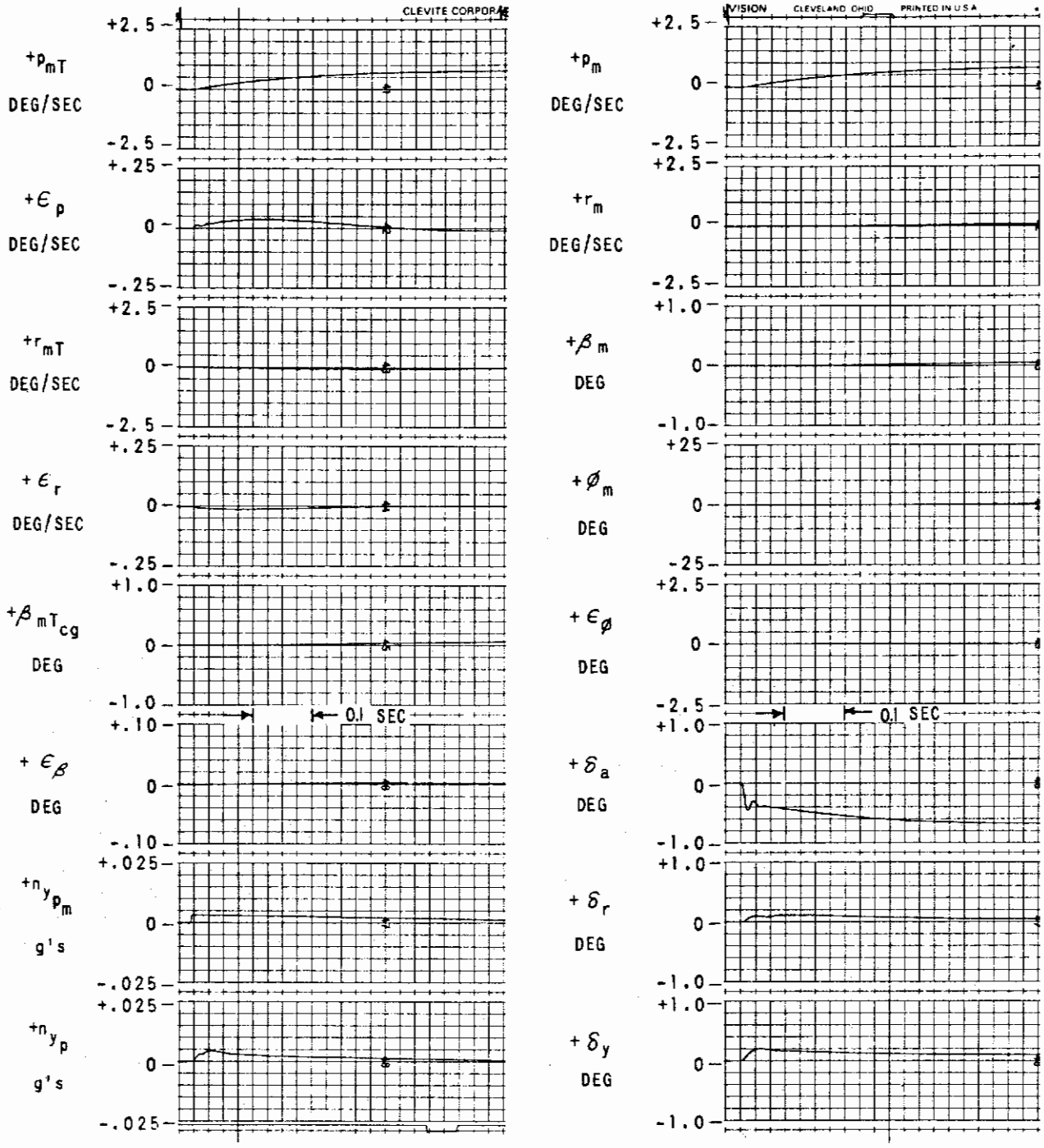

Figure 4.26a ALTERNATE n_y SYSTEM MODEL-FOLLOWING, COMPARISON OF SYSTEM TRANSIENT RESPONSES - 10 Hz SURFACE SERVOS δ_{a_m} = -0.5° STEP, EXPANDED TIME SCALE

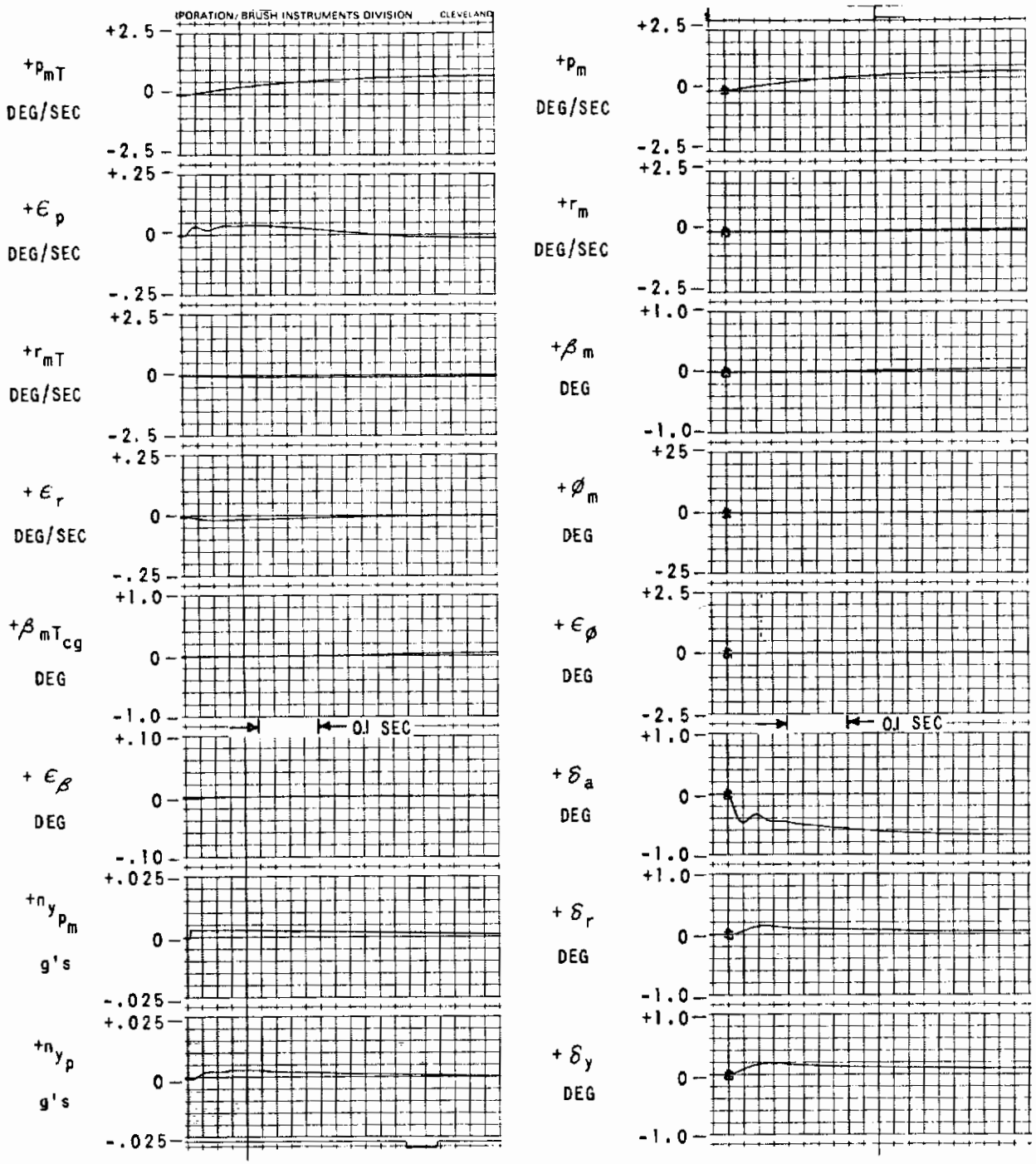

Figure 4.26b ALTERNATE n_y SYSTEM MODEL-FOLLOWING, COMPARISON OF SYSTEM TRANSIENT RESPONSES - 4 Hz SURFACE SERVOS δ_{a_m} = -0.5° STEP, EXPANDED TIME SCALE

4.4 SIX-DEGREE-OF-FREEDOM ANALOG REPRESENTATION

One of the final and more inclusive aids used to design the model-following system of a variable stability airplane is that of six-degree-of-freedom (6 DOF), nonlinear equations-of-motion simulation using the analog computer. Here, both airplanes, model and TIFS, are computerized to represent as complete a physical system as possible consistent with available data and computer equipment. The equations of motion and other data used in this representation are given below. Data for feedback and feedforward loops are the same as those used in the linear analysis and are not presented here.

Results of application to the 6 DOF representation of the system designs developed during the linear analysis phase are not available for this report. However, checkout of individual airplane representation by comparison with digital solutions has been completed, and the major error loops are shown to be functioning. A study plan to investigate various flight conditions, initial conditions and input magnitudes has been developed and will be carried out in the near future. Modification of some of the aerodynamic derivatives appearing below is probable on the basis of TIFS wind tunnel data and revised data received from the Boeing Company.

The equations of motion and other data describing the model-following system as programmed for the six-degree-of-freedom analog design study are now to be given. For clarity, the equations may be categorized as follows:

Airframe statics and dynamics, including Euler angles
Axis transformations
Engine statics and dynamics
Control surface actuator dynamics

A general diagram (Figure 4.27) of the computerized system follows the description of the equations.

4.4.1 Airframe Statics and Dynamics

The following equations were used for both the TIFS and SST model. They are presented in symbolic forms; values of the various quantities used in this study are also given here. Section 2.1 describes the development of these equations including simplifying assumptions and approximations.

Expansion of some aerodynamic coefficients differs between the two representations because of either lack of data or because of nonexistence of some terms in one or the other. Therefore, expansions show the maximum number of terms in either case, and if this number is zero, it is so noted in the succeeding table of numerical values. Terms describing the auxiliary force and moment producing surfaces are also included, although they exist only for the TIFS representation. (These have subscripts x, y, and z.) Note also that the descriptions presented here are based only on data available at the time of this study; descriptions of additional effects, etc., will be presented in succeeding reports.

X Force Equation (wind axes)

$$\dot{V} = -\frac{\rho V^2 S C_D}{2m} - g \sin\gamma + \frac{T}{m}$$

where:

$$C_D \equiv A_{C_D} + B_{C_D}\,\alpha + C_{C_D}\,\alpha^2 + C_{D_{\delta_z}}\,\delta_z$$

Z Force Equation (body axes)

$$\dot{\alpha} = -\frac{\rho V S}{2m} C_L + \frac{g}{V}\cos\theta\cos\phi + q - \frac{\alpha \dot{V}}{V}$$

where:

$$C_L \equiv C_{L_0} + C_{L_\alpha}\,\alpha + C_{L_{\delta_e}}\,\delta_e + C_{L_{\delta_z}}\,\delta_z$$

Y Force Equation (body axes)

$$\dot{\beta} = \frac{\rho V S}{2m} C_{y_s} + \frac{1}{4}\rho S b\, C_{y_D} + \frac{g}{V}\cos\theta\sin\phi - r + \alpha p$$

where: $C_{y_s} \equiv C_{y_\beta}\,\beta + C_{y_{\delta_r}}\,\delta_r + C_{y_{\delta_y}}\,\delta_y$

$$C_{y_D} \equiv C_{y_p}\,p + C_{y_r}\,r$$

Rolling Moment Equation (body axes)

$$\dot{p} = \frac{1}{I_{xx}}\left[I_{xz}\,\dot{r} + \frac{1}{2}\rho V^2 S b\, C_{l_s} + \frac{1}{4}\rho V S b^2 C_{l_D}\right]$$

where:

$$C_{l_s} \equiv \left(C_{l_{\beta_{\alpha=0}}} + C_{l_{\beta\alpha}}\,\alpha\right)\beta + \left(C_{l_{\delta_{r_{\alpha=0}}}} + C_{l_{\delta_r^2}}\,\alpha\right)\delta_r + C_{l_{\delta_a}}\,\delta_a + C_{l_{\delta_a^2}}\,\delta_a^2 + C_{l_{\delta_y}}\,\delta_y$$

and

$$C_{l_D} \equiv \left(C_{l_{r_{\alpha=0}}} + C_{l_{r\alpha}} \alpha \right) r + C_{l_p} p$$

Pitching Moment Equation (body axes)

$$\dot{q} = \frac{1}{I_{yy}} \left[z_T T + \frac{1}{2} \rho V^2 S c \, C_{m_S} + \frac{1}{4} \rho V S c^2 \, C_{m_D} + \frac{1}{2} \rho V^2 S \bar{x} \, C_L \right]$$

where:

$$C_{m_S} \equiv C_{m_o} + C_{m_\alpha} \alpha + C_{m_{\delta_e}} \delta_e + C_{m_{\delta_z}} \delta_z$$

and

$$C_{m_D} \equiv C_{m_q} q + C_{m_{\dot{\alpha}}} \dot{\alpha}$$

Yawing Moment Equation (body axes)

$$\dot{r} = \frac{1}{I_{zz}} \left[I_{xz} \dot{p} + \frac{1}{2} \rho V^2 S b \; C_{n_S} + \frac{1}{4} \rho V S b^2 C_{n_D} \right]$$

where:

$$C_{n_S} \equiv C_{n_\beta} \beta + C_{n_{\delta_r}} \delta_r + C_{n_{\delta_a}} \delta_a$$

and

$$C_{n_D} \equiv C_{n_r} + \left(C_{n_{p\alpha=0}} + C_{n_{p\alpha}} \alpha \right) p$$

$$n_{z_p} = - \frac{\frac{1}{2} \rho V^2 S C_L}{g m} - \frac{\ell_p}{g} \dot{q}$$

$$n_{y_p} = \frac{\frac{1}{2} \rho V^2 S C_y}{g m} + \frac{\ell_p}{g} \dot{r}$$

$$\dot{\psi} = \frac{q \sin \phi + r \cos \phi}{\cos \theta}$$

$$\dot{\theta} = q \cos \phi - r \sin \phi$$

$$\dot{\phi} = p + \dot{\psi} \sin \theta$$

$$\sin \gamma = \sin \theta - \beta \cos \theta \sin \phi - \alpha \cos \theta \cos \phi$$

$$\dot{h} = V \sin \gamma$$

$$\rho = \rho_o + \rho_h h + \rho_{h^2} h^2$$

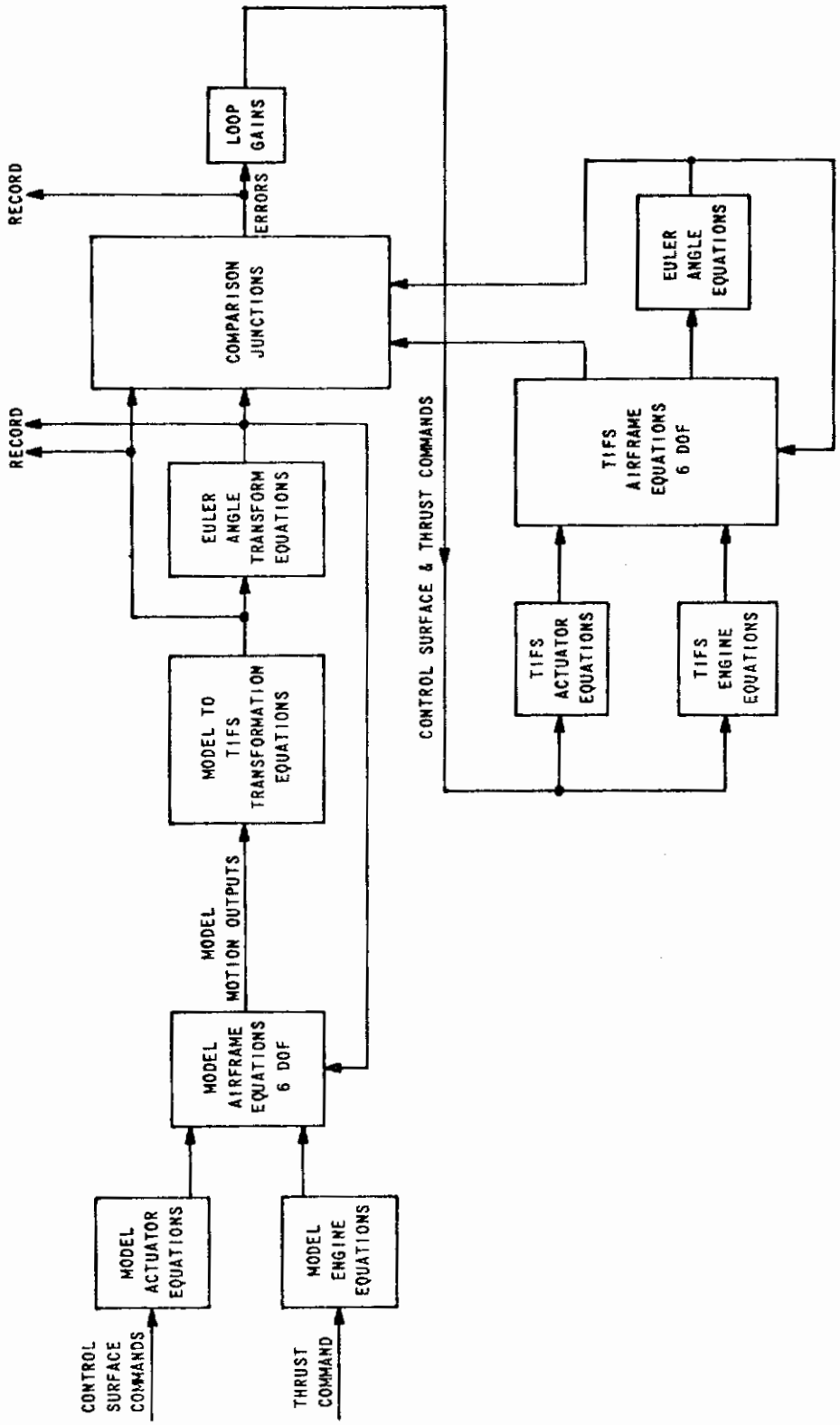

Figure 4.27 FUNCTIONAL DIAGRAM OF SIX-DEGREE-OF-FREEDOM COMPUTERIZED MODEL-FOLLOWING SYSTEM

4.4.2 Axis Transformation Equations

The following equations transfer motion from the SST cockpit floor axis to the TIFS body axis through an angle, i_m, of 4 degrees. Detailed development is shown in Reference 4.4; pertinent relationships are noted here. Subscript "m_T" means model referred to TIFS body axes, "m" refers to model (SST).

$$p_{m_T} = p_m + i_m r_m$$
$$q_{m_T} = q_m$$
$$r_{m_T} = r_m - i_m p_m$$
$$n_{x_{m_T}} = n_{x_m} + i_m n_{z_m}$$
$$n_{y_{m_T}} = n_y$$
$$n_{z_{m_T}} = n_z$$
$$V_{m_T} = V_m$$
$$\beta_{m_T} = \beta_m$$
$$\alpha_{m_T} = \alpha_m - i_m$$
$$\dot{\theta}_{m_T} = q_{m_T} \cos \phi_{m_T} - r_{m_T} \sin \phi_{m_T}$$
$$\dot{\phi}_{m_T} = p_{m_T} + (q_{m_T} \sin \phi_{m_T} + r_{m_T} \cos \phi_{m_T}) \tan \theta_{m_T}$$
$$\dot{\psi}_{m_T} = (q_{m_T} \sin \theta_{m_T} + r_{m_T} \cos \phi_{m_T}) \sec \theta_{m_T}$$
$$\dot{\alpha}_{m_{T_{cg}}} = \dot{\alpha}_m - \left(\frac{\ell_m - \ell_T}{V_m}\right) q_m$$
$$\dot{\beta}_{m_{T_{cg}}} = \dot{\beta}_m + \left(\frac{\ell_m - \ell_T}{V_m}\right) r_m + \frac{\ell_T i_m}{V_m} \dot{p}_m$$

where:

ℓ_m = distance of model c.g. to simulation pilot's station.

ℓ_T = distance of TIFS c.g. to simulation pilot's station.

4.4.3 Engine Statics and Dynamics

A. TIFS (see also subsection 2.3.1)

$$\ddot{T} + 2\zeta\omega_n \dot{T} + \omega_n^2 T = \omega_n^2 (\delta_x - 34°) \left[K_1 + K_2 h + V(K_3 + K_4 h)\right]$$

$\zeta = 0.5$, $\omega_n = 14$ rad/sec

Rate limit on $\dot{T}$ is 9000 lb/sec

B. SST

$$\ddot{T} + 2\zeta\omega_n \dot{T} + \omega_n^2 T = \omega_n^2 \left[\frac{T}{\delta_T}\right] \delta_T$$

$\zeta = 0.8, \omega_n = 1.85$ rad/sec

Rate limit on $\dot{T}$ is 14,500 lb/sec

$\frac{T}{\delta_T}$ = 2530 lb/percent max thrust

4.4.4 Control Surface Dynamics

A. TIFS

$$\ddot{\delta}_e + 2\zeta\omega_n \dot{\delta}_e + \omega_n^2 \delta_e = \omega_n^2 \delta_{e_c}$$

$\zeta = 0.7, \quad \omega_n = 44$ rad/sec

Same for δ_a, δ_r, δ_y, and δ_z

B. SST

$$\dot{\delta}_e + K\delta_e = K\delta_{e_c}$$

$K = \frac{1}{\tau}$; $\tau = 0.05$ sec

Same for δ_a and δ_r

4.4.5 Numerical Data

The following numerical data (not previously noted) were used for the 6 DOF study. Aerodynamic coefficients appear in the same order as they do in the equations of motion and are in radian measure where applicable.

A. TIFS (α in radians for nonlinear coefficients)

W = 45,000 lb

Flight Condition - See below

S = 920 ft^2

b = 105.3 ft

c = 9.52 ft

$\ell = \ell_T$ = 34 ft

I_{xx} = 241,600 slug-ft^2

I_{yy} = 350,000 slug-ft^2

I_{zz} = 680,900 slug-ft^2

I_{xz} = 3000 slug-ft^2

$\bar{x}$ = 1.058 ft

A_{C_D} = 0.0327

B_{C_D} = 0.126

C_{C_D} = 1.44

C_{L_o} = 0.3

C_{L_α} = 5.73

$C_{L_{\delta_e}}$ = 0.7

$C_{l_{\delta_a}}$ = 1.1

C_{y_β} = -1.14

$C_{y_{\delta_r}}$ = 0.35

$C_{y_{\delta_y}}$ = 0.298

$C_{l_{\beta_{\alpha=0}}}$ = -0.11

$C_{l_{\beta\alpha}}$ = 0.358

$C_{l_{\delta_{r\alpha=0}}}$ = 0.026

$C_{l_{\delta_r\alpha}}$ = 0.382

$C_{l_{\delta_a}}$ = -0.095

$C_{l_{\delta_a^2}}$ = 0.0341

$C_{l_{\delta_y}}$ = -0.01

$C_{l_{r\alpha=0}}$ = 0.0420

$C_{l_{r\alpha}}$ = 0.382

C_{l_p} = -0.528

C_{m_o} = 0.08

C_{m_α} = -0.99

$C_{m_{\delta_e}}$ = -2.0

$C_{m_{\delta_y}}$ = +0.15

C_{m_q} = -45.0

$C_{m_{\dot{\alpha}}}$ = -17.0

C_{n_β} = 0.09

$C_{n_{\delta_r}}$ = -0.126

$C_{n_{\delta_a}}$ = 0

$C_{n_{\delta_y}}$ = 0

C_{n_r} = -0.125

$C_{n_{p_{\alpha=0}}}$ = 0

$C_{n_{p_\alpha}}$ = -0.28

K_1 = 320 lb/deg

K_2 = 0.00632 lb/deg-ft

K_3 = -0.364 lb-sec/deg-ft

K_4 = 8.88×10^{-6} lb-sec/deg-ft^2

B. SST

W = 381,000 lb

Flight Condition - See below

S = 9000 ft^2

b = 105.74 ft

c = 158.06 ft

$\ell = \ell_m$ = 170 ft

I_{xx} = 4.27×10^6 slug-ft^2

I_{yy} = 40.2×10^6 slug-ft^2

I_{zz} = 44.2×10^6 slug-ft^2

I_{xz} = 0.25×10^6 slug-ft^2

$\bar{x}$ = 0

A_{C_D} = 0.04

B_{C_D} = -0.252

C_{C_D} = 0.125

C_{L_0} = -0.05

C_{L_α} = 0.255

$C_{L_{\delta e}}$ = 0.09

$C_{L_{\delta_y}}$ = 0

C_{y_β} = -0.229

$C_{y_{\delta r}}$ = 0.120

$C_{y_{\delta_y}}$ = 0

$C_{l_{p_{\alpha=0}}}$ = -0.159

$C_{l_{\beta\alpha}}$ = 0

$C_{l_{\delta r_{\alpha=0}}}$ = 0.00372

$C_{l_{\delta r^\alpha}}$ = 0

$C_{l_{\delta a}}$ = 0.0647

$C_{l_{\delta a^2}}$ = 0

$C_{l_{r_{\alpha=0}}}$ = 0

$C_{l_{r\alpha}}$ = 0

C_{l_r} = -0.547

C_{m_0} = 0

C_{m_α} = -0.04

$C_{m_{\delta e}}$ = -0.036

C_{m_q} = -0.33

$C_{m_{\dot{\alpha}}}$ = -0.1

C_{n_β} = 0.0837

$C_{n_{\delta_r}}$ = -0.063

$C_{n_{\delta_y}}$ = 0

$C_{n_{\delta_a}}$ = 0.00315

C_{n_r} = -0.239

$C_{n_{p_{\alpha=0}}}$ = -0.0812

$C_{n_{p_\alpha}}$ = 0

4.4.6 Flight Conditions

This preliminary mechanization of the 6 DOF representation is based on aerodynamic data approximately consistent with a velocity and altitude for both airplanes of 393 ft/sec (V_{true}) and 10,000 ft (h_p), respectively. Future model-following design studies will encompass a range of flight conditions. In particular, the TIFS airplane will include all important points in the speed-altitude envelope.

4.5 REFERENCES

4.1 Myers, William and Hazen, Samuel: Model Following for SST. CAL Full-Scale Division Memorandum 403, October 1966.

4.2 Reynolds, P.A., Pritchard, F.E., and Schelhorn, A.E.: Preliminary Design Study for a General Purpose Airborne Simulator. CAL Report No. TE-1795-F-1, August 1963.

4.3 Clark, D.: Simulation of the C-5A Transport by Model-Following With a B-26 Variable Stability Aircraft. CAL Full-Scale Division Memorandum 370, July 1965.

4.4 Hazen, Samuel: Model Incidence Angle. CAL TIFS Memo No. 71, 8 May 1967.

SECTION V

TIFS MODEL-FOLLOWING SYSTEM DESIGN USING LINEAR OPTIMAL CONTROL THEORY*

5.1 INTRODUCTION

The problem of achieving acceptable steady state and dynamic simulation of specified aircraft when the TIFS mass characteristics and aerodynamics are not precisely known is a difficult one. The TIFS concept involves six linearly independent controls and therefore, more possible control loops than have been previously studied for in-flight simulation purposes. To cope with the problem of lack of precise knowledge, the model-following approach using high gains is most promising. However, it is not as intuitively obvious as it has been with simpler systems which control loops are best for model following. The general application of linear optimum control theory, an analytical procedure for designing complex multiloop systems, is natural for the TIFS control problem.

The difficulties in specific application of the theory have been studied in support of the TIFS development program and the results reported in this section. These difficulties include the following: obtaining a set of feedback gains which are high but not higher than specified limits, obtaining an optimal control solution which does not depend on the time history of the evaluation pilot's inputs to the model, and obtaining an optimal type-one system for model following, that is, a system which has a forward loop integration to erase steady state errors.

Linear optimal control theory is applied in this section to a servo problem in model following in which the model is driven by an arbitrary input.

The optimal control law of the servo generally depends on the nature of the input. One of the tasks of this analysis is the formulation of a performance index which generates an optimal control law with fixed gains that does not depend on the input shape.

---

*The symbols and notation used in this section are defined in Section 5.14 starting on page 5-37.

In the conventional approach, good model following is achieved with high gains. With the formulation of an "ideal" system which provides "perfect model following" at any feedback gain, the high-gain requirement for good model following is eliminated. But a high feedback gain is still required to reduce the sensitivity of the plant output to variations in the parameters of the plant. The ability to determine an "ideal" system compounded with the requirement for high feedback gains leads to the examination of an important problem in optimal control theory, stated as "Given a set of maximum feedback gains, what are the highest feedback gains which provide a stable and optimal system?" With this groundwork, the design of a "perfect model-following" system which is least sensitive to variations in the plant involves the following steps:

1. Compute the highest feedback gains from a set of maximum gains, and
2. Determine the feedforward gains for perfect model following.

This approach combines the conventional approach of maintaining a high-gain closed-loop control system with choice of the proper compensation outside the loop to exactly match the model.

5.2 THE REGULATOR PROBLEM IN MODEL FOLLOWING

Two distinct formulations are given in References 5-1, 5-2, and 5-3 for the model following of a regulator problem in which the model is driven by arbitrary initial conditions.

The objective of the first formulation is to provide a good match between the dynamics of the plant and the dynamics of the model. The dynamics of the system and the performance index are given by:

$$\left.\begin{array}{ll} \text{Plant} & \dot{x} = Fx + Gu \\ \text{Model} & \dot{\eta} = L\eta \\ \text{Performance Index} & 2V = \int_0^\infty \left[(\dot{y} - Ly)^T Q (\dot{y} - Ly) + u^T R u \right] dt \\ \text{where} & y = Hx \end{array}\right\} \qquad (5\text{-}1)$$

The first term in the performance index in Equation 5-1 tends to zero as the dynamics of the plant approach the dynamics of the model. Inspection of the root square locus expression in:

$$\left| I + R^{-1} G^T (-Is - F^T)^{-1} H^T (-Is - L^T)\, Q (Is - L)\, H (Is - F)^{-1} G \right| = 0 \qquad (5\text{-}2)$$

reveals that the loci originate at the roots of the plant $[Is - F = 0]$ and terminate at the roots of the model $[Is - L = 0]$ when the plant and the model are of the same order.

The second formulation aims at the minimization of the squared error between the output of the plant, x_p, and the output of the model, x_m. The dynamics of the system and the performance index in this case are given by:

$$\left.\begin{aligned} &\text{Plant} && \dot{x}_p = F_p x_p + G_p u \\ &\text{Model} && \dot{x}_m = F_m x_m \\ &\text{Performance Index} && 2V = \int_0^\infty \left[(x_p - x_m)^T H^T Q H (x_p - x_m) + u^T R u \right] dt \end{aligned}\right\} \qquad (5\text{-}3)$$

Minimization of the performance index in Equation 5-3 yields the optimal control law u_o:

$$u_o = -R^{-1} G_p^T P_{11} x_p - R^{-1} G_p^T P_{12} x_m \qquad (5\text{-}4)$$

where P_{11} and P_{12} satisfy the following matrix Riccati equations:

$$\left.\begin{aligned} \dot{P}_{11} + P_{11} F_p + F_p^T P_{11} - P_{11} G_p R^{-1} G_p^T P_{11} + H^T Q H = 0 \\ \dot{P}_{12} + P_{12} F_m + F_p^T P_{12} - P_{11} G_p R^{-1} G_p^T P_{12} - H^T Q H = 0 \end{aligned}\right\} \qquad (5\text{-}5)$$

The root square locus expression in this case reduces to:

$$\left| I + R^{-1} G_p^T (-Is - F_p^T)^{-1} H^T Q H (Is - F_p)^{-1} G_p \right| = 0 \qquad (5\text{-}6)$$

Unlike the model-following problem formulated in (5-1), the root square locus is independent of the dynamics of the model. The elements of the weighting matrices Q and R are selected such that the poles of the closed-loop plant

are moved to the left of the poles of the model, leaving the model poles as the predominant roots of the system.

The second formulation is applied to the servo problem in model following treated in this section for the following reasons:

1. It forces the output of the plant to follow the output of the model instead of matching the dynamics of the two systems.
2. It is less sensitive to variations in the parameters of the plant.
3. The dynamics of the model are not required to determine the feedback gains.

5.3 PRINCIPLES OF OPTIMALITY AND CONTROLLABILITY IN A SERVO PROBLEM

Before proceeding with the formulation of various performance indices, the requirements for a stable minimum should be established for a servo problem.

In Reference 5.5, it is shown that a system described by:

$$\left.\begin{array}{ll} \text{Performance Index} & 2V = \int_0^\infty \left[x^T \phi x + u^T R u \right] dt \\ \text{Plant Dynamics} & \dot{x} = Fx + Gu \end{array}\right\} \qquad (5\text{-}7)$$

has a stable minimum if R is positive-definite, ϕ is non-negative definite. If these conditions are met, and if the plant (F, G) is completely controllable, the Riccati equations have a unique positive-definite symmetric solution, P, and the optimal control is generated as a feedback control law by:

$$u = -R^{-1} G^T P x \qquad (5\text{-}8)$$

For the model-following problem, the dynamics of the plant and model and the description of the model input are governed by the following linear state equations.

$$\left.\begin{array}{ll} \text{Plant} & \dot{x}_p = F_p x_p + G_p u \\ \text{Model} & \dot{x}_m = F_m x_m + G_m u_m \\ \text{Input} & \dot{u}_m = D u_m \end{array}\right\} \qquad (5\text{-}9)$$

where x_p is the output of a controllable plant, (n-vector), x_m is the output of a given model (n-vector), u_m is the model input (m-vector) and u is the control (r-vector).

Defining an enlarged state vector x, the dynamics of the system and the weighting matrix ϕ in the performance index are expressed as:

$$\left.\begin{aligned} &\dot{x} = Fx + Gu \\ &\text{where } x = \begin{bmatrix} x_p \\ x_m \\ u_m \end{bmatrix};\ F = \begin{bmatrix} F_p & 0 & 0 \\ 0 & F_m & G_m \\ 0 & 0 & 0 \end{bmatrix};\ G = \begin{bmatrix} G_p \\ 0 \\ 0 \end{bmatrix};\ \phi = \begin{bmatrix} \phi_{11} & \phi_{12} & \phi_{13} \\ \phi_{12}^T & \phi_{22} & \phi_{23} \\ \phi_{13}^T & \phi_{23}^T & \phi_{33} \end{bmatrix} \end{aligned}\right\} \quad (5\text{-}10)$$

The enlarged system is not controllable since from Reference 5-5

$$\text{Rank}\ \left[G, FG, \ldots F^{2n+m-1}G\right] < 2n+m$$

as expected from the fact that neither the model nor the model input are controllable. To establish the optimality condition for model following Pontryagin's maximum principle will be used in the formulation of the problem. The Hamiltonian H, the optimal control that minimizes the Hamiltonian, u, and the canonical equations are given by:

$$\text{Hamiltonian} \quad 2H = x^T \phi x + u^T R u + 2\lambda^T (F_p x_p + G_p u) \qquad \text{(a)}$$

$$\text{Optimal Control} \quad u = -R^{-1} G_p^T \lambda = -R^{-1} G_p^T (P_{11} x_p + P_{12} x_m + P_{13} u_m) \qquad \text{(b)} \qquad (5\text{-}11)$$

$$\text{Canonical Equations} \begin{cases} \dot{x}_p = F_p x_p - G_p R^{-1} G_p^T \lambda & \text{(c)} \\ -\dot{\lambda} = \phi_{11} x_p + F_p^T \lambda + \phi_{12} x_m + \phi_{13} u_m & \text{(d)} \end{cases}$$

Substituting $\lambda = P_{11} x_p + P_{12} x_m + P_{13} u_m$, and requiring that the canonical equations be satisfied for every x_p, x_m and u_m, yields the following Riccati equations:

$$\left.\begin{aligned} &\dot{P}_{11} + P_{11} F_p + F_p^T P_{11} + \phi_{11} - P_{11} \Lambda P_{11} = 0 && \text{(a)} \\ &\dot{P}_{12} + P_{12} F_m + F_p^T P_{12} + \phi_{12} - P_{11} \Lambda P_{12} = 0 && \text{(b)} \\ &\dot{P}_{13} + P_{12} G_m + P_{13} D + F_p^T P_{13} + \phi_{13} - P_{11} \Lambda P_{13} = 0 && \text{(c)} \end{aligned}\right\} \quad (5\text{-}12)$$

where

$$\Lambda = G_p R^{-1} G_p^T; \quad P_{ij}(\infty) = 0,\ i = 1, 2, 3$$

The solution of these equations is obtained by setting $\dot{P}_{ij}(\infty) = 0$. If ϕ_{11} is non-negative definite, R is positive-definite and the plant (F_p, G_p) is completely controllable, (5-12a) has a unique positive-definite and symmetric solution, P_{11} , and the closed loop plant is stable, as indicated by Kalman in Reference 5.5. In addition to these requirements, (5-12b and c) must have steady state solutions. These equations are rewritten as:

$$\left.\begin{aligned} (F_p - \Lambda P_{11})^T P_{12} + P_{12} F_m &= -\phi_{12} \\ (F_p - \Lambda P_{11})^T P_{13} + P_{13} D &= -\phi_{13} - P_{12} G_m \end{aligned}\right\} \qquad (5\text{-}13)$$

A necessary and sufficient condition for Equation 5-13 to have a solution for all ϕ_{12} , ϕ_{13} is that $\lambda_i + \mu_j \neq 0$ and $\lambda_i + \upsilon_j \neq 0$ for $i,j = 1,2\ldots$ where λ_i is an eigenvalue of the closed-loop plant $(F_p - \Lambda P_{11})$, μ_j is an eigenvalue of the model F_m , and υ_j is an eigenvalue of the model input, D, Reference 5.4.* Thus the conditions for a stable minimum are established for a servo problem.

The minimum value of the performance index for the servo problem in model following is given by: $\left[x_p(0) = x_m(0) = 0 \right]$

$$\left.\begin{aligned} 2V_{min} &= x_0^T P(0) x_0 = u_{m0}^T P_{33}(0) u_{m0} \\ \text{where} \quad P &= \begin{bmatrix} P_{11} & P_{12} & P_{13} \\ P_{12}^T & P_{22} & P_{23} \\ P_{13}^T & P_{23}^T & P_{33} \end{bmatrix} \end{aligned}\right\} \qquad (5\text{-}14)$$

and where P_{33} is the solution of the Riccati equation:

$$\dot{P}_{33} + P_{33} D + D^T P_{33} = P_{13}^T \Lambda P_{13} - P_{23}^T G_m - G_m^T P_{23} \qquad (5\text{-}15)$$

*The necessary and sufficient condition stated holds for matrices of arbitrary dimensions.

For a step input, $D=0$ (the right hand side of Equation 5-15 is not necessarily zero), $\dot{P}_{33} \neq 0$, P_{33} most likely increases without bounds and the minimum value of the performance index tends to $+\infty$. To avoid this difficulty, the performance index for a servo problem can be expressed as:

$$2V = \lim_{t_f \to \infty} \frac{1}{e^{at_f}} \int_0^{t_f} \left[x^T \phi x + u^T R u \right] dt \qquad (5\text{-}16)$$

and an $[a>0]$ can be found for every plant such that $2V$ is finite. But since the optimal control which minimizes Equation 5-16 also minimizes Equation 5-7, the limiting process is dropped for convenience.*

5.4 THE NOMINAL MODEL FOLLOWING SYSTEM

The nominal system is defined by Equations 5-7 and 5-10 where the weighting matrix ϕ in (5-10) is given by

$$\phi = \begin{bmatrix} H^T Q H & -H^T Q H & 0 \\ -H^T Q H & H^T Q H & 0 \\ 0 & 0 & 0 \end{bmatrix} \qquad (5\text{-}17)$$

where H is a transformation on the state vectors x_p and x_m that provides model following between a new set of output vectors $y_p = Hx_p$ and $y_m = Hx_m$. The feedback gain, P_{11}, and the feedforward gain from the model output, P_{12}, do not depend on the companion matrix of the input, D, while the feedforward from the input, P_{13}, depends on D, as noted from Equations 5-11b and 5-12. This is an undesirable situation, requiring the determination of a different control law for every input condition.

The first task in this investigation is to develop a system for which the optimal control does not depend on the input. Since the optimal control theory provides a unique control law which minimizes a given performance index, the problem reduces to that of finding a performance index which yields an optimal control law independent of the input.

---

*In the remainder of this section, the limits of integration are from 0 to ∞, and the steady state solutions of the Riccati equations ($\dot{P}=0$) are sought.

5.5 MODIFIED SYSTEM WITHOUT FEEDFORWARD FROM THE MODEL INPUT

The objective of this method is to force the feedforward gain from the model input, P_{13}, to zero by properly formulating a performance index.

Starting with a generalized performance index,

$$\left.\begin{aligned} &\text{Index:} \quad 2V = \int_0^\infty \left[x^T \phi x + 2 x^T \mathcal{H} u + u^T R u \right] dt \\ &\text{where:} \quad \phi = \begin{bmatrix} H^T Q H + \xi & -H^T Q H & N \\ -H^T Q H & H^T Q H & -N \\ N^T & -N^T & \xi \end{bmatrix}; \quad \mathcal{H} = \begin{bmatrix} M \\ S \\ W \end{bmatrix} \end{aligned}\right\} \quad (5\text{-}18)$$

and where the optimal control is obtained as:

$$u_0 = -R^{-1} \left[(M^T + G_p^T P_{11}) x_p + (S^T + G_p^T P_{12}) x_m + (W^T + G_p^T P_{13}) u_m \right]$$

the following observations are made:

1. The control-state cross product terms, $2x^T \mathcal{H} u$, in the performance index add additional terms to the optimal control law which are not effective in making $P_{13} = 0$.* Therefore, these terms are dropped. The Riccati equations with $(M = S = W = 0)$ are those of Equation 5-12 with $\phi_{11} = H^T Q H + \xi$, $\phi_{12} = H^T Q H$, and $\phi_{13} = N$.

2. Selecting $\xi = 0$ (x_p and x_m form a perfect quadratic term) and $N = P_{12} G_m$ makes $\dot{P}_{13}(t) = 0$. The boundary condition is $P_{13}(t_f) = 0$, hence, $P_{13}(t) = 0$ at all times. Thus, the feedforward from the model input is eliminated. The first two matrix Riccati equations in this case are the same as those for the regulator problem given by Equation 5-5. This implies that the optimal control law which minimizes the performance index in Equation 5-3 for the regulator problem is identical to the optimal control law which minimizes the performance index:

$$\left.\begin{aligned} 2V = \int_0^\infty \left[(x_p - x_m)^T H^T Q H (x_p - x_m) + 2 u_m^T N^T (x_p - x_m) + u^T R u \right] dt \\ \text{where} \quad N = -P_{12} G_m \end{aligned}\right\} \quad (5\text{-}19)$$

*These terms were originally included for making $P_{13} = 0$.

for the servo problem. Experience has shown that the optimal control for the regulator problem does not provide good model following for the servo problem. Therefore, ξ is retained and the performance index is written as:

$$\left.\begin{aligned} 2V &= \int_0^\infty f_1(x_p, x_m, u_m, u)\,dt^* \\ \text{where } f_1(\cdot) &= (x_p - x_m)^T H^T Q H (x_p - x_m) + u^T R u + x_p^T \xi x_p + u_m^T \xi u_m \\ &\quad + 2 u_m^T N^T (x_p - x_m) \end{aligned}\right\} \quad (5\text{-}20)$$

and where ξ and N are selected such that:

$$\left.\begin{aligned} N &= -P_{12} G_m \\ \xi &= \frac{1}{2}\left[(P_{12} G_m) + (P_{12} G_m)^T\right] \end{aligned}\right\} \quad (5\text{-}21)$$

In this method, the first two matrix Riccati equations in Equation 5-12 are coupled through ξ. Therefore, the sufficiency conditions for a minimum stated in Section 5.3 do not apply to this method, and the Riccati equations do not necessarily have a unique solution.

The concept behind the selection of N and ξ can be outlined as follows:

The nominal system provides a relationship among P_{11}, P_{12} and P_{13} through which good model following is obtained. When P_{13} is made zero, the relationship required for good model following is disturbed unless the relationship between P_{11} and P_{12} is modified in such a way as to restore the property of good model following. The modified system described above provides this relationship as evidenced from the first-order example given below.

Figure 5.1 shows the steady state response to a step input of the first-order system described in Appendix I (Section 5.15). The output of the nominal system $x_{p_{ss_n}}$, the output of the modified system $x_{p_{ss_m}}$, q and P_{12} are plotted in this figure versus the feedback gain P_{11}, from which the following observations are made:

*Addition of quadratic terms of x_m and u_m to the performance index does not affect the optimal control law.

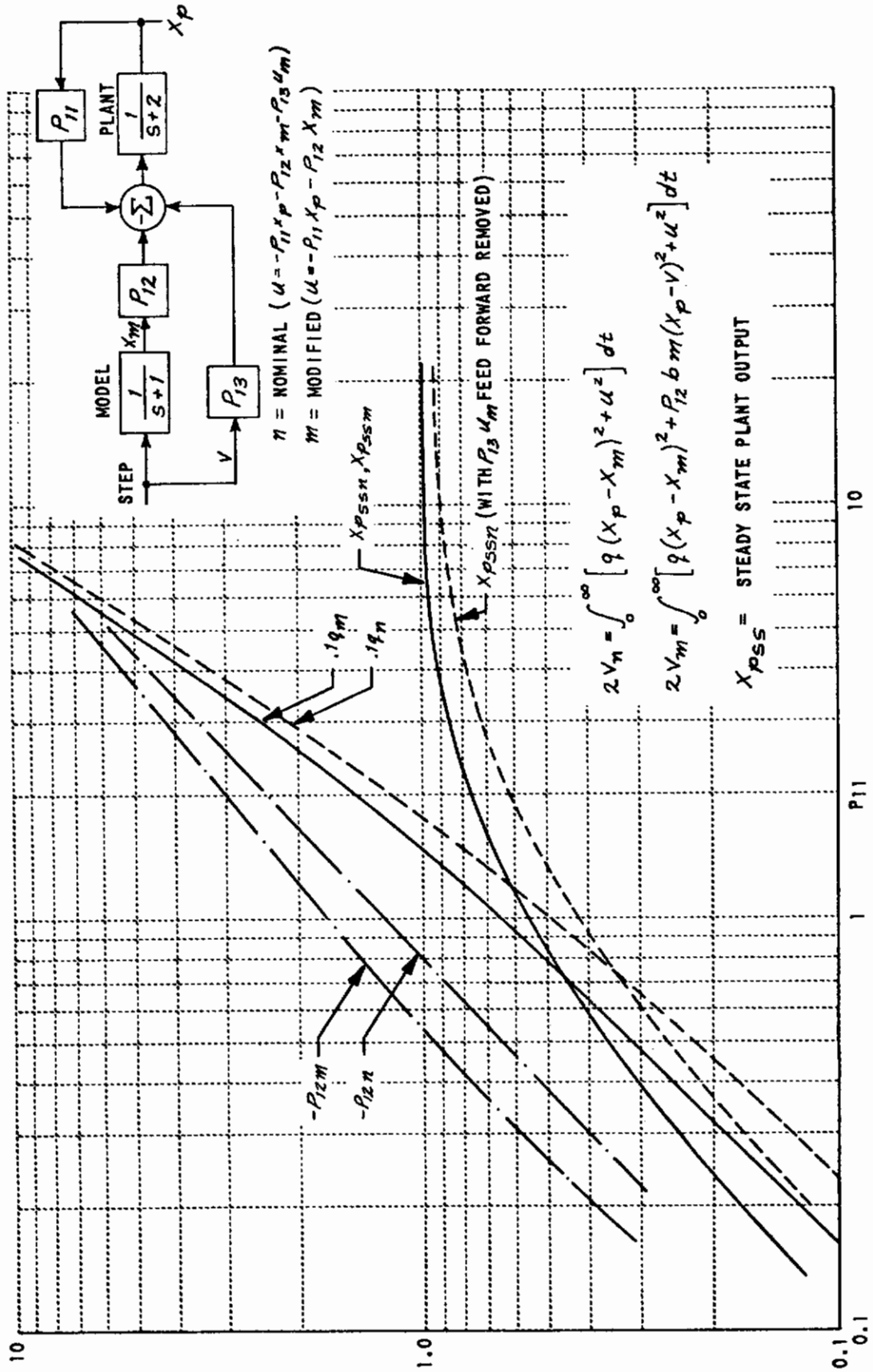

Figure 5.1 MODEL FOLLOWING FOR A FIRST-ORDER SYSTEM

1. For the same feedback gain P_{11}, the nominal and the modified systems provide the same percent steady state error. (The q's are different for each system.)

2. P_{12} and q for the modified system are higher than those for the nominal system.

3. Removing the feedforward from the model input for the nominal system deteriorates the model following as noted from the dotted line in the same figure.

Thus, the quality of the model following is improved by this method over the nominal case with the feedforward from the model input removed.

The step response of the second-order example described in Appendix I is plotted in Figure 5.2 for various q's.

5.6 MODIFIED SYSTEM WITH FEEDFORWARD FROM THE MODEL INPUT

A second method for making the optimal control insensitive to the model input is to eliminate the term $P_{13}D$ in the third Riccati equation in Equation 5-12 by properly formulating a performance index which provides a fixed feedforward gain from the model input for any input condition. The performance index in this case is given by:

$$2V = \int_0^\infty \left[(x_p - x_m)^T H^T Q H (x_p - x_m) + 2\dot{u}_m^T M^T (x_p - x_m) + u^T R u\right] dt; \qquad M = -P_{13}$$

or by

$$2V = \int_0^\infty \left[x^T \phi\, x + u^T R u\right] dt \qquad (5\text{-}22)$$

where

$$\phi = \begin{bmatrix} H^T Q H & -H^T Q H & MD \\ -H^T Q H & H^T Q H & -MD \\ D^T M^T & -D^T M^T & 0 \end{bmatrix}$$

M in Equation 5-22 is related to N in Equations 5-18 by $N = MD$. The optimal control for the nominal system is identical with the optimal control resulting from this formulation when the input is a step, $D = 0$. Therefore, the step response of this system shown in Figure 5.3 is the same as the step response of the nominal system. Since a step is a severe input condition which excites all the frequencies, it is conceivable that a system designed for a step input will behave fairly well with other inputs. Therefore, in this method, the optimal control is always determined for a step input regardless of the type of input applied to the system.

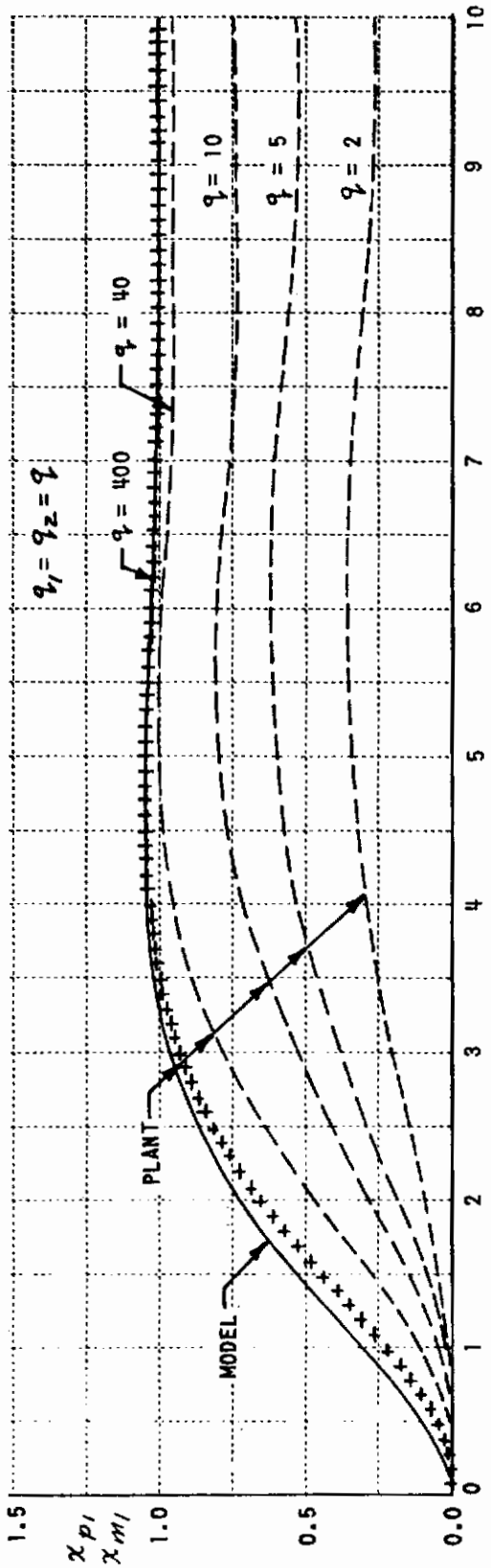

Figure 5.2 STEP RESPONSE - MODIFIED SYSTEM WITHOUT FEEDFORWARD FROM THE MODEL INPUT

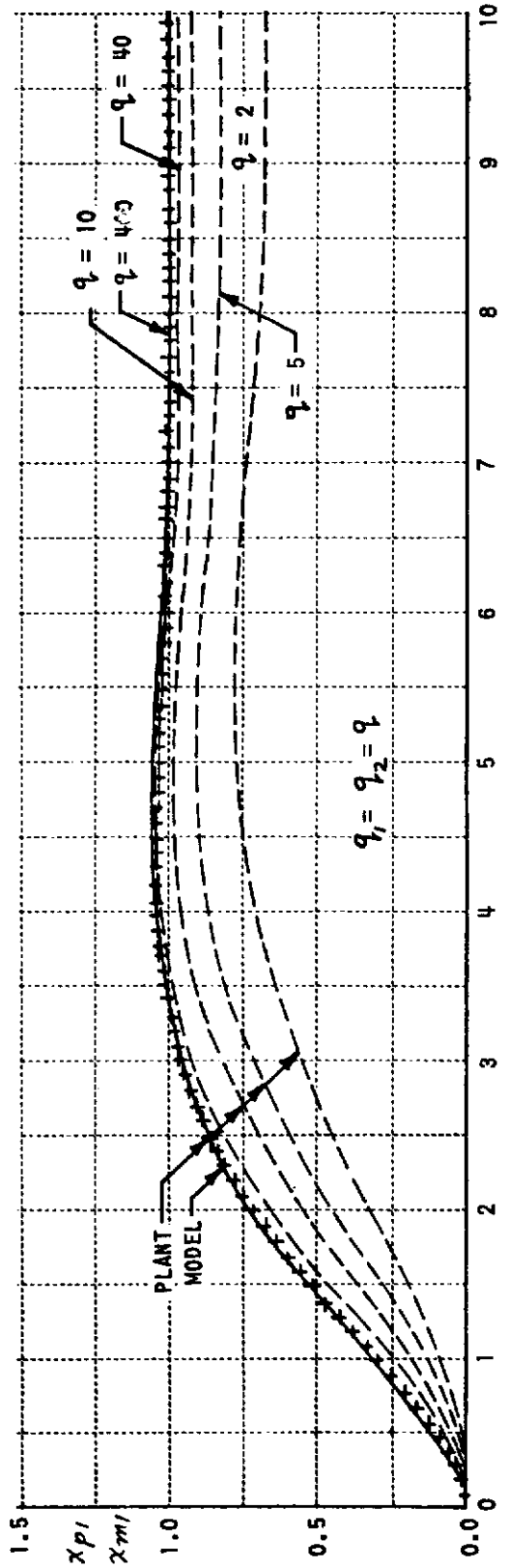

Figure 5.3 STEP RESPONSE - NOMINAL SYSTEM AND MODIFIED SYSTEM WITH FEEDFORWARD FROM THE MODEL INPUT

With this formulation, the Riccati equation in Equation 5-12a is independent of P_{12} and P_{13} ($\phi_{11}=H^TQH$), and the sufficiency conditions stated in Section 5.3 are valid. P_{13} can always be found from Equation 5-13 since the the closed loop of the optimal system (F_p-1P_{11}) is invertible.

With the nominal system designed for a sinusoidal input and the modified system with feedforward from the model input designed for a step input, the sinusoidal responses of the three systems discussed above are plotted in Figure 5.4. A comparison of the step response of the modified systems without and with feedforward from the model input shown in Figures 5.2 and 5.3 respectively, and the sinusoidal response of the three systems plotted in Figure 5.4 indicate the necessity of retaining the feedforward from the model input for better model following.*

5.7 IDEAL TYPE-ZERO MODEL-FOLLOWING SYSTEM

The systems presented above require high gains for improved model following as evidenced from Figures 5.1 through 5.4. The question arises whether it is possible to formulate a performance index which provides "perfect model following" at any feedback gain.

Starting with the performance index

$$\left.\begin{aligned} 2V &= \int_0^\infty \Big[(x_p-x_m)^T H^TQH(x_p-x_m) + 2\dot{u}_m^T M^T(x_p-x_m) + u^TRu \\ &\quad + 2(Sx_m+Lu_m)^T(x_p-u_m)\Big]dt \\ \text{or}\quad 2V &= \int_0^\infty \left[x^T\phi x + u^TRu\right]dt \\ \text{where}\quad x &= \begin{bmatrix} x_p \\ x_m \\ u_m \end{bmatrix}; \quad \phi = \begin{bmatrix} H^TQH & -H^TQH+S & MD+L \\ -H^TQH+S^T & H^TQH & -MD-S^T \\ D^TM^T+L^T & -D^TM^T-S & -L-L^T \end{bmatrix} \end{aligned}\right\} \quad (5\text{-}23)$$

*A fair comparison between the modified systems with and without feedforward from the model input should be based on identical feedback gain matrices P_{11}. But, for a multivariable problem, it was not possible to make all the elements of P_{11} identical with the proper selection of Q.

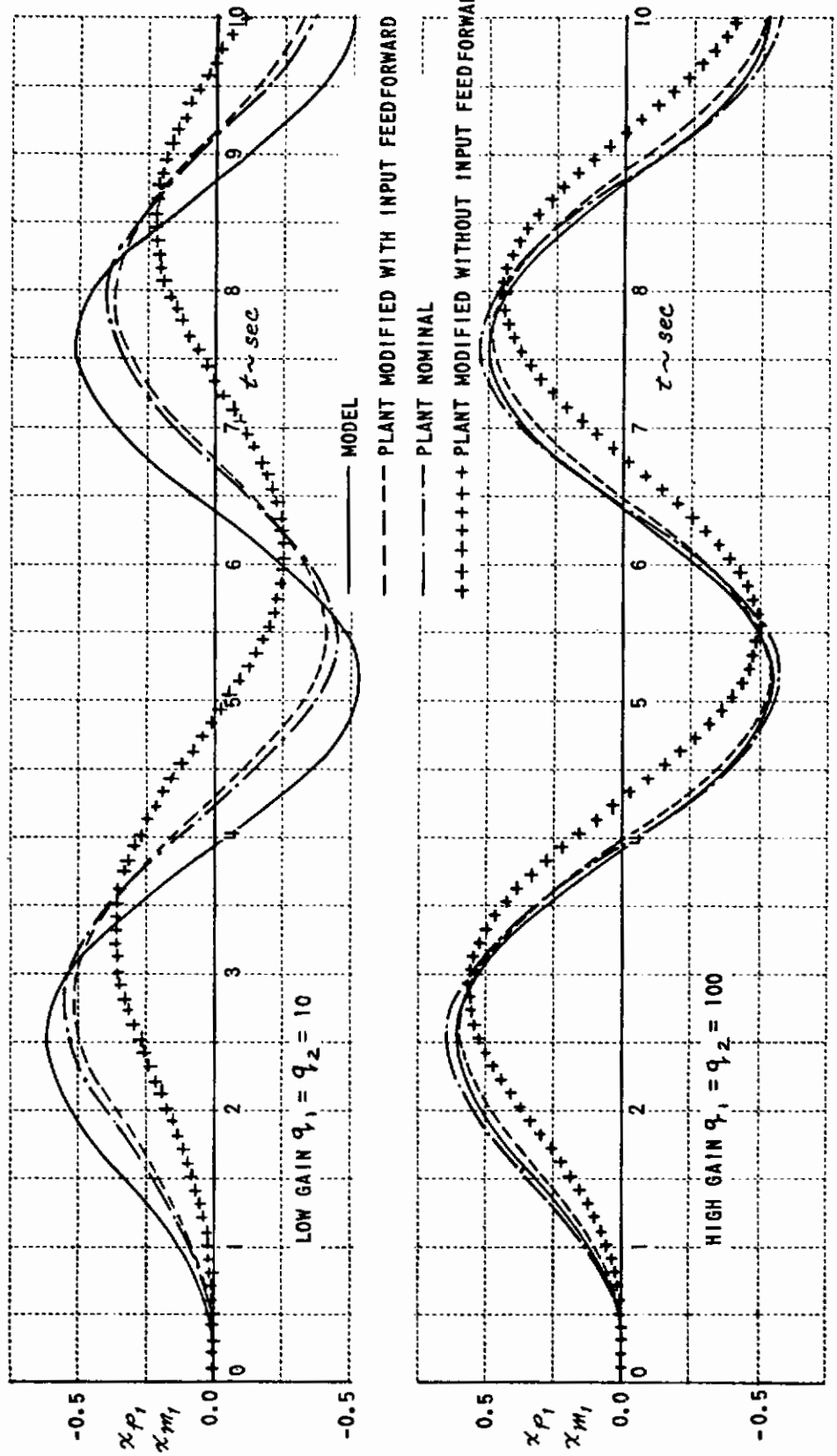

Figure 5.4 RESPONSE OF A SECOND-ORDER SYSTEM TO A SINUSOIDAL INPUT

the relationship between $\mathcal{S}$, $\mathcal{L}$, and ρ_{ij}, which provides "perfect model following" is sought. M has the same meaning as in the previous subsection and makes the optimal control insensitive to the description of the model input.

The optimal control and the Riccati equations are given by:

$$\left.\begin{aligned} u_o &= -R^{-1}G_p^T\left[P_{11}x_p + P_{12}x_m + P_{13}u_m\right] && \text{(a)}\\ \dot{P}_{11} &+ P_{11}F_p + F_p^T P_{11} + H^T Q H - P_{11}\Lambda P_{11} = 0 && \text{(b)}\\ \dot{P}_{12} &+ P_{12}F_m + F_p^T P_{12} - H^T Q H + \mathcal{S} - P_{11}\Lambda P_{12} = 0 && \text{(c)}\\ \dot{P}_{13} &+ P_{12}G_m + P_{13}D + F_p^T P_{13} + MD + \mathcal{L} - P_{11}\Lambda P_{13} = 0 && \text{(d)} \end{aligned}\right\} \quad (5\text{-}24)$$

where $\Lambda = G_p R^{-1} G_p^T$

Selecting:

$$\left.\begin{aligned} M &= -P_{13}\\ \mathcal{S} &= -(P_{11}+P_{12})F_m - F_p^T(P_{11}+P_{12})\\ \mathcal{L} &= -(P_{11}+P_{12})G_m - F_p^T P_{13} \end{aligned}\right\} \quad (5\text{-}25)$$

yields the following relationship between the feedforward gains and the feedback gains:

$$\left.\begin{aligned} \Lambda P_{13} &= -G_m\\ \Lambda P_{12} &= F_p - F_m - \Lambda P_{11} \end{aligned}\right\} \quad (5\text{-}26)$$

Substituting the optimal control from Equation 5-24 into the differential equation of the plant and using the relationship in Equation 5-26 yields:

$$\frac{d}{dt}(x_p - x_m) = -(\Lambda P_{11} - F_p)(x_p - x_m)$$

since $x_p(0) = x_m(0) = 0$, $x_p(t) = x_m(t)$ at all times, implying perfect model following.

The sufficiency condition for a stable minimum stated in Section 5.3 holds for the ideal system, since $H^T Q H$ is nonnegative definite, R is positive-definite and the plant (F_p, G_p) is completely controllable. The solution of 5-24b, P_{11}, is unique positive-definite and symmetric.

The existence of feedforward gains which satisfy the necessary condition for perfect model following stated in Equation 5-26 depends on the nature of the plant and model.

1. If G_p is invertible, a unique P_{12} and P_{13} exist and the feedforward gains are determined from

$$\left.\begin{aligned} K_v &= -R^{-1} G_p^T P_{13} = G_p^{-1} G_m \\ K_m &= -R^{-1} G_p^T P_{12} = K_p + G_p^{-1}\left[F_m - F_p\right] \end{aligned}\right\} \qquad (5\text{-}27)$$

   where the feedback gain $K_p = R^{-1} G_p^T P_{11}$

   In this case, the plant perfectly follows <u>any</u> model of the same order.

2. If G_p is not a square matrix and if the number of linearly independent controls, r, is larger than or equal to the number of linearly independent model inputs, m, the plant follows exactly any <u>transformed</u> model of the same order (Reference 5.6).

If, in addition to the requirement that $r \geq m$ when G_p is not square, a transformation, T, can be found such that:

$$\left.\begin{aligned} T^{-1} F_m T &= \begin{bmatrix} F_o \\ \overline{F}_m \end{bmatrix} \begin{matrix} \rightarrow (n-r)\times n \\ \rightarrow r \times n \end{matrix} & T^{-1} G_m &= \begin{bmatrix} 0 \\ \overline{G}_m \end{bmatrix} \begin{matrix} \rightarrow (n-r)\times m \\ \rightarrow r \times m \end{matrix} \\ T^{-1} F_p T &= \begin{bmatrix} F_o \\ \overline{F}_p \end{bmatrix} \begin{matrix} \rightarrow (n-r)\times n \\ \rightarrow r \times n \end{matrix} & T^{-1} G_p &= \begin{bmatrix} 0 \\ \overline{G}_p \end{bmatrix} \begin{matrix} \rightarrow (n-r)\times r \\ \rightarrow r \times r \end{matrix} \end{aligned}\right\} \qquad (5\text{-}28)$$

where $\bar{G}_p$ is invertible, the plant follows exactly that model which satisfies the conditions of Equation 5-28. P_{12} and P_{13} in this case are not unique, but the feedforward gains are unique and given by:

$$\left.\begin{aligned} K_y &= \left[\bar{G}_p\right]^{-1} \bar{G}_m \\ K_m &= K_p + \left[\bar{G}_p\right]^{-1} \left[\bar{F}_m - \bar{F}_p\right] \end{aligned}\right\} \qquad (5\text{-}29)$$

In many control problems, the number of linearly independent controls is equal to the number of degrees of freedom; the excess state variables over the control variables are the derivatives of the other state variables. The matrix, F_o in this case, is of the form:

$$F_o = \begin{bmatrix} 0 \ldots 0 \; 1 \; 0 \ldots 0 \\ \cdots\cdots\cdots \\ 0 \ldots\ldots 1 \; 0 \\ 0 \ldots\ldots 0 \; 1 \end{bmatrix} \qquad (5\text{-}30)$$

that is, it is composed of rows each containing only one nonzero entry, that being a one. If the model is selected from the same class of systems as the plant (for instance, TIFS airplane and the SST), it can be represented in the same form by definition of the class. Therefore, for such control problems, perfect model following is possible.

The block diagram of the ideal type-zero system is shown in Figure 5.5. With feedforward gains determined from Equations 5-27 or 5-29, a fictitious compensation network is inserted which makes the transfer function from the model output to the plant output unity, as shown in Figure 5.5b.

The block diagram of the conventional response-feedback system described in Reference 5.8 is shown in Figure 5.6 for comparison. With this system the gains are selected from:

$$\left.\begin{aligned} G_p K_m &= G_m \\ G_p K_p &= F_p - F_m \end{aligned}\right\} \qquad (5\text{-}31)$$

in order to provide an exact match between the plant and model outputs. Note that the feedback gain is tailored to provide the matching and therefore, this system is highly sensitive to variations in the parameters of the plant, whereas with the ideal system, there is complete freedom in selecting the feedback gains to reduce the sensitivity. Furthermore, since the response feedback is not the outcome of an optimal design, very little can be said about the optimality and the stability of such a system.

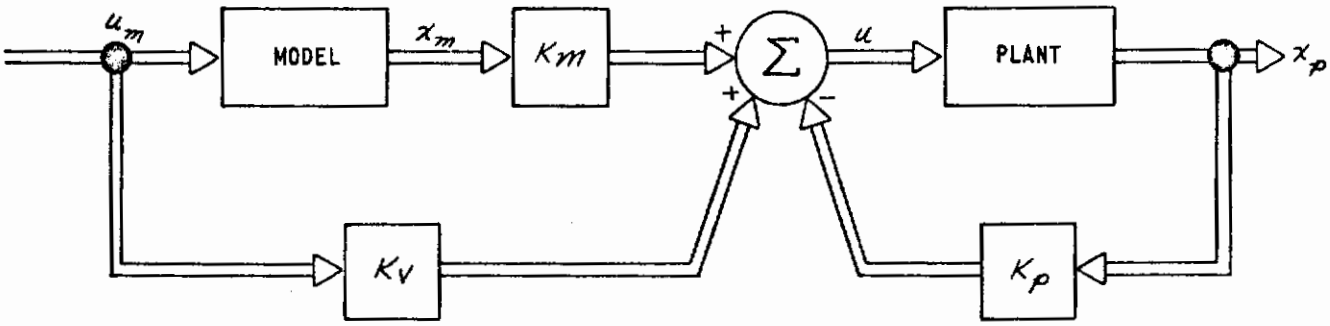

a) ACTUAL BLOCK DIAGRAM

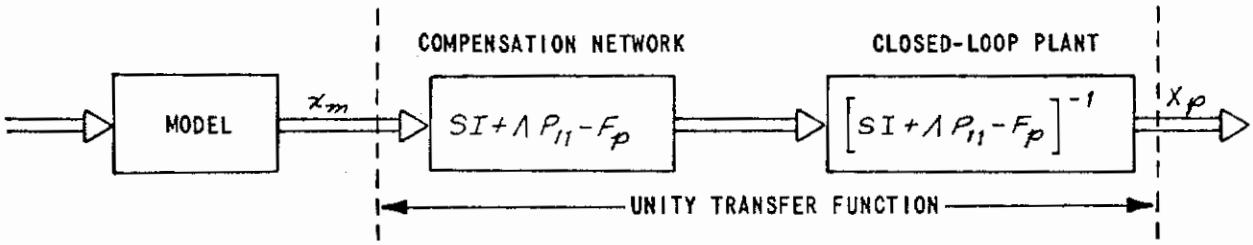

b) CONCEPTUAL BLOCK DIAGRAM

Figure 5.5 BLOCK DIAGRAM OF THE IDEAL TYPE-ZERO SYSTEM

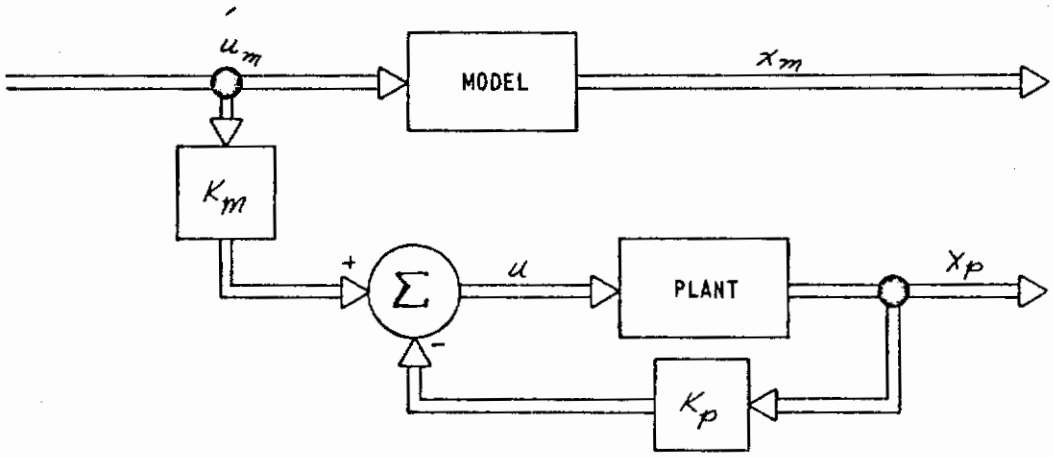

Figure 5.6 BLOCK DIAGRAM OF A RESPONSE-FEEDBACK SYSTEM

The response of the second-order ideal model-following system is shown in Figure 5.7. The step responses of the linearized three-degree-of-freedom longitudinal dynamics of the aircraft are shown in Figures 5.8 and 5.9 for a unit elevator displacement input and for a unit throttle input, respectively (see Appendix I). These figures show the perfect model following provided by the ideal type-zero system.

It should be mentioned as a closing remark that the ideal system is not restricted to optimal systems, since Equations 5-27 and 5-29 give the feedforward gains in terms of the feedback gains regardless of their source.

5.8 TYPE-ONE MODEL-FOLLOWING SYSTEM

Before investigating the sensitivity problem associated with various model-following systems developed above, a type-one system will be treated for the sake of completeness of this study.

The effect of a type-one system in eliminating steady state errors to a step input is well known from conventional control theory. The development that follows presents a means of formulating a type-one system on the basis of linear optimal control theory.

The performance index for a type-one system is given by

$$2V = \int_0^\infty \left[x^T \phi x + u^T R u + \dot{u}^T T \dot{u} \right] dt \qquad (5\text{-}32)$$

where x is defined in (5-10), R and T are positive-definite weighting matrices.

Two formulations for the type-one system will be presented.

Formulation A

If the controls are linearly independent, a matrix S exists such that:

$$\left.\begin{aligned} S &= G_p \left[G_p^T G_p \right]^{-1} R \left[G_p^T G_p \right]^{-1} G_p^T \\ R &= G_p^T S G_p \end{aligned}\right\} \qquad (5\text{-}33)$$

The performance index and the dynamics of the system can then be written in terms of an enlarged state vector z as:

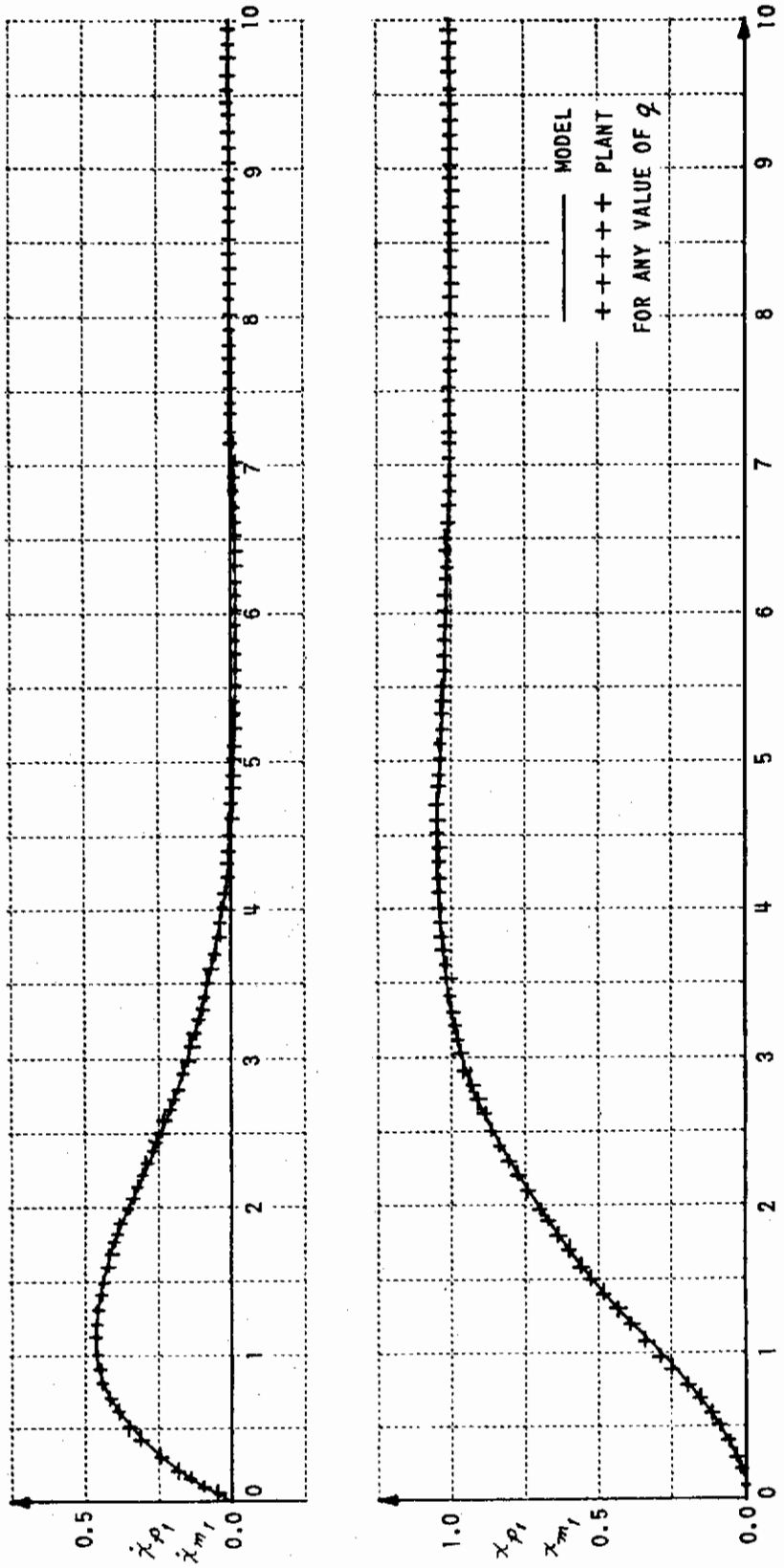

Figure 5.7 STEP RESPONSE - PERFECT MODEL FOLLOWING

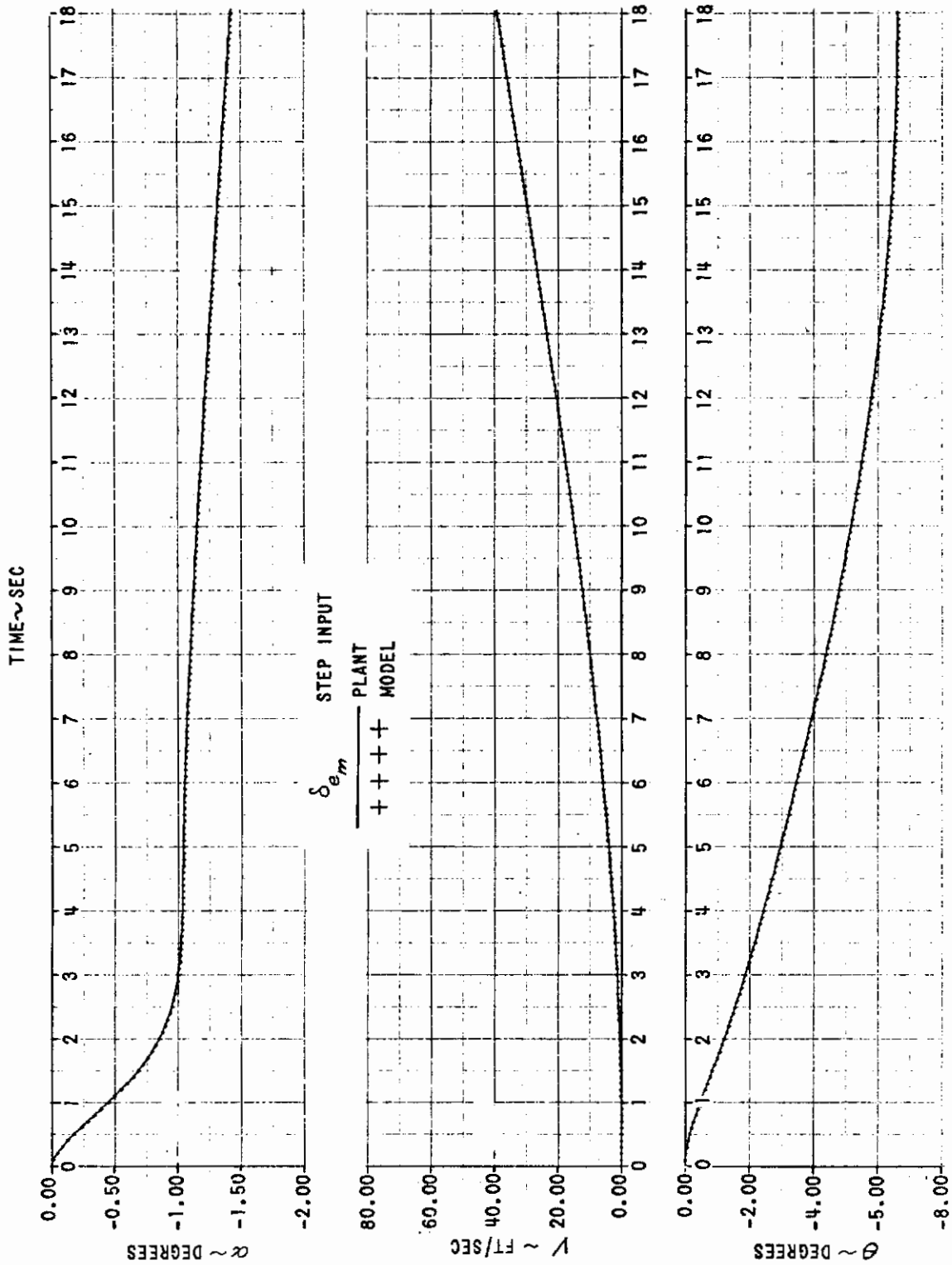

Figure 5.8a RESPONSE OF THE AIRCRAFT TO A UNIT ELEVATOR STEP INPUT

$[Q = 10I, R = I]$

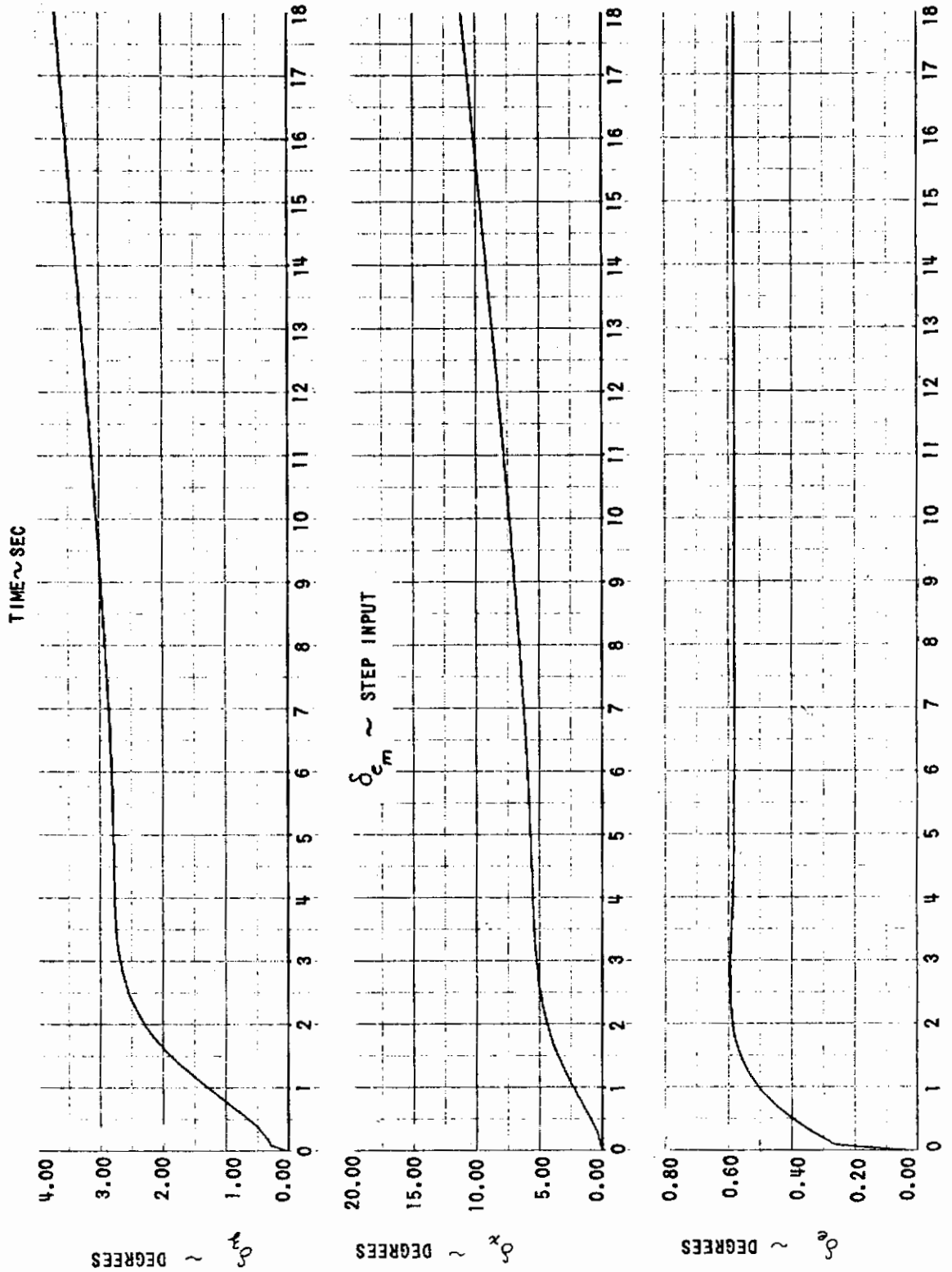

Figure 5.8b RESPONSE OF THE AIRCRAFT TO A UNIT ELEVATOR STEP INPUT

$[Q = I0I, R = I]$

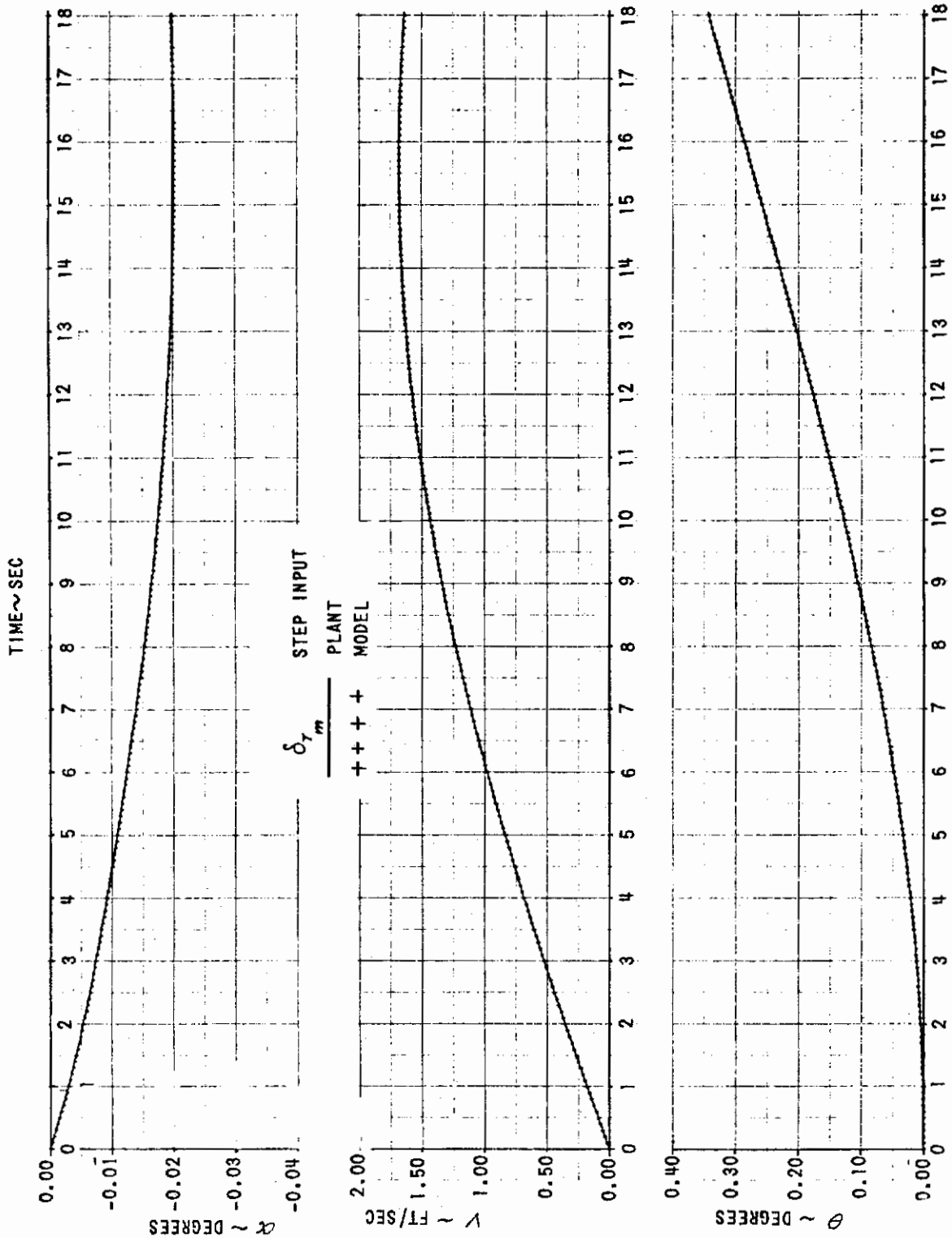

Figure 5.9a RESPONSE OF THE AIRCRAFT TO A UNIT THROTTLE STEP INPUT
$[Q = 10\,I, R = I]$

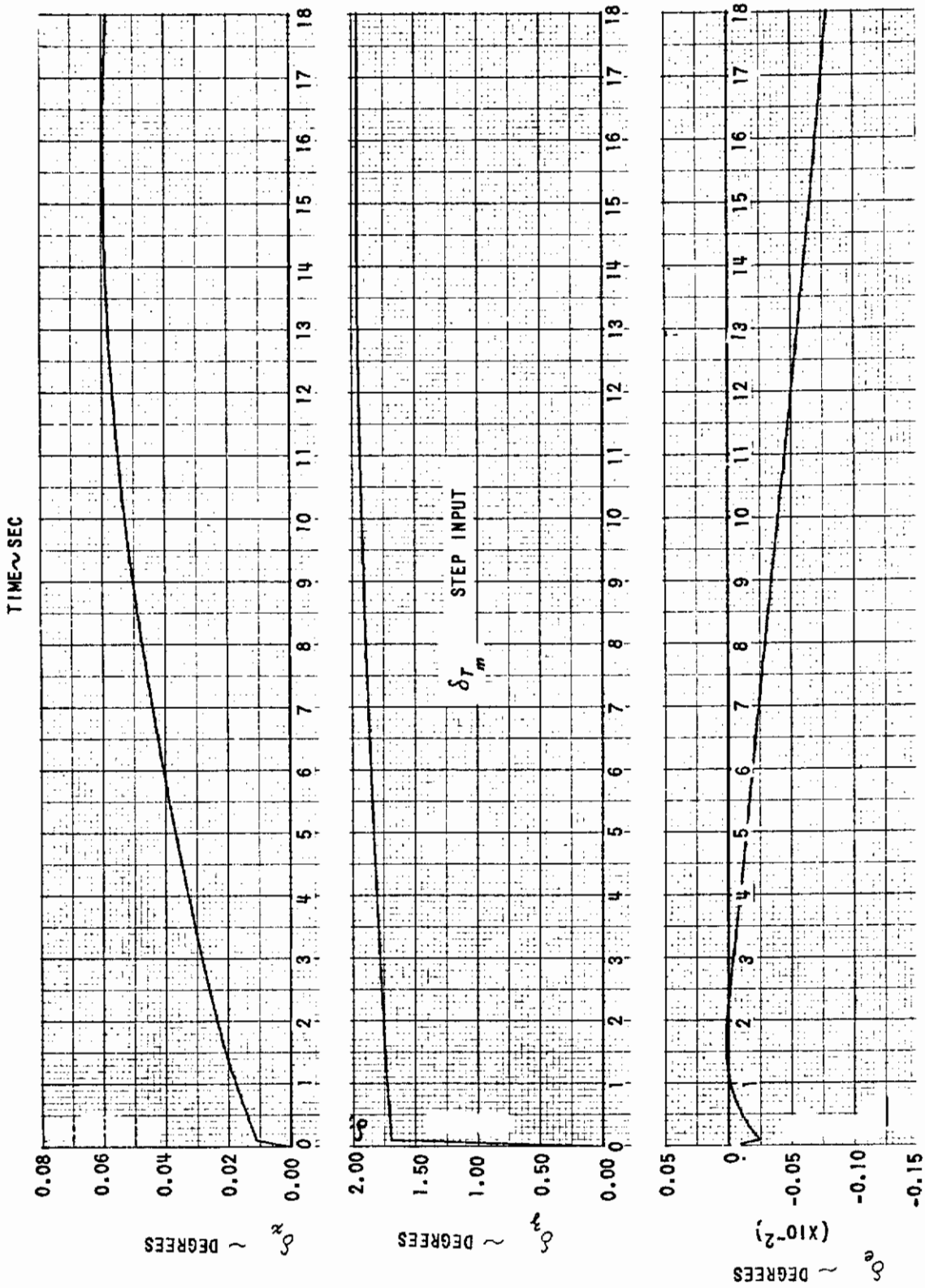

Figure 5.9b RESPONSE OF THE AIRCRAFT TO A UNIT THROTTLE STEP INPUT

$[Q=10\,I, R=I]$

$$2V = \int_0^\infty \left[z^T \mathcal{H} z + \dot{u}^T T \dot{u} \right] dt$$
$$\dot{z} = Az + B\dot{u}$$

where $z = \begin{bmatrix} x \\ \dot{x} \end{bmatrix}$; $A = \begin{bmatrix} 0 & I \\ 0 & F \end{bmatrix}$; $B = \begin{bmatrix} 0 \\ G \end{bmatrix}$

$$\mathcal{H} = \begin{bmatrix} \phi & 0 \\ 0 & 0 \end{bmatrix} \qquad (5\text{-}34)$$

These equations are in standard form in terms of z and $\dot{u}$ for which the optimal control and the matrix Riccati equation follow:

$$\dot{u} = -T^{-1} B^T P z$$
$$\mathcal{H} + A^T P + PA + \dot{P} - PBT^{-1}B^T P = 0 \qquad (5\text{-}35)$$

For the model-following problem, F, G and ϕ are substituted from Equations 5-10 and 5-17 and the optimal control is expressed as:

$$\dot{u} = -T^{-1} G_p^T \left[P_{14}^T x_p + P_{24}^T x_m + P_{34}^T u_m + P_{44} \dot{x}_p + P_{45} \dot{x}_m + P_{46} \dot{u}_m \right]$$

(a) $\dot{P}_{11} + H^T Q H - F_p^T S F_p - P_{14} G_p T^{-1} G_p^T P_{14}^T = 0$

(b) $\dot{P}_{12} - H^T Q H - P_{14} G_p T^{-1} G_p^T P_{24}^T = 0$

(c) $\dot{P}_{13} - P_{14} G_p T^{-1} G_p^T P_{34}^T = 0$

(d) $\dot{P}_{14} + P_{11} + P_{14} F_p - P_{14} G_p T^{-1} G_p^T P_{44} = 0$

(e) $\dot{P}_{15} + P_{12} + P_{15} F_m - P_{14} G_p T^{-1} G_p^T P_{45} = 0$

(f) $\dot{P}_{16} + P_{13} + P_{15} G_m + P_{16} D - P_{14} G_p T^{-1} G_p^T P_{46} = 0$

(g) $\dot{P}_{24} + P_{12}^T + P_{24} F_p - P_{24} G_p T^{-1} G_p^T P_{44} = 0$

(h) $\dot{P}_{44} + P_{14} + F_p^T P_{44} + P_{44} F_p + P_{14}^T - P_{44} G_p T^{-1} G_p^T P_{44} = 0$

(i) $\dot{P}_{45} + P_{15} + F_p^T P_{45} + P_{24}^T + P_{45} F_m - P_{44} G_p T^{-1} G_p^T P_{45} = 0$

(j) $\dot{P}_{46} + P_{16} + F_p^T P_{46} + P_{34}^T + P_{45} G_m + P_{46} D - P_{44} G_p T^{-1} G_p^T P_{46} = 0$

(k) $\dot{P}_{34} + P_{13}^T + P_{34} (F_p - G_p T^{-1} G_p^T P_{44}) = 0$

where $P = \begin{bmatrix} P_{11} \cdots P_{16} \\ P_{16}^T \cdots P_{66} \end{bmatrix}$ (5-36)

Equations (5-36 c and k) are homogeneous differential equations of P_{13} and P_{34}. The solution of these equations with a boundary condition $P_{13}(\infty) = P_{34}(\infty) = 0$ yields $P_{13}(t) = P_{34}(t) = 0$, $0 \le t \le \infty$, hence, the optimal control does not depend explicitly on u_m (depends on $\dot{u}_m$). If $R=0$, $(S=0)$, $P_{14} = P_{24}$ is a sufficient condition which satisfies 5-36a and b. This condition indicates that in the steady state ($\dot{x}_p = \dot{x}_m = \dot{u}_m = \dot{u} = 0$) the error between the plant and model outputs is zero, $x_p(\infty) = x_m(\infty)$. If $R \neq 0$ the sum of Equations 5-36a and 5-36b is:

$$-F_p^T S F_p = P_{14} G_p T^{-1} (G_p^T P_{14}^T + G_p^T P_{24}^T) \tag{5-37}$$

$-P_{14} = P_{24}$ is not a solution to Equation 5-37 and x_p is not equal to x_m in the steady state. This implies that the steady-state outputs of the plant and model are equal if and only if no quadratic control term appears in the performance index ($R=0$).

The plant A_p, B_p in formulation A is uncontrollable unless G_p is invertible. To prove this statement, we form the matrix Δ :

$$\Delta = \left[B_p, A_p B_p \cdots A_p^{2n-1} B_p \right] = \begin{bmatrix} 0 & G_p & \cdots & F_p^{2n-2} G_p \\ G_p & F_p G_p & \cdots & F_p^{2n-1} G_p \end{bmatrix} \tag{5-38}$$

where

$$A_p = \underset{2n \times 2n}{\begin{bmatrix} 0 & I \\ 0 & F_p \end{bmatrix}}, \quad B_p = \underset{2n \times r}{\begin{bmatrix} 0 \\ G_p \end{bmatrix}}$$

If G_p is $n \times n$ and invertible, the determinant of the first $2n \times 2n$ matrix of Δ can be evaluated by Gauss's algorithm (Reference 5.7) as:

$$\det \left| \Delta_1 \right| = \det \left| G_p \right| \det \left| G_p \right| \neq 0 \tag{5-39}$$

Therefore, the rank of Δ is $2n$, the plant (A_p, B_p) is controllable and the Riccati equations have a unique solution if G_p is invertible.

---

* $P_{14} = -P_{24}$ is a sufficient condition. If P_{14} is invertible, $G_p T^{-1} G_p^T P_{14}^T = -G_p T^{-1} G_p^T P_{24}^T$ is the necessary and sufficient condition which satisfies Equations 5-36a and 5-36b.

If G_p is not square, the plant (A_p, B_p) is not controllable. This statement can be verified by showing that at least two rows of the matrix Δ are identical when the actual plant is represented in phase variable form, Reference 5-6.

Formulation A is useful to demonstrate the good steady state model following of a type-one system. But since the plant is not controllable, a different formulation will be presented.

Formulation B

A different enlarged state vector z and the matrices A, B and $\mathcal{H}$ in (5-34) are redefined as:

$$z = \begin{bmatrix} u \\ x \end{bmatrix}, \quad \underset{(n+r)\times(n+r)}{A} = \begin{bmatrix} 0 & 0 \\ G & F \end{bmatrix} \begin{matrix} \} r \times n \\ \} n \times n \end{matrix}, \quad B = \begin{bmatrix} I \\ 0 \end{bmatrix} \begin{matrix} \} r \times r \\ \} n \times r \end{matrix}, \quad \mathcal{H} = \begin{bmatrix} R & 0 \\ 0 & \phi \end{bmatrix} \tag{5-40}$$

The controllability matrix in this case is given by

$$\left.\begin{aligned} \Delta &= \left[B_p, A_p B_p \cdots A_p^{n+r-1} B_p \right] = \begin{bmatrix} I & 0 & 0 & \cdots & 0 \\ 0 & G_p & F_p G_p & \cdots & F_p^{n+r-2} \end{bmatrix} \\ \text{where} \quad A_p &= \begin{bmatrix} 0 & 0 \\ G_p & F_p \end{bmatrix}; \quad B_p = \begin{bmatrix} I \\ 0 \end{bmatrix} \} r \times r \end{aligned}\right\} \tag{5-41}$$

Taking the first r columns and n linearly independent remaining columns and applying Gauss's algorithm, the $(n+r)\times(n+r)$ determinant can be evaluated as:

$$\det |\Delta_1| = \det |I| \cdot \underset{n\times n \text{ portion of}}{\det} \left[G_p, F_p G_p \cdots F_p^{n-1} G_p \right] \overset{*}{\neq} 0$$

The determinant of Δ has rank $n+r$, the plant A_p, B_p is controllable and the Riccati equations have a unique solution.

The optimal control and the matrix Riccati equations have the same form of Equation 5-35 from which:

---

*The second determinant has rank n since the actual plant G_p, F_p is controllable.

$$\dot{u} = -T^{-1}\left[P_{11}u + P_{12}x_p + P_{13}x_m + P_{14}u_m\right]$$

(a) $\dot{P}_{11} - P_{11}T^{-1}P_{11} + R + G_p^T P_{12}^T + P_{12}G_p = 0$

(b) $\dot{P}_{12} - P_{11}T^{-1}P_{12} + G_p^T P_{22} + P_{12}F_p = 0$

(c) $\dot{P}_{13} - P_{11}T^{-1}P_{13} + G_p^T P_{23} + P_{13}F_m = 0$

(d) $\dot{P}_{14} - P_{11}T^{-1}P_{14} + G_p^T P_{24} + P_{13}G_m + P_{14}D = 0$

(e) $\dot{P}_{22} - P_{12}^T T^{-1}P_{12} + H^T Q H + F_p^T P_{22} + P_{22}F_p = 0$

(f) $\dot{P}_{23} - P_{12}^T T^{-1}P_{13} - H^T Q H + F_p^T P_{23} + P_{23}F_m = 0$

(g) $\dot{P}_{24} - P_{12}^T T^{-1}P_{14} + F_p^T P_{24} + P_{23}G_m + P_{24}D = 0$

(5-42)

where $P = \begin{bmatrix} P_{11} & \cdots & P_{14} \\ P_{14}^T & \cdots & P_{44} \end{bmatrix}$

Since a term $P_{ij}(x_p - x_m)$ does not explicitly appear in the control law, the quality of the model following provided by a type-one system is not clear in Formulation B. The implementation of a type-one system should be based on the block diagram in Figure 5.10, associated with Formulation B.

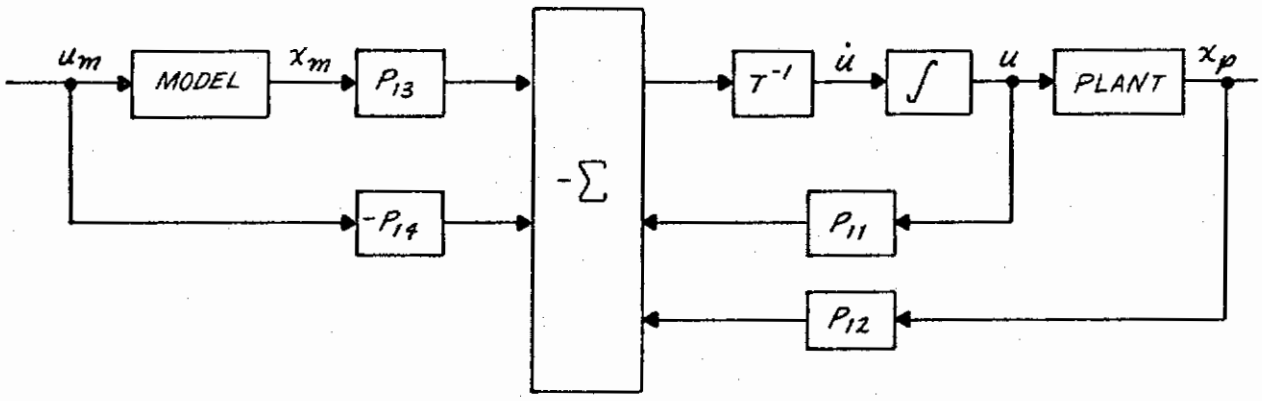

Figure 5.10 BLOCK DIAGRAM OF A TYPE-ONE MODEL-FOLLOWING SYSTEM (FORMULATION B)

P_{14} and P_{24} in Equation 5-42 depend on the companion matrix of the model input, D. To make the optimal control insensitive to the input, $P_{14}D$ and $P_{24}D$ are eliminated by introducing the performance index:

$$2V = \int_0^\infty \left[(x_p - x_m)^T H^T Q H (x_p - x_m) + \dot{u}^T T \dot{u} - 2 u^T \rho_{14} \dot{u}_m - 2 (x_p - x_m)^T \rho_{24} \dot{u}_m \right] dt$$

or by $$2V = \int_0^\infty \left[x^T \mathcal{R} x + \dot{u}^T T \dot{u} \right] dt$$

where

$$\mathcal{R} = \begin{bmatrix} 0 & 0 & 0 & \rho_{14} D \\ 0 & H^T Q H & -H^T Q H & \rho_{24} D \\ 0 & -H^T Q H & H^T Q H & -\rho_{24} D \\ D^T \rho_{14}^T & D^T \rho_{24}^T & -D^T \rho_{24}^T & 0 \end{bmatrix} \qquad (5\text{-}43)$$

In Reference 5.6, it is shown that forcing ρ_{16} and ρ_{46} to zero in Formulation A is equivalent to eliminating the terms $\rho_{14} D$, $\rho_{24} D$ in Formulation B. This is a matter of minor interest omitted from the contents of this report.

The step response of the second-order type-one system is shown in Figure 5.11. This figure shows an improvement in the steady state model following with a tradeoff in high frequency performance.

5.9 IDEAL TYPE-ONE MODEL-FOLLOWING SYSTEM

The ideal type-zero system provides perfect model following for the flight condition for which F_p and G_p in the differential equations of the plant are the same as those used to compute the gains. If F_p and G_p deviate from these values for different flight conditions, the output of the plant will also deviate from the perfect model-following case, Reference 5.6.

In some cases, it might be desirable to provide perfect model following at a given flight condition and perfect steady state model following (or near perfect model following during the low frequency motion of the aircraft) at any other flight condition. This leads to the investigation of an ideal type-one system discussed below.

Starting with Formulation A and the performance index in Equation 5-36 where $\mathcal{R}$ is given by:

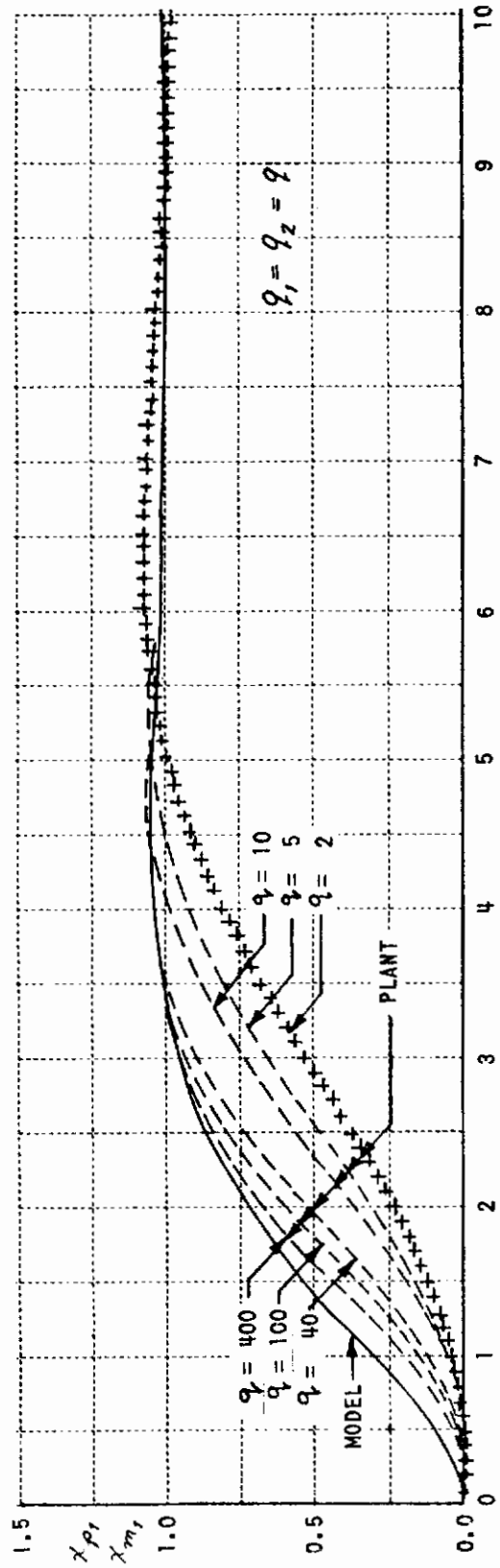

Figure 5.11 STEP RESPONSE OF A TYPE-ONE SYSTEM

$$\mathcal{H} = \left[\begin{array}{cccccc} H^T Q H & -H^T Q H & 0 & 0 & 0 & 0 \\ -H^T Q H & H^T Q H & 0 & 0 & 0 & 0 \\ 0 & 0 & 0 & 0 & 0 & 0 \\ 0 & 0 & 0 & 0 & L & 0 \\ 0 & 0 & 0 & L^T & 0 & 0 \\ 0 & 0 & 0 & 0 & 0 & 0 \end{array}\right] \qquad (5\text{-}44)$$

$$-L = (\bar{P}_{44} + \bar{P}_{45}) F_m + F_p^T (\bar{P}_{44} + \bar{P}_{45})^*$$

and substituting the optimal control in Equation 5-36 into the differential equations of the plant yields the conditions for perfect model following:

$$\left.\begin{array}{l} G_p T^{-1} G_p \bar{P}_{46} = -G_m \\ G_p T^{-1} G_p^T (\bar{P}_{44} + \bar{P}_{45}) = F_p F_m \end{array}\right\} \qquad (5\text{-}45)$$

Because of the inability to solve the Riccati equations of Formulation A the optimal control is expressed in terms of the Riccati matrices of Formulation B as:**

$$G_p \dot{u} = -G_p T^{-1}(P_{11} u + P_{12} x_p) - \left\{ G_p \Gamma \Omega H (F_p^{-1} F_m - I) - G_p T^{-1} P_{12} F_p^{-1} F_m + (F_p - F_m) F_m \right\} x_m - \left\{ G_p \Gamma \Omega H F_p^{-1} G_m - G_m D + (F_p - F_m) G_m - G_p T^{-1} P_{12} F_p^{-1} G_m \right\} u_m \qquad (5\text{-}46)$$

where $\Gamma \Gamma^T = T^{-1}; \quad \Omega^T \Omega = Q$

This expression provides a means for solving the problem on a digital computer. The system gains required for the implementation of the control law cannot be determined from Equation 5-46 unless G_p is invertible. Therefore, it is unlikely that a general solution for a type-one model-following system can be formulated.

---

* To differentiate between the two formulations the P's associated with Formulation A are denoted by $\bar{P}$

** This expression is valid if F_p^{-1} exists, that is, if the plant has no poles at the origin. See Appendix II (Section 5.16) for the derivation.

5.10 SENSITIVITY OF THE PLANT OUTPUT TO VARIATIONS IN THE PARAMETERS OF THE PLANT

The primary need for using model following arises from the uncertainty associated with the parameters of the plant. Having developed an ideal system which provides perfect model following at any gain, the sensitivity of the plant output to variations in the parameters of the plant is investigated next.

For a type-zero system, the gains K_p , K_m and K_v are computed for a given flight condition for which the parameters of the plant F_p and G_p are known. The optimal control is obtained from:

$$u_o = -\left[K_p x_p + K_m x_m + K_v u_m\right] \tag{5-47}$$

where the gains K_p , K_m and K_v are kept constant while F_p and G_p are allowed to change for various flight conditions. The output of the plant at any instant is given by the solution of:

$$\left.\begin{aligned} \dot{x}_p - F_p x_p + G_p\left[K_p x_p + K_m x_m + K_v u_m\right] &= 0 \\ \dot{x}_m - F_m x_m - G_m u_m &= 0 \end{aligned}\right\} \tag{5-48}$$

For the purpose of investigating the sensitivity problem, it is reasonable to simplify the problem by considering the steady state deviation of the plant output caused by variations in F_p and G_p . Setting $\dot{x}_p = 0$ in Equation 5-48, taking the variation of x_p and neglecting the products of the variations yields:

$$\Delta x_p = \left[G_p K_p - F_p\right]^{-1}\left\{\Delta F_p - \Delta G_p\left[G_p^T G_p\right]^{-1} G_p^T F_p\right\} x_p \tag{5-49}$$

$(G_p K_p - F_p)$ has an inverse since it is the closed loop of an optimal system (no poles at the origin). This expression depends on the parameters of the closed-loop plant, F_p , G_p and K_p . Therefore, for the same feedback gain, K_p , the same relative deviation in x_p is obtained regardless of whether the nominal or the ideal system is used for model following. Also, the effect of high feedback gains in reducing the sensitivity is noted from this expression. This idea is not new; it has been the primary objective in the design of model following by conventional techniques.

For the first-order example the sensitivities reduce to:

$$\frac{b_\rho}{a_\rho}\left(\frac{1}{x_\rho}\frac{\partial x_\rho}{\partial b_\rho}\right) = -\left(\frac{1}{x_\rho}\frac{\partial x_\rho}{\partial a_\rho}\right) = \frac{1}{b_\rho K_\rho + a_\rho}$$

With the ideal model-following system, the need for high feedback gains arises from the sensitivity problem and not from the requirement for good model following. Hence the design of a perfect model-following system reduces to the following steps:

1) Determine the highest feedback gains which provide a stable optimal system.

2) Compute the feedforward gains for perfect model following.

5.11 DETERMINATION OF THE MAXIMUM FEEDBACK GAINS

The first step stated above implies that the highest possible gains which are computed on the basis of optimal control theory should be used in order to arrive at a stable and optimal system.

The maximum gains are determined from the physical limitations of the control effectiveness due to actuator gain limits, sensor noise, etc. If the maximum gains are used to compute H^TQH, this matrix might be negative definite, thus violating the conditions for a stable minimum. Therefore a constraint is imposed upon the gains such that H^TQH is at least non-negative definite.

The ability to determine H^TQH from a given set of maximum feedback gains is a problem of considerable importance in optimal control theory not restricted to the application of model following.

The inability to translate a constraint on K as a constraint on ρ (G_ρ is normally noninvertible) and the requirement for a nonnegative definite H^TQH suggests an iteration scheme which starts with diagonal Q and R whose elements are positive.

The elements of R can be selected such that:

$$R = \begin{bmatrix} r_1 & & 0 \\ & \ddots & \\ 0 & & r_m \end{bmatrix}; \quad r_1 = 1; \quad r_i = \left(\frac{u_{1\,max}}{u_{i\,max}}\right)^2 \quad i = 2, 3, m \qquad (5\text{-}50)$$

where $u_{i_{max}}$ is the maximum excursion of the control variable u_i . With this selection, it is conceivable that the percent deflection ($u_i / u_{i_{max}}$) of each control variable will be nearly equal, thus providing a uniform utilization of the control effort.

The elements of Q are systematically incremented until the feedback gains K_{ij} come as close as possible to the maximum feedback gains $K_{m_{ij}}$.

5.12 CONCLUDING REMARKS

Several control systems are developed for the model following of a servo problem: modified system without feedforward from the model input, modified system with feedforward from the model input, ideal type-zero system, type-one system, and ideal type-one system.

The theoretical development leading to these systems provides some understanding of the effect of various terms in the performance index on the response of the system and on the quality of the model following. The result of this investigation can be summarized as follows:

1. A feedforward from the model input can improve the quality of model following.
2. An optimal type-zero system generally provides better dynamic model following than an optimal type-one system. A type-one system is desirable for low frequency applications where the system gains are limited.
3. The ideal type-zero system provides perfect model following at any gain and is applicable to systems which satisfy the conditions stated in Section 5.7. The requirement for high feedback gains for the alleviation of the sensitivity problem compounded with the ability to design an ideal system for model following leads to the investigation of an important problem in optimal control theory stated as "Given a set of maximum feedback gains, what are the highest feedback gains which provide a stable optimal system".

4. The ideal type-one system is somewhat restricted to plants with equal number of state and control variables (G_p invertible). This system guarantees zero steady state error between the outputs of the plant and model in the entire flight envelope. However, the dynamic response of the system has the drawbacks of a type-one system.

5. Optimal control theory is a mathematical tool which generates an optimal control strategy that minimizes a given performance index. The main problem is to formulate a performance index which adequately describes the requirements of the control system. For the model-following problem, it seems logical from an engineering point of view to use the performance index in Equation 5-3. Yet the analysis above indicates that additional terms such as those in Equation 5-23 are needed for an ideal control system.

5.13 REFERENCES

5.1 Tyler, J.S., Jr.: "The Characteristics of Model-Following Systems as Synthesized by Optimal Control," IEEE Transactions on Automatic Control, October 1965.

5.2 Rynaski, E.G., Whitbeck, R.F.: The Theory and Application of Linear Optimal Control, CAL Report No. 1H-1943-F-1, October 1965, (Also AFFDL-TR-65-28).

5.3 Rynaski, E.G., Whitbeck, R.F., Wierwille, W.W.: Optimal Control of a Flexible Launch Vehicle, CAL Report No. 1H-2089-F-1, July 1966.

5.4 Bellman, R.: Introduction to Matrix Analysis. McGraw Hill Book Company, New York, 1960.

5.5 Kalman, R.E., Englar, T.: Fundamental Study of Adaptive Control Systems, Vol. I and II, ASD-TR-61-27, March 1961 and March 1962.

5.6. Asseo, S.J.: Application of the Model Following Concept to a Servo Problem, TIFS Memo No. 64, Cornell Aeronautical Laboratory, Inc., April 1967.

5.7 Gantmacher, F.R.: The Theory of Matrices, Vol. I, Chelsea Publishing Co., New York, 1960.

5.8 Clark, D.C., Kroll, J.: General Purpose Airborne Simulator-Conceptual Design Report, CAL Report No. BM-1950-F-1, Contract No. NAS4-607, July 1965.

5.14 NOMENCLATURE FOR SECTION V

t_f Upper limit of the Performance Index

$\mathcal{V}$ Performance Index

Vectors

u Control vector - input to the plant

u_m Model input vector

x State vector associated with the differential equations of the system

y Output vector

z Enlarged state vector, defined in respective equations

η Fictitious state associated with the model

Matrices

D Companion matrix of the model input

F Matrix defining the interaction of the state variables

G Matrix defining the effect of control on the state rates

H Matrix transformation on x that defines the output y

I Identity matrix

K Matrix of gains

L Model system matrix

Q Matrix of weighting factors associated with the output vector

R Matrix of weighting factors associated with the control vector

P Matrix of Riccati coefficients

T Matrix of weighting factors associated with the control rate vector

$A, B, M, N, S, W, \bar{G}_p, \bar{G}_m, \mathcal{H}, \Gamma, \Omega, \phi, \Psi, \xi$ - Matrices defined in respective equations.

Dimensions

n Dimension of the state x_p or x_m

r Dimension of the control u

m Dimension of the model input u_m

Subscripts

p Plant

m Model

v Input to the model

ss Steady state

Superscript $(\quad)^T$ - Transpose

Operator

$|A|$ Determinant of Matrix A

5.15 APPENDIX I: EXAMPLES

5.15.1 Step Response of a First-Order System

For a first-order system described by:

$$\left.\begin{aligned} \dot{x}_p &= -a_p x_p + b_p u \\ \dot{x}_m &= -a_m x_m + b_m u_m \\ \dot{u}_m &= 0 \end{aligned}\right\} \qquad (5\text{-}51)$$

The optimal control for the nominal system is given by:

where:

$$\left.\begin{aligned} u_o &= -b_p \left[P_{11} x_p + P_{12} x_m + P_{13} u_m \right] \\ P_{11} &= \frac{-a_p + \alpha}{b_p^2} \\ P_{12} &= -\frac{q}{a_m + \alpha} \\ P_{13} &= -\frac{b_m q}{\alpha (a_m + \alpha)} \\ \alpha &= \sqrt{a_p^2 + q b_p^2} \end{aligned}\right\} \qquad (5\text{-}52)$$

The optimal control for the modified system without feedforward from the model input is given by:

where

$$\left.\begin{aligned} u_o &= -b_p P_{11} x_p - b_p P_{12} x_m \\ P_{12} &= -\frac{q}{a_m + a_p + b_p^2 P_{11}} \end{aligned}\right\} \qquad (5\text{-}53)$$

and where P_{11} is obtained from the roots of

$$\dot{P}_{11} + q - 2a_p P_{11} - b_p^2 P_{11}^2 - \frac{b_m q}{a_m + a_p + b_p^2 P_{11}} = 0 \qquad (5\text{-}54)$$

The Riccati equation in Equation 5-54 has two stable roots, an unstable root and a point at which $\dot{P}_{11} = \infty$.

The steady state outputs of the plant for the nominal and the modified system are:

$$\left.\begin{aligned} &\text{Nominal} \qquad x_{p_{ss_n}} = \frac{b_m b_p^2 q u_m}{a_m(a_p^2 + q b_p^2)} \\ &\text{Modified} \qquad x_{p_{ss_m}} = \frac{b_n b_p^2 q u_m}{a_n(a_p + b_p^2 P_{11})(a_p + a_n + b_p^2 P_{11})} \end{aligned}\right\} \qquad (5\text{-}55)$$

For a given feedback gain P_{11} q is computed from Equation 5-52 for the nominal system and from Equation 5-54 for the modified system. The computed values of $x_{p_{ss_m}}$, $x_{p_{ss_n}}$, q and P_{12} are plotted in Figure 5.1, and the results are discussed in Section 5.5.

5.15.2 Second-Order System

The block diagram of a second-order system is shown in Figure 5-12.

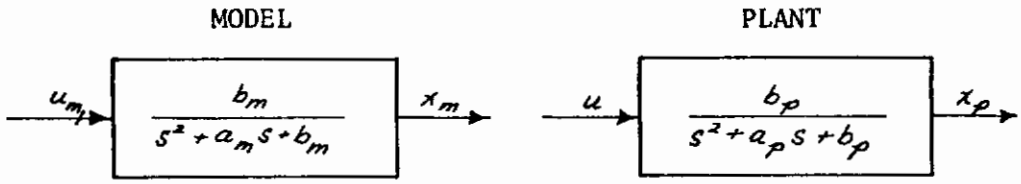

Figure 5.12 BLOCK DIAGRAM OF A SECOND-ORDER SYSTEM

The dynamics of the system are governed by:

$$\left.\begin{aligned} \begin{bmatrix} \dot{x}_{p_1} \\ \dot{x}_{p_2} \end{bmatrix} &= \begin{bmatrix} 0 & 1 \\ -b_p & -a_p \end{bmatrix} \begin{bmatrix} x_{p_1} \\ x_{p_2} \end{bmatrix} + \begin{bmatrix} 0 \\ b_p \end{bmatrix} u \\ \begin{bmatrix} \dot{x}_{m_1} \\ \dot{x}_{m_2} \end{bmatrix} &= \begin{bmatrix} 0 & 1 \\ b_m & -a_m \end{bmatrix} \begin{bmatrix} x_{m_1} \\ x_{m_2} \end{bmatrix} + \begin{bmatrix} 0 & 0 \\ b_m & 0 \end{bmatrix} \begin{bmatrix} u_{m_1} \\ u_{m_2} \end{bmatrix} \\ \begin{bmatrix} \dot{u}_{m_1} \\ \dot{u}_{m_2} \end{bmatrix} &= \begin{bmatrix} 0 & \alpha \\ \beta & 0 \end{bmatrix} \begin{bmatrix} u_{m_1} \\ u_{m_2} \end{bmatrix} \\ H = I, \quad R = 1, \quad Q &= \begin{bmatrix} q_1 & 0 \\ 0 & q_2 \end{bmatrix} \end{aligned}\right\} \qquad (5\text{-}56)$$

A step input is described by $\alpha = \beta = u_{m_2}(t) = 0$, $u_{m_1}(t) = u_{m_{10}}$ and a sinusoidal input by $\alpha = -\beta = \omega$, $u_{m_1}(t) = \sin \omega t$.

5.15.3 Application of Perfect Model Following to an Aircraft Control Problem

The linearized three-degree-of-freedom longitudinal equations of the aircraft are governed by the following vector differential equations:

Dynamics of the aircraft (Plant):

$$\begin{bmatrix} \dot{\theta}_p \\ \ddot{\theta}_p \\ \dot{V}_p \\ \dot{\alpha}_p \end{bmatrix} = \begin{bmatrix} f_{11} & f_{12} & f_{13} & f_{14} \\ 1 & 0 & 0 & 0 \\ 0 & f_{32} & f_{33} & f_{34} \\ 1 & f_{42} & f_{43} & f_{44} \end{bmatrix} \begin{bmatrix} \theta_p \\ \dot{\theta}_p \\ V_p \\ \alpha_p \end{bmatrix} + \begin{bmatrix} g_{11} & g_{12} & g_{13} \\ 0 & 0 & 0 \\ 0 & g_{32} & 0 \\ g_{41} & g_{42} & g_{43} \end{bmatrix} \begin{bmatrix} \delta_e \\ \delta_x \\ \delta_y \end{bmatrix} \tag{5-57}$$

Dynamics of the model aircraft:

$$\begin{bmatrix} \dot{\theta}_m \\ \ddot{\theta}_m \\ \dot{V}_m \\ \dot{\alpha}_m \end{bmatrix} = \begin{bmatrix} \ell_{11} & \ell_{12} & \ell_{13} & \ell_{14} \\ 1 & 0 & 0 & 0 \\ \ell_{31} & \ell_{32} & \ell_{33} & \ell_{34} \\ \ell_{41} & \ell_{42} & \ell_{43} & \ell_{44} \end{bmatrix} \begin{bmatrix} \theta_m \\ \dot{\theta}_m \\ V_m \\ \alpha_m \end{bmatrix} + \begin{bmatrix} h_{11} & h_{12} \\ 0 & 0 \\ h_{31} & h_{32} \\ h_{41} & h_{42} \end{bmatrix} \begin{bmatrix} \delta_{e_m} \\ \delta_{T_m} \end{bmatrix} \tag{5-58}$$

Making use of the fact that the second rows in G_p and G_m are zero, the feed-forward gains are expressed in terms of the feedback gains as

$$\left.\begin{aligned} K_m &= -R^{-1} G_p^T P_{12} = \left[\bar{G}_p\right]^{-1} \mathcal{H} + K_p \\ K_v &= -R^{-1} G_p^T P_{13} = \left[\bar{G}_p\right]^{-1} \bar{G}_m \\ K_p &= R^{-1} G_p^T P_{11} \end{aligned}\right\} \tag{5-59}$$

where:

$$\left.\begin{aligned} \bar{G}_p &= \begin{bmatrix} g_{11} & g_{12} & g_{13} \\ 0 & g_{32} & 0 \\ g_{41} & g_{42} & g_{43} \end{bmatrix} ; \quad \bar{G}_m = \begin{bmatrix} h_{11} & h_{12} \\ h_{31} & h_{32} \\ h_{41} & h_{42} \end{bmatrix} \\ \mathcal{H} &= \begin{bmatrix} \ell_{11} - f_{11} & \ell_{12} - f_{12} & \ell_{13} - f_{13} & \ell_{14} - f_{14} \\ \ell_{31} & \ell_{32} - f_{32} & \ell_{33} - f_{33} & \ell_{34} - f_{34} \\ \ell_{41} - 1 & \ell_{42} - f_{42} & \ell_{43} - f_{43} & \ell_{44} - f_{44} \end{bmatrix} \end{aligned}\right\} \tag{5-60}$$

In the computer simulation of this problem, provision was made to follow the motion of the model aircraft with respect to a transformed set of longitudinal axes centered at the pilot's station. The results are plotted in Figures 5.8 and 5.9.

5.16 APPENDIX II: IDEAL TYPE-ONE SYSTEM

From Equations 5-36a, b, d, and g:

$$\left.\begin{aligned} \rho_{14} &= -\rho_{24} \\ \rho_{11} &= -\rho_{12} = -\rho_{12}^T \end{aligned}\right\} \tag{5-61}$$

Substituting Equation 5-45 into 5-36f for a step, $D = 0$:

$$\rho_{15} = -\rho_{14} \tag{5-62}$$

Combining Equations 5-62, 5-36h and 5-36i yields $\angle$ in Equation 5-44. The following relationship exists between ρ's of the two formulations:

Formulation A		Formulation B
ρ_{11}	=	$G_\rho^T \bar{\rho}_{44} G_\rho$
ρ_{12}	=	$G_\rho^T (\bar{\rho}_{14}^T + \bar{\rho}_{44} F_\rho)$
ρ_{13}	=	$G_\rho^T (\bar{\rho}_{24}^T + \bar{\rho}_{45} F_m)$
ρ_{14}	=	$G_\rho^T (\bar{\rho}_{34}^T + \bar{\rho}_{45} G_m + \bar{\rho}_{46} D)$

(5-63)

Using the condition for perfect model following in Equation 5-45 and the relationship in Equation 5-63,

$$\begin{aligned} G_\rho T^{-1} \rho_{13} &= G_\rho \Gamma \Omega H (F_\rho^{-1} F_m - I) - G_\rho T^{-1} \rho_{12} F_\rho^{-1} F_m + (F_\rho - F_m) F_m \\ G_\rho T^{-1} \rho_{14} &= G_\rho \Gamma \Omega H F_\rho^{-1} G_m - G_m D + (F_\rho - F_m) G_m - G_\rho T^{-1} \rho_{12} F_\rho^{-1} G_m \end{aligned} \tag{5-64}$$

where $\Gamma \Gamma^T = T^{-1}$

$\Omega^T \Omega = Q$

and substituting into the optimal control expression in Equation 5-42 yields Equation 5-46.

SECTION VI

MECHANICAL AND STRUCTURAL DESIGN

6.1 INTRODUCTION

The conversion of a C-131B airplane into the Total In-Flight Simulator involves many mechanical and structural design tasks. These fall into a number of general groups according to their basic purposes. The tasks, which will be described in greater detail subsequently, may therefore be grouped in the following manner.

6.1.1 Simulation of the Pilot's Environment

A major objective of the TIFS program is to make accurate simulation of different cockpits possible. This will be achieved through use of various interchangeable assemblies or by provision for change or adjustment within those assemblies (Section 6.2).

6.1.2 Simulation of Airplane Behavior and Cockpit Motions

This task involves the fitting of positioning servos to the elevator, rudder, and aileron surfaces. It also involves new aileron-type flaps outboard of the nacelles, movable vertical surfaces on the wings and servos on the engine power controls (Section 6.3).

6.1.3 Installation of the Electronic Control System

Provision has to be made for two engineer's consoles, computers, electronic racks, electrical power supply racks, sensor installations, recording oscillographs, a strip-chart recorder and other units associated with the electronic control system (Section 6.4).

6.1.4 Provision of Hydraulic Power for TIFS

A separate hydraulic power supply system is to be installed for TIFS in addition to the existing ship's hydraulic system. The only connection between the TIFS system and the existing ship's system will be at the outboard flaps which may be operated from either system (Section 6.5).

6.1.5 Provision of Seats and Emergency Equipment for the Maximum TIFS Crew

The largest crew which will be carried in the TIFS airplane will consist of two safety pilots, two evaluation pilots, two test engineers and four additional persons such as the aircraft crew chief, other evaluation pilots and observers. Adequate seating and equipment will be provided for this size of crew (Section 6.6).

6.1.6 Conversion of C-131B to C-131H Specification

Although the actual conversion is not a part of the TIFS contract between the USAF and CAL a very close design liaison in certain areas is required between the USAF, CAL, Allison Division GMC and Pacific Airmotive Corp. (Section 6.7).

6.1.7 Analyses and Computations

A considerable amount of structural analysis will be required for the TIFS modifications as well as computation of weight and balance (Section 6.8).

6.2 SIMULATION OF THE PILOT'S ENVIRONMENT

Under the present contract, cockpits simulating the Boeing SST and a generalized USAF AMSA are being designed. The major assemblies or modifications required to reproduce true pilot's environment of these two aircraft are shown in Figure 6.1.

6.2.1 C-131B Fuselage Nose Modification

The forward end of the C-131B fuselage is to be modified considerably to provide support and aerodynamic fairing for the simulation cockpit and to provide an access tunnel from the cabin to the simulation cockpit.

6.2.1.1 Bulkhead at Station 6.5

A new bulkhead at this point forms the forward end of the nose wheel box. This bulkhead contains three large openings: a center opening for an in-flight emergency exit; a left hand opening, normally covered by a door which provides access into the fuselage structure, and a right hand opening

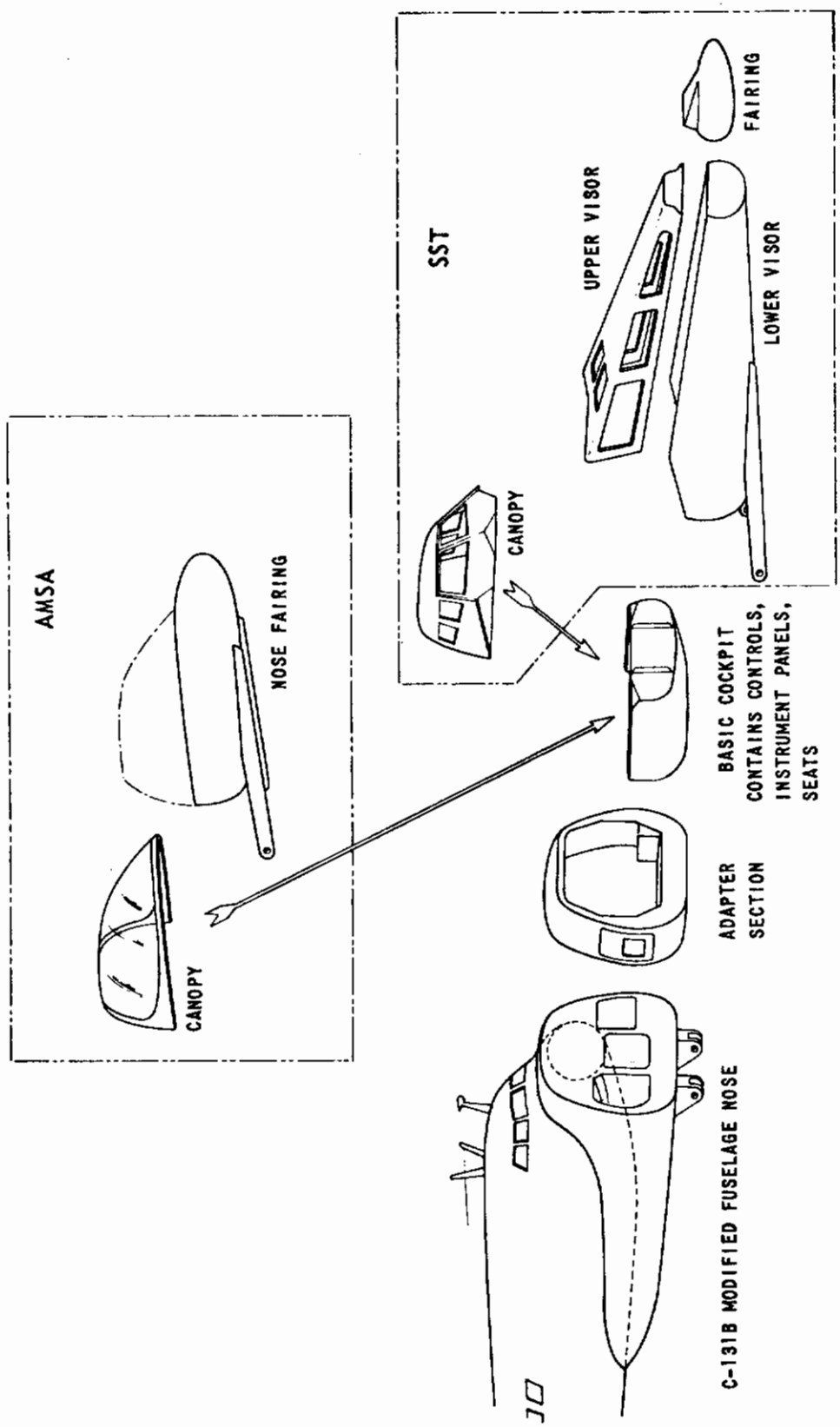

Figure 6.1 PROVISION OF TRUE ENVIRONMENT FOR PILOTS

which is the forward end of the access tunnel from the cabin. The aft face of the bulkhead structure is at station 9.0. A jacking point is incorporated in the bottom center of the bulkhead at station 7.75.

6.2.1.2 Fuselage Shape

The shape of the modified fuselage is a constant section from station 6.5 to station 42.0. It becomes asymmetrical about the center line of the aircraft aft of station 42.0. The asymmetry is due to the position of the main entrance doorway between stations 140.0 and 176.5 on the left side of the cabin and the access tunnel whose entrance from the cabin is between the same stations but on the right side. It was deemed undesirable to build a fairing over the door opening because of the way in which the door and stairway open.

6.2.1.3 Frame Shapes

Providing an access tunnel requires that a portion of each fuselage frame from stations 26.0 to 158.25 inclusive has to be cut away and a new piece of frame added on (see Figure 6.2). When the cabin is pressurized, the asymmetric shape of the frame modification introduces large bending moments in addition to the effect of cutting out a part of the frame. Where a cutout already exists, such as at the door opening between frames 140.00 and 176.50, considerable reinforcement of the existing frame becomes necessary.

6.2.1.4 Sound Proofing

Noise and vibration levels which are experienced in the Allison-engined C-131H are such that particular attention must be given to soundproofing in the cabin tunnel entry area in order to minimize transmission of noise to the simulation cockpit. Sound deadening material will be applied to the inside of the fuselage skin in the forward areas. The sides and upper part of the tunnel wall are to be composed of a soft perforated plastic material wherever possible to attenuate low frequency noise generated by the propellers.

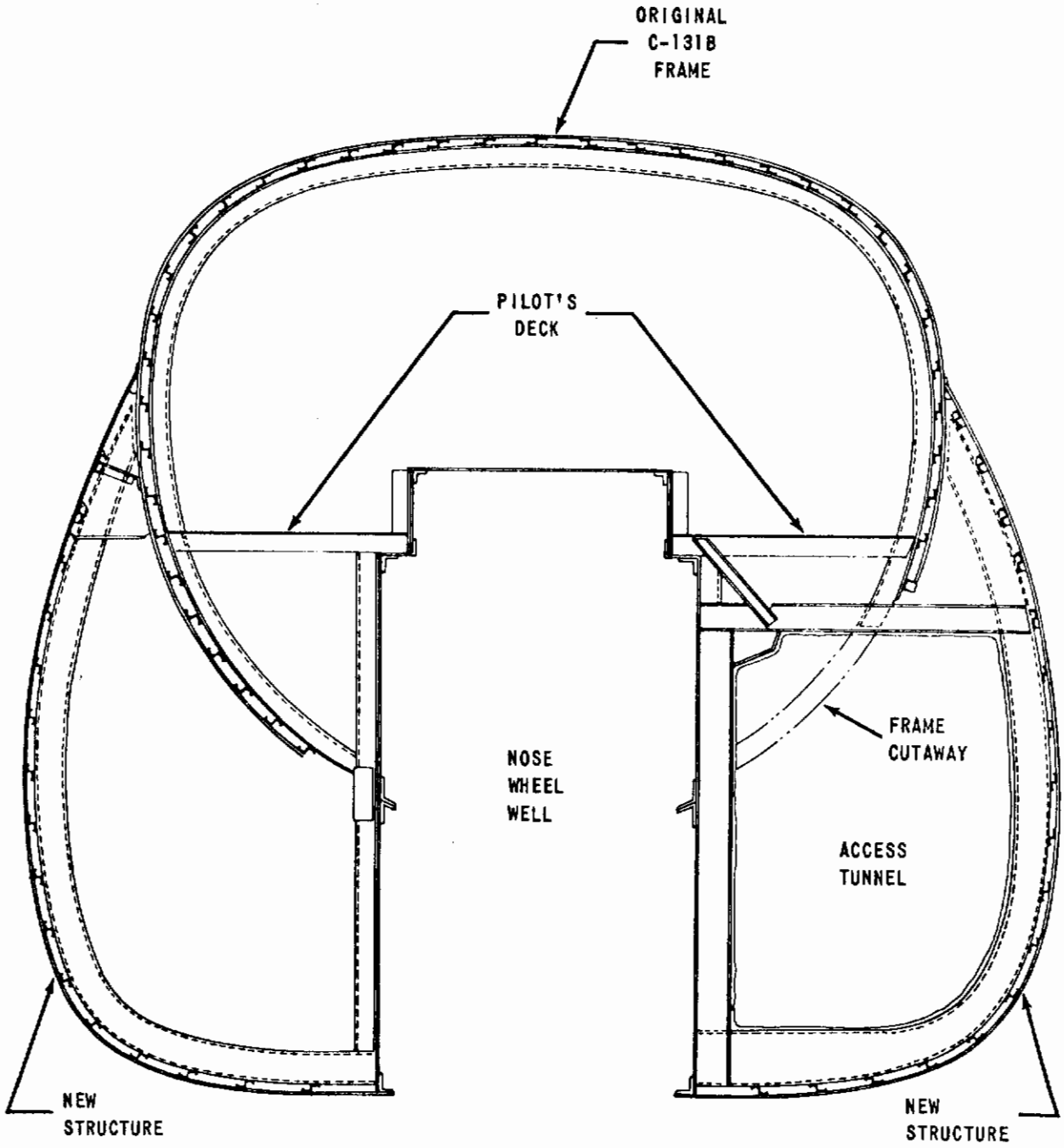

FRAME AT STA 42.0 VIEWED LOOKING FORWARD

Figure 6.2 FRAME MODIFICATION

6.2.1.5 Miscellaneous Changes

Reconstruction of the forward end of the fuselage entails a number of modifications which are not structural. The elevator control system has been modified between stations 92.0 and 227.0 to clear the tunnel entrance. The linkage to the right hand brake cylinder has been modified to clear the top of the tunnel. Main and emergency inverters have been relocated. Items which have to be repositioned include the oxygen filler and gauge in the right hand wheel well wall; cabin pressure lines between stations 140 and 176; all electrical cables on the right hand side of the nose under the pilot's floor from station 9.0 to 176; hot air pipes on the right hand side of the cockpit; hydraulic reservoir drain at station 89; and cabin pressure static ports at station 63. The nose wheel undercarriage doors have been removed.

6.2.2 Adapter Section

This unit is essentially a large spacer for the forward cockpit section (see Figure 6.1); it provides space for movement behind the pilots' seats. But the reason for incorporating the adapter section as a separate bolt-on assembly is to make it possible to achieve a gross change in cockpit and nose attitude relative to the aircraft water line datum by substituting another adapter section if required (see Figure 6.3). The adapter section is a simple structure with two frames and a double skin. The inner skin is the pressurization boundary and is riveted. The outer skin is detachable for access to the bolts which attach the adapter section to bulkhead 6.5 and to the basic cockpit and canopy assemblies. A standard C-131B ground emergency window exit is incorporated in the right hand side.

6.2.3 Basic Cockpit

This unit, which forms the lower and major part of the simulation cockpit, is illustrated in Figure 6.4. It will contain dual sets of pilot's controls with variable artificial feel servos, seats, instrument panels, center console and other units. The pilot's seat center width may be varied by moving servo packages and seat rails sideways to alternative positions. The AMSA configuration, for example, requires that the seats be eighteen inches

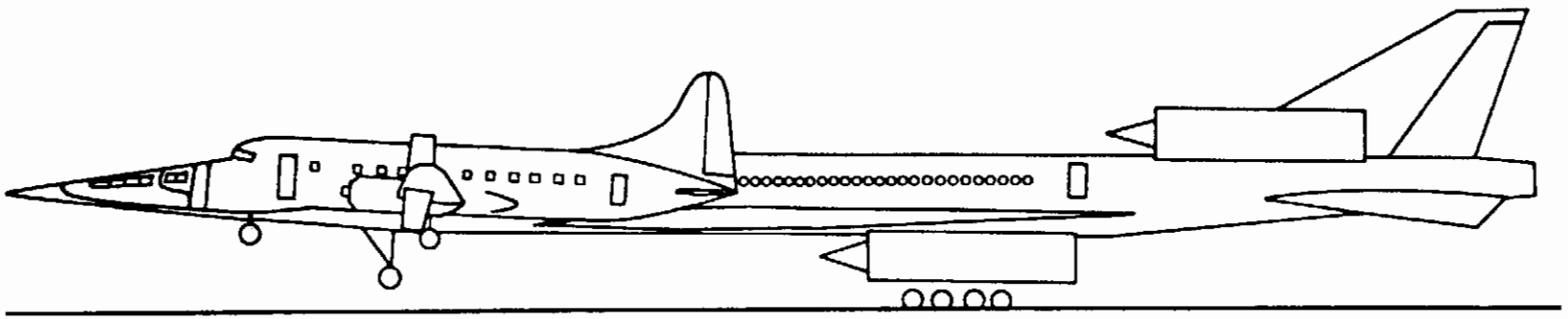

(a) NORMAL LANDING - WINGS FORWARD

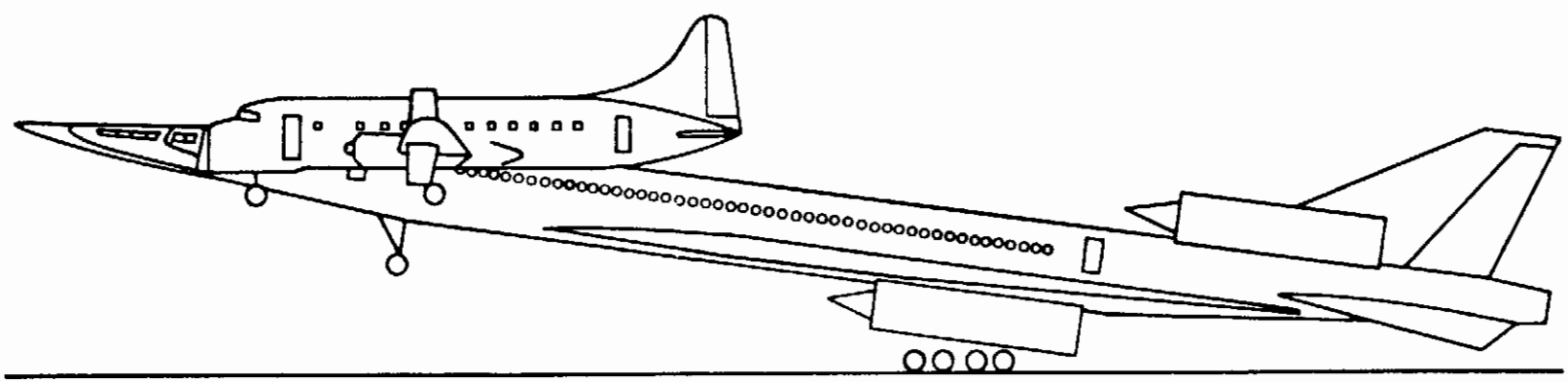

(b) EMERGENCY LANDING - WINGS BACK

Figure 6.3 TIFS SIMULATING LANDING OF VARIABLE GEOMETRY SST

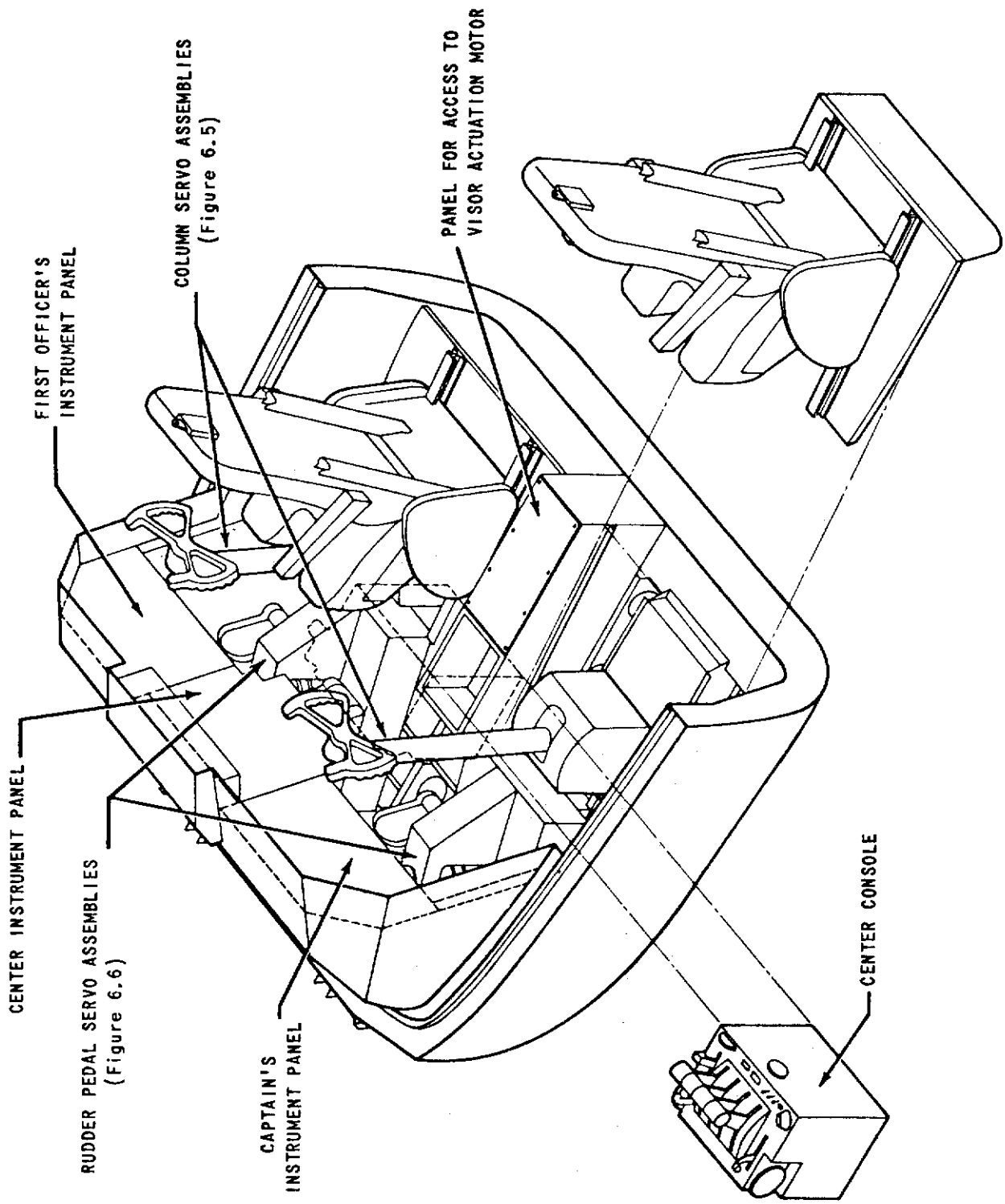

Figure 6.4 BASIC COCKPIT

from the center line of the airplane as compared with nineteen and three quarter inches for the Boeing SST. The instrument panels and center console will be easily removable so that other units may be substituted as required.

6.2.3.1 Cockpit Dimensions

Seats and controls are positioned so that the relative positions of the seat reference point, column hinge point, the arc of the control wheel finger reference point and the instrument panels are similar to those in the Boeing SST cockpit design.

6.2.3.2 Structure of Basic Cockpit

This unit consists of an assembly of U frames, fore and aft beams, horizontal sills and an outer skin. Initially, a flat floor and 707 type pilot's seats will be used, but the frame design is such that a stepped floor compatible with actual Boeing SST pilot's seats might be installed later. The 707 seats have a deep cleft in the front edge which allows a simple straight control column, with an internal cable system for the aileron control, to be used. This system will not have the backlash inherent in the multibevel and shaft drive arrangement which is to be used in the Boeing SST bent column design and is therefore more suitable for feel servo operation in the TIFS simulation cockpit.

6.2.4 SST Canopy and Visor

6.2.4.1 Window Configuration

The position, sizes and arrangement of the windows in the SST canopy and visor relative to the eye-reference point are similar to those of the Boeing SST design from the eye-reference point station forward.

6.2.4.2 SST Canopy Structure

The SST type canopy assembly attaches to the horizontal sill of the basic cockpit and to the forward vertical face of the adapter section. The assembly has a metal frame structure with alclad outer skin and all skin joints are sealed for pressurization. All window assemblies bolt

into position or are held in position by retaining strips. The window assemblies duplicate as far as is practical at the present time those which are planned for the Boeing SST cockpit.

6.2.4.2.1 Windshield Configuration

There are two window openings in the front of the canopy assembly. In each of these windshield openings is a five-ply inner panel and a monolithic outer panel with air space between. The five-ply inner panel consists of alternate layers of tempered glass (3) and vinyl (2) with phenolic cotton fabric framing around the edges and one-piece 2024-T3 inserts to carry loads over into the panel proper. The five-ply panel is held in position against a seal by screws around its periphery through the framing and inserts. The monolithic outer panel is tempered glass and is clamped into a rubber channel section. The actual type of glass which will be used on the TIFS cockpit windshield is yet to be determined as is the question of gold coating certain surfaces to simulate the SST vision through similar coatings.

6.2.4.2.2 Side Window Configuration

There are two window openings on each side of the canopy assembly. In each opening there is an inner monolithic panel, then an air gap, a three-ply panel, another air gap and an outer monolithic panel. The monolithic panels are tempered glass seated in rubber channels and held in place by retaining strips. The three-ply panel which has a vinyl center layer sandwiched between tempered glass panels is inserted into rubber channels clamped by retaining members. Like the windshield panels, the actual type of glass and the question of gold coating is yet to be determined.

6.2.4.2.3 Windshield Bird Strike Resistance

To improve the shock load absorbency, the vinyl layers in the five-ply panel are kept in a plastic condition by heating the windshield. This is accomplished by passing a low current through busbars embedded in the top and bottom of the panel and across a conductive coating inside the panel. The temperature of the panels is controlled by a system which reacts on temperature registration from thermistors embedded in the panels.

6.2.4.2.4 Anti-Icing and Defogging

Since the heated panels are not exposed to outside air temperature but are protected by the outside monolithic glass and air gaps, it is difficult to assess in advance what may be required for anti-icing and defogging protection. Such protection will probably be provided according to the recommendations of the subcontractor concerned.

6.2.4.3 SST Visor

The visor is a three-part construction which consists of:

(a) upper visor assembly
(b) lower visor assembly
(c) visor nose fairing

The visor is hinged so that it can be drooped in flight. At a maximum of 22° down, the pilots in the simulation cockpit have completely unobscured vision through the windshield windows. At any intermediate position the windshield is partially covered. Provisional design of the visor actuation uses a link and cable system operated by an electric-motor driven capstan which will be situated in the basic cockpit under the floor.

6.2.4.3.1 Upper Visor Assembly

The upper assembly contains windows whose position, size, shape and optical qualities are similar to those in the Boeing SST forebody. The initial design is for a metal structure, but a fiberglass structure is being seriously considered to gain cost and possibly weight advantages.

6.2.4.3.2 Lower Visor Assembly

The lower assembly incorporates two long arms which extend rearwards to pivot points on brackets under the fuselage at station 7.7. The initial design is for an all-metal structure, but a composite fiberglass/metal structure is being investigated for cost and weight saving.

6.2.4.3.3 Visor Nose Fairing

The nose fairing for the visor is a fiberglass shell similar to a large radome.

6.2.5 AMSA Canopy and Fairing

6.2.5.1 AMSA Canopy

This canopy is to be a large molded plexiglass assembly which attaches to the horizontal sill of the basic cockpit and to the forward face of the adapter section. The size and shape of the canopy are such that internal masking can be installed to reproduce various arrangements of windshields and side windows for projected AMSA designs.

6.2.5.2 Fairing for AMSA Canopy

A fixed nose fairing is required for aerodynamic reasons when the AMSA canopy is installed. This fairing is to be a composite fiberglass/metal structure which will attach at the same pivot points as the SST visor but will be locked in one position by an attachment on the front of the basic cockpit.

6.2.6 Elevator, Aileron and Rudder Feel Systems

The test pilot's flight controls in the simulation cockpit are connected to variable reaction electrohydraulic servos which provide artificial feel, and not to the C-131B flight controls. The two sets of controls for the left and right test pilots are not linked mechanically to each other but track together through the media of the electronic feel system using position signals fed to the electrohydraulic servo units. There are two column control assemblies and two rudder control assemblies. Maximum limit pilot-applied loads for the design of the controls are:

TYPE OF AIRCRAFT	AMSA	SST
AUTHORITY	MIL-A-8865 TABLE III	FAR 25 PARA 25.397
AILERON CONTROL	80 D* IN.-LB	80 D* IN.-LB
ELEVATOR (WHEEL)	300 LB	200 LB
RUDDER	300 LB	300 LB

*D = WHEEL DIAMETER (INCHES)

Since these limit loads determine relief valve settings in the hydraulic feel servos, two different settings will be available for use in the elevator feel system so that either aircraft may be simulated correctly.

6.2.6.1 Column Servo Assemblies

The main items in each column servo assembly are a control wheel, control column, elevator feel servo and aileron feel servo. The general configuration of the column servo assembly is shown schematically in Figure 6.5. Each assembly can be removed from the aircraft for bench testing or ground checkout use. Pilot's input forces are sensed by strain gages mounted on the spokes of the control wheel.

6.2.6.2 Rudder Control Assemblies

Each rudder control assembly includes rudder pedals and a rudder feel servo. Pilot's input forces are sensed by pedal dynamometers. The control assemblies are mounted on slides which permit 7.0 inches of movement in the fore and aft direction for leg adjustment. This movement is controlled by a jack screw assembly remotely operated by an adjusting control mounted conveniently for operation by the pilot concerned. The general configuration of the rudder control assembly is shown schematically in Figure 6.6.

6.2.7 Cockpit Installations

6.2.7.1 Center Console

The design of the center console used in the SST configuration is based on that of the forward part of the Boeing SST center aisle control stand design. On it will be reproductions of the thrust, wing sweep, flap, roll trim, pitch trim, yaw trim and speed brake controls of the Boeing console. Each simulated control will operate a rotary potentiometer wired to the computers in the main cabin. The thrust controls will be part of a system which will include electromechanical position servos on the Allison engine power controls. Also on the center console will be a number of feel engage system control switches and system status lights. A console generally similar in design but narrower will be fitted for the AMSA configuration.

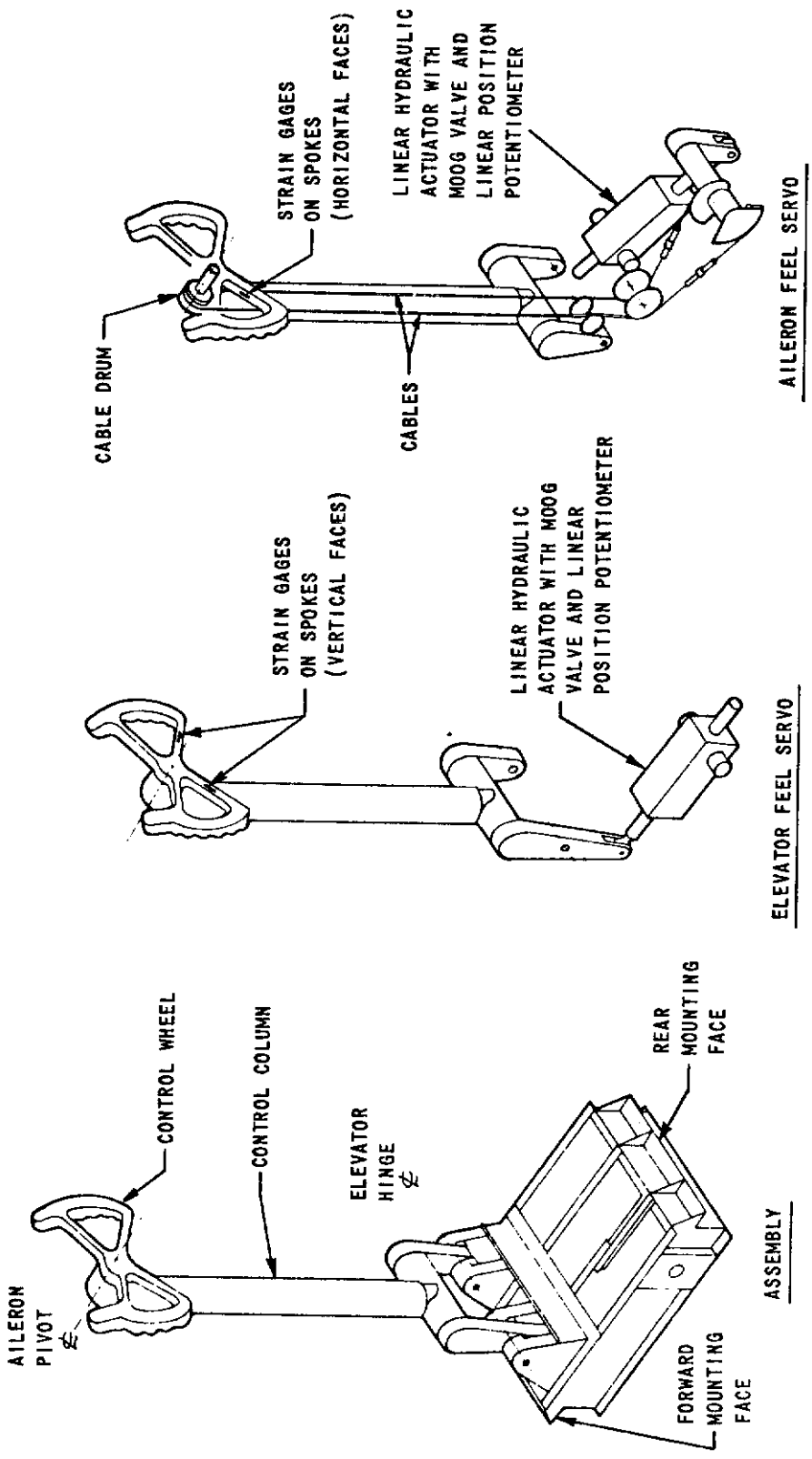

Figure 6.5 COLUMN SERVO ASSEMBLY

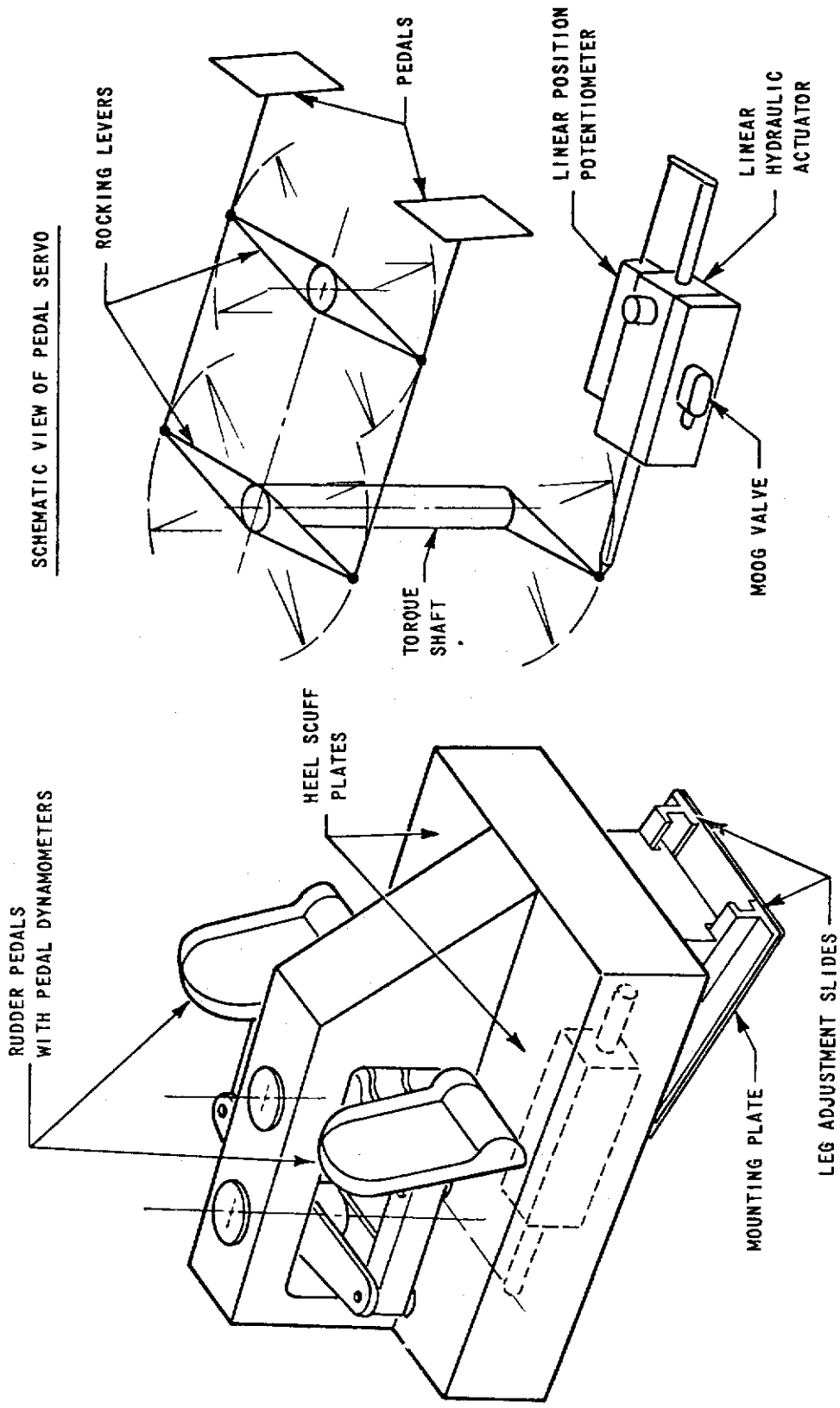

Figure 6.6 RUDDER PEDAL SERVO ASSEMBLY

6.2.7.2 Instrument Panels

The Boeing SST instrument panel is comprised of a Captain's panel on the left, a center panel, and a First Officer's panel on the right. Panels similar in appearance will be installed in the simulation cockpit for the SST configuration. The majority of instruments on these panels will be electrically driven and will receive inputs either from the computer model or from actual TIFS sensors. It should be noted that the speed, altitude, attitude, etc., displayed will be for the simulated airplane rather than for the C-131H. The various panels will be detachable and will have electrical pigtails leading to suitably positioned multipin connectors. This will make removal of panels and substitution of other panels easier. Some instruments will be nonworking and installed for appearance simulation only.

6.2.7.3 Overhead Panels

The Boeing SST overhead pilot's panel carries hydraulic annunciators, autopilot system controls, stability augmentation system controls, electric command system controls, some navigation switches and various other miscellaneous controls. In the TIFS reproduction, some of the items listed will be simulated working and some will be nonworking. As in the instrument panels, the overhead panel will be easy to remove.

6.2.7.4 Eye-Reference Point and Seats

The eye-reference points (ERP) for SST simulation are situated at TIFS station -37.5, water line 55.6 and left and right buttock lines 19.75. For AMSA simulation the station and water line are unchanged but the eye-reference points are at buttock lines 18.00. For the SST canopy, ERP indicators will be hinged from the cockpit ceiling. These indicators will be spring loaded to fold flat against the ceiling when not in use. In use, the test pilot adjusts his seat until his eyes fit the indicator and then adjusts the rudder pedals to suit the seat position. Seats in the simulation cockpit will be 707 type Weber Aircraft Corp. Models No. 148A and No. 157A, respectively for pilot and copilot. These seats are adjustable vertically and horizontally. Movement at the mean seat-reference-point is $\pm$2.50 inches vertically, 2.0 inches forward and 6.0 inches aft horizontally.

6.2.7.5 Escape Hatch

The cockpit area is provided with two emergency exits which are:

(a) ground emergency exit in the right hand side of the adapter section.

(b) bailout door in center of bulkhead 6.5 into the nose wheel well area.

The ground emergency window exit hatch is a standard C-131B assembly incorporated into the structure of the adapter section. The bailout door (see Figure 6.12), which can also be used for access into the cockpit when the aircraft is on the ground, is a pressure-tight door hinged along its upper edge which swings back and up in the wheel well. Uplocks are to be provided to hold the door open. A grab rail is to be fitted on the forward face of the bulkhead just above the door opening to facilitate feet-first egress through the opening.

6.2.7.6 Miscellaneous

There will be storage for three parachute chest packs on the forward upper face of bulkhead 6.5 and/or on the left inner wall of the adapter section. These packs are for two test pilots and one observer in the simulation cockpit in the event that the bailout door there has to be used. Note that three additional parachute chest packs for the same personnel will be stored back in the main cabin.

6.3 TRUE SIMULATION OF AIRPLANE BEHAVIOR AND COCKPIT MOTIONS

The TIFS airplane will have the ability to vary all three components of the total aerodynamic moment and all three components of the total aerodynamic force acting on the aircraft. To help make this possible, "position" servos are to be added to the existing elevator, aileron and rudder surfaces; new servo-operated outboard flaps for variable lift will be installed; new vertical servo-operated all-moving surfaces will be mounted on the wings to provide variable side force; and servos added to the engine controls for variable thrust control.

6.3.1 Elevator Position Servo

The general arrangement of the elevator position servo is shown in Figure 6.7. An electrohydraulic linear actuator operates a bellcrank which is linked directly to the elevator torque tube by a push-pull rod. The actuator assembly is installed between the frames at stations 820.95 and 851.212. The elevator pivot point is at station 871.25. Access to the elevator position servo installation is through the door in the aft cabin bulkhead (station 798).

6.3.2 Aileron Position Servo

The proposed arrangement of the aileron position servo is shown in Figure 6.8. Motion from an electrohydraulic linear actuator is transmitted into the existing aileron control system via the drum previously used for the autopilot drive. The aileron autopilot is to be relocated or eliminated. The servo is accessible by lifting a center floorboard just forward of the front engineer's station.

6.3.3 Rudder Position Servo

It is proposed to mount the rudder position servo with an electrohydraulic linear actuator connected directly to a horizontal arm on the rudder torque tube in the vicinity of water line 88.0. The arrangement is shown in Figure 6.9. Access to the installation will be through a door in the right side of the fairing between the fuselage and the rudder. The actuator will, of course, operate the rudder directly and not through the spring tab. During movement of the rudder by the actuator, the spring tab will be affected by some aerodynamic force and by the inertia forces of the complete control system back to the rudder pedals in the normal C-131B cockpit. Whether it will be desirable or not to lock out the spring tab when on the TIFS system has yet to be decided.

6.3.4 Flaps

The TIFS flap system will consist of large aileron-type flaps outboard of the nacelles and standard Fowler-type flaps inboard of the nacelles.

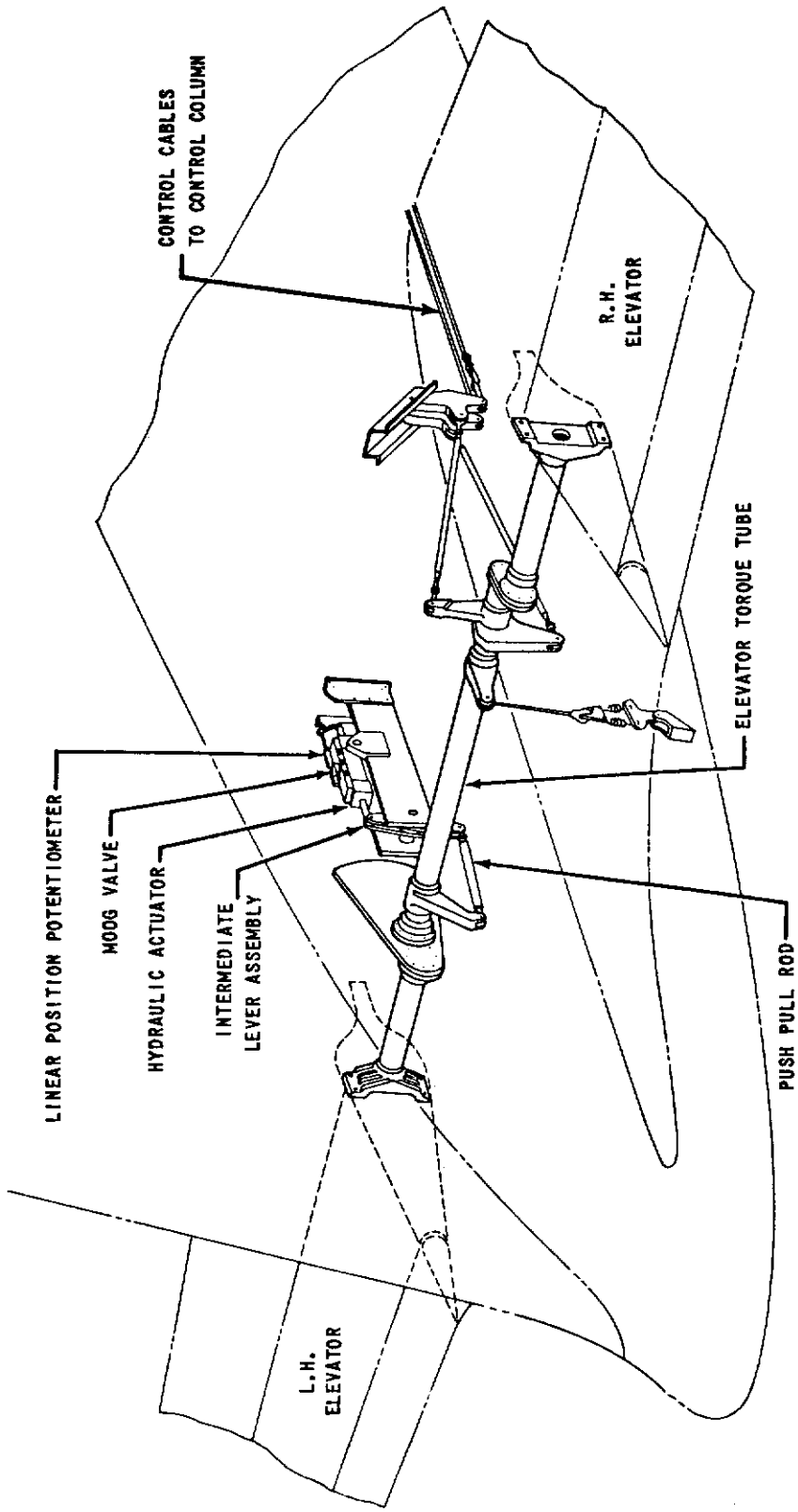

Figure 6.7 ELEVATOR POSITION SERVO

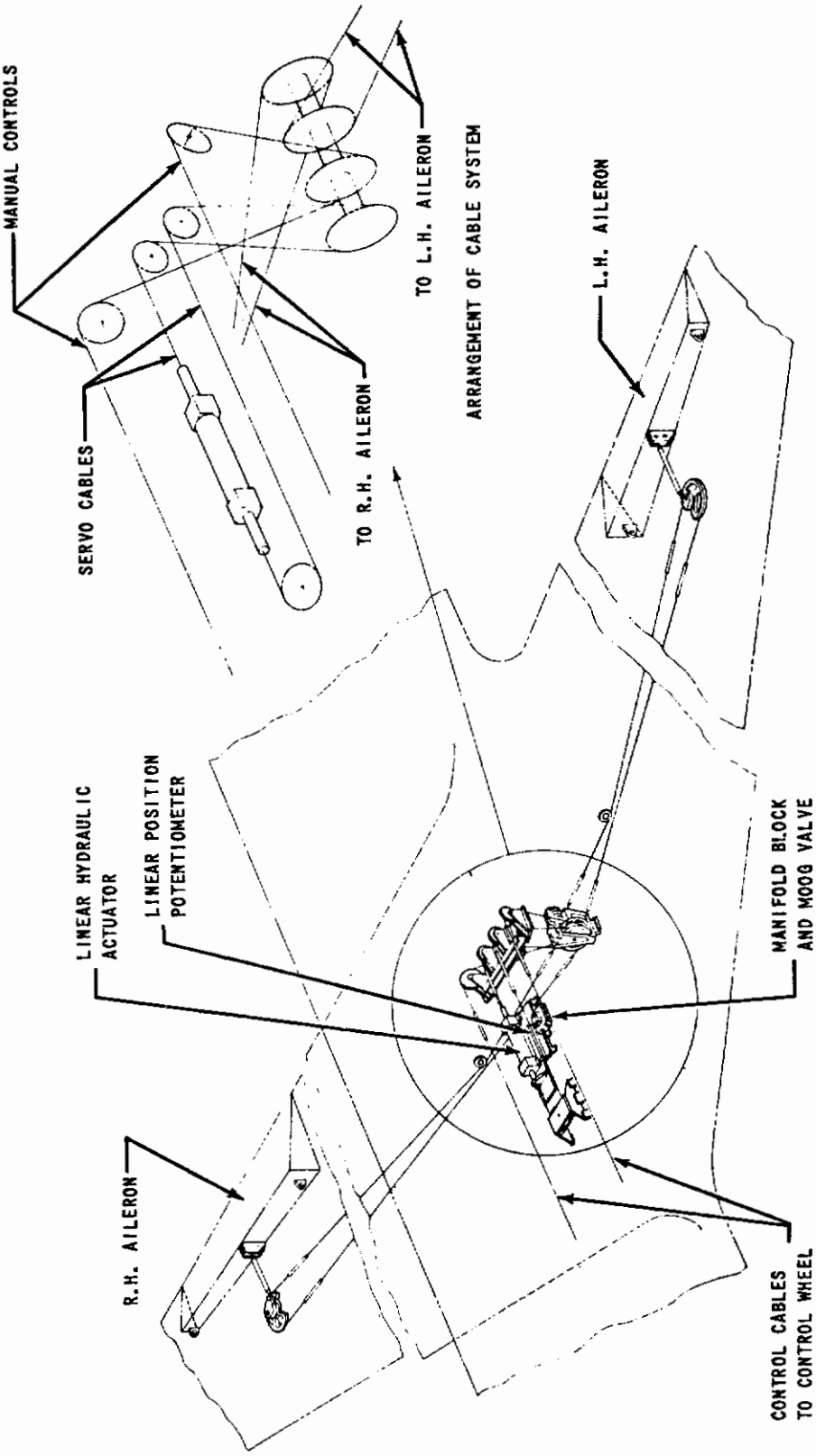

Figure 6.8 AILERON POSITION SERVO

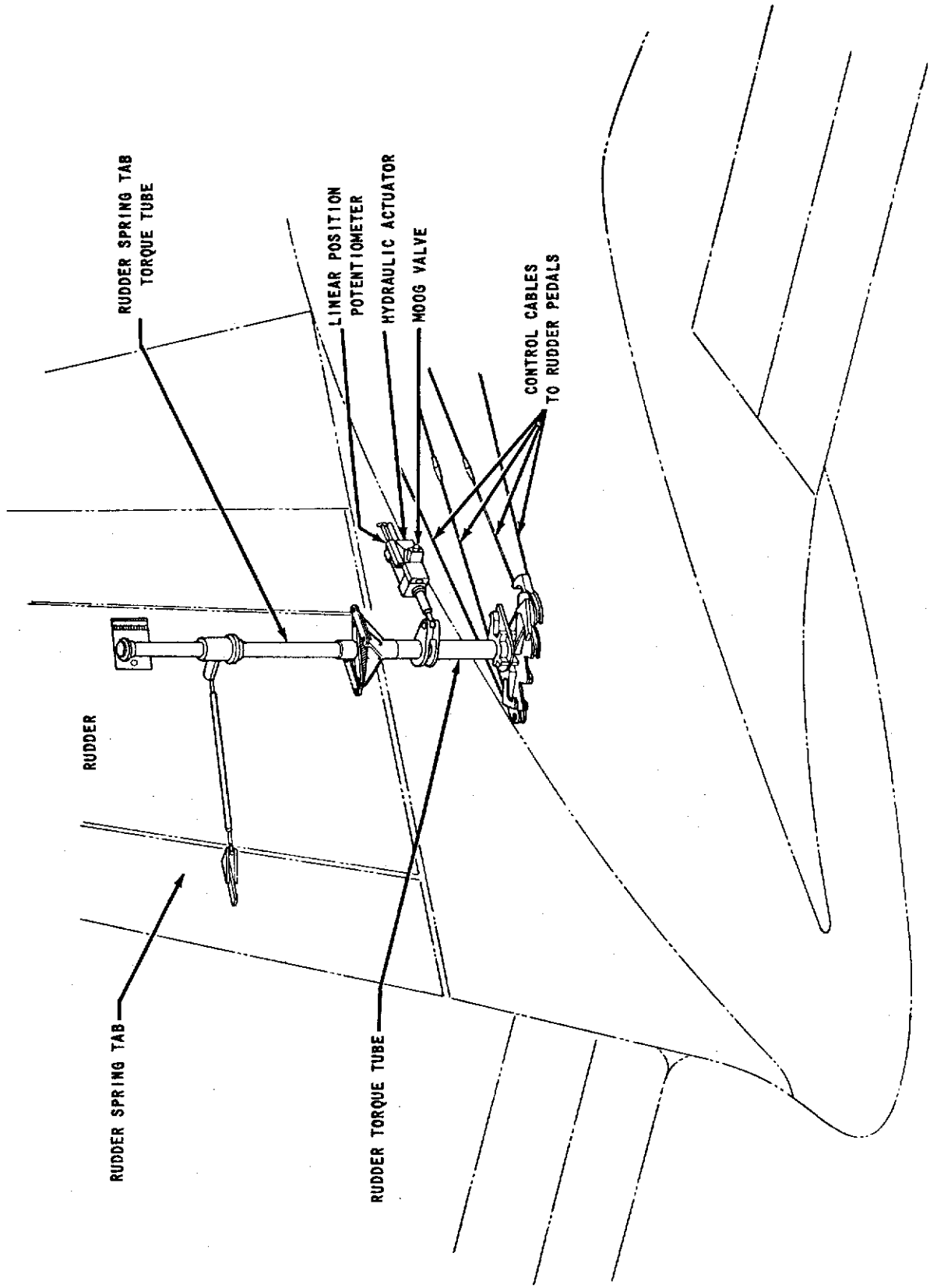

Figure 6.9 RUDDER POSITION SERVO

6.3.4.1 Outboard Flaps

The arrangement of the outboard flaps is shown in Figure 6.10. These flaps extend from wing station 174 (outboard side of nacelle) to wing station 416 (inboard end of ailerons). They are hinged along a line parallel to the rear spar and a constant distance of 21 inches from it. The leading edge of the flap is counter balanced and a curtain seal is incorporated. Each flap is supported on three hinges and is driven by a single actuator connected mechanically to arms at the inner and outer hinge points. Flap construction consists basically of a single spar near the hinge line with ribs cantilevered out both sides. The trailing edge is formed from a small machined triangular section. The counterweights are bolted on the leading edge.

6.3.4.2 Inboard Flaps

The inboard flaps are standard C-131B Fowler type. However, the two Fowler flaps are now operated from a single rotary hydraulic actuator moved from a wing position to a point near the center of the fuselage. A standard flap-position-indicator assembly has been mounted near the actuator and is operated from the flap torque shaft by a Browning gearbelt and pulley system.

6.3.4.3 Flap Controls

The existing cockpit flap control will be used for the Fowler inboard flaps. This is a rate control system. The position of the two inboard flaps will be shown on a single flap indicator in the safety cockpit. The outboard flaps will have a dual control system. When on the TIFS system, these flaps will be controlled by the computer and powered by the TIFS hydraulic system. When off the TIFS system, the outboard flaps will be controlled from the safety cockpit and powered by the normal hydraulic system. In the "off TIFS" case, the safety cockpit control will be a position-determining type and will be near the inboard flap control but separate from it. The positions of the left and right outboard flaps will be shown on a dual needle type indicator in the safety cockpit. If the position of the left and right outboard flaps should vary significantly at any time, the TIFS system will kick off automatically.

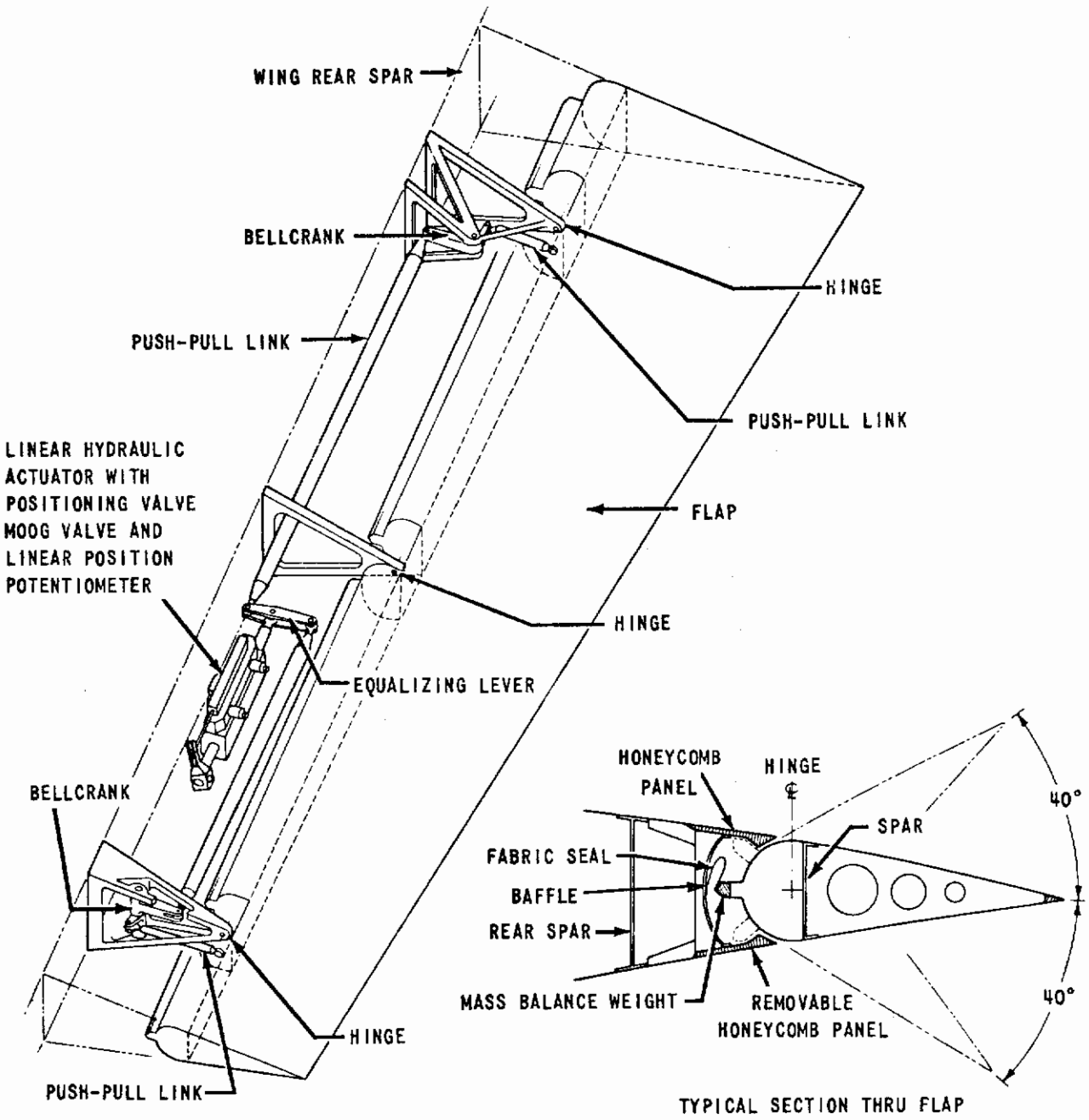

Figure 6.10 OUTBOARD FLAPS

The design of the outboard flap dual control is in a preliminary state. The selection of suitable "off-the-shelf" components in the hydraulic system may be difficult because of the high flow rates required. Preliminary estimates show that a peak flow of about 21 gallons per minute will be required for operating each outboard flap.

6.3.5 Side-Force Surfaces

The vertical all-moving surfaces used to generate side forces on the TIFS aircraft will be installed at wing station 375. The vertical pivot will be about 10.5 inches forward of the front spar, normal to the wing manufacturing chord plane in the lateral vertical plane and tilted 3 degrees forward (at the top) in the longitudinal vertical plane. This means that the pivot line is tilted 1 degree back (at the top) relative to the fuselage water lines. The surfaces are each about twenty-five square feet in area. The tip sections will be made of a frangible material since it is possible that the tips of the lower surfaces might scrape the ground under certain landing conditions. In the first TIFS designs, the side-force surfaces were pivoted between front and rear spars and subsequent wind tunnel tests indicated that the effectiveness of the surfaces was not as good as predicted. Additional wind tunnel tests are to be made to determine whether positioning the side-force surfaces forward at the front spar will improve their effectiveness sufficiently or whether a more complicated arrangement of a moving surface with a geared rudder on it is necessary. Figure 6.11 shows the proposed configuration for the simpler all-moving surfaces.

6.3.6 Thrust Control Servos

Movement of the engine power controls by servos will be accomplished through the use of capstans driven by electromechanical rotary actuators. Rotary position potentiometers in the system will give indications of the power lever angle at the engines. The engine thrust is linearly proportional to the power lever angle position.

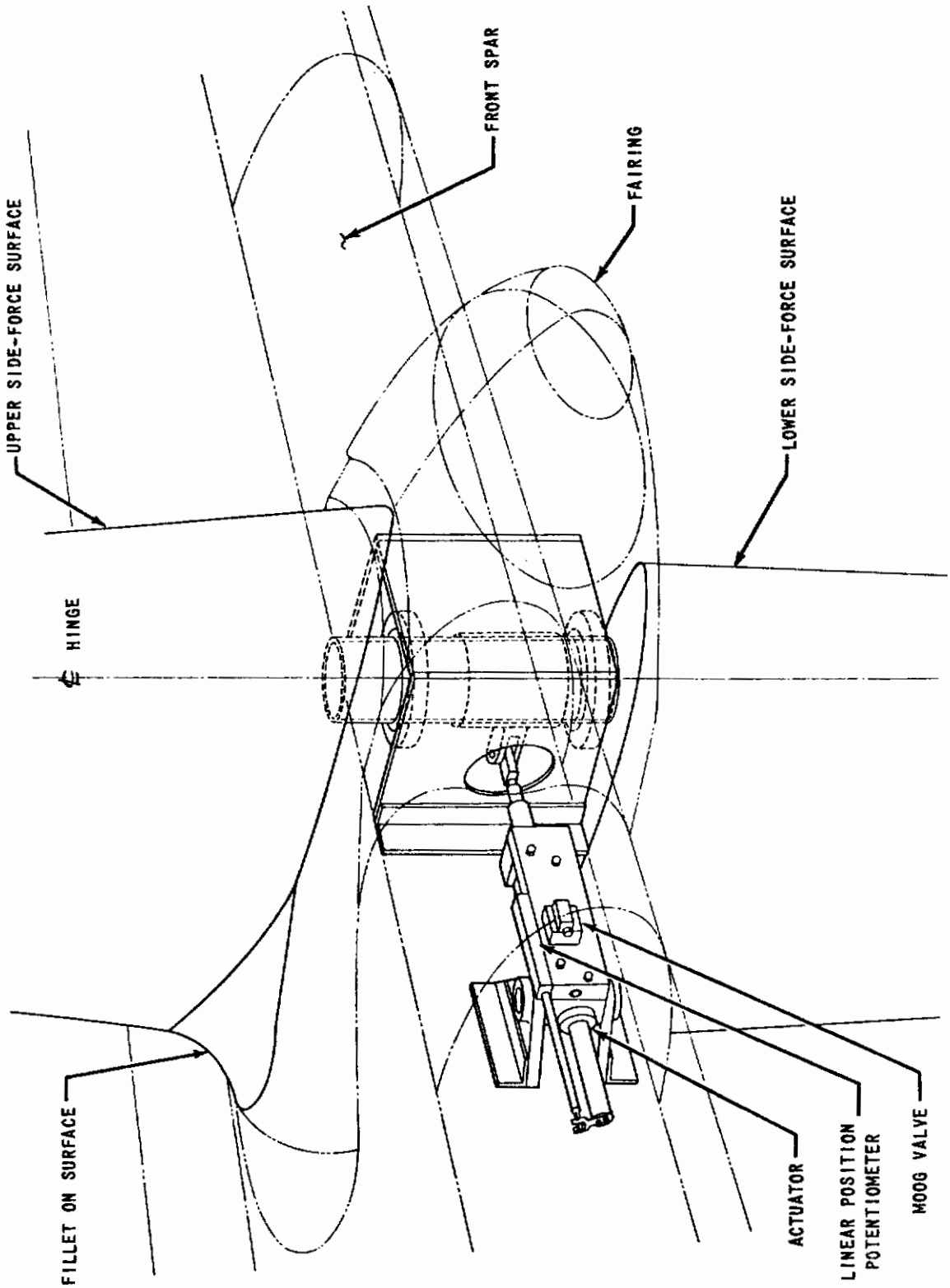

Figure 6.11 SIDE-FORCE SURFACE

6.4 ELECTRONIC CONTROL SYSTEM

The major part of the electronic control system is housed in a series of enclosure units mounted in the rear half of the cabin between stations 420 and 712. Provision for two test engineers' stations, computers, patch panels, electronic drawers, electrical power supply units, a recording oscillograph, a strip chart recorder and other units is made in this group of enclosures (see Figure 6.12). In addition, a number of sensor units are installed in other areas of the fuselage.

6.4.1 Electronic Enclosures

The basic framework of the electronic enclosures is constructed from standard Emcor components. Two units form the No. 2 test engineer's console between stations 420 and 469. A space between the enclosures at stations 469 to 514 provides access to both test engineers' stations, but is primarily intended to give a clear passageway to the right side bailout door. The enclosures are bolted together and diagonally braced where necessary. Floor attachments are designed for the emergency landing condition loads established in CAM4b. (This memorandum was used in the original design of the C-131B.)

6.4.2 Sensor Units

A sensor package near the c.g. of the airplane will contain a three-axis linear accelerometer and a three-axis angular accelerometer. A two-axis linear accelerometer will be mounted in the simulation cockpit at the evaluation pilot's position. A radio altimeter is to be mounted in the underside of the tail of the fuselage. α and β vanes are to be installed but no positions for these have been determined as yet.

6.5 HYDRAULIC POWER SUPPLY SYSTEM

A new hydraulic power supply system is to be installed to operate the TIFS servos. This system, which will use MIL-H-5606 fluid, will be Type I, 3000 psi class as defined in MIL-H-5440D. It will power the six variable feel servos (Figure 6.13) and seven surface position servos (Figure 6.14). Preliminary rough estimates indicate that the maximum no-load flow rate required for all servos might total about 75 gallons per minute. This is a "worst-case"

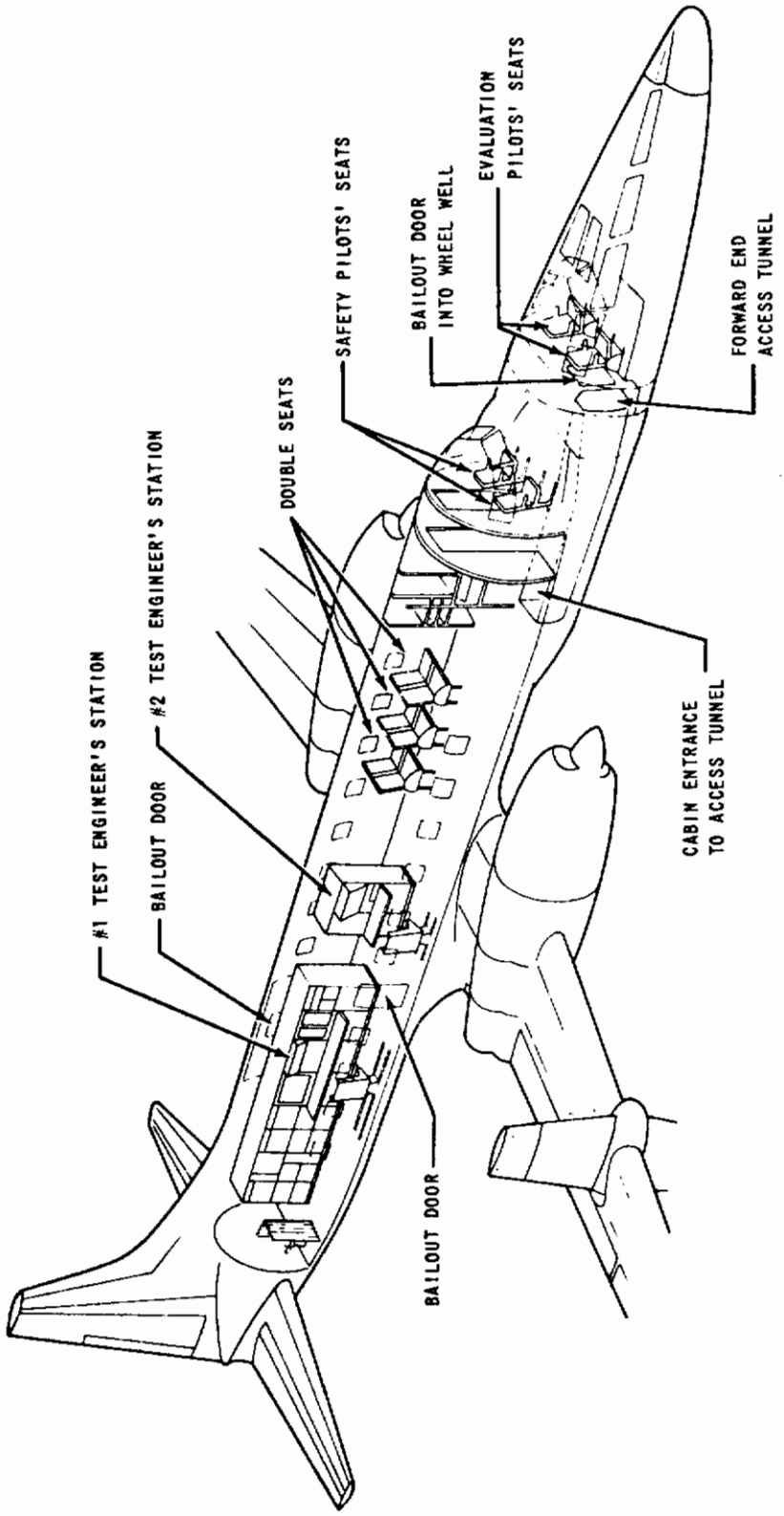

Figure 6.12 -- TIFS Internal Arrangement

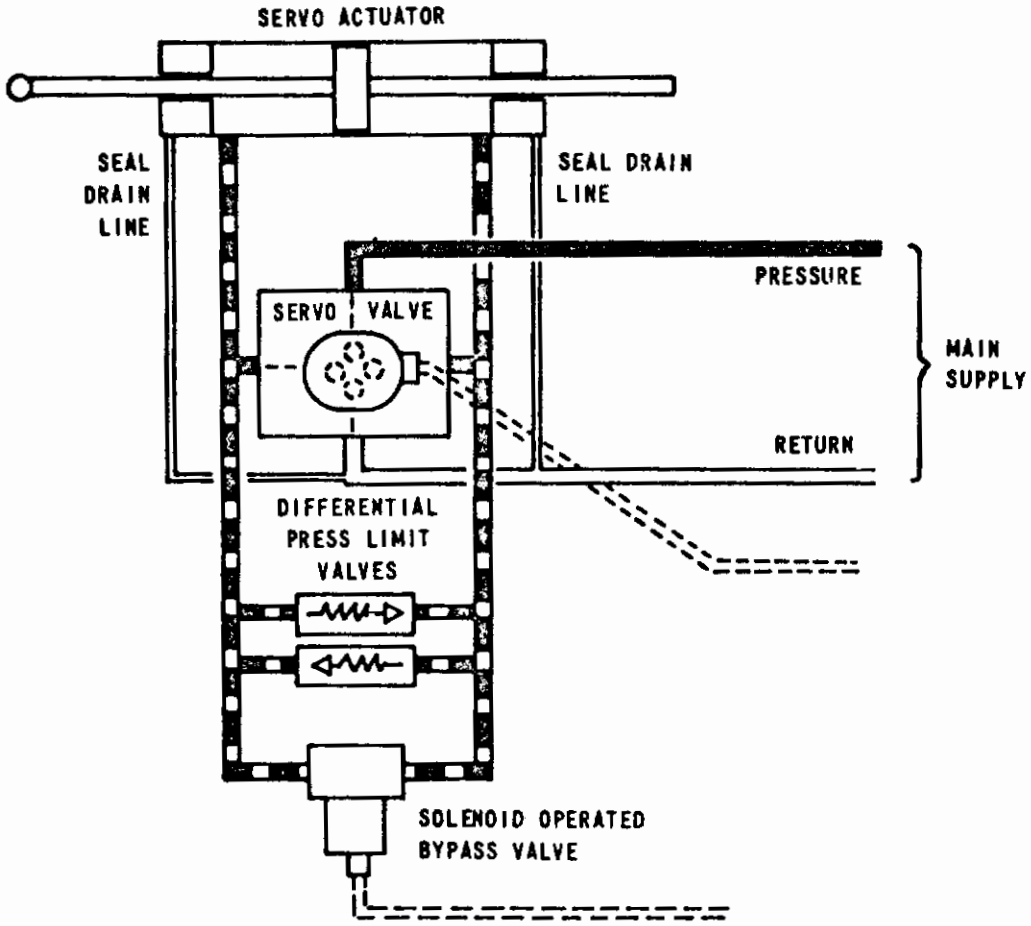

Figure 6.13 SCHEMATIC DRAWING OF TYPICAL FEEL SERVO HYDRAULIC SYSTEM

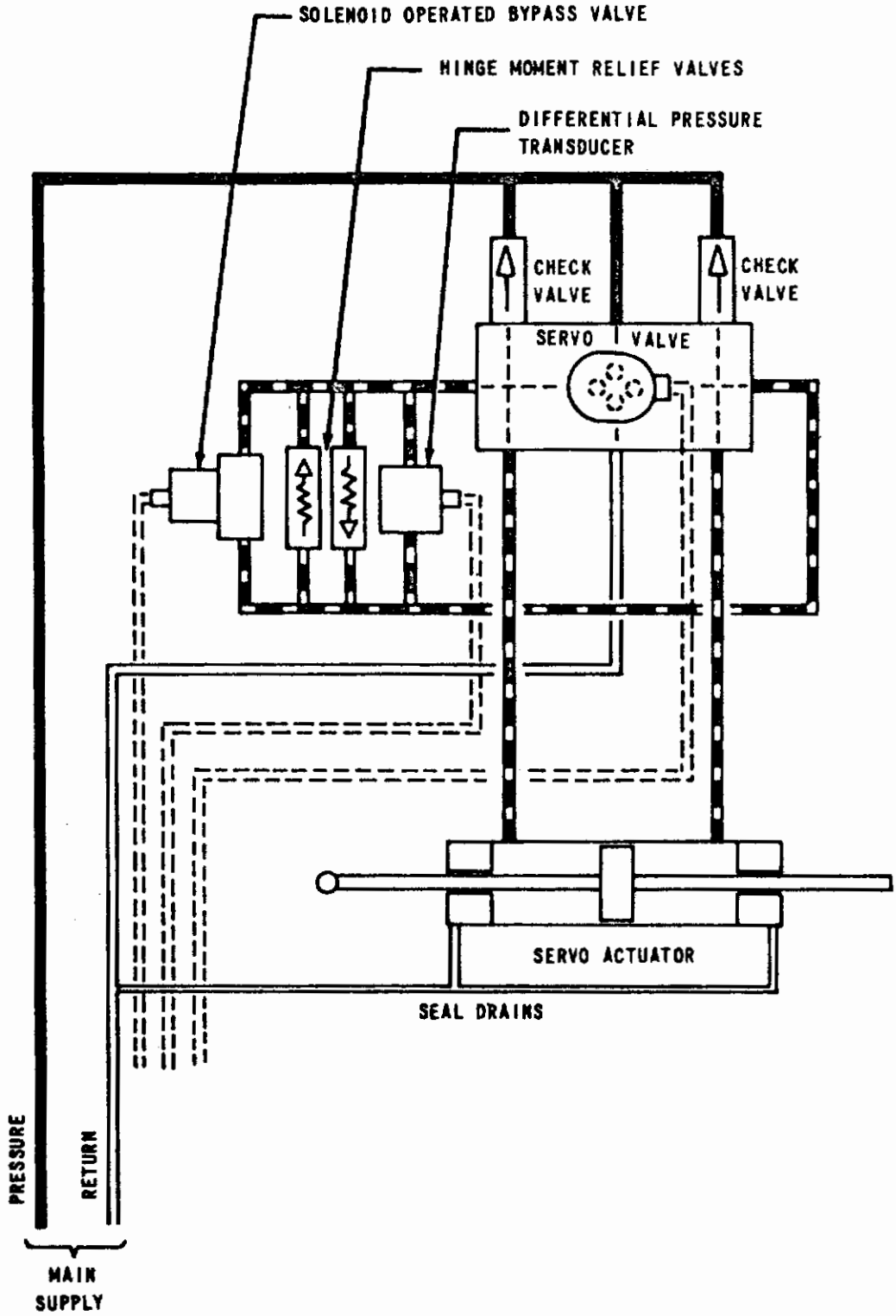

Figure 6.14 SCHEMATIC DRAWING OF TYPICAL SURFACE POSITION SERVO HYDRAULIC SYSTEM

condition with all actuators working simultaneously. The probability of a sustained demand at such a flow rate is very small and it is possible that a pump supplying about 70 percent of this flow rate, i.e., 53 gallons per minute, will be satisfactory if supplemented by accumulators in the system.

6.5.1 Hydraulic Pumps

The standard arrangement of engine-driven accessories on each of the Allison 501-D13 engines which will be installed in the TIFS airplane is shown on Figure 6.15. It is proposed to remove the DC generator from the right side engine and mount an additional hydraulic pump on this pad. The power available corresponding to the pad RPM and continuous torque rating shown is 95 HP. The largest pump which can be installed on this pad is one like the Abex AP12V type as used on the F-111 aircraft. This pump can deliver 42.5 gallons per minute at 3100 psi when driven at 5800 RPM. This pump weighs 17 lb, but has a QAD type flange mounting. A suitable Abex adapter is available to mount the pump on an AND 20002 generator pad. However, this pump does not have an integral boost element for low inlet pressure conditions and would require a separate boost pump to produce the 40 psi inlet pressure specified by Abex. The difference between the 42.5 gallons per minute output of a pump such as the Abex and the 53 gallons per minute approximately required for the TIFS system would require a motor-driven auxiliary pump. Ample AC electric power is available for such a unit. In fact an 8 gpm AC motor-driven pump (Vickers No. EA50182-8) is installed during the Allison conversion because only one engine-driven pump is used in the standard C-131H conversion.

6.5.2 Hydraulic Linear Actuator Sizing

A number of factors determine the physical dimensions of each actuator. These are:

(a) Force required

(b) Minimum stroke of 4 inches

(c) Maximum differential pressure across the piston of about 1000 psi (1/3 system pressure).

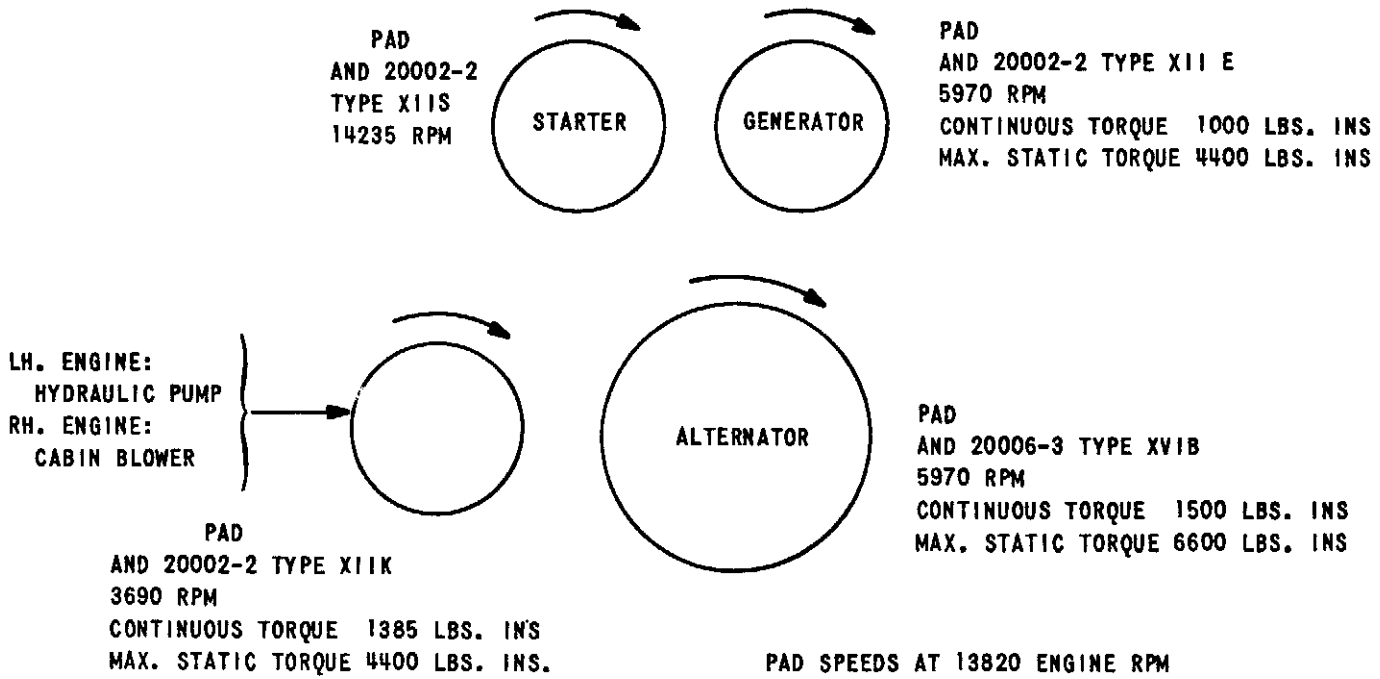

Figure 6.15 STANDARD ARRANGEMENT OF ACCESSORY PADS ON ALLISON 501-013 ENGINES, C-131H VIEWED LOOKING FORWARD

The forces required are determined from the maximum usable hinge moments in the case of the position servos or the maximum pilot applied loads in the case of the feel servos. The minimum stroke of 4 inches is specified to give good resolution of the linear position potentiometers. The limiting of the differential pressure across the piston to about 1/3 system pressure ensures that valve flow rates are most nearly linear with load. The selection of the nearest commercially available size results in some deviation from 1/3 system pressure.

6.5.3 Hydraulic Linear Actuator Selection

It is intended to use commercially available actuators for all linear servos. CAL has accumulated a wealth of experience in aircraft installations with actuators made by the Miller Fluid Power Division of the Flick-Reedy Corporation. This company supplies off-the-shelf actuators incorporating lapped metallic seals instead of the more common "O" ring type and CAL has been able to achieve lower friction levels with these actuators than any other type. Low friction in the actuators is desirable for one of two reasons. If it is for a feel servo, friction in the system shows up as an increment of pilot applied force which is always present and prevents very low force values being achieved. In the case of those position servos which are not disengaged mechanically when "off the system," any friction in the actuator shows up as an increase in "stick" force at all times. For the TIFS installations, all the feel servos and the rudder, elevator and aileron position servos will be of the metallic seal type. The side-force surface and flap servos will be Miller lock-seal type with Teflon seals and wipers such as have been used for a number of years on the USAF/CAL T-33 L/D petal system.

6.5.4 Accumulators

It is anticipated that it will be necessary to install some accumulators at various points in the TIFS hydraulic system in order to supplement the pump delivery under conditions of peak servo demands. Analysis is required to indicate the required size of the accumulators. At present, however, it is thought that it will be essential to install an accumulator in the simulation cockpit area adjacent to the six feel system servos which are situated at a

considerable distance from the hydraulic pump. It is also anticipated that an accumulator may be required in each wing adjacent to the outboard flap servos. These servos have peak flow rate requirements of 80.8 $in.^3$/sec (21 gpm) each, which will require a fluid velocity of about 11 ft/sec through 1.00°/D x 0.083 wall tubing.

6.5.5 Filters

A "no bypass" filter will be installed on the pressure side of the pumps. The filter element will be 2 micron nominal, 10 micron absolute. Another filter will be installed in the return line to the reservoir. This filter will use a 10 micron nominal, 25 micron absolute filter element. Since the flap actuator may be operated from either the TIFS hydraulic system or the normal ship's hydraulic system, there will be an interchange of fluid between the two systems. To protect the TIFS system from contamination, a "no bypass" filter with 2 micron nominal, 10 micron absolute filter will be installed in the supply line from the ship's system to the outboard flap actuators.

6.5.6 Servo Valves

The electrohydraulic actuator control valves will be Moog flow control type. Preliminary estimates indicate that model 31 valves should be satisfactory for all servos except those on the side-force surfaces and outboard flaps which will require model No. 32 and model No. 34 valves, respectively. Valve flow rates will be chosen to match the maximum no-load flow rates as closely as possible to avoid excessive flow rates through the valve in force-limited operation. Valves will be fabricated with axis cut spool and bushing to provide minimum distortion around null.

6.5.7 System Safeguards

Two groups of safeguards are provided to ensure that the flight control surfaces can be easily operated by a safety pilot when the TIFS system is "off." The first group consists of a solenoid-operated shutoff valve fitted as a bypass control in each surface position servo piping system (see Figure 6.14). When deenergized, these valves are normally open, and there are neither differential

pressures across the servo actuator pistons nor any impediment to the free flow of fluid from one side of each piston to the other side. The second safeguard is provided in case any one of the shutoff valves just mentioned fails to open when deenergized. This consists of a single solenoid-operated shutoff valve (not shown in Figure 6.14), connecting the pressure supply for all surface position servos to the common return line, and a pair of check valves (shown in Figure 6.14) fitted in each position-servo manifold block. The latter shut-off valve, also normally open when deenergized, dumps the supply pressure, thus permitting flow through the check valves. Should any servo bypass fail to operate, fluid can escape freely through one of the check valves when movement of the relevant surface by the safety pilot causes the servo piston to move in the cylinder.

6.5.8 System Controls and Indicators

Separate solenoid-operated shutoff valves of the normally closed type are provided for the feel pressure supply and the surface position pressure supply. This enables the feel servo system to be operated independently of the surface position servo system. Controls and indicators for the TIFS hydraulic system are situated on the simulation system control panel in the safety pilot's cockpit and in the feel-engage panel in the simulation cockpit. Pressure warning transducers for the feel servo system and the position servo system are set to come on at 2600 psi and off at 2200 psi. These are connected to green display lights on the simulation system control panel. Upstream of the shutoff valves in the feel pressure supply and surface position pressure supply lines, another pressure warning transducer is set to be off between 2200 and 2600 psi.

6.5.9 Piping and Fittings

All pressure lines will be annealed stainless steel 18-8 tubing conforming to MIL-T-8504 with wall thicknesses appropriate for a 3000 psi system. Return lines will be 6061-T6 aluminum tubing conforming to MIL-T-7081, except forward of the firewall in the nacelle area where MIL-T-8504 stainless steel tubing is mandatory. Nuts and sleeves will be steel. Fittings in the nacelle area or those in pressure lines larger than 3/4 tubing size will be steel, all

other fittings will be aluminum. For ground checkout work, self-sealing pressure and return connections will be provided.

6.6 CREW INSTALLATIONS

Three standard C-131B forward-facing double seats will be installed in the left forward central part of the cabin for the use of two evaluation pilots, and four other personnel during landing and takeoff. Stowage for ten parachute chest packs will be provided on the right side of the cabin between the tunnel mouth and the most forward electronic enclosure. Two swivelling seats will be installed at the test engineers' stations. These seats, which will slide on tracks parallel to the electronic enclosures, are Aircraft Mechanics, Inc. Model No. 649 swivel type E-1 built to specification MIL-S-7852 Seat, aircrew, adjustable. They can be occupied during takeoff and landing.

6.7 C-131H CONVERSION

The C-131B as delivered to CAL is fitted with standard R2800 Pratt and Whitney radial engines. Before the present CAL program is completed, the C-131B will be sent to Pacific Airmotive Corp. (PAC) in California under a USAF contract for conversion to a C-131H. The major portion of this conversion consists of modifying the nacelles and installing Allison model 501-D-13 jet-prop engines. After conversion, the airplane will return to CAL for completion of the TIFS modifications. This engine conversion program in the middle of the CAL program entails some problems in design, fabrication and installation. These problems are in three general areas: electric cabling, thrust servos and rudder fairing.

6.7.1 Cable Routing

During conversion to C-131H specification, most of the electrical cabling is replaced. Much of the cabling involved is normally routed along the lower right side of the fuselage in the area where the TIFS airplane access tunnel will be constructed. It has been necessary to reroute the existing C-131B cables to stay above the tunnel top and bypass the tunnel entry in the cabin floor and the PAC cabling must follow substantially the same routing. However, the new AC control panel which is normally located in the area where the cabin entrance to the TIFS tunnel is, will have to be installed in another position and this will entail a change to the standard PAC cable harness.

6.7.2 Power Controls

The TIFS thrust control servos will be installed in the cable control system to the engines. During the C-131H modification, a new pilot's pedestal is installed in the cockpit at the forward end of these controls and the power levers on the new engines are connected to the aft end of the throttle cable system which otherwise remains unaltered. It is necessary to obtain further data from Allison about the cable travel and cable loads before the design of the thrust servo installation can be completed.

6.7.3 Rudder Fairing

Part of the C-131H modification consists of increasing the size of the rudder and as a result of this, the fairing between the bottom end of the rudder and the fuselage is modified. This is the fairing in which CAL proposes to install the rudder position servo. The final design and installation of this servo may be delayed until the aircraft returns from PAC with the fairing modified.

6.8 ANALYSES AND COMPUTATIONS

6.8.1 Structural Analyses

The various TIFS modifications to the C-131B are being designed so that they are at least equal in strength to the unmodified structure. The CAL stress analyses will use the original Convair analyses as a base. Where applicable, flight and landing conditions which designed the original structure are used to design the modifications, thus the July 1950 revision of CAM4b which was used in the original CV340 and C-131B design is the guide. The Air Force Handbook of Instructions for aircraft design (AFSCM 80-1) is also being used. Because of the extent of the modification to the forward end of the fuselage, and the necessity for balancing the new nose and cockpit arrangement with mass at the aft end, the shear and bending moment distributions in the fuselage are changed. The original Convair fuselage stress analyses are being examined to determine whether the bending moments and shear stresses produced by the TIFS modification are within the capabilities of the existing structure or not.

The side-force surfaces will impose new loads on the wing structure. These will be included with the design wing loads used by Convair and the Convair stress analysis reviewed to be sure that structure margins are adequate. The loads transmitted to the existing flap hinge structure are also being checked to determine that positive margins are maintained. Additional dynamic loads on the nose gear due to the changed mass distribution of the TIFS modification will be assessed. Maximum hinge moments applied by the position servos to the elevator, aileron and rudder are limited, where necessary, so that the maximum permissible airframe and empennage structural loadings will not be exceeded in any variable stability flight condition. The servo installations are designed, generally speaking, for stiffness and long fatigue life. This usually results in overstrength structures.

6.8.2 Weight and Balance

Preliminary estimates of weight and balance are being constantly updated as design and fabrication progresses. Considerable trouble, since resolved, was experienced at first in reconciling the data in the TO-1B-40 Weight and Balance Handbook which accompanied the airplane when delivered to CAL with the original weight and balance data used by Convair in their analyses. At delivery, the airplane had 700 lb of ballast in the tail. An additional 1000 lb of ballast is necessary for the TIFS modification. Present estimates show that with a crew of eight and full fuel tanks (11062.5 lb fuel), the TIFS airplane will have a gross weight of 51027 lb, well within the 53200 lb maximum gross weight of the standard C-131H. The c.g. position at any time is dependent on whether the crew are seated in their landing and takeoff positions or are at their working stations; whether the undercarriage is up or down; and what amount of fuel is in the tanks. The following table lists a number of combinations and the resultant c.g. position for each.

CREW POSITION	UNDERCARRIAGE	FUEL WEIGHT	C.G. POSITION
LANDING AND TAKEOFF	DOWN	11062.5	19.76
WORKING	UP	11062.5	15.36
WORKING	UP	1585	10.58
WORKING	DOWN	1585	12.56
LANDING AND TAKEOFF	DOWN	1585	15.96
WORKING	UP	0	9.76
LANDING AND TAKEOFF	DOWN	0	15.30

These figures are within the normal C-131H forward c.g. limits of 8.5% for flight and 13% for takeoff and landing.

SECTION VII

DESIGN OF TIFS ELECTRONIC SYSTEMS

7.1 INTRODUCTION

A general description of the TIFS electronic design is presented in this section.

7.1.1 TIFS Electronic Subsystems

The electronic system for TIFS is composed of the subsystems arranged in Figure 7.1 and listed as follows:

1. Sensors and Sensor Electronics - The sensors measure various angles, rates and accelerations of the NC-131H aircraft. These sensor outputs are converted to properly scaled DC voltages representing parameters used in the control of the TIFS.

2. Feel System - A feel system for each evaluation pilot provides variable force versus position gradients for the elevator and aileron control wheel and the rudder pedals. This control system can simulate a linear spring feel or nonlinear feel characteristics composed of variable amounts of deadband, breakout force and hysteresis.

3. Surface and Throttle Servos - Electrohydraulic servos control the position of the elevator, aileron, rudder, flaps and side force surfaces. Magnetic powder clutch servos are used for the throttle position servos. Rate and acceleration stabilization techniques are provided to shape the dynamic responses of these servos.

4. Model-Following - Response-Feedback Patch Panel Electronics - The MF-RF patch panel ties together all of the other subsystems of the TIFS electronics. The most important function of the electronics is to process the error signals between the model variables and airplane variables to provide the required surface and throttle position commands.

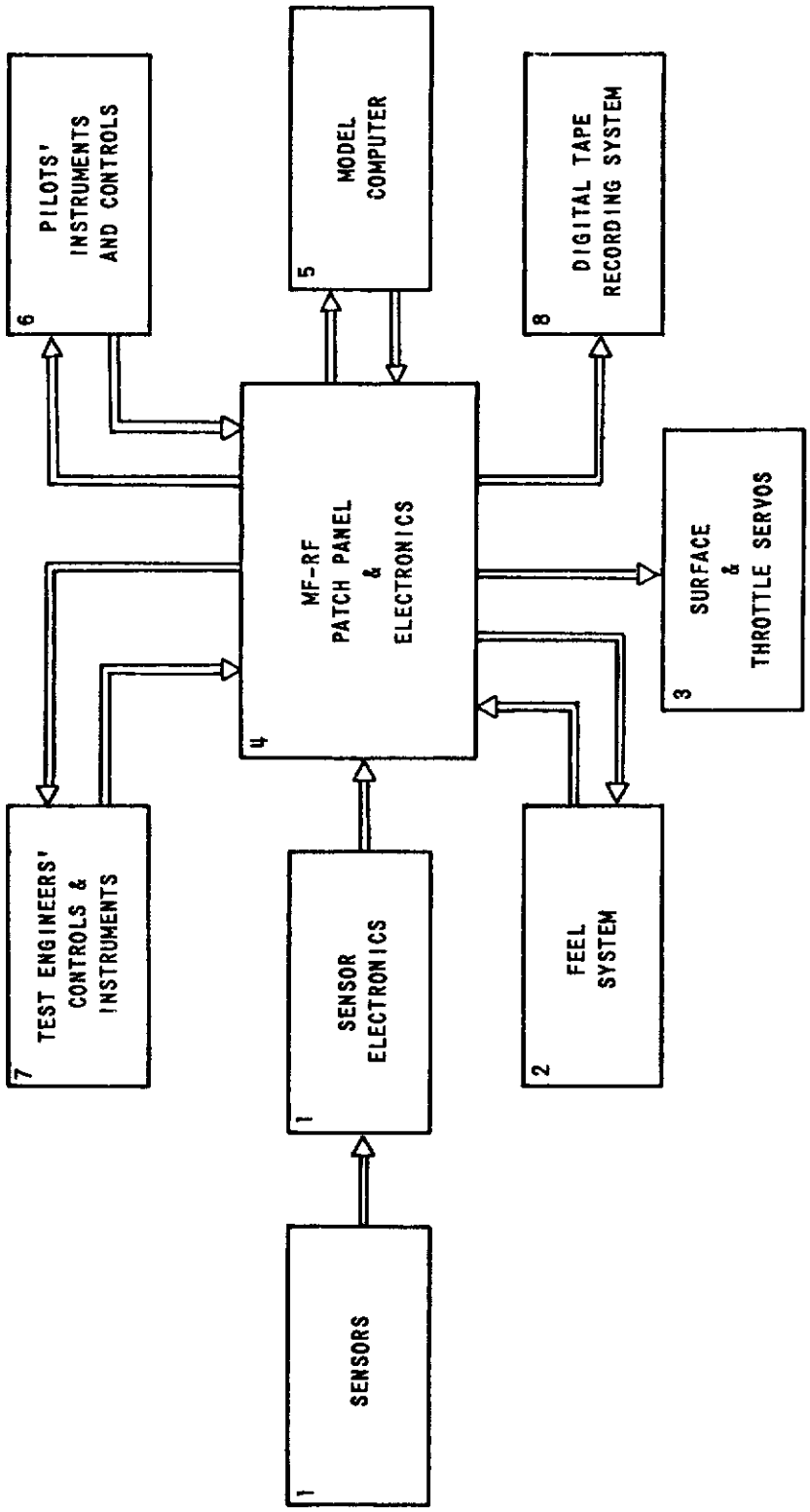

Figure 7.1 TIFS ELECTRONIC SYSTEM BLOCK DIAGRAM

5. Model Computer - The equations of motion of the simulated aircraft are programmed on the model computer. In the MF mode of operation, the input commands to the model computer are the feel system motions. The electrical outputs of the computer represent the simulated aircraft motions.

6. Pilot Instruments and Controls - Servo driven flight and engine instruments are provided for each evaluation pilot. The inputs to each instrument can be patched on the MF-RF panel from the sensors or the model computer. Throttle, wing-sweep, flap, and speed-brake levers are mounted on the center control console. Each provides a proportional electrical signal for simulated control inputs.

7. Test Engineers' Control and Instrument Panels - Two test engineers control and monitor the operation and performance of the TIFS system on separate panels. One panel contains switches and status lights that control and indicate the engagement sequence of the various subsystems. The other panel contains instruments and a strip chart recorder to monitor the model-following performance.

8. Digital Tape Recording System - Fifty-eight channels of digital recording are provided with tape coding compatible with the IBM 360 computer system. A ground playback unit is provided which can play back any 8 channels simultaneously on an analog recorder.

7.1.2 Equipment Design Philosophy

The major portion of the electronic hardware will be fabricated into standard equipment enclosures located in the rear half of the TIFS cabin. Figure 7.2 illustrates the general arrangement of the various subsystems. Each enclosure contains equipment drawers which are removable for each adjustment or modification. Fourteen printed circuit boards may be mounted in each drawer. The circuit boards have plug-in amplifiers and discrete components so that major functional channels are complete on each board. The plug-in amplifiers are commercially available, all-silicon, encapsulated units. The various units purchased fall into the following categories:

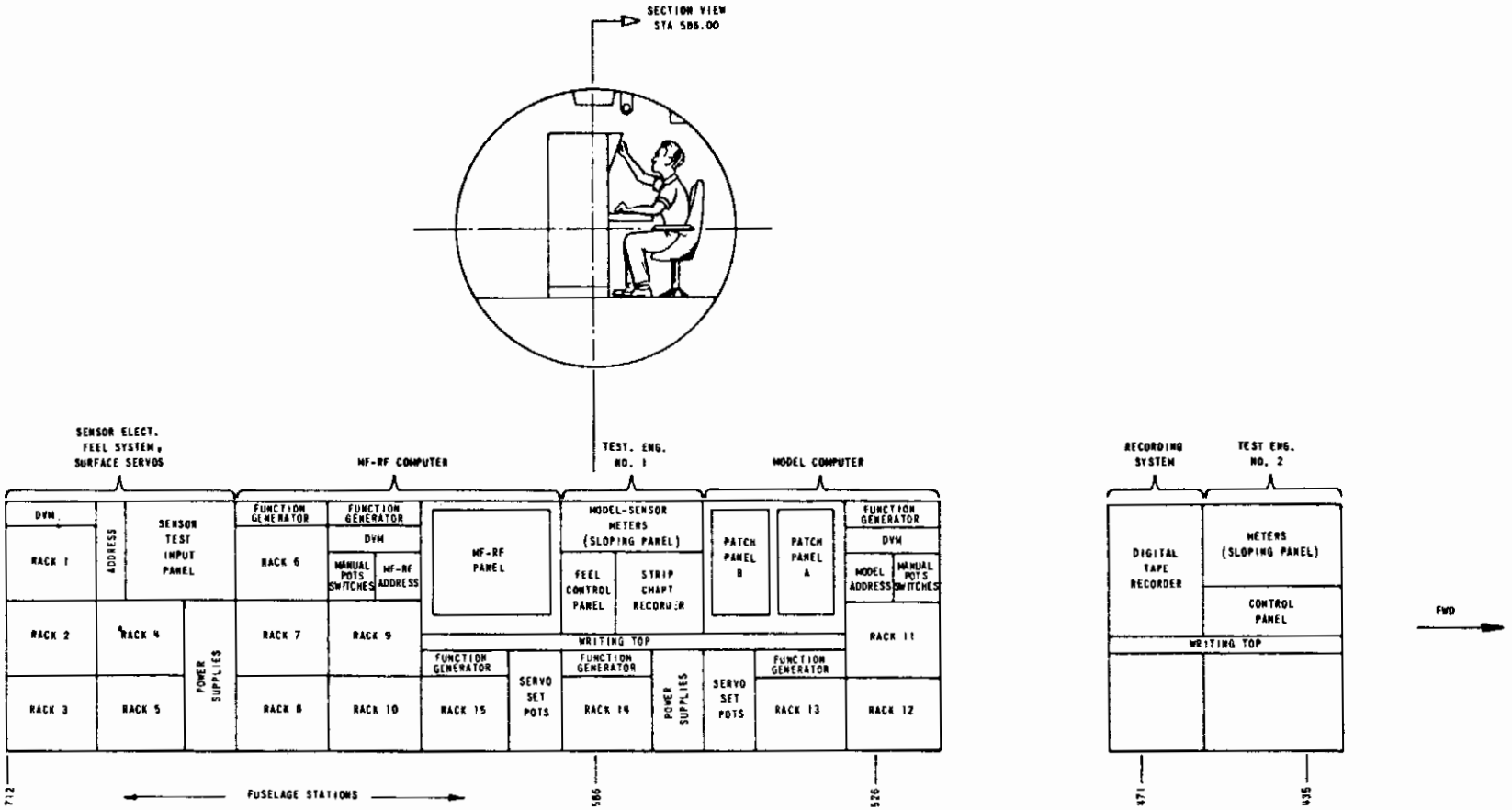

Figure 7.2 ELECTRONIC EQUIPMENT ENCLOSURES

1. chopper stabilized
2. differential input
3. high input impedance.

From CAL's experience in recent variable stability system design and amplifier manufacturer data, an expected mean time between failures (MTBF) for the electronic system is 50 to 100 operational hours. Test points and adjustments are conveniently located on each board for use when the system is operating. Since complete channels are on a single printed circuit board, extensive modification can be made in a particular channel by plugging in another circuit board.

The TIFS subsystems consist of 10-volt analog amplifiers for most computations. Some sensors are AC carrier; however, these signals are immediately demodulated and filtered before being used in any computation. All computations performed are general analog operations, such as summing, integration, resolving, multiplication, division and function generation. After evaluating various analog computers, it became apparent that superior computing performance for the TIFS task can be best obtained from a custom-built analog computer. Special circuits were developed to perform multiplication, function generation and memory with greater capabilities than normally found in commercially available analog computers. The pulse-width type multiplier has the advantage that at small signal levels, accurate multiplication is performed (0.01%) and that several quantities can be multiplied by one variable. The unit can also perform accurate division even with divisor signals of less than 5 percent of full scale. The function generator employs a technique whereby a best-fit straight line is fitted to the desired function. The difference between the straight line and the desired function is expanded and programmed on a 20-segment function generator. The nonlinear function is rescaled and summed with the straight line approximation to yield the desired function to approximately 0.01 percent accuracy for most functions.

On normal analog computers, memory is performed with chopper stabilized integrators. This technique is adequate for short-term memory only. A memory circuit that utilizes the extremely high (greater than 10^{12} ohms) input impedance of a field effect transistor (FET) operational amplifier is used for balance and

hold operations on the TIFS program. Memory with a long-term decay time constant in excess of 3,000 hours is achieved. This corresponds to a maximum fall-off rate of approximately 0.02 mv/sec and can be considered linear for the first few hours of memory.

7.2 DETAILED DISCUSSION OF TIFS ELECTRONIC SUBSYSTEM

7.2.1 Sensors and Sensor Electronics

This subsection describes the electronics and measurement devices required to characterize the TIFS aircraft motions in inertial and air mass reference frames. Table 7-1 is a list of the sensor signals developed for the TIFS system. The signals are subdivided into groups of similar signals, i.e., positions, rates, accelerations, etc....; also included is the maximum variation for each parameter. A unique portion of the sensor electronics is the inertially compensated Air-Data System. Its outputs are altitude, rate of climb, indicated airspeed, Mach number, true airspeed and true airspeed rate. The inputs to the air-data computer are static pressure, dynamic pressure, air temperature, and inertial terms desired from accelerations and attitude.

Complementary filters are used to blend the slower heavily filtered pressure-derived data with the high frequency inertial terms. This results in a wide-band measurement which is not too sensitive to aerodynamically induced noise. The signal flow through the air-data complementary filter is illustrated in Figure 7.3. The equations that relate the air-data input-output variables are listed in Table 7-2. Also included are the equations that relate the air data output variables h , $\dot{h}$, γ and $\dot{V}$ to the pressure and inertial variables from which they are derived. The air-data system implements the transfer functions represented by these equations. The transition from low frequency pressure data to high frequency inertial data is accomplished in such a fashion that the resultant variable has a flat frequency response through the transition region.

Similar techniques are also used to obtain sideslip angle (β). Equation 5 of Table 7-3 represents the complementary blending of the β vane

Table 7-1

SENSOR SIGNALS DEVELOPED FOR THE TIFS

(NUMBERS IN PARENTHESES REFER TO NOTES AT END OF TABLE)

	SENSOR SIGNAL		MAXIMUM SCALE FACTOR
ATTITUDE GYRO			
	$20 \sin \theta$		10V = SIN 30°
	$10 \cos \theta$		10V = COS 0°
	$10 \sin \phi$		10V = SIN 90°
	$10 \cos \phi$		10V = COS 0°
	$10 \sin \psi$		10V = SIN 90°
	$10 \cos \psi$		10V = COS 0°
	$0.1\ \phi$		9V = 90°
	$0.5\ \Delta\phi$		10V = 20°
RATE GYROS AND ANGULAR ACCELEROMETERS			
	$0.2\ p$		10V = 50°/SEC
	$0.5\ q$		10V = 20°/SEC
	$0.5\ r$		10V = 20°/SEC
	$0.04\ \dot{p}$		10V = 250°/SEC^2
	$0.1\ \dot{q}$		10V = 100°/SEC^2
	$0.1\ \dot{r}$		10V = 100°/SEC^2
LINEAR ACCELEROMETERS			
	$20\ n_x$		10V = .5g
	$10\ n_y$		10V = 1g
	$10\ n_{y_p}$		10V = 1g
	$4\ n_z$		10V = 2.5g
	$4\ n_{z_p}$		10V = 2.5g
	$4\ \Delta n_z$		10V = 2.5g
	$4\ \Delta n_{z_p}$		10V = 2.5g
AIR DATA	$p_s/3$	(1)	10V = 30" Hg
	$h_p/2500$		10V = 25,000'
	$2\ \bar{q}_c$	(2)	10V = 5" Hg
	$25\ \bar{q}_c/p_s$		10V = .4
	20M	(3)	10V = .5M
	$0.02\ V_p$	(4)	10V = 500'/SEC
	$V_i/30$	(5)	10V = 300 KNOTS
	$1/6\ [t_c + 10]$	(6)	10V = +50°C
	$0.5\ [t_K]^{1/2}$	(7)	10V = $\sqrt{400°K}$
INERTIAL COMPUTATIONS			
	$\ddot{h}_I/10$		10V = 100'/SEC^2
	$0.5\ \dot{V}_I$		10V = 20'/SEC^2
AIR DATA COMPLEMENTARY FILTER COMPUTATIONS			
	$h/2500$		10V = 25,000'
	$0.1\ \dot{h}$		10V = 100'/SEC
	$0.04\ \Delta V$		10V = 250'/SEC
	$V/50$		10V = 500'/SEC
	$0.5\dot{V}$		10V = 20'/SEC^2

Table 7-1 (CONCLUDED)

	SENSOR SIGNAL		MAXIMUM SCALE FACTOR
RADAR ALTIMETER			
	$0.01\,h_R$		10V = 1000'
	$0.2\,\dot{h}_R$		10V = 50'/SEC
ANGLE OF ATTACK			
VANE	$0.5\,\alpha_{VANE}$	(8)	10V = 20°
	$0.5\,(\alpha_I + \alpha_g)$	(9)	10V = 20°
	$0.1\,(\dot{\alpha}_I + \dot{\alpha}_g)$		10V = 100 /SEC
INERTIAL	$0.5\,\alpha_I$		10V = 20°
	$0.5\,\dot{\alpha}_I$		10V = 20°/SEC
GUST	$0.5\,\alpha_g$		10V = 20°
	$0.5\,\dot{\alpha}_g$		10V = 20°/SEC
ANGLE OF SIDESLIP			
VANE	$0.5\,\beta_{VANE}$		10V = 20°
	$0.5\,(\beta_I + \beta_g)$		10V = 20°
	$0.5\,(\dot{\beta}_I + \dot{\beta}_g)$		10V = 100°/SEC
INERTIAL	$0.5\,\beta_I$		10V = 20°
	$0.5\,\dot{\beta}_I$		10V = 20°/SEC
GUST	$0.5\,\beta_g$		10V = 20°
	$0.5\,\dot{\beta}_g$		10V = 20°/SEC
FUEL WEIGHT			TO BE DETERMINED
GEAR POSITION			TO BE DETERMINED
LOCALIZER			TO BE DETERMINED
GLIDE SLOPE			TO BE DETERMINED
SPEED BRAKE			TO BE DETERMINED
WING SWEEP			TO BE DETERMINED
HEADING ERROR			TO BE DETERMINED
THROTTLE HANDLE POSITIONS (QUANTITY 4)			TO BE DETERMINED
FLAP POSITION			TO BE DETERMINED
HEIGHT MEASUREMENT	$0.01\,h_e$	(10)	10V = 1000 FT

NOTES:

(1) p_s IS STATIC PRESSURE
(2) $\bar{q}_c$ IS COMPRESSIBLE DYNAMIC PRESSURE
(3) M IS MACH NUMBER
(4) TRUE AIRSPEED FROM PRESSURE MEASUREMENT
(5) INDICATED AIRSPEED
(6) t_c IN °C
(7) t_k IN °K
(8) VANE DEFLECTION
(9) VANE DEFLECTION COMPENSATED FOR POSITION ERROR
(10) h_e IS EFFECTIVE LANDING GEAR HEIGHT (SEE FIG. 7.4)

Table 7-2
AIR DATA EQUATIONS

AIR DATA EQUATIONS

$$h_p = f_1(p_s)$$

$$M = f_2(\bar{q}_c / p_s)$$

$$V_p = 65.77 M \sqrt{t_K}$$

$$V_i = f_3(\bar{q}_c)$$

INERTIAL EQUATIONS

$$\ddot{h}_I = g n_x \sin\theta - g \cos\theta \left[n_y \sin\phi + n_z \cos\phi \right] - g$$

$$\dot{V}_I = g \left[n_x \cos\alpha_I \cos\beta_I + n_y \sin\beta_I + n_z \sin\alpha_I \cos\beta_I - \sin\gamma \right]$$

$$\dot{V}_I \cong g \left[n_x + n_y \beta_I + n_z \alpha_I - \sin\gamma \right]$$

COMPLEMENTARY FILTER EQUATIONS

$$\dot{h} = h_p \frac{s}{(\tau s + 1)^2} + \dot{h}_I \frac{2\tau\left(\frac{\tau s}{2} + 1\right)}{(\tau s + 1)^2}$$

$$h = h_p \frac{1}{\tau s + 1} + \dot{h} \frac{\tau}{\tau s + 1}$$

$$\dot{V} = V_p \frac{s}{(\tau s + 1)^2} + \dot{V}_I \frac{2\tau s\left(\frac{\tau s}{2} + 1\right)}{(\tau s + 1)^2}$$

$$V = V_p \frac{1}{\tau s + 1} + \dot{V} \frac{\tau}{\tau s + 1}$$

Table 7-3

ANGLE OF ATTACK AND SIDESLIP EQUATIONS

ANGLE OF ATTACK COMPUTATIONS

$$.5\alpha_I = .5(57.3)\left[\frac{-\sin\gamma + \sin\theta - \beta_I/57.3\cos\theta\sin\phi}{\cos\theta\cos\phi}\right] \quad (1)$$

$$.5\dot{\alpha}_I = \frac{.5(57.3)(32.2)}{V}\left[n_z + \cos\theta\cos\phi - \frac{\alpha_I \dot{V}}{(57.3)(32.2)}\right] + .5q - \frac{.5p\beta_I}{57.3} \quad (2)$$

$$50\sin\gamma = \frac{.1\dot{h}(10)}{V/50} \quad (3)$$

ANGLE OF SIDESLIP COMPUTATIONS

$$.5\dot{\beta}_I = \frac{.5(57.3)(32.2)}{V}\left[n_y + \cos\theta\sin\phi + \frac{\beta_I \dot{V}}{(57.3)(32.2)}\right] + \frac{.5\alpha_I p}{57.3} - .5r \quad (4)$$

$$.5\beta_I \cong \frac{\overbrace{\beta_I + \beta_g}^{VANE}}{(\tau s+1)^2} + \frac{\overbrace{\dot{\beta}_I 2\tau\left(\frac{\tau s}{2}+1\right)}^{INERTIAL}}{(\tau s+1)^2} \quad (5)$$

FOR τ = 10 SEC

$$.5\beta_I \cong \frac{\beta_I + \beta_g}{(10s+1)^2} + \frac{\dot{\beta}_I 20(5s+1)}{(10s+1)^2} \quad (6)$$

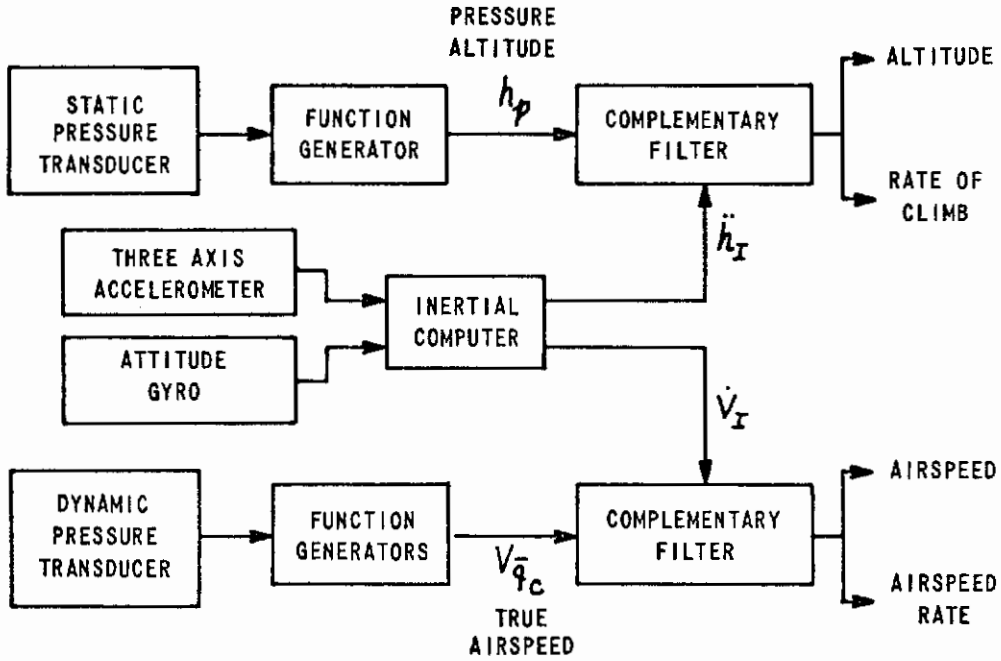

Figure 7.3 AIR DATA BLOCK DIAGRAM

signal with the β_I inertial signal. An analog mechanization that employs the blended β variable and the variables of Equations 1, 2 and 4 of Table 7-3 yield the α_I, $\dot{\alpha}_I$ and $\dot{\beta}_I$ signals. The angle of attack and angle of sideslip are obtained by all-aerodynamic and also, by all-inertial methods so that gust information can be obtained.

A radar altimeter will be used for height and descent rate measurements during simulated landings. This device is a standard Honeywell, Inc. AN/APN-171(v) radar altimeter. Since the TIFS will not actually touch the runway, the altitude above the runway of the simulated aircraft's gear (h_e) will be computed from the radar altitude and attitude information. This computation is illustrated in Figure 7.4. Self-test and calibration features will be provided for the entire system. Because of the interrelation between many of the parameters, a complete operational check of the system requires an auxiliary analog computer to provide a consistent set of inputs which are processed to form the various outputs.

7.2.2 Feel Systems

The TIFS feel system provides force versus position characteristics at the controls of each test pilot. The principle used is to measure the applied control forces and to command the control position of the hydraulic actuators.

A typical feel system block diagram is illustrated in Figure 7.5. The voltages from a force measuring system that represent the forces applied by the pilot and copilot are summed to form a total force command. These voltages are used as position commands to the actuators connected to each pilot's control wheel and rudder pedals.

The resultant feel system provides the following characteristics at the elevator, aileron or rudder controls of each test pilot:

1. Linear adjustable force vs position gradient.
2. Adjustable breakout force.
3. Adjustable hysteresis.
4. Adjustable split hysteresis (combination of breakout force and hysteresis).

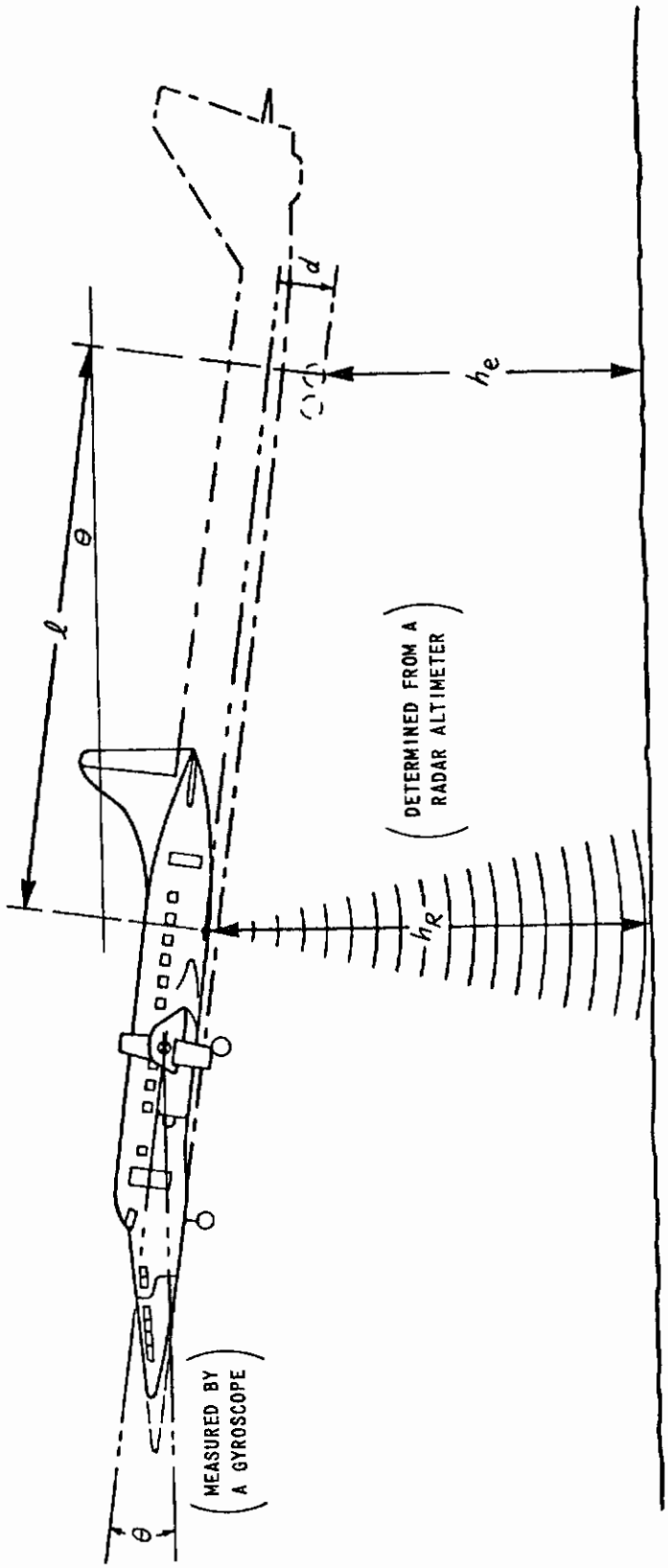

Figure 7.4 DETERMINATION OF EFFECTIVE LANDING GEAR HEIGHT FROM MEASUREMENT OF ALTITUDE AND PITCH ATTITUDE OF TIFS

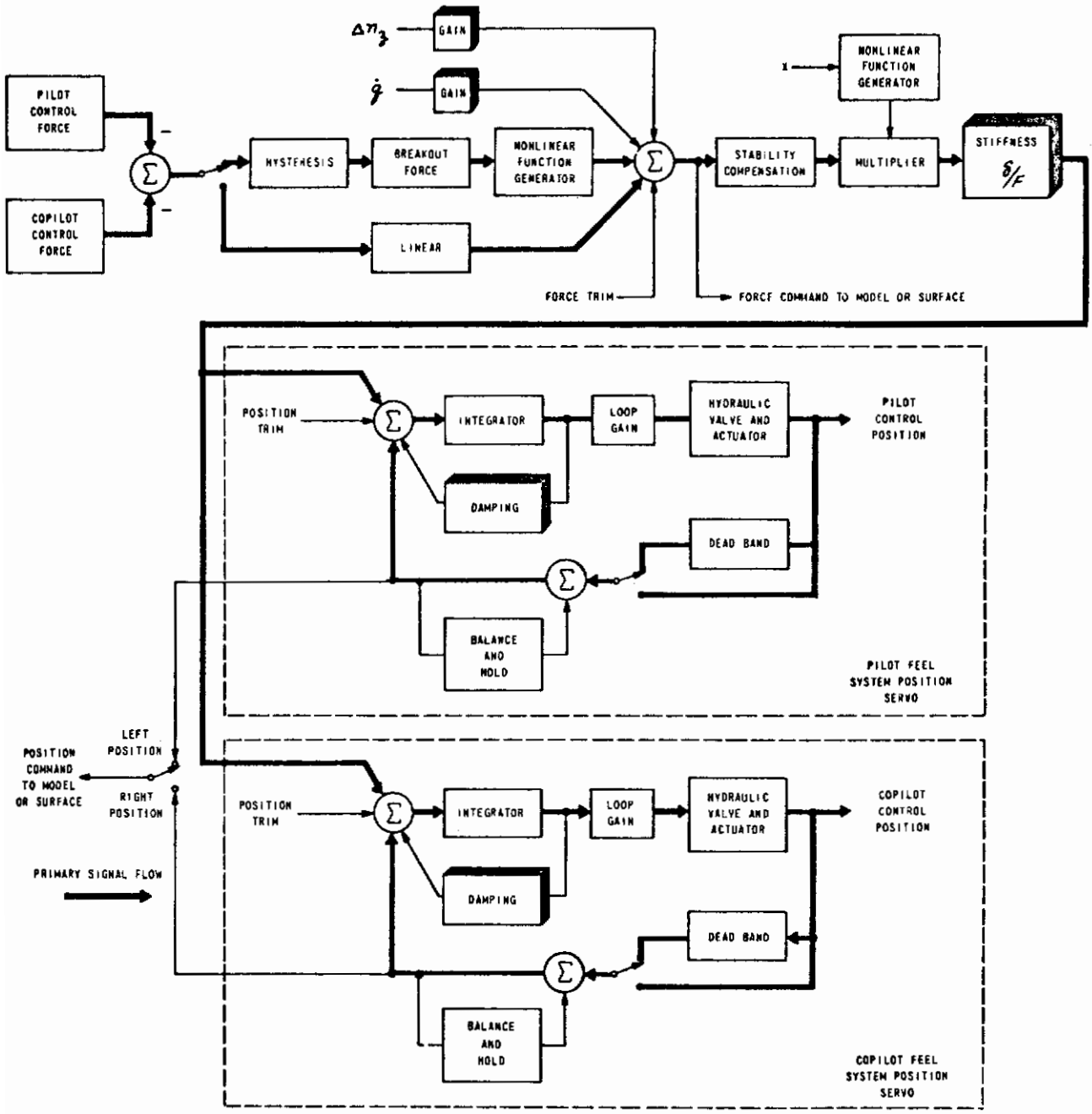

Figure 7.5 FEEL SYSTEM BLOCK DIAGRAM

5. Adjustable deadband.

6. Bobweight effects such as those due to normal acceleration (Δn_z) and pitching acceleration ($\dot{q}$).

7. Variation of the force gradient as a nonlinear function of some arbitrary variable (x , in Figure 7.5).

The breakout force, hysteresis, and nonlinear functions are inserted in the force channel. Control deadband is inserted in each of the position feedback loops. The control force gradient can be preset to a constant value or varied as a function of another variable such as dynamic pressure.

Table 7-4 is a list of the maximum ranges for the nonlinear characteristics listed above.

Table 7-4

NONLINEAR CHARACTERISTICS

	ELEVATOR	AILERON	RUDDER
BREAKOUT FORCE	±20 LB	±10 LB	±50 LB
HYSTERESIS	±20 LB	±10 LB	±50 LB
SPLIT HYSTERESIS	±40 LB	±20 LB	±100 LB
DEADBAND	±1 IN.	±10 DEG	±0.5 IN.
MAXIMUM FORCE	200 LB	100 LB	500 LB
MINIMUM GRADIENT	1 LB/IN.	0.1 LB/DEG	10 LB/IN.

In addition to providing the above feel characteristics, the feel system position is related to the force command by a second-order transfer function with known, independently variable natural frequency and damping. The natural frequency can be varied from 0 to 50 rad/sec and damping ratio is adjustable from 0 to 2.0. This provides a precise means for evaluating transfer functions between airplane responses and pilot inputs.

An additional capability is to simulate the various trim systems of different aircraft. The trim system provides the following rate and proportional trim capabilities.

1. Trim to the feel system position loop.
2. Trim to the feel system force loop.
3. Trim to the aircraft surface servo.

By injecting the trim into the force or position channels, it is possible to trim the feel system which in turn trims the surface. It is also possible to inject the trim signal directly into the surface to simulate a movable stabilizer trim.

The maximum trim rate for each axis of the feel system is tabulated in Table 7-5.

Table 7-5

MAXIMUM TRIM RATES FOR TIFS FEEL SYSTEM

MODE	ELEVATOR	AILERON	RUDDER
POSITION	1 IN./SEC	10 DEG/SEC	0.5 IN./SEC
FORCE	8 LB/SEC	4 LB/SEC	20 LB/SEC
SURFACE	2 DEG/SEC	2 DEG/SEC	2 DEG/SEC

The proportional trim will be initially installed in the TIFS with the capability of being switched to a rate trim at a later time. Maximum proportional trim capabilities are listed in Table 7-6.

Table 7-6

MAXIMUM PROPORTIONAL TRIM

MODE	ELEVATOR	AILERON	RUDDER
POSITION	±5 IN.	±50 DEG	±2.5 IN.
FORCE	±40 LB	±20 LB	±100 LB
SURFACE	±10 DEG	±6.25 DEG	±5 DEG

The command signal for positioning the control surface can be derived from either control force or position. Zero displacement force command operation is directly available. A first-order lag with rate limit can be provided to simulate a boosted control system. The control to surface gearing is obtained with a potentiometer gain adjustment.

Maximum gear ratios have been selected and are listed in Table 7-7.

Table 7-7
MAXIMUM GEAR RATIOS

ELEVATOR	AILERON	RUDDER
δ_{e_c}/δ_{ES} = 10 DEG/IN.	δ_{a_c}/δ_{AS} = 1 DEG/DEG	δ_{r_c}/δ_{RP} = 20 DEG/IN.
δ_{e_c}/F_{ES} = 0.5 DEG/LB	δ_{a_c}/F_{AS} = 1 DEG/LB	δ_{r_c}/F_{RP} = 0.2 DEG/LB

7.2.3 Surface and Throttle Servos

A simplified block diagram of a typical surface servo is presented in Figure 7.6. The surface position feedback signal is subtracted from the command signal, with the resultant error signal used to current drive the hydraulic flow control valve. The dynamic feedback response of the system is obtained from the strut position while the low frequency and DC feedback are obtained from the surface position. The surface rate and acceleration terms are available to shape the dynamic response of the servo.

An additional feature of the servo loop is the auto balance system which electronically nulls surface command signals before system engagement to avoid undesirable transients.

An electronic safety trip system is built into the MF-RF panel electronics. If a predetermined maximum safe surface rate is exceeded or if a system failure causes an abrupt high level surface rate command, the system is automatically disconnected. Also available on the panel are the outputs of electrical differential pressure gages mounted across each actuator. Any combination of these signals may be monitored by the electronic safety trip system.

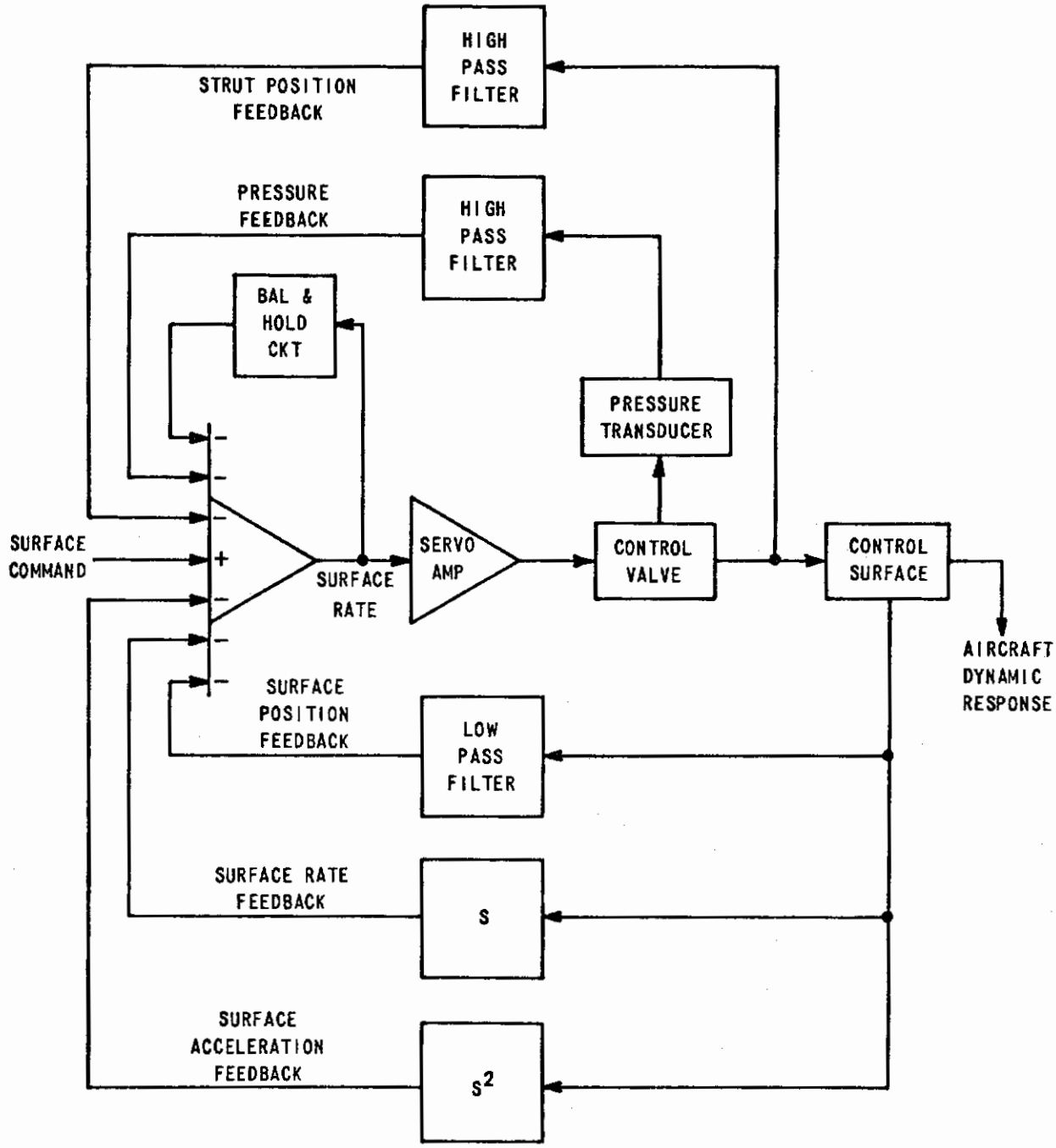

Figure 7.6 SIMPLIFIED DIAGRAM OF TYPICAL SURFACE POSITION SERVO

Pressure limiting check valves are coupled around each hydraulic actuator to prevent damage to the surfaces due to excessive surface hinge moments. In addition to these precautions, either safety pilot may disengage the system at any time by using a dump button if he feels that excessive control rates or vibrations are occurring.

To ensure that the flight control surfaces can be easily operated by the safety pilot when the TIFS system is "off", several safeguards are provided. These are described in Section 6.5.7.

A simplified block diagram of a throttle servo is presented in Figure 7.7. The throttle actuator consists of a constant speed motor and two dry magnetic particle clutches which transmit the motor torque to the cable capstan. The clutch operation provides an angular acceleration output at the capstan proportional to the throttle servo amplifier input. Rate feedback used in conjunction with position feedback produces an accurate high performance position servo. The balance servo is used to null signals to the position loop prior to throttle servo engagement to avoid undesirable engagement transients.

An adjustable electrical limit circuit allows independent variable minimum and maximum limits on the throttle command. As an additional safety precaution, the motor torque is limited to allow the safety pilots to override the throttle servos during normal operation. When the throttle servo system is disengaged, a solenoid-operated clutch disconnects the motor and drive assembly from the capstan.

7.2.4 MF-RF Patch Panel and Electronics

The MF-RF subsystem consists of a 5120-hole patch panel to provide the necessary flexibility for the variety of functions this subsystem must perform. The patch board contains ample capacity for programming all the possible TIFS loop configurations expected. In actuality, the MF-RF subsystem is a large analog computer designed for signal summation, filtering, switching, balance and hold, monitoring, and other special functions. The major function of the MF-RF subsystem is to interconnect the other major subsystems as illustrated in Figures 7.8 and 7.9.

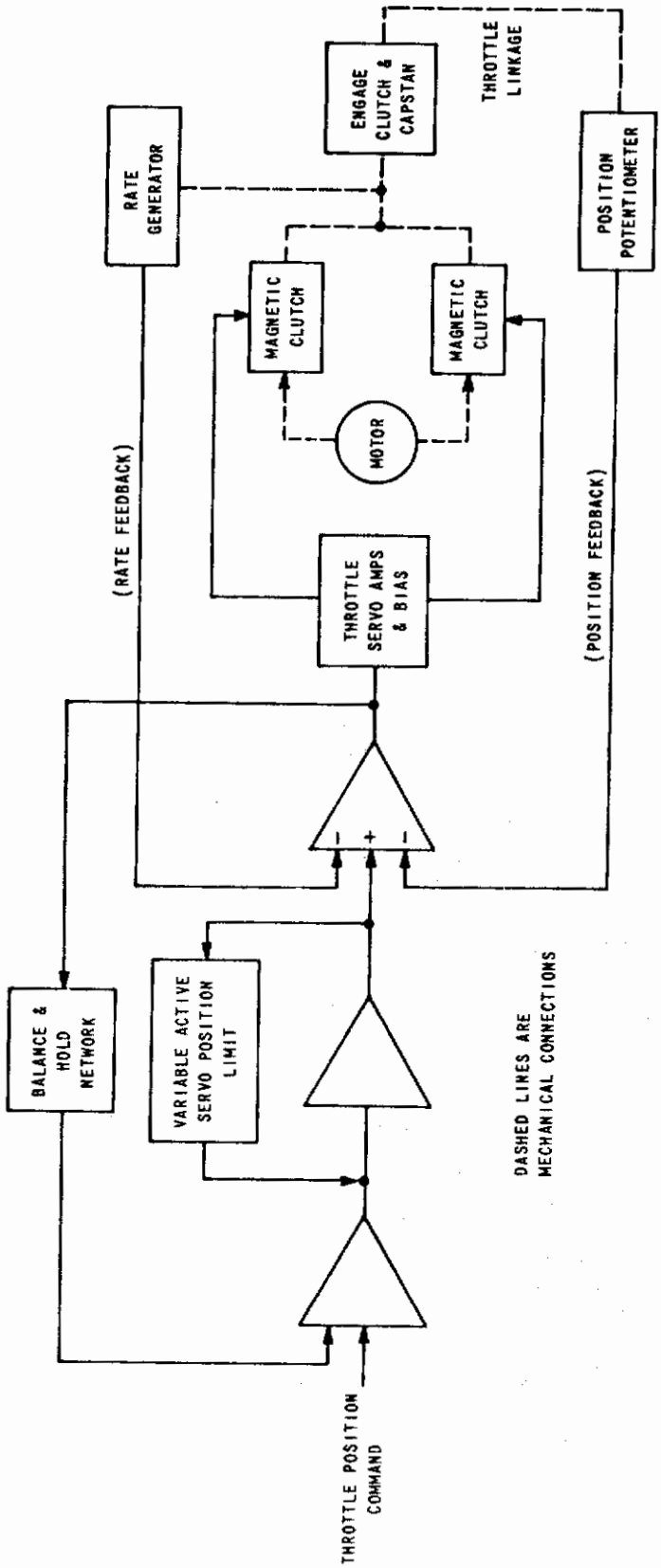

Figure 7.7 SIMPLIFIED DIAGRAM OF THROTTLE SERVO

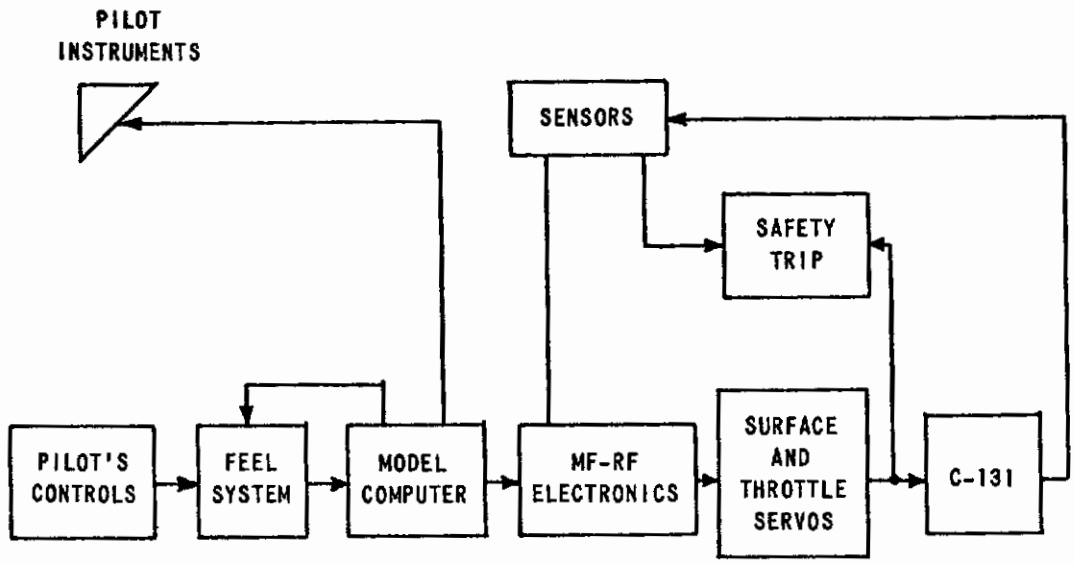

Figure 7.8 SYSTEM CONFIGURATION IN MODEL-FOLLOWING MODE

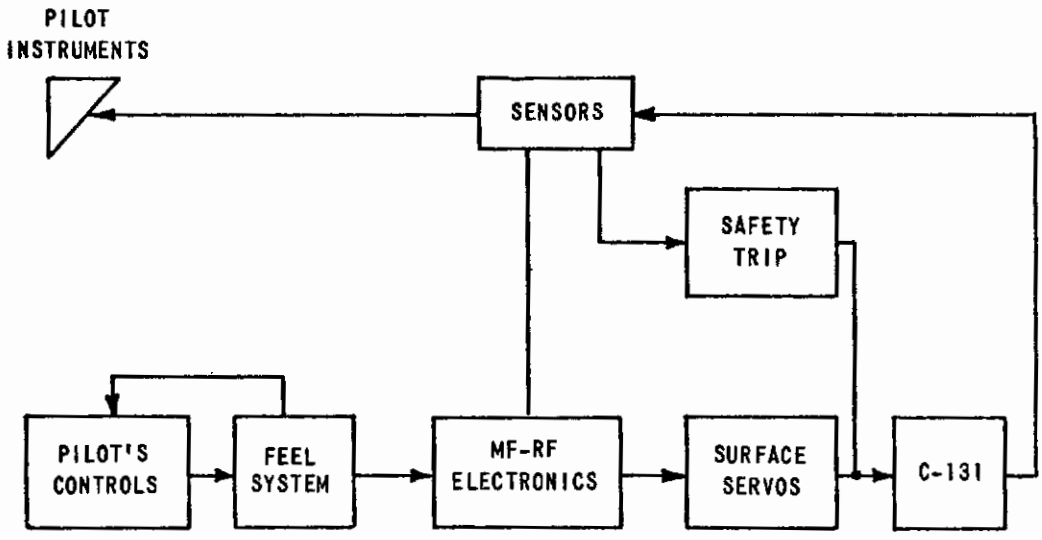

Figure 7.9 SYSTEM CONFIGURATION IN RESPONSE-FEEDBACK MODE

The MF-RF patch panel provides a means for:

1. Patching desired model and sensor signals to MF loops or RF loops.
2. Patching the MF and RF loops to servo command amplifiers.
3. Patching any system signal to any recording channel.
4. Patching appropriate signals to cockpit instruments.
5. Patching appropriate signals to test engineers' instruments.
6. Patching any desired signals to the safety trip system.
7. Function generator patching for feel system and any MF-RF loops.
8. Model input signal level and loop gain adjustment for the MF-RF system.
9. Interface functions between the ground computer and the airborne TIFS subsystems.

The present MF-RF subsystem capacity is 239 amplifiers. Of this total, 164 amplifiers are committed to multipliers, function generators and other nonlinear elements as follows:

- 8 special committed amplifiers
- 4 amplifiers used in balance and hold networks
- 120 amplifiers used in 20 multiplier-function generators (6 amplifiers are installed on each of 20 multiplier-function generators)
- 30 amplifiers used in 10 function generators for driving instruments (3 amplifiers are installed on each of 10 function generators)
- 2 amplifiers used in safety trip system.

The uncommitted amplifiers are all chopper stabilized and are divided as follows:

- 5 amplifiers used as integrators
- 64 amplifiers used as summers
- 6 amplifiers used as servo command amplifiers.

The fully expanded MF-RF subsystem capacity is 359 amplifiers. The future expansion consists of 120 amplifiers used in 20 multiplier-function generators.

Any signal available at the MF-RF patch panel may be monitored by a safety trip device. The safety trip system is a fail-safe device which disconnects the entire TIFS system when either the power is removed from the safety trip unit or if one of the input voltages to the safety trip exceeds a pre-determined safe limit. Eight safety trip inputs are available for monitoring signals that have the same positive as negative trip level. There are also six inputs for signals that require independent positive and negative trip settings. Provisions have been made to allow additional input signal circuits to be patched.

7.2.5 Model Computer

The model computer is a special-purpose, CAL-designed analog computer with the majority of the amplifiers chopper-stabilized. Nonlinear six-degree-of-freedom equations of motion of the aircraft to be simulated can be programmed on the computer. The computer is split into two identical parts (A and B) with two separate 2560-hole patch boards. There are proportionately more function generators and multipliers and fewer integrators than would be found in a general purpose computer.

The breakdown of the major components of the model computer is the following:

40 inverters
40 summers
20 integrators
8 resolvers
10 dual multipliers
8 quad multipliers
10 multiplier-dividers
10 balance and hold units
16 active limiters (with two pots in each unit)
120 servo set pots (non-center tapped)
20 manual set pots (center tapped)
10 function generators

The multipliers are all-electronic equivalents of servo multipliers with two and four inputs multiplied by a common variable. There are 300 amplifiers in the model computer of which 116 are committed to multipliers, function generators and other nonlinear networks. The remaining 184 uncommitted amplifiers are chopper-stabilized units and are grouped as follows:

40 inverters
40 summers
20 integrators
32 summers associated with 8 resolvers
20 summers associated with 10 dual multipliers
32 summers associated with 8 quad multipliers

The model computer has a total of 300 trunk lines which are grouped as follows:

80 output trunks to the MF-RF panel
80 input trunks from the MF-RF panel
60 trunks between sections A and B of computer
80 trunks to auxiliary equipment.

7.2.6 Pilot Instruments and Controls

Instruments

The flight panels in front of the pilot's and copilot's positions will contain operating flight instruments. These instruments will be servo or DC meters, driven from electrical signals, patchable on the MF-RF panel. It is possible to present data from either the TIFS sensors or the model computer on the flight instruments. The instrument panel will be divided into sections to allow the instruments to be readily removable and displays varied.

The initial TIFS installation will consist of the basic components of the USAF PI-FAX display. The following list details the instruments selected for TIFS.

Attitude Indicator - This instrument presents angle of pitch, angle of roll, turn rate, horizontal and vertical steering needles, GSI/Flight path angle/ displacement pointer and warning flags. A Lear type 4058 E supplied by the USAF will be used.

Auxiliary Landing Instruments

1) Landing Sequence Indicator - This instrument displays marker and altitude status to flare and touchdown. This instrument is Lear type 8703 E which has a multicolored electroluminescent display.

2) Speed Error Indicator - This instrument displays speed error on a meter mechanism and speed error rate on a strobed electroluminescent field. A Lear type 2717 A indicator is used.

3) Lateral Indicator - This instrument displays heading error and localizer data on two meter movements. Localizer rate information is displayed on a strobed electroluminescent field. This instrument is a Lear type 2716 A.

These instruments are driven from a display computer that supplies the 500 volt strobed rate field for the electroluminescent lighting.

Radar Altitude and Vertical Velocity Indicator - This "sandwich" type indicator will present absolute altitude (radar) and vertical velocity. (A special instrument will be built for this device.)

Horizontal Situation Display - This instrument is used to display magnetic heading, omni-DME or tacan, localizer, and a manual set command heading. A standard USAF instrument type AF/A24J-1 will be used for this display.

Machmeter, Airspeed, Rate of Climb, and Altimeter - These instruments will have presentations similar to standard Air Force indicators. The instruments will be DC servo or meter movements and specially built for this program.

Wing Sweep, Flaps, Landing Gear and Speed Brake Indicators - These instruments will be driven by the analog computer responding to cockpit controls and will be meter movement or light indications.

Angle of Attack, Accelerometer, Flight Path Angle - These instruments are not part of the PI-FAX display but may be added if necessary. These will be DC meter movement type instruments.

Engine Instruments - 4 each

% Thrust
% RPM
EGT (Exhaust Gas Temperature)
Fuel Flow

These sixteen instruments will be DC meter movement types driven by the analog computer.

Pilot's Controls

In addition to the feel and trim system controls, levers for thrust (4), wing sweep, flap, speed brake, and landing gear will be provided. Each will actuate potentiometers to produce electrical signals that can be used as inputs to the analog computer.

7.2.7 The Test Engineers' Consoles

The test engineers' consoles are the central monitoring stations for the TIFS. Because of the size and complexity of the system, two test engineer's consoles are provided. The No. 1 console is the central location for tasks related to model-following and response-feedback system performance, i.e., to compare model parameters to respective NC-131H variables, etc. The No. 2 console is the central monitoring station for the overall electronic and hydraulic systems operation.

No. 1 Flight Test Engineer's Console

The monitoring systems on the No. 1 test console fall into three distinct groups. The first consists of a series of dual needle indicators that display the primary flight variables. One pointer on each instrument displays the TIFS variable while the other displays the respective model variable. These dual indicators permit the test engineer to review quickly

the simulation fidelity since the difference between pointer indications represents model-following errors. A four-channel Brush Mark 240 strip chart recorder is the second major monitoring system located on the No. 1 test console. The recorder permits in-flight monitoring of the model and variable stability system variables. For each of the four channels, there is a ten-position switch for rapid selection of signals pre-patched on the MF-RF Panel. The wide bandwidth (full output frequency response of 55 Hz) of the Brush Mark 240 permits direct monitoring of flutter and servo responses.

The servo set pot system, the MF-RF and the model address systems comprise the third major monitoring system associated with the No. 1 test console. Although these subsystems are not on the No. 1 test console, they are located directly adjacent to the console within easy reach of the No. 1 test engineer. The MF-RF address system located to the left of the No. 1 test console can be used to monitor amplifiers and pots associated with the MF-RF control loops. The address system also contains a keyboard for selecting potentiometer coefficients. The address keyboard in the pot set mode selects a specific potentiometer and a servo drives that potentiometer to the coefficient indexed on the coefficient keyboard.

The model address panel located to the right of the No. 1 test console is the monitoring station for the model computer amplifiers and potentiometers. The model address panel also has a pot set mode similar to the MF-RF address system for servo setting the model potentiometers.

No. 2 Flight Test Engineer's Console

The No. 2 test engineer's console is the central monitoring station for the TIFS variable stability system operation. The primary electrical power sources are controlled and monitored at this location. Also, surface positions and safety features that include the engagement state are monitored and displayed at this console.

Engage and disengage switches, meters and lights are available for operation and monitoring. The digital recording system is located on the No. 2 test engineer's console.

Another major task of the No. 2 test engineer is to monitor the operation of the digital tape recording system.

7.2.8 Digital Tape Recording System

A digital tape recording system provides 58 channels of recorded information that is compatible with the IBM 360 system. The system can record at speeds of 50 to 100 samples of each channel per second. The system will record a 10-bit binary number plus a sign bit. The resulting recording system accuracy is approximately .2% or better. Each channel is filtered to avoid aliasing errors. The filter cutoff frequency changes automatically with system record speed so that the best possible recording bandwidth is utilized. The tape recorder is a 9-track, 800-byte-per-inch unit.

A complete ground playback system is provided for quick-look purposes. Any 8 of the 58 channels can be selected and played back on a strip chart recorder in analog form.

The complete digital tape recording system is on order from Aeroscience Electronics, Inc. 3800 Oakcliff Road, Atlanta, Georgia. The system is to be delivered in January 1968.

Performance Specification

The digital tape recording system will operate to the following specifications over the entire system environment specified.

Input:

Signal Capacity:	58 channels of analog information and up to 6 true-false inputs (0 and +28 VDC)
Frame Size:	60 channels normal, or 30 channels when one multiplexer is not installed.
Frame Rate:	100 frames per second and 50 frames per second for 60 channels.
Clock Stability:	System timing shall derive from a crystal oscillator stable within $\pm$ .05%.
Impedance:	1 megohm minimum shunted by less than 100 picofarads.
Level:	0 to 5 volts bipolar.

Encoding:

Code: Each sample will be encoded into a 10-bit-plus-sign code of sign-plus-absolute-value configuration.

Linearity: Conversion linearity will be within ± .05% ± 1/2 LSB (least significant bit).

Aperture: Encoding time is approximately 12 microseconds permitting data frequencies up to 10 Hz without increase in error.

Accuracy:

Total system accuracy from input signal level to digital codes shall be ± 0.2% of full scale for steady state signals. This includes multiplexing, digitizing linearity, comparator and reference drift, and quantizing errors. No aperture or aliasing errors are included in this figure since these values depend upon signal rate of change and frequency content.

Recorder:

Input Level: 0 VDC ± 1V for "0", 4 VDC ± 1V for "1".

Input Impedance: 10K ohm minimum.

Input Format: NRZ (nonreturn to zero) mark (NRZ-IBM).

Bit Packing: 800 bytes per inch.

Interchannel Timing: 6 microseconds max @ 60 in./sec

Dropout Rate: Approximately one bit in 10^6 bits.

Temperature: 0°C to 60°C

Vibration: 5 g random per procedure XIII of MIL-E-5272C

Shock: 25 g for 11 milliseconds

Altitude: 12,000 ft

7.3 LIST OF TECHNICAL MEMOS PERTAINING TO THE ELECTRICAL SUBSYSTEMS

A tabulation of the TIFS memos that pertain to the various electrical subsystems is presented in Table 7-8. These memos contain detailed descriptions and operational characteristics of each electrical subsystem.

Table 7-8
TIFS ELECTRONICS MEMOS

MEMO NO.	DATE	AUTHOR	SUBJECT
25	1/12/67	A. SCHELHORN	SENSOR BLOCK DIAGRAMS
26	1/20/67	A. SCHELHORN	MF-RF PATCH PANEL
27	1/20/67	A. SCHELHORN	AIRBORNE ANALOG COMPUTER ESTIMATE
35	2/6/67	A. SCHELHORN	FLIGHT DIRECTOR SIMULATION
40	2/13/67	R.H. ARENDT	OPERATIONAL AMPLIFIERS TO BE PURCHASED FOR THE TIFS
43	2/21/67	A. SCHELHORN	SURFACE SERVO BLOCK DIAGRAMS
44	2/22/67	A. SCHELHORN	PULSE-WIDTH MULTIPLIER-DIVIDER
46	2/27/67	R.H. ARENDT	TIFS FEEL SYSTEM
52	3/13/67	J. DITTENHAUSER	TIFS SENSOR BLOCK DIAGRAMS
REV. 1 OF 46	3/20/67	A. SCHELHORN	TIFS FEEL SYSTEM (REVISION 1)
53	3/20/67	J. DITTENHAUSER	DIODE FUNCTION GENERATORS

UNCLASSIFIED
Security Classification

DOCUMENT CONTROL DATA - R & D

(Security classification of title, body of abstract and indexing annotation must be entered when the overall report is classified)

1. ORIGINATING ACTIVITY *(Corporate author)*
Cornell Aeronautical Laboratory, Inc.
Buffalo, New York 14221

2a. REPORT SECURITY CLASSIFICATION
Unclassified

2b. GROUP

3. REPORT TITLE
Total In-Flight Simulator (TIFS) -- Preliminary Design Report

4. DESCRIPTIVE NOTES *(Type of report and inclusive dates)*
Technical Report, November 1966 - June 1967

5. AUTHOR(S) *(First name, middle initial, last name)*
Flight Research Department Staff
Cornell Aeronautical Laboratory, Inc.

6. REPORT DATE	7a. TOTAL NO. OF PAGES	7b. NO. OF REFS
August 1971	239	24

8a. CONTRACT OR GRANT NO.
F33615-67-C-1157
b. PROJECT NO.
684B
c.
d.

9a. ORIGINATOR'S REPORT NUMBER(S)

9b. OTHER REPORT NO(S) *(Any other numbers that may be assigned this report)*
AFFDL-TR-71-119

10. DISTRIBUTION STATEMENT
Approved for Public Release; Distribution Unlimited

11. SUPPLEMENTARY NOTES

12. SPONSORING MILITARY ACTIVITY
Air Force Flight Dynamics Laboratory
Wright-Patterson AFB, Ohio 45433

13. ABSTRACT

The TIFS research airplane has been developed by the Cornell Aeronautical Laboratory under the sponsorship of the Air Force Flight Dynamics Laboratory. As the most advanced in-flight simulation vehicle yet developed, it has been designed to provide Total In-Flight Simulation. This capability depends on two basic features of the aircraft. First is the addition of an evaluation cockpit which is entirely separate from the normal airplane's safety pilots' cockpit. Second is the control by a variable stability system of not only the moments about all three axes, but also the forces acting along the three axes. This report describes the TIFS airplane development during the period from November 1966 to June 1967.

DD FORM 1 NOV 65 1473

UNCLASSIFIED
Security Classification

UNCLASSIFIED
Security Classification

14. KEY WORDS	LINK A		LINK B		LINK C	
	ROLE	WT	ROLE	WT	ROLE	WT
In-Flight Simulation						
Simulation						
Research Aircraft						

*U.S.Government Printing Office: 1972 — 759-081/293

UNCLASSIFIED
Security Classification